INTERFERENCE HEATING DUE TO SHOCK IMPINGEMENT

ROBERT A. HASLETT
LOUIS G. KAUFMAN II
RICHARD F. ROMANOWSKI
MICHAEL URKOWITZ

"Approved for public release; distribution unlimited"

FOREWORD

This document presents experimental data for the pressure and heating amplification that occurs due to shock-boundary layer interactions. Design methods are developed from correlations of the data. The study was conducted by Grumman Aerospace Corporation under Contract F33615-71-C-1383, Project Number 1366, issued by the Air Force Flight Dynamics Laboratory, Wright-Patterson Air Force Base. This final report, originally submitted in May 1972, covers the complete contract duration from May 1971 to July 1972. The experimental program was conducted in Tunnel B at the Arnold Engineering Development Center with three test periods of approximately one week duration each in November 1971, February 1972 and March 1972.

The contract effort was directed by Mr. Gerald Burke (AFFDL/FXG) and Mr. Richard Neumann (AFFDL/FXG) of the Flight Dynamics Laboratory. The test Project Engineers at AEDC were Mr. Robert Hiers and Mr. Herbert Little of ARO Inc.

This technical report has been reviewed and is approved.

Philip P. Antonatos

PHILIP P. ANTONATOS

Chief, Flight Mechanics Division
Air Force Flight Dynamics Laboratory

ABSTRACT

Investigation of the interference heating phenomenon was conducted at Mach number 8 over a Reynolds number range from $.4 \times 10^6$ to 3.7×10^6 per ft in Hypersonic Wind Tunnel B of the von Karman Gas Dynamics Facility, Arnold Engineering Development Center. Shock generator models consisted of 1.5, 5, 10 and 15 deg wedges; 2.5, 7.5 and 12.5 deg cones; .5 and 2.0 in. diameter hemispheres and an orbiter-type vehicle. Shock receiver models included sharp and blunt flat plates and a booster vehicle. Both pressure distributions and heat transfer distributions (thermocouple and phase change paint) were obtained in the regions of shock impingement. The test program was organized in a building-block approach. A limited number of sharp plate runs were performed with a boundary layer trip to obtain turbulent data for comparison with other experiments. Our heating amplification for two-dimensional shocks agreed with previous results that

$$\frac{h_{peak}}{h_{Und}} = \left(\frac{p_{peak}}{p_{Und}}\right)^{.8}$$

Turbulent correlations were also obtained for three-dimensional conical and spherical shocks. The majority of our testing used wedge shocks impinging on the sharp plate with an initially laminar boundary layer. A wide range of Reynolds numbers were covered by testing at four tunnel pressures and three x locations on the plate. Laminar interactions correlated as

$$\frac{h_{peak}}{h_{Und}} = \left(\frac{p_{peak}}{p_{Und}}\right)^{.7}$$

Interactions that resulted in a turbulent boundary layer after impingement correlated as

$$\frac{h_{peak}}{h_{Und}} = 1.9\, p_{Und}^{.22} \times .55 \left(\frac{p_{peak}}{p_{Und}}\right)^{.8}$$

The effects of a very blunt leading edge and three-dimensional shock generators on laminar interactions were studied and some trends noted, but the data are not extensive enough for definite conclusions. Finally, the major correlations and trends resulting from the simple geometry testing were applied to the orbiter/booster configuration and compared to the actual test data.

CONTENTS

		Page
I	INTRODUCTION	1
II	EXPERIMENTAL PROGRAM	3
	1. Description of Models	3
	2. Test Conditions	7
	3. Data Reduction	8
III	TEST DATA OBTAINED	12
	1. Sharp Plate	12
	2. Blunt Plate	22
	3. Booster and Orbiter/Booster Configurations	24
	4. Data Log	29
IV	DATA CORRELATION	32
	1. Analytical Considerations	32
	2. Sharp Plate/Wedge Turbulent Interactions	36
	3. Sharp Plate/Wedge Initially Laminar Interactions	37
	4. Three Dimensional Shock Generators	39
	5. Blunt Plate Receiver	41
	6. Booster Receiver	41
	7. Design Methods	43
	8. Application of Methods to Orbiter/Booster	44
V	CONCLUSIONS	46
	REFERENCES	48

ILLUSTRATIONS

Figure		Page
1	Shock Generators and Sharp Flat Plate Receiver	66
2	Orbiter and Booster Paint Models	66
3	Wedge Shock Generator	67
4	Hemisphere - Cylinder Shock Generators	67
5	Cone-Cylinder Shock Generators (2.5^{o}, 7.5^{o})	67
6	Cone-Cylinder Shock Generators (7.5^{o}, 12.5^{o})	67
7	Orbiter Vehicle Shock Generator	68
8	Flat Plate Shock Receiver	69
9	Booster Vehicle Shock Receiver	70
10	Wedge Generator Installed in Forward Position with Sharp Flat Plate Receiver	71
11	Orbiter Generator Installed with Booster Receiver	72
12	Typical Thin Skin and Pressure Insert Cross-Sections	73
13	Reference Grid - Teflon Booster	74
14	Reference Grid - Teflon Orbiter	75
15	Planar Model Pressure Tap and Thermocouple Locations	76
16	Orbiter Model Pressure Tap and Thermocouple Locations	77
17	Booster Model Pressure Tap and Thermocouple Locations	78
18	Tunnel Cross-Section Showing Camera Set-Up for Phase Change Paint Tests	79
19	Position of Flat Plate Model in Test Section	80
20	Position of Booster Model in Test Section	81
21	Data Uncertainty	82
22	Undisturbed Heating Distribution on Sharp LE Plate; p_o = 400 psia (Groups 52 & 53)	83
23	Shadowgraph Photographs of Undisturbed Flow on Sharp LE Plate; p_o = 400 psia (Group 52)	83
24	Distributions of Undisturbed Heating Rates on Sharp LE Flat Plate	84
25	Undisturbed Pressure Distribution on Sharp LE Plate	85
26	Shadowgraph and Schlieren Photographs of Undisturbed Flows on Sharp LE Plate; p_o = 850 psia (Groups 108 & 254)	86
27	Shadowgraph and Schlieren Photographs of Tripped Boundary Layers on Sharp LE Plate; p_o = 850 psia (Groups 3 & 246)	87

ILLUSTRATIONS (Cont.)

Figure		Page
28	Undisturbed Pressure and Heating Distributions for Tripped Boundary Layers on Sharp LE Plate; p_o = 850 psia (Group 246; 3 & 4)	88
29	Heating and Pressure Distributions on Sharp Plate Caused by 10° Wedge Shock; p_o = 400 psia, x_i = 22 in. (Groups 63 & 282)	89
30	Shadowgraph and Schlieren Photographs of Interaction Caused by 10° Wedge Shock; p_o = 400 psia, x_i = 22 in. (Groups 63 & 282)	90
31	Heating and Pressure Distributions on Sharp Plate Caused by 15° Wedge Shock; p_o = 75 psia, x_i = 5 in. (Groups 96 & 317)	91
32	Shadowgraph and Schlieren Photographs of Interaction Caused by 15° Wedge Shock; p_o = 75 psia, x_i = 5 in. (Groups 96 & 317)	92
33	Heating and Pressure Distributions on Sharp Plate Caused by 1½° Wedge Shock; p_o = 850 psia, x_i = 11 in. (Groups 115 & 271)	93
34	Shadowgraph and Schlieren Photographs of Interaction Caused by 1½° Wedge Shock; p_o = 850 psia, x_i = 11 in. (Groups 115 & 271).	94
35	Heating and Pressure Distributions on Sharp Plate Caused by 10° Wedge Shock, p_o = 850 psia, x_i = 22 in. (Groups 217 & 268)	95
36	Shadowgraph and Schlieren Photographs of Interaction Caused by 10° Wedge Shock; p_o = 850 psia, x_i = 22 in. (Groups 217 and 268)	96
37	Heating and Pressure Distributions on Sharp Plate Caused by 15° Wedge Shock; p_o = 850 psia, x_i = 22 in. (Groups 218 & 275)	97
38	Shadowgraph and Schlieren Photographs of Interaction Caused by 15° Wedge Shock; p_o = 850 psia, x_i = 22 in. (Groups 218 & 275)	98
39	Boundary Layer Correction for Wedge and Cone Shock Strength Calculations	99
40	Pressure Amplification for the Wedge Generators and the Sharp Flat Plate (No Trip)	100
41	Shadowgraph of Interaction Caused by 5° Wedge Shock; p_o = 75 psia, x_i = 5 in.	101
42	Shadowgraph of Interaction Caused by 10° Wedge Shock; p_o = 75 psia, x_i = 5 in. (Group 95)	101

ILLUSTRATIONS (Cont.)

Figure		Page
43	Pressure Amplification for Cone and Hemisphere Cylinder Generators and Sharp Flat Plate (No Trip)	102
44	Lateral Heating and Pressure Distribution for p_o = 200 psia, and Nominal Impingement at 22 in. on Sharp Flat Plate (No Trip)	103
45	Shadowgraphs of Three Interactions at p_o = 200 psia and x_i = 22 in.	104
	a) 10° wedge (Group 85)	
	b) 12 ½° cone (Group 77)	
	c) 2 in. dia. hemisphere cylinder at Z_m = 1 in. (Group 82)	
46	Heating Distributions for Three Interactions on Sharp Flat Plate at p_o = 200 psia and x_i = 22 in.	105
	a) 10° wedge (Group 85)	
	b) 12 ½° cone (Group 77)	
	c) 2 in. dia. hemisphere cylinder at Z_m = 1 in. (Group 82)	
47	Heating Distribution on Sharp LE Plate Caused by 2.0 inch Hemisphere-Cylinder p_o = 850 psia, x_i = 5 inches	106
48	Heating and Pressure Distributions, on Plate with BL Trip, Caused by 10° Wedge Shock; p_o = 850 psia, x_i = 22 in. (Groups 8 & 250) . . .	107
49	Shadowgraph and Schlieren Photographs of 10° Wedge Shock Interacting with Tripped Boundary Layer; p_o = 850 psia, x_i = 22 in. (Groups 8 & 250)	108
50	Comparison of Measured Pressure Ratios for Wedge Generators with Tripped and Untripped BL at 850 psia and x_i = 22 in.	109
51	Heating and Pressure Distributions, on Plate with BL Trip, caused by 15° Wedge Shock; p_o = 850 psia, x_i = 22 in. (Groups 6 & 251) . . .	110
52	Shadowgraph and Schlieren Photographs of 15° Wedge Shock Interacting with Tripped Boundary Layer; p_o = 850 psia, x_i = 22 in. (Groups 6 & 251)	111
53	Heating and Pressure Distributions, on Plate with BL Trip, Caused by Raised 15° Wedge Shock; p_o = 850 psia, x_i = 22 in. (Groups 210 & 259)	112

ILLUSTRATIONS (Cont.)

Figure		Page
54	Shadowgraph and Schlieren Photographs of Raised 15° Wedge Shock Interacting with Tripped Boundary Layer; p_o = 850 psia, x_i = 22 in. (Groups 210 & 259)	113
55	Heating and Pressure Distributions, on Plate with BL Trip, Caused by $7\frac{1}{2}^o$ Cone Shock; p_o = 850 psia, x_i = 22 in. (Groups 19 & 248)	114
56	Shadowgraph and Schlieren Photographs of $7\frac{1}{2}^o$ Cone Shock Interacting with Tripped Boundary Layer; p_o = 850 psia, x_i = 22 in. (Groups 19 & 248)	115
57	Frames from Motion Pictures Taken During Temperature Sensitive Paint Run for $7\frac{1}{2}^o$ Cone Shock Interacting with Tripped Boundary Layer; p_o = 850 psia, x_i = 22 in. (Group 377) (2 sheets)	116
58	Comparisons of Heating Distributions on Sharp LE Plate Caused by 0.5 in. Hemisphere and 7.5° Cone for Turbulent and Laminar Boundary Layers	118
59	Undisturbed Pressure and Heating Distributions on Blunt Plate; p_o = 850 psia (Groups 348, 104, & 105)	119
60	Shadowgraph and Schlieren Photographs of Undisturbed Flows on Blunt LE Plate; p_o = 850 psia, (Groups 104, 105, and 348)	120
61	Faired Distributions of Undisturbed Heating Rates and Pressures on Blunt LE Plate	121
62	Heating and Pressure Distributions on Blunt Plate Caused by 10° Wedge Shock; p_o = 850 psia, x_i = 22 in. (Groups 45 & 347)	122
63	Shadowgraph and Schlieren Photographs of 10° Wedge Shock Interacting with Blunt Plate Boundary Layer; p_o = 850 psia, x_i = 22 in. (Groups 45 & 347)	123
64	Heating and Pressure Distributions on Blunt Plate Caused by 10° Wedge Shock; p_o = 75 psia, x_i = 22 in. (Groups 137, 138, & 356)	124
65	Shadowgraph and Schlieren Photographs of 10° Wedge Shock Interacting with Blunt Plate Boundary Layer, p_o = 75 psia, x_i = 22 in. (Groups 137, 138, & 356)	125
66	Heating and Pressure Distributions on Blunt Plate Caused by 10° Wedge Shock; p_o = 850 psia, x_i = 7 in. (Groups 46, 345, & 346).	126

ILLUSTRATIONS (Cont.)

Figure		Page
67	Shadowgraph and Schlieren Photographs of 10^{o} Wedge Shock Interacting with Blunt Plate Boundary Layer; p_o = 850 psia, x_i = 7 in. (Groups 46, 345 & 346)	127
68	Heating and Pressure Distributions on Blunt Plate Caused by 10^{o} Wedge Shock; p_o = 75 psia, x_i = 7.6 in. (Groups 135 & 357)	128
69	Shadowgraph and Schlieren Photographs of 10^{o} Wedge Shock Interacting with Blunt Plate Boundary Layer; p_o = 75 psia, x_i = 7.6 in. (Groups 135 & 357)	129
70	Heating and Pressure Distributions on Blunt Plate Caused by 15^{o} Wedge Shock; p_o = 75 psia, x_i = 7 in. (Groups 136 & 359)	130
71	Shadowgraph and Schlieren Photographs of 15^{o} Wedge Shock Interacting with Blunt Plate Boundary Layer; p_o = 75 psia, x_i = 7 in. (Groups 136 & 359)	131
72	Heating Distribution on Blunt Plate Caused by α = 0 Orbiter Shock; p_o = 850 psia, x_i = 7 in. (Group 44)	132
73	Shadowgraph Photographs of α = 0 Orbiter Shock Interacting With Blunt Plate Boundary Layer; p_o = 850 psia, x_i = 7 in.	132
74	Undisturbed Heating Distributions on Booster; p_o = 850 psia (Groups 150 & 151)	133
75	Undisturbed Heating Distributions on Booster, p_o = 75 psia (Groups 176 & 177)	134
76	Undisturbed Pressure Distributions on Booster, p_o = 75 and 850 psia (Groups 363 & 372)	135
77	Frames from Motion Pictures Taken during Temperature-Sensitive Paint Run. Phase change temperature = 573^{o} R, Booster Alone, p_o = 850 psia (Group 194)	136
78	Undisturbed Heating and Pressure Distributions on Orbiter at Zero Angle of Attack	137
79	Undisturbed Heating and Pressure Distributions on Orbiter at 10 Degree Angle of Attack	138
80	Interference Heating Distributions on Booster Caused by 0.5 inch Hemisphere; p_o = 850 psia (Group 157)	139

ILLUSTRATIONS (Cont.)

Figure		Page
81	Interference Heating Distributions on Booster Caused by Oribter at $\alpha_{ORB} = 0$, $p_o = 850$ psia (Groups 391 & 392)	140
82	Interference Heating Distributions on Booster Caused by Orbiter at $\alpha_{ORB} = 10^o$, $p_o = 850$ psia (Groups 403 & 404)	141
83	Interference Heating Distributions on Booster Caused by 10^o Wedge, $p_o = 75$ and 850 psia (Groups 179 & 153)	142
84	Frames from Motion Pictures Taken during Temperature-Sensitive Paint Run. Phase change temperature = 810^o R, Booster and 10^o Wedge, $p_o = 850$ psia (Group 196)	143
85	Frames from Motion Pictures Taken during Temperature-Sensitive Paint Run. Phase change temperature = 960^oR, Booster and 10^o Orbiter, $p_o = 850$ psia (Group 462)	144
86	Interference Pressure Distributions on Booster Caused by 10^o Wedge, $p_o = 75$ and 850 psia (Groups 364, 373, 447, and 452)	145
87	Interference Heating Distributions on Booster Caused by Orbiter ($\alpha_{ORB} = 0$) at Three Different Separation Distances from Booster, $p_o = 75$ psia (Groups 409-416).	146
88	Interference Pressure Distributions on Booster Caused by Orbiter ($\alpha_{ORB} = 0$) at Two Different Separation Distances from Booster, $p_o = 75$ psia (Groups 442 and 444)	147
89	Interference Heating Distributions on Booster Caused by 0.5 inch Hemisphere, $p_o = 75$ psia (Group 182)	148
90	Interference Heating and Pressure Distributions on Forward Part of Booster Caused by 10^o Wedge, $p_o = 75$ psia (Groups 178 & 374). . .	149
91	Interference Heating Distributions on Orbiter ($\alpha_{ORB} = 0$) Caused by Booster at Three Different Separation Distances Between Orbiter and Booster, $p_o = 75$ psia (Groups 411, 414, 417, and 434-436). . .	150
92	Interference Heating Distributions on Orbiter $\alpha_{ORB} = 0$ and 10^o) Caused by Booster, $p_o = 75$ and 850 psia (Groups 393, 405, 426, and 431)	151
93	Interference Pressure Distributions on Orbiter Centerline Caused by Booster ($\alpha_{ORB} = 0$ and 10^o), $p_o = 75$ and 850 psia (Groups 442-444, 447, and 452)	152

ILLUSTRATIONS (Cont.)

Figure		Page
94	Ratio of Apparent Start of Boundary Layer Before & After Shock Impingement	153
95	Sharp Plate - Wedge Data, Turbulent Boundary Layer	153
96	Sharp Plate - Wedge Data, Initially Laminar Boundary Layer	154
97	Transition Pressure Ratio	155
98	Sharp Plate Laminar Baseline Data	156
99	Correlation of Apparent Start of Turbulent Boundary Layer	156
100	Sharp Plate - Cone Data, Turbulent Boundary Layer	157
101	Sharp Plate - Sphere Data, Turbulent Boundary Layer	157
102	Correlation of Sphere Data	158
103	Sharp Plate - Cone Data, Initially Laminar Boundary Layer	159
104	Sharp Plate - Sphere Data, Initially Laminar Boundary Layer	160
105	Blunt Plate - Wedge Data, Initially Laminar Boundary Layer	161

TABLES

I	Run Schedule Overview	50
II	Data Obtained on Flat Plate with Sharp Leading Edge	51
III	Data Summary	52
IV	Reference Conditions for Heat Transfer Data	63
V	Data Obtained on Flat Plate with Blunt Leading Edge	64
VI	Data Obtained on Booster and Booster-Orbiter Configurations	64
VII	Flow Properties for Heat Transfer Equations	65

LIST OF SYMBOLS

C_p	Specific heat (BTU/lb_m)
D	Shock generator diameter (in.)
h	Heat transfer coefficient (BTU/ft^2 - hr - ^oR)
h_{REF}	Reference heat transfer coefficient based on heating at stagnation point of 1 in. dia sphere at wind tunnel conditions (BTU/ft^2 - hr - ^oR)
k	Thermal conductivity (BTU/ft - hr - ^oR)
M	Mach number
Nu	Nusselt Number - hx/k
p	Absolute static pressure (psf)
p_o	Tunnel stagnation pressure (psia)
Pr	Prandtl number - $\mu C_p/k$
Re	Reynolds' number - $\rho Vx/\mu$
T	Static temperature (^oR)
T_o	Tunnel stagnation temperature (^oR)
V	Velocity (ft/sec)
x	Distance from boundary layer origin (ft.)
x_i	Nominal location of shock impingement measured from receiver leading edge (in.)
Z	Vertical separation between shock generator $\mathbb{Q}$ and receiver (in.)
Z_m	Minimum vertical separation between shock generator and receiver (in.)
α	Angle of attack (deg.)
δ	Boundary layer thickness (ft)
δ^*	Boundary layer displacement thickness (ft)
ρ	Density (lb/ft^3)
μ	Viscosity (lb_m/ft^3)

Subscripts

aw	Based on adiabatic wall temperature
BL	Point where shock strikes boundary layer
LAM	Laminar boundary layer
peak, PK	Value at location of maximum amplification
plate	Point where generator shock strikes receiver
T	Value at boundary layer transition
TURB	Turbulent boundary layer
Und	Based on undisturbed boundary layer
w	Based on wall temperature
1	Value upstream of generator shock
2	Value downstream of generator shock
3	Value downstream of reflected generator shock
*	Evaluated at Eckert's reference temperature
∞	Free stream condition

Section I

INTRODUCTION

The increase in heating that occurs when a shock wave impinges on a vehicle surface can be a major design problem at high speeds. Consequently, the subject has received increasing attention as aircraft and missile speeds increase. Ryan, in Ref. 1, summarizes the analytical and experimental literature from 1947 to 1968. Shock interaction with a turbulent boundary layer has been treated mostly by experiment. Sayano, in 1962 (Ref 2), presented an empirical correlation of the heating amplification as a function of the pressure amplification which, in turn, can be determined by a straightforward inviscid calculation. Several analytical approaches to the laminar case have been proposed. Murphy, in Ref 3, reviewed three of the methods, and concluded that they agreed with the data at low Mach numbers and shock strengths but deviated for strong shock waves at hypersonic speeds. Rose, in Ref 4, proposed a two-layer approach applicable to laminar or turbulent boundary layers. While all the analytical methods provide insight into the problem, they are not yet refined to the point of being applicable for design calculations at hypersonic speeds. Markarian, therefore in Ref 5, presented empirical correlations of heating amplification data for various shock strengths and laminar, transitional and turbulent boundary layers. The purpose of our study is to extend the empirical approach of Sayano and Markarian to provide the design engineer with a simple method of making preliminary heating estimates. Turbulent amplifications are relatively well behaved and several investigators have proposed the correlation,

$$\frac{h_{peak}}{h_{Und}} = \left(\frac{p_{peak}}{p_{Und}}\right)^{N}$$

where N is .8 to .85. We therefore took only limited turbulent data, primarily to show consistency with other data, although some new data with three-dimensional shocks were also taken. The main emphasis of our program is to investigate the laminar/transitional regime at a hypersonic Mach number. Our goal is a correlation of flat plate heating amplification as a function of Reynolds number and wedge shock strength. Since the design engineer faces practical problems where the incident shock cannot be considered two-dimensional, we have also taken data using cone and sphere shock generators. The effect of plate pressure gradient is investigated using a blunt leading edge. Finally we will treat the practical problem of two airplane shapes (orbiter and booster) in close proximity. Predictions

based on the correlations of simple shape data will be compared to the airplane test data. The sharp flat plate receiver and the various shock generators are shown in Figure 1. The orbiter and booster phase change paint models are shown in Figure 2.

Section II

EXPERIMENTAL PROGRAM

This section will summarize the model design and the test program. Detailed discussion and drawings of the models are contained in the test report (Ref 6).

1. DESCRIPTION OF MODELS

The models consist of a set of stainless steel shock generators which include one 6 x 9 in. flat plate wedge, two hemisphere-cylinders having respective diameters of 2.0 and .5 in., one 2.5 deg semi-vertex angle cone-cylinder with a .5 in. base diameter, two 7.5 deg semi vertex angle cone-cylinders with respective base diameters of 1.5 in. and 2.5 in., one 12.5 deg semi-vertex angle cone-cylinder with a 2.5 in. base diameter, and an aerodynamic configuration representative of a typical shuttle orbiter vehicle having a spherical nose radius of .25 in. These generators are shown schematically in Fig. 3 thru 7.

Each generator may be positioned above any one of three instrumented shock receiver configurations: namely, a flat plate having interchangeable blunt and sharp leading edges; a 1.0 in. diameter hemisphere-cylinder (not used in the current program); and an aerodynamic configuration representative of a typical shuttle booster vehicle (See Fig. 8 and 9).

Schematics of typical generator-receiver arrangements are shown in Figures 10 and 11. All support members are fabricated from stainless steel. Wedge generator angles of attack were selected at 1.5, 5, 10 and 15 deg by rotating the support blade sector with respect to the support blade. The sector rotates about a fixed point relative to the support blade, which is coincident with the reference point of each shock generator when that generator is mounted on the sector.

The model support system allows independent horizontal and vertical positioning of the generators above the receiver. The support blade is free to slide vertically in the forward end of the horizontal support arm. A total of 7 inches of vertical travel in 0.1-in. increments is possible. The shaft of the support arm is free to slide horizontally in a split clamp located at the upper end of the support stand, allowing a total of 20 in. of horizontal travel in 0.1-in. increments.

The flat plate shock receiver (Fig. 8) is essentially a frame designed to accept three interchangeable 24 x 24 x .5 in. instrumented inserts for the separate acquisition of pressure,

thin-skin heat transfer and phase change paint heat transfer distribution data. The receiver frame will also accept either a blunt or sharp leading edge.

Typical cross-sections of the thin skin (thermocouple) and pressure inserts are shown in Fig. 12. The thin-skin insert consists of a nominal .050-in. thick sheet of AISI 321 stainless steel mounted on a slab of Teflon. Low friction slide washers and lock nuts are used to fasten the skin to the slab as shown in Fig. 12a. This permits the skin to slide on the Teflon, which is free to slide on the frame. Such a design was utilized for expansion compensation. The stainless steel sheet is instrumented with 121 laser welded thermocouples primarily along its longitudinal centerline. A .75-in. wide channel is cut through the Teflon slab in instrumented areas to minimize heat conduction from the skin into the Teflon slab in this region.

The pressure insert is a solid stainless steel plate instrumented with 121 pressure taps at the same locations as the thermocouples of the thin-skin insert. The insert is bolted to the receiver frame as shown in Fig. 12b. Slide washers are used to provide compensation for thermal expansion.

The phase change paint insert is a solid slab of black Teflon which is secured to the frame in the same manner as the thin skin insert. Ten thermocouples, five to either side of the longitudinal centerline, are also embedded in the slab for initial temperature measurement.

All three flat plate inserts are equipped for installation of a boundary layer trip device 1.5 in. from their forward edges. This locates the trip 4.0 in. aft of the model leading edge when the inserts are installed on the receiver frame (See Fig. 8). The trip is constructed of .125-in. diameter ball bearings set .371-in. apart from center to center, which are recessed and soldered into beveled steel strips. Due to the recess, the effective trip height with respect to the strip upper surface is .081 in. The trips are installed for selected sharp flat plate runs to investigate shock interaction with an initially turbulent boundary layer.

Two booster vehicle shock receivers of identical configuration are available. The first is fabricated from black Teflon. This model is used solely for the acquisition of phase change paint heat transfer distribution data. A reference grid pattern of embedded white Teflon rod is incorporated to facilitate data reduction (See Fig. 13). The second booster model is fabricated from stainless steel and is designed for the separate acquisition of pressure and thin-skin heat transfer distribution data. The model consists of three sections, i.e., nose, body and wing. (See Fig. 9). Three interchangeable nose pieces are

available: the first is pressure-instrumented and contains 56 taps; the second is instrumented with 118 thermocouples, and the third is a spare containing no instrumentation at all. A single wing section has provision to accept interchangeable inserts as indicated by the cross-hatched areas of Fig. 9. Three are provided: a pressure insert with 44 taps; a thin-skin insert with 82 thermocouples; and an uninstrumented spare. The instrumented wing inserts are similar in design to those of the flat plate receiver. The booster wing and nose sections attach to a common body section which accepts the support sting.

Two orbiter vehicle shock generators of identical configuration are also available. The first is fabricated from black Teflon. This model is tested with the Teflon booster receiver for the determination of mutual interference heat transfer distributions using the phase change paint technique. The model incorporates an embedded white Teflon reference grid pattern as shown in Fig. 14. The second orbiter model is fabricated from stainless steel and is designed for the separate acquisition of pressure and thin-skin heat transfer distribution data. This model may also be used as an uninstrumented shock generator. As in the case of the booster wing section, the steel orbiter can accept three interchangeable inserts: pressure instrumented, thermocouple instrumented and uninstrumented spare. The pressure insert contains 100 taps and the thin skin insert 200 thermocouples. Insert location is indicated by the cross-hatched areas of Fig. 7.

a. Instrumentation

Thirty gage chromel-alumel premium grade wire was used for all thermocouple instrumentation. All thermocouples used to acquire thin-skin data were laser welded to nominal .050 in. thick AISI 321 stainless steel.

The thin-skin flat plate insert contains 121 thermocouples located and identified as shown in Fig. 15. One hundred sixteen of these are installed .2 in. apart along the longitudinal centerline of the insert. The remaining five are spaced .8 in apart along a line normal to the centerline at a station 21.5 in. aft of the insert's front edge (24 in. from the leading edge).

Ten thermocouples are embedded in the Teflon phase change paint flat plate insert. These are used for initial temperature measurement of the material prior to model injection. Five thermocouples are positioned 5 in. apart along longitudinal lines located 2.5 in. to either side of the insert centerline.

The thin-skin orbiter insert contains 200 thermocouples located and identified as shown in Fig. 16. They are positioned along six rays which emanate from a point on the

longitudinal centerline located 2.253 in. aft of the nose section. Thermocouples are spaced .2 in. apart along their respective rays.

The locations of booster thermocouples and their numerical identification are shown in Fig. 17. The instrumented nose piece contains 118 thermocouples which are distributed .2 in. apart along three longitudinal rays and 10 deg apart along the circumferences of two cross-sections. The longitudinal rays emanate from the nose origin and are defined by the intersection of the booster lower surface contour and the θ=0, 60, and 90 deg radial planes. Instrumented cross-sections are located 1.983 in. and 7.957 in. aft of the nose origin.

The booster wing thin-skin insert is instrumented with 82 thermocouples as shown in Fig. 17. Thirty-four of these lie along each extension of the θ=60 deg and θ=90 deg nose piece longitudinal rays. The remaining 14 lie along a line normal to these extensions at a station 15.6 in. aft of the booster nose origin.

Stainless steel tubing of .063 in. outside diameter and .012 in. wall thickness was used for all pressure instrumentation. This tubing is silver soldered to larger tubing of .093 in. outside diameter and .012 in. wall thickness approximately 1 ft. aft of the base of the assembled models. The extension tubing is 18 ft. in length.

The flat plate pressure insert contains 121 pressure taps whose locations are identical to those of the thermocouples installed in the thin-skin insert. Additional pressure taps are installed in the interchangeable blunt and sharp flat plate receiver nose pieces. Each piece contains two pressure taps located 1 in. and 2 in. aft of the leading edge stations. This instrumentation is in line with the insert instrumentation when the nose pieces are installed on the receiver frame (See Fig. 15).

One hundred pressure taps are installed on the orbiter pressure insert. These are distributed along the longitudinal centerline (Ray 3) and Rays 1 and 2 (See Fig. 16), and duplicate the thermocouple locations on those rays.

The pressure-instrumented booster nose contains 56 taps which are distributed along longitudinal rays determined by the θ=90 and 120 deg radial planes. Forty-six of these are installed at locations identical to those of thermocouples 324-369 on the thin-skin booster nose. The remaining 10 are uniquely positioned .4 in. apart, symmetrically opposite to the locations of thermocouples 431, 433, 435, 437, 439, 441, 443, 445, 447 and 449 (See Fig. 17).

The booster wing pressure insert contains 44 taps which are positioned along the

extensions of the θ=90° and 120° nose piece longitudinal rays. Thirty-four of these are installed at locations identical to those of thermocouples 370-403 on the thin-skin booster wing insert. The remaining ten are uniquely positioned .4 in. apart symmetrically opposite to the locations of thermocouples 451, 453, 455, 457, 459, 461, 463, 465, 467 and 469 as shown in Fig. 17.

Model surface pressures were measured by 1 psid and 15 psid transducers.

Phase change paint data pictures were obtained with 70 mm Varitron cameras at 2 frames per second framing rate up to 15 seconds; after 15 seconds the rate was reduced to 1 frame per second. Fluorescent bulb light banks were used to illuminate the test section. The film used was Kodak TR1-X Pan black and white. The time of each picture taken was recorded on magnetic tape and, when correlated with wind tunnel conditions, was used to calculate the heat-transfer coefficient corresponding to the particular elapsed time and melt temperature of the paint. Fig. 18 shows the camera setups used to acquire phase change paint data.

2. TEST CONDITIONS

Prior to each run, the shock generator was set at the proper angle of attack and positioned above the receiver at a predetermined location. Generator locations were defined by the horizontal and vertical coordinates of the generator reference point denoted as X_{z_m} and Z_m, respectively. Reference coordinate systems applying to each receiver are shown in Fig. 19 and 20. The models were injected into the flow following the establishment of the required test conditions. Injection time from fully retracted to fully injected positions was 2.05 seconds. The approximate locations in the test section of the flat plate and booster receivers during data acquisition are shown inFig. 19 and 20. Receiver alignment with the flow was monitored visually by use of an externally located scope. Adjustments were accomplished by varying the angle of the main sting support system. Alignment was adjusted, following tunnel pressure changes, to compensate for attitude variation due to changing air loads.

All thin-skinned model installations were followed by a continuity check of the individual thermocouples. A thin-skin run was initiated by model injection and the data acquisition period varied from 5 to 10 seconds depending on the configuration. Shadowgraphs were taken through either or both the viewing ports while data was being recorded. Following model retraction from the test section, high pressure air was used for cooling.

All pressure model installations were followed by leak check of the individual pressure taps. A pressure run was initiated by model injection. The model remained in the test section while stabilization of the surface pressures were monitored in the control room. Stabilization periods were lengthy and varied according to the configuration. Once the pressures were considered stabilized, data acquisition was initiated. Schlieren photographs were taken through either or both of the viewing ports while data was being recorded. A phase change paint run was initiated by model injection. Cameras were activated just prior to the time the model reached its fully injected position in the test section. Data was acquired over about a 60 second interval and filming was terminated as model retraction began. High pressure air was used for cooling following each run.

In all, a total of 290 thermocouple, 141 pressure and 41 phase change paint runs were made. Table I shows an overview of the run schedule and the four nominal free stream test conditions.

3. AEDC DATA REDUCTION

a. Thermocouple Heat Transfer Data

The reduction of thin skin thermocouple data normally involves only the calorimetric heat balance which, in coefficient form, is

$$h_T = \rho_{STL} \, B \, C_{p,STL} \left[\frac{d\,T_W/dt}{T_o - T_W} \right] \qquad (1)$$

h_T = Heat transfer coefficient $BTU/ft^2\text{-}hr\text{-}^oR$

ρ_{STL} = Density of stainless steel model skin, lb/ft^3

B = Model skin thickness at thermocouple location, ft

$C_{p,\,STL}$ = Specific heat of stainless steel, $BTU/lb\text{-}^oR$

dT_w/dt = slope of temperature-time curve, $^oR/hr.$

t = time, hr.

T_o = Tunnel Total Temperature, ^oR

T_w = Skin temperature, ^oR

Radiation and conduction losses are neglected in this heat balance and data reduction simply requires evaluation of dT_w/dt from the temperature-time data and determination of model material properties. For these tests, radiation effects were negligible; however, lateral conduction in the thin skin was potentially significant in the impingement regions of the models where large gradients in heating rates were expected.

Separation of variables and integration of Equation (1) assuming constant ρ_{STL}, B, $C_{p,\,STL}$ and T_o yields

$$\frac{h_T}{\rho_{STL}\, B\, C_{p,\,STL}} (t-t_i) = \ell n \left[\frac{T_o - T_{w,i}}{T_o - T_w} \right] \tag{2}$$

where i refers to initial conditions.

Differentiation of Equation (2) with respect to time gives

$$\frac{h_T}{\rho_{STL}\, B\, C_{p,\,STL}} = \frac{d}{dt} \left[\ell n \left(\frac{T_o - T_{w,i}}{T_o - T_w} \right) \right] \tag{3}$$

Since the left side of Equation (3) is a constant, plotting $\ell n \left[\frac{T_o - T_{w,i}}{T_o - T_w} \right]$ versus time will give a straight line if conduction is negligible.

The data were evaluated in this manner and, generally, a linear portion of the curve was found for all thermocouples. For high heating rates, such as experienced in the impingement regions, the linear portion was quite short. A linear least squares curve fit of $\ell n \frac{T_o - T_{wi}}{T_o - T_w}$ versus time was applied to the data beginning at the time at which the model reached the tunnel centerline and extending for a time span which was a function of the heating rate, shown below:

Heating Rate, $^oR/sec$	Time Span of Data Used, Sec	Number of Data Points Used
$4 \leq dT_w/dt$	0.5	11
$2 \leq dT_w/dt < 4$	0.6	13
$dT_w/dt < 2$	1.0	21
$dT_w/dt < 1$	2.0	41

Strictly, the value of CP STL is not constant as assumed, and the relation

$$C_{p,\,STL} = A_o + A_1 (T_w) + A_2 (T_w)^2 + A_3 (T_w)^3, \tag{4}$$

was used with appropriate coefficients and the value of T_w at the midpoint of the curve fit. The maximum variation of $C_{p,\,STL}$ over any curve fit was less than one percent; thus the assumption of constancy was not grossly violated. A constant 494 lb_m/ft^3 was used for ρ_{STL} and measured values of skin thickness, B, for each thermocouple were used. Use of the data reduction equations in coefficient form, and restriction of the fit times to linear portions of the curve should preclude the necessity for correcting for lateral conduction errors.

The data include a wide range of heat-transfer rates, the lowest of which have temperature-time slopes which are at the lower limit of descrimination of the data acquisition system (0.2 deg R/sec). The uncertainty of the data is a function of the temperature slope, and Fig. 21 illustrates the uncertainties encountered. First the uncertainty (1σ) of the straight-line data fit is shown. Also shown is the uncertainty curve for the total system, including test condition variations, variations in model pitch angles caused by wind loads for different configurations, and plate surface irregularities occurring as a result of shock impingement.

b. Phase Change Paint Heat Transfer Data

Phase change paint data were reduced according to the semi-infinite slab solution of the transient one-dimensional heat conduction equation as developed in Ref. 7. The solution is given as

$$\bar{T} = 1 - e^{\beta^2} \operatorname{erfc} \beta$$

Where the complementary error function is given as

$$\operatorname{erfc} \beta = \frac{2}{\pi} \int_{\beta}^{\infty} e^{-\lambda^2} d\lambda$$

The temperature parameter T is defined as

$$\bar{T} = \frac{T_{pc} - T_i}{R(T_o) - T_i}$$

where i refers to initial conditions and

T_{pc} = phase change temperature of the paint, ^{o}R

R = Recovery factor

The parameter, $\bar{T}$, therefore, is a constant for a particular run. Corresponding to each value of $\bar{T}$ there exists a singular value of β
This parameter was used to compute the heat transfer coefficient corresponding to a phase change line at any time during the run from the equation

$$h = \frac{\beta \left[(\rho_{TEF}) \ (C_{p,\,TEF}) \ (k_{TEF}) \right]^{.5}}{t^{.5}}$$

Where

h = Heat transfer coefficient, $BTU/ft^2 - hr - {}^{o}R$

ρ_{TEF} = Density of Teflon model material, lb/ft^3

$C_{p,TEF}$ = Specific heat of Teflon model material, $BTU/lb - {}^{o}R$

k_{TEF} = Thermal conductivity of Teflon model material, BUT/ft-hr-^{o}R

t = Time for initial exposure to the flow, hr

A constant value of 2.190 BUT/ft^2 -hr$^{.5}$-^{o}R was used for $\left[\rho_{TEF}\, C_{P,\,TEF}\, k_{TEF}\right]^{.5}$ and t = 0 was established at .85 sec before the model reached tunnel centerline. Thermocouples embedded in the Teflon flat plate insert enabled measurement of model material temperature prior to injection. The Teflon booster and orbiter models were not so equipped and initial material temperature was assumed as ambient. Accuracy of the phase change paint technique is discussed in Ref. 7.

c. Pressure Data

The model surface pressures were measured by two types of transducers. All odd-numbered ports were connected to 15 psid transducers while the even-numbered ports were connected to paralleled 1 psid and 15 psid transducers. For the even-numbered ports, all pressures below 1 psia were read on the 1 psid transducers to give accurate results for the undisturbed pressures. Uncertainties are given below:

Transducer	Uncertainty
1 psid	± 0.001 psia
15 psid	± 0.003 psia or 1/2% of reading, whichever is greater.

d. Data Output

The test output consists of tabulations, data plots and photographs for each run. All runs are denoted by a group number. The total data output is contained in 22 volumes issued by AEDC, and is catalogued in detail in Ref. 6.

Section III

TEST DATA OBTAINED

Pressure and heating rate distributions and profile flow photographs were obtained for the flat plate and booster models with various shock generators for the test conditions given in paragraph II-2. As described in the previous section, two methods were used to obtain the heating rate distributions: thermocouples on thin-skin models, and phase change paints on teflon models. Both methods use initial heating of the model. Thus, the heat transfer data obtained are for "cold wall" conditions. The static pressure measurements, conversely, require several minutes to stabilize. During this stabilization time, the model heats and the wall temperature approaches the adiabatic wall temperature. Therefore, the pressure data are for essentially adiabatic wall conditions, whereas the heat transfer data are for cold wall conditions. Of course, this difference in conditions is undesirable because wall temperature affects both boundary layer transition and also separation. It was expedient, however, to fabricate the models for standard data measuring techniques and thereby avoid the complexities of either cooling the pressure models or using steady state heat transfer gauges.

The data obtained on the flat plate and booster models with the various generators are indicated in this section. The sample runs chosen are used to describe features of different types of interaction flows and the effects on the resulting pressure and heat transfer distributions. Finally, a complete data log presents a summary of all data obtained.

1. SHARP PLATE

The shock generators used and the types of data obtained on the sharp leading edge flat plate are indicated in Table II. The tunnel stagnation pressure (p_o) and nominal location of the generated shock on the plate surface (x_i) are listed in the first two columns. The remaining columns indicate the shock generators and the type of data obtained (p = pressure, T = thermocouple heating rates, P = temperature-sensitive paint heating rates). The row with "trip" in the first column indicates the data obtained with the boundary layer trip installed on the flat plate.

Pressure distributions were obtained for nearly all cases where thermocouple heating rate distributions were obtained. However, only limited temperature sensitive paint data were obtained. Profile flow photographs were taken for all test configurations; shadowgraphs on thermocouple runs and schlierens on pressure runs.

a. Undisturbed Flow

Undisturbed (no shock generator) pressure and heating rate distributions on the flat plate surface were measured for all tunnel stagnation pressure levels. These were used as reference conditions to determine the pressure rises and heating amplifications caused by the generated shock wave boundary layer interactions.

The heat transfer distributions, obtained on the thin-wall thermocouple model with no boundary layer trip, exhibited an anomalous behavior near the trailing edge of the plate. This anomalous behavior, which was most pronounced at a tunnel flow stagnation pressure of 400 psia, is evidenced by the heat transfer data shown in Fig. 22. Although there is considerable scatter, particularly for the lower heating rates, the distribution dips (at x = 23.5 in.) and then rises at the trailing edge. We attribute this to separation and reattachment of the boundary layer due to a slight warping of the thin wall surface near the trailing edge of the plate.

The slight warping can also be ascertained by examining carefully the shadowgraph photographs taken during the same tunnel run (Fig. 23). The triangular shapes on the lower surface of the model are photo reference guides located 8.0 and 22.0 in. downstream of the leading edge. The square grid on the tunnel windows has a spacing of 4.5 in. In addition to showing the slight concave curvature of the plate trailing edge, these shadowgraphs clearly show a displaced white line above the plate surface, indicating that the boundary layer was laminar over the entire extent of the plate.†

The measured heating rates for tunnel flow stagnation pressures of 850 psia and 200 psia also exhibit an anomalous dip near the plate trailing edge (Fig. 24), but not as severe as for the 400 psia case mentioned above. When the sharp plate receiver was tested with shock generators, it was found that the great majority of peak interaction heating rates were measured well upstream of the regions that appeared separated on the undisturbed plate, and therefore would be unaffected by the separation. There were five cases where the peak interaction heating rates were measured upstream of, but in proximity to, the beginning of the separated regions. It is believed that in these cases as well, the measured peak heating rates were unaffected by warping of the plate trailing edge, primarily because the peaks occurred upstream of the separated regions, but also because these data were not inconsistent with all other sharp plate data. For these reasons, the smoothly faired curves of

†As described by Chapman, Kuehn and Larson (Ref. 8), a white line appears above laminar boundary layers in shadowgraph photographs. This line remains parallel to the plate surface while the boundary remains laminar, converges to the surface in the boundary layer transition region, and disappears when the flow is fully turbulent.

Figs. 22 and 24, were used to define reference levels of undisturbed heating. There was one case (Group 60; 1/2 in. dia. sphere; p_o = 400 psia; x_i = 22 in.) where the peak heating rate was measured at a point within the region affected by the warping of the plate, and this is noted in the data summary of Table III. It has not been determined if the peak heating rate in this case was affected by the warped trailing edge.

Although a Mach wave emanating from the nose-plate junction is visible in the shadowgraph photographs (joint at x = 2.5 in., see Fig. 23), this joint was quite smooth and did not affect either the heat transfer or pressure distributions. The pressure model remained quite smooth (no local warping of the surface), and there were no anomalies in the undisturbed pressure distributions (see Fig. 25).

Schlieren and shadowgraph flow photographs (Fig. 26) show no boundary layer transition on the plate surface even for the highest tunnel flow stagnation pressure (850 psia). In order to obtain turbulent boundary layer interaction data on the sharp flat plate, it was necessary to use boundary layer trips (described in the previous section). As indicated in Table II, the trips were used on the sharp flat plate only for the highest tunnel flow stagnation pressure (850 psia).

Schlieren and shadowgraph photographs of the tripped boundary layer (taken during the pressure and heat transfer tunnel runs, respectively) are shown in Fig. 27. The corresponding pressure and heat transfer rate distributions are shown in Fig. 28a and b, respectively. The curves faired through the data were used as undisturbed reference conditions for the tripped boundary layer interactions. Heating rate distributions for laminar and turbulent boundaries on a sharp flat plate with constant wall temperature were calculated using Eckert's reference temperature method (Ref 9):

$$h_{LAM} = 0.332 \frac{k_*}{x} (Pr_*)^{\frac{1}{3}} \sqrt{Re_{x*}}$$

for laminar boundary layers, and

$$h_{TURB} = 0.0296 \frac{k_*}{x} (Pr_*)^{\frac{1}{3}} (Re_{x*})^{0.8}$$

for turbulent boundary layers. The reference temperature is:

$$T_* = \frac{1}{2} (T_w + T_e) + 0.22 (T_r - T_e)$$

where

T_w	=	wall temperature
T_e	=	temperature at boundary layer edge
T_r	=	recovery temperature
h	=	heat transfer coefficient
Pr	=	Prandtl number
Re_{x*}	=	Reynolds number based on x
k	=	gas thermal conductivity

and * conditions are based on the reference temperature. Heating rates predicted using this method are also shown in Fig. 28b. Reference conditions for the heat transfer data are listed in Table IV.

b. Laminar Upstream of Interaction

In all cases without the trip, the boundary layer was initially laminar upstream of the interaction caused by the generator shocks. The generator shock waves were usually strong enough to separate the boundary layer, and frequently were sufficiently strong to cause boundary layer transition prior to reattachment (Ref. 10).

Heating rate and pressure distributions for a shock wave generated by a 10^o wedge incident on the flat plate surface at a nominal value of x = 22 in., are plotted in Fig. 29. These distributions, obtained for a tunnel stagnation pressure of 400 psia, are compared with the undisturbed distributions for the same tunnel pressure. The heat transfer starts to dip below the undisturbed value approximately 11-1/4 in. downstream of the plate leading edge. The schlieren photograph in Fig. 30 confirms this as the start of a separated flow region. Unfortunately, the shadowgraph does not show the start of separation because the model was located further downstream and the separation location was between the two tunnel viewing windows.

In this case, the shock wave emanating from the separation location impinges on the wedge, is reflected, and merges with the wedge shock (evident in both the shadowgraph and schlieren in Fig. 30). The flow in the impingement region is quite complex in these cases. Nevertheless, the peak heating rate and pressure values occur approximately at the chosen nominal impingement location, 22 in. downstream of the leading edge. The peak heating rate is more than 60 times the undisturbed value; the peak pressure is nearly 30 times as large as the undisturbed pressure.

The pressure measurements were made by reading 16 pressure transducers at 8 different valve positions. Since several minutes were required for the pressure readings at

any one valve position to stabilize, only the portion of the pressure distributions in the region of impingement was recorded during most tunnel runs. It was therefore possible to obtain more peak pressure rises than would have been possible if complete pressure distributions had been taken. This was desirable in order to obtain a maximum number of data points for the correlations of peak pressure and heating described in the following section. Of course, incomplete pressure distributions make it more difficult to correlate other parameters such as separation distance and wall temperature effects.

Finally, also evident in Fig. 30, is a lip shock emanating from the trailing edge of the wedge, immediately downstream of the expansion fan. As described by Hama (Ref. 11), the flow around the expansion corner (the wedge trailing edge in our case) overexpands appreciably and then is recompressed through the lip shock and separates from the wedge base. In certain instances, this lip shock impinged on the plate surface and led to locally increased pressures and heating rates on the plate surface.

The shock wave emanating from the boundary layer separation location on the plate surface was sufficiently strong in some cases to cause boundary layer separation from the wedge surface. This was the case, for example, for the 15 deg wedge shock impinging at $x_i = 5$ in. for a tunnel flow stagnation pressure of 75 psia. The heat transfer and pressure distributions (Fig. 31), and the corresponding shadowgraph and schlieren flow photographs (Fig. 32), indicate laminar boundary layer separation essentially from the leading edge of the plate with an accompanying separation shock. This shock merged with the plate bow wave and impinged near the trailing edge of the wedge, causing the laminar boundary layer on the wedge to separate. For the "cold wall" case (shadowgraph), separation occurred downstream of the wedge mid-chord (cold walls generally delay separation); for the "hot wall" case (schlieren), separation occurred upstream of the wedge mid-chord. In both cases, the wedge separation shock merged with the shock wave generated by the wedge before interacting with the plate boundary layer. The peak pressure was measured on the plate surface at $x \approx 4.8$ in., and the peak heating rate on the plate was measured at $x \approx 5.2$ in.

In both cases, the plate shock is reflected from near the wedge trailing edge and results in additional local peaks (most notably in the pressure data) in the heating rate and pressure distributions on the plate surface.

When the wedge was moved further aft, on occasion the plate bow wave impinged essentially at the wedge leading edge and, particularly for the small wedge angle (1.5 deg), considerably strengthened the shock wave generated by the wedge (Figs. 33 and 34). For

the 1.5 deg wedge with a nominal x_i = 11 in., and a tunnel flow stagnation pressure of 850 psia, the wedge generated shock wave impinged on the plate boundary layer, was reflected, impinged on the wedge near the trailing edge, was again reflected and again impinged on the plate boundary layer. This caused the multiple peaks in the heat transfer and pressure distributions evident in Fig. 33.

Heat transfer and pressure distributions along the plate centerline, and the corresponding shadowgraph and schlieren flow photographs, for a 10 deg wedge shock impinging at a nominal location 22 in. downstream of the leading edge, are shown in Fig. 35 and 36 for a tunnel stagnation pressure of 850 psia. Data distributions and flow photographs for a 15 deg wedge shock, for the same tunnel flow pressure and nominal impingement location, are shown in Fig. 37 and 38. The shadowgraph photographs for both wedges indicate a separation location further downstream than that shown in the corresponding schlieren photographs. The "cold wall" delayed separation of the boundary layer from the plate surface. This effect is also evidenced by the centerline data distributions in Fig. 37. The heat transfer data first diverge from the undisturbed values approximately 10.5 in. downstream of the leading edge. Whereas the pressure data, obtained on a "hot wall" model, start to increase above the undisturbed pressure values approximately 9.5 in. downstream of the leading edge.

The pressure rises to a laminar separation plateau level that is well approximated by Hill's (Ref 12) correlation:

$$\frac{p_{p_\ell}}{p_1} = 1 + 1.22\, M_1^2 \left[(M_1^2 - 1)\, Re_{sep} \right]^{-\frac{1}{4}} \qquad (5)$$

where p_{p_ℓ} is the laminar plateau pressure level, subscript 1 refers to undisturbed conditions, and Re_{sep} is the Reynolds number based on undisturbed conditions and distance from the leading edge to the separation location. The value obtained from Eq 5, $p_{p_\ell} = 1.7\, p_1$, as shown in Fig. 37, is just slightly below the measured values.

The measured pressure amplifications were compared with calculated amplifications and a number of significant differences and trends were noted. These are discussed below.

(1) Calculated Pressure Ratios

For wedge and cone generators, oblique shock relations (Ref. 13) were used to obtain the shock angle and the inviscid properties behind the shock. At this point, a first order correction for the effect of the generator boundary layer displacement thickness was made.

Using the computed downstream properties and simplified boundary layer equations (Ref 14), the generator boundary layer displacement thickness was computed, and the corrected cone or wedge angle was determined (Fig. 39).

Properties downstream of the generated shock were recomputed using the corrected generator angle. It was assumed that along the plate center line it would be acceptable to treat the reflected shock as a planar shock for the case of a cone generator, as well as for the wedge generators. Oblique shock relations were then used to determine the properties behind the reflected shock.

For the hemisphere-cylinder generators, it was first necessary to define the shape of the incident shock. For this purpose Lukasiewicz (Ref 15) blast analogy for hypersonic flow was used. The local shock angle at the centerline impingement point was computed, and the wave at this location was treated as a section of an oblique shock. The remainder of the computation then becomes identical to the wedge calculation, although no boundary layer correction was required.

(2) Measured Pressure Ratios - Wedge Generators

The flow fields observed during testing were significantly more complex than the idealized flow field shown in Fig. 39, resulting in differences between measured and predicted pressure amplifications. The general trends observed in the wedge/sharp flat plate data are indicated in Fig. 40, where measured pressure ratios are compared with calculated ratios for testing at 850 psia and 75 psia. These data are presented at "nominal impingement locations", which are the idealized locations calculated for the simplified flowfield. Although these locations are referred to throughout the report for simplicity, the actual locations for impingement with the plate, as well as peak amplification, differ from the nominal values, as seen in Table III.

As described previously, for the 11- and 22-inch impingement locations, there are additional shock waves that impinge on the flat plate and increase the pressure ratio above that value predicted for a simple shock generated by the wedge. Four phenomena, each leading to an additional shock wave, are: 1) reflection of the plate leading edge shock by the wedge surface, 2) reflection of a shock wave emanating from the start of a separated flow region on the plate by the wedge surface, 3) a shock wave emanating from a separated flow region on the wedge surface, and 4) a wedge lip shock. In each case, the additional shock reinforces the simple wedge generated shock wave and results in measured pressure amplifications on the plate surface that are substantially larger than those predicted for the simple wedge shock (Fig. 39).

However, at the forward (5 inch) impingement location, the measured pressure amplifications agree relatively well with the calculated amplifications. To obtain a forward impingement, the generator was positioned with its leading edge upstream of the plate leading edge shock. With the generator in this position, the forward portion of the plate tended to be free of extraneous shocks (Figure 41), with separation shocks a common exception (Figure 42). As seen in these figures, the reflection of the plate leading edge shock from the wedge strikes the plate well downstream of the nominal impingement point. The separation shocks were either not reflected (Figure 42), or if reflected, they also struck the plate well aft of the nominal impingement point. The result is that with the wedge generator in the forward position, there was no impingement of extraneous shocks in the interaction region or upstream of this region. The net pressure amplification (p_{peak}/p_{Und}) therefore remained approximately unchanged from the value predicted for the idealized flow field.

(3) Three-Dimensional Generators-Cones and Hemisphere Cylinders

Measured pressure amplifications for the cone and hemisphere cylinder generators were significantly lower than predicted (Fig. 43), and therefore also below the wedge generator data. It is believed that this trend is a result of the highly three-dimensional nature of the flow field downstream of the 3D generator shock.

The strength of the reflected 3D generator shock continuously decreases away from the plate centerline. The resulting divergence of the flow downstream of the reflected shock provides relief which reduces the pressure amplification. The divergent nature of the flow downstream of the 3D generator shock is illustrated in Figure 44 which compares the lateral heat transfer and pressure distributions for wedge and cone generators of approximately equal calculated shock strengths. It should be noted that the transverse data were obtained downstream of the point of peak amplification.

As a result of three dimensional flow relief, the 3D generators did not produce the large separated regions in the plate boundary layer, and the resulting separation shocks that were observed with the wedge generators. This is seen in Figures 45 and 46 where the interactions caused by a wedge, cone, and hemisphere-cylinder of approximately equal shock strengths are compared. The wedge generator shock produced an extensive separated region (Fig. 46a). The accompanying separation shock is reflected by the generator and merges with the generator shock prior to impinging on the plate boundary layer (Fig. 45a). There is no visible evidence in the shadowgraphs of Figures 45b and 45c that the cone and hemisphere cylinder generators caused separation of the plate boundary layer. The heat transfer distributions for the 3D generators (Figs 46b and 46c), however, indicate possible small regions of separation.

The three dimensional nature of the interaction heating distribution caused by the 2.0 in. diameter hemisphere-cylinder is further evidenced by photographs taken during the temperature-sensitive paint runs, as shown in Fig. 47. The particular photograph shown in this figure was taken 26.92 secs after the model first entered the tunnel flow. The paint chosen for this run had a phase change temperature of 710°R, which was the temperature along the boundary of the dark crescent shaped region on the plate surface at the time the photograph was taken. The corresponding heating rate at the boundary ($h_T = 0.21\ h_{REF}$) agrees with the thermocouple data shown in the figure.

c. Turbulent Upstream of Interaction

As noted earlier in this section, even at the highest tunnel flow stagnation pressure (850 psia) it was necessary to use boundary layer trips in order to obtain turbulent boundary layers on the sharp leading edge flat plate. In order to have as high a Reynolds number as possible, the nominal impingement location was chosen near the trailing edge of the plate for all tripped boundary layer cases (see Table II). A comparison of the undisturbed flows over the sharp leading edge plate, without and with the boundary layer trip, is shown by the flow photographs in Figs. 26 and 27. The shadowgraph photographs were obtained on a colder wall than the schlieren photographs, which is expected to delay transition. The heat transfer data, shown in Fig. 28, indicate that the tripped boundary layer became fully turbulent (end of transition) approximately 18 in. downstream of the leading edge. For the pressure data, obtained on hot wall models, transition is expected to have occurred somewhat further upstream.

Some effects of the boundary layer trip on the interaction caused by a 10 deg wedge shock generator can be ascertained by comparing the untripped data of Fig. 35 and 36 with the tripped boundary layer data shown in Figs. 48 and 49. For the colder wall (heat transfer data), Fig. 35a indicates separation approximately 11 in. downstream of the leading edge, whereas for the tripped boundary layer, Fig. 48a indicates separation approximately 20 in. downstream of the leading edge. Similarly, the pressure distributions also indicate that separation is delayed by the trip. Thus, as expected, separation is much less extensive for the tripped turbulent boundary layer than for the initially laminar boundary layer for both the "cold" and "hot wall" models.

The tripped boundary layers, with relatively small separated regions, did not exhibit the strong separation shocks which were characteristic of the interactions between wedge generator shocks and laminar boundary layers. As a result, the measured pressure amplifications for wedge generators and tripped boundary layers were lower than the

amplifications measured for the untripped boundary layers, and in general showed better agreement with predicted values (Fig. 50).

The 15 deg wedge shock generator was used at two different heights above the flat plate for the tripped boundary layer. Heat transfer and pressure distributions for the lower height, shown in Fig. 51, indicate separation approximately 19-1/2 in. downstream of the leading edge for the cold wall (heating data), whereas separation occurred less than 15 in. downstream of the leading edge for the hot wall (pressure data). The pressure distribution exhibits a plateau region indicating that the boundary layer was initially laminar at the beginning of the separated flow region. The schlieren photographs in Fig. 52 support the conclusion that the extent of separation was considerably larger for the pressure run than for the heat transfer run. At the greater generator height, the data distributions and flow photographs indicate turbulent separation for both the heat transfer and the pressure runs (Figs. 53 and 54).

Heating rate distributions on the sharp leading edge flat plate with the boundary layer trip were obtained with both thermocouples and temperature-sensitive paint. Thermocouple heating data and the pressure distribution resulting from the interaction caused by a 7-1/2 deg cone are presented in Fig. 55. They indicate a relatively small region of increased heating and pressure starting approximately 20 in. downstream of the leading edge. Flow photographs for this configuration are shown in Fig. 56. Photographs showing temperature-sensitive paint results, and the corresponding heat transfer rates, are presented in Fig. 57. Times are measured from when the model first enters the tunnel flow. For this run, 1.23 seconds were required from time zero until the model was on the tunnel centerline. The phase change temperature of the paint chosen was 710°R. In each frame, this is the temperature along the boundary of the melted (dark colored) and unmelted (light colored) paint regions. This boundary also marks a line of constant heating rate; the heating rates are lower in the light colored region and higher in the dark colored, crescent shaped, region on the plate surface.

Because a spherical shock wave is attenuated by expansion waves and becomes weaker away from the centerline, one might expect a conical shock wave to cause a greater disturbance outboard of the centerline than that caused by the spherical shock wave, for equal shock strengths on the centerline and approximately equal peak heating rates. The photographs shown in Fig. 58a bear this out. For equal heating rates, the conical shock interaction with the turbulent boundary layer is more extensive than the spherical shock interaction. However, for laminar boundary layers (Fig. 58b), the conical and spherical shock interactions extend equal distances outboard of the centerline.

2. BLUNT PLATE

Interaction data on the blunt leading edge flat plate were obtained at three tunnel flow stagnation pressure levels (850, 400 and 75 psia) for two nominal impingement locations (x_i = 7 in. and 22 in.). The particular shock generators used are indicated in Table V. As indicated in the table, no temperature sensitive paint data were obtained for the blunt leading edge flat plate.

As with testing of the sharp leading edge plate, shadowgraph flow photographs were obtained during the initial heating of the model on thermocouple runs and schlieren photographs were obtained during the pressure data runs when the model wall was hot.

a. Undisturbed

The blunt leading edge led to a substantial favorable pressure gradient over the entire flat plate surface as illustrated by Fig. 59, for a tunnel flow stagnation pressure of 850 psia. The corresponding undisturbed heating distribution indicates that boundary layer transition started approximately 14 in. downstream of the blunt leading edge for 850 psia. The shadowgraph and schlieren flow photographs for these tunnel runs are shown in Fig. 60. Comparing the flow photographs and heat transfer data, for the highest tunnel flow pressure, it appears that the boundary layer was transitional over the downstream portion of the flat plate.

Undisturbed distributions at the lower tunnel pressures indicated entirely laminar boundary layer flow over the flat plate surface. Curves were faired through all the undisturbed data distributions, see Fig. 61, and used as reference conditions for the downstream ($x_i \approx 22$ in.) and upstream ($x_i \approx 7$ in.) interactions.

b. Downstream Interactions

Centerline heating and pressure distributions, for a 10 deg wedge generating a shock impinging at a nominal location approximately 22 in. downstream of the leading edge, are shown in Fig. 62 for a tunnel flow stagnation pressure of 850 psia. The corresponding shadowgraph and schlieren photographs are in Fig. 63. The cold wall heating rate distribution initially dips below the undisturbed distribution, approximately 16 1/2 in. downstream of the leading edge, and then attains a peak heating amplification at approximately 21 1/2 in. The pressure distribution rises upstream of 15 in. to a plateau level and then attains a peak value 21 in. downstream of the leading edge.

Similar distributions and flow photographs, but for the lowest tunnel flow pressure (75 psia), are given in Fig. 64 and 65. Separation is considerably more extensive for the low tunnel pressure than for the high one. The heat transfer rates drop below the undisturbed

values 11 in. downstream of the leading edge, and attain a peak value at 19 in. The limited pressure distribution indicates separation well upstream of 15 in. and a peak value just downstream of 19 in. A second, lower, peak is apparent in both the heating and pressure distributions. This is probably caused by additional shock waves being reflected by the wedge surface and impinging on the plate. However, the density at these low tunnel pressures is insufficient to discern reflected shocks in the flow photographs.

c. Upstream Interactions

Heating and pressure distributions for the upstream impingement location are shown in Fig. 66 for a 10 deg wedge for 850 psia, the corresponding flow photographs are shown in Fig. 67. These photographs clearly show the strong and complex interaction flow between the wedge and plate. The heating rate is an order of magnitude higher than the undisturbed value at the start of the instrumentation. The pressure distribution also greatly exceeds the undisturbed one; even at the most forward tap location (x = 1 in.), the pressure is four times larger than the undisturbed pressure. The pressure level remains very high until near the wedge trailing edge, and then drops, indicating an accelerating flow downstream of the wedge trailing edge.

Corresponding data, obtained at the low tunnel pressure, are shown in Figs. 68 and 69. In this case the wedge was moved aft 0.6 in., which placed the wedge leading edge just downstream of the bow shock from the blunt leading edge of the plate. Again, the flow between the wedge and plate is quite complex; normal shock waves are visible between the wedge and plate surfaces.

When the wedge was pitched to 15° deg, for the pressure run, the model blocked the tunnel flow. It was necessary to increase the tunnel flow stagnation pressure to 100 psia, inject the model, and then reduce the pressure to 75 psia in order to avoid blocking the tunnel flow for the pressure run. For the heat transfer run for this model configuration, the tunnel back pressure was slightly lower and the tunnel flow started during a second injection of the model. The heating and pressure distributions for the 15 deg wedge, and the corresponding flow photographs, are in Fig. 70 and 71, respectively. The heating rate peaks just downstream of x = 4 in. to a value 14 times higher than the undisturbed heating rate. The pressure distribution rises at x = 4 in., and then continues to rise slowly until a peak value almost 15 times as large as the undisturbed pressure is attained approximately 7 1/2 in. downstream of the leading edge. [The shadowgraph photographs in Figs. 67 and 71 show a shock interaction pattern near the wedge leading edge very similar to one first described by Edney (Ref. 16 Fig. 6-11). As noted by Edney, this type of interaction results in an impingement on the wedge surface that results in particularly severe heating.]

As a final example of the blunt leading edge plate data, Figs. 72 and 73 show the heating distribution measured along the plate centerline and the corresponding shadowgraph photograph for the orbiter shock generator parallel to the plate for a tunnel stagnation pressure of 850 psia. The peak heating, at x = 7 in. is almost six times the undisturbed heating rate. The measured heating then drops to a level approximately 4 times higher than the undisturbed level, and maintains this amplification until the trailing edge of the orbiter.

3. BOOSTER AND BOOSTER/ORBITER CONFIGURATIONS

Table VI presents an overview of the data obtained on the booster and booster-orbiter configurations. Again, p indicates pressure data, T indicates thermocouple heat transfer data, and P indicates temperature-sensitive paint heat transfer data. As with testing of the flat plate models, heat transfer rates were obtained during the initial heating of the model, using both the thin-wall thermocouple and temperature sensitive paint techniques, and therefore the heating rates correspond to a relatively "cold wall" condition. Pressure data were obtained for model wall temperatures approaching the adiabatic wall temperature.

Undisturbed heating rate and pressure distributions were obtained by testing the booster alone at 0 deg angle of attack and the orbiter alone at 0, 5 and 10 deg angles of attack. As indicated in Table VI, various shock generators were used with the booster model. The orbiter shock generator model was instrumented. Heat transfer and pressure distributions were measured on the lower surface of the orbiter as well as the upper surface of the booster. In this section data are presented for: the undisturbed flows over the booster and orbiter alone, the effects on the booster caused by the interaction flows, and the effects on the orbiter caused by the interaction flows.

a. Undisturbed Flows

Heat transfer rates measured on the upper surface of the booster with no shock generator, at tunnel flow stagnation pressures of 850 and 75 psia, are indicated in Figs. 74 and 75. Two streamwise distributions and one spanwise distribution are shown in each figure. One streamwise distribution is in the booster centerplane (row 1) and the other is along the surface in a plane at 30^{o} with respect to the centerplane (row 2). The spanwise

distribution is on the wing surface at station x = 15.6 in. (see Fig. 17). The off centerline distributions (row 2) exhibit an increased level downstream of x = 10 inches. This increase can be attributed to turbulence introduced by the shock emanating from the booster canards. As would be expected, there is considerably more scatter in the heat transfer rates measured at the lower stagnation pressure.

Streamwise pressure distributions for the same tunnel pressures are given in Fig. 76 in the centerplane (row 1) and in a plane at 30^{o} with respect to the centerplane (row 3). The pressures do not exhibit a sizable jump downstream of the booster canards; the distributions along the two rows are essentially identical for each tunnel flow pressure. However, booster pressures at the 75 psia tunnel pressure are slightly higher than those at the 850 psia tunnel pressure, indicating a thicker boundary layer at the lower tunnel pressure.

Temperature-sensitive paint (TSP) runs were made to determine the undisturbed heating rate distributions over the surface of the booster. Frames from motion pictures taken using three cameras during a TSP run are shown in Fig. 77. For this run (group 194), p_o = 850 psia, the phase change paint temperature chosen was 573^{o}R. This relatively low temperature paint melted on the booster nose, canard and wing leading edges before the model reached the tunnel centerline. Higher heating rates are also evident where the wing and canard shocks strike the body and in the wake region behind the canards. The spanwise heating rate across the wing and fuselage is seen to agree qualitatively with the spanwise distribution plotted in Fig. 74.

Heat transfer and pressure distributions were obtained along rays on the lower surface of the orbiter (see Fig. 16). The undisturbed distributions were obtained by locating the orbiter high above the booster, above the booster bow shock, and measuring the heat transfer rates and surface pressures for orbiter angles of attack, (α_{orb}), of 0, 5 and 10 degrees.

Distributions of heating rates along two rays on the lower surface of the orbiter, for the highest and lowest tunnel flow stagnation pressures, are indicated in Fig. 78 for $\alpha_{orb} = 0$. At the higher tunnel pressure, the inboard ray heating rates are as much as four times as large as the heating rates measured along the outboard ray, whereas, at the lower tunnel pressure, the heating rates along the inboard ray are less than those along the outboard ray. The pressure distribution along the centerline of the lower surface of the orbiter is indicated in the last portion of Fig. 78.

Corresponding heat transfer and pressure distributions for $\alpha_{orb} = 10^{o}$ are indicated in Fig. 79. In these cases, the outboard ray heating rates are consistently higher than those along the inboard ray. The pressures along the centerline are nearly constant for $\alpha_{orb} = 10^{o}$.

Curves were faired through the measured data values and used as the undisturbed reference conditions to indicate the effects of interactions caused by the shock generators on the booster and by the booster on the orbiter.

b. Interaction Effects on Booster

Changes in the heat transfer rate distributions, resulting from the interaction flow caused by the 0.5" diameter hemisphere-cylinder, are indicated in Fig. 80 for a tunnel flow stagnation pressure of 850 psia. Along the centerline (row 1), the heating rate drops below the undisturbed value at x = 12 in., and then rises sharply downstream of x = 15 in. Along row 2, which is 30^{o} off the centerplane of the booster, the heating rate starts to drop below the undisturbed value at x = 15 in., and doesn't rise above the undisturbed value until x≈17 in. The spanwise distribution of heating rates is affected only near the centerplane of the booster.

The orbiter, which has a 0.5 inch diameter spherical nose, affects the booster heating distribution much more extensively than the smaller hemispherical shock generator even when relatively far away from the booster. At a separation distance, Z_m, of two inches, the booster bow shock reflects from the lower surface of the orbiter and interacts with the boundary layer on the booster surface. These effects are evidenced in the heating rate distributions shown in Fig. 81 and also in the corresponding schlieren flow photographs. The heating rates along both rows 1 and 2 drop below the undisturbed values at x = 8 in. The interference heating rates are considerably larger than the undisturbed values at x = 12 in., and exhibit a second drop-then-rise near the booster base. The spanwise distribution, from the fuselage centerline outboard on the wing surface, is also substantially affected by the interaction.

As shown in Fig. 82, the interference heating is greatly aggravated when the orbiter is pitched to a 10^{o} angle of attack. The drop in heating rates, which is associated with the onset of separation, occurs upstream of x = 8 in. Both streamwise distributions of heating rates attain maximum values of approximately $h_T = 0.4\ h_{REF}$ at x = 16 in. These values represent magnifications of approximately 18 times the undisturbed heating rate for row 2 (30^{o} off centerplane) and approximately 53 times the undisturbed heating rate for row 1 (in the centerplane). The spanwise heating rate distribution at station x = 15.6 inches indicates

severe heating on the fuselage, which is in the region of reattachment, and a decrease in heating outboard on the wing surface, which is in a separated flow region.

Finally, the most extensive region of separated flow and greatest heating was caused by the 10^{o} wedge, as indicated in Fig. 83. The boundary layer flow separates from the booster upper surface at x = 7 in. There are two peaks in the downstream heating distributions, one at x = 13.5 in. and another at x = 16 in. The spanwise heating distribution remains high over the entire extent of the instrumentation on the upper surfaces of the booster and wing. Reynolds number effects on the heating distributions are also indicated in Fig. 83. The filled symbols represent data obtained at the highest tunnel flow stagnation pressure whereas the open symbols represent the corresponding data obtained for the lowest tunnel flow pressure level.

Frames from motion pictures taken during the temperature-sensitive paint runs for the 10^{o} wedge and 10^{o} orbiter and booster, for a tunnel stagnation pressure of 850 psia, are shown in Figs. 84 and 85, respectively. A paint having a phase change temperature of 810^{o}R was chosen for the wedge generated interaction. The times of the sample frames and the corresponding heat transfer rates along the boundaries of the melted paint regions are indicated in Fig. 84. Sample values, obtained from these frames, are plotted in Fig. 83. The paint and thermocouple results are seen to agree quite well along the booster centerplane. However, the paint data indicate a dip in the spanwise heating rate on the wing surface that is not indicated by the thermocouple data. For this particular run (group 196), it appears that too heavy a coat of paint was sprayed on portions of the booster surface, which may have caused this effect.

Along the wing leading edge, in both Figs. 84 and 85, there is a localized inboard region of intense heating and an outboard region of increased heating. The inboard "hot spot" is attributed to self-induced shock impingement resulting from boundary layer separation from the surface ahead of the wing-fuselage junction (Ref 17). The outboard region of increased heating results from the shock generated by the wedge or orbiter.

A paint having a phase change temperature of 960^{o}R was chosen for the 10^{o} orbiter shock interaction. The associated, relatively long times and comparatively high heating rates are indicated for the motion picture frames shown in Fig. 85. The heating rates from these frames are plotted in Fig. 82; they agree well with the thermocouple data.

Changes in the pressure distributions caused by the 10^{o} orbiter and 10^{o} wedge interactions are indicated in Fig. 86 for the highest and lowest tunnel flow stagnation pressure levels. At the higher tunnel pressure level, the pressures along the booster centerline start to rise to a plateau level at x = 7 inches for the orbiter generated shock interaction.

The pressure peak occurs at x = 17 in. Separation occurs somewhat earlier for the lower tunnel pressure, but the downstream pressure peak still occurs at x = 17 in. In both cases, for the orbiter generated shock interactions, the centerline pressure distributions exhibit well defined plateau regions, indicative of laminar separation.

Only the downstream pressures were measured for the wedge generated shock interactions shown in Fig. 86. The peak pressures are larger than for the orbiter generated shock interactions, and occur further upstream. As noted in the figure, the pressure distributions in both the centerplane (row 1) and in a plane 30^{o} off centerplane (row 3) were essentially identical for the wedge generated shock interactions.

Streamwise heating rate distributions along rows 1 and 2 on the booster surface, measured for three different separation distances between the orbiter (at $\alpha = 0$) and booster for $p_o = 75$ psia, are presented in Fig. 87. As the separation distance decreases, interaction effects occur closer to the booster nose, and there are multiple peaks in the heating distributions. These peaks correspond to the multiple shock reflections and interactions between the booster and the orbiter. Similar peaks are evident in the centerline pressure distributions shown in Fig. 88.

The half inch hemisphere-cylinder, when placed near the booster nose, increased the heating along the booster centerline from x = 2 inches to x = 18 inches, as shown in Fig. 89. The increased heating is associated with many shock reflections between the booster and hemisphere cylinder. However, the heating was not increased along row 2 nor on the wing surface outboard of y = 2 inches. Downstream of $x \approx 16$ in., the data can be affected by shocks from the model support structure, and therefore may not be valid. Conversely, the 10^{o} wedge increased the heating and pressure both on the booster centerline and in the plane 30^{o} off centerplane, as shown in Fig. 90.

c. Interaction Effects on Orbiter

Heat transfer rates and pressures were measured along rays on the lower surface of the orbiter. Changes in the heating rates, caused by the interaction flow between the orbiter (at $\alpha = 0$) and the booster at three separation distances, can be ascertained by comparing Figs. 78 and 91. At the greatest separation distance, the heating rates dip below the undisturbed values on the orbiter and then rise to peak values downstream of x = 6 inches. The amplification is most severe along ray 4, which is at an angle of 4^{o} with respect to the orbiter centerline. For example, at x = 7 inches the interference heating along ray 4 is 8 times larger than the undisturbed value. The interference heating along the most outboard ray (No. 1), is 50 to 75 percent larger than the undisturbed heating. The locations of peak heating move forward as the separation distances decrease. At the closest distance, there

are multiple peaks in the heating distributions, corresponding to multiple shock reflections between the booster and orbiter.

Similar to the undisturbed flow heating rates, the interference heating rates on the orbiter are affected strongly by changes in the tunnel flow stagnation pressure. These effects are evident by comparison of Figs. 91a and 92a for $\alpha_{orb} = 0$, and by comparison of parts b and c of Fig. 92 for $\alpha_{orb} = 10^{o}$. The heating amplification factors are several times larger for the higher tunnel flow stagnation pressures. At zero angle of attack, the amplification of the heating rate along the centerline is doubled and the amplification of the heating rate along ray 2 is tripled at the higher tunnel pressure level. At a ten degree angle of attack, the peak heating rates along rays 2 and 3 are 4 to 5 times larger for $p_o = 850$ psia than for $p_o = 75$ psia. This clearly indicates the importance of Reynolds number effects for shock interactions with laminar boundary layers.

As expected, the $\alpha_{orb} = 10^{o}$ cases result in higher interference heating on the orbiter than the $\alpha_{orb} = 0^{o}$ cases. At the higher tunnel flow pressure level, the heating along both rays 2 and 3 was essentially identical.

Data obtained from the corresponding temperature-sensitive paint run (Fig. 85), agree well with the thermocouple data, as shown in Fig. 92.

Centerline pressure distributions, corresponding to the heat transfer rate distributions shown in Figs. 91 and 92, are shown in Fig. 93. The multiple shock reflections that occur as the orbiter and booster move closer together are evident in Fig. 93. In part b, the influence of tunnel flow pressure level is indicated clearly. At $p_o = 75$ psia and at $p_o = 850$ psia, the pressure peaks at approximately x = 6 inches. In both cases the initial pressure is higher than the undisturbed value (cf. Fig. 79).

4. DATA LOG

Table III summarizes the significant data obtained from each test run. The table is organized by type of receiver (i.e., sharp flat plate, booster, etc.) and then type of generator (i.e., wedge, cone, etc.). Heat transfer data obtained from thermocouple and paint runs, and pressure data are presented.

For each test configuration, the table identifies the test group numbers, the stagnation pressure, the generator and the nominal location for shock intersection with the receiver (Nominal x_i). In addition, the location at which the impingement shock strikes the boundary layer edge (x_{BL}), and the actual location of shock intersection with the receiver plate (x_{plate}) are presented. These dimensions were measured from the profile photographs.

Also noted for each run is the location of peak amplified pressure or heating rate, (x_{peak}), and the undisturbed pressure or heating rate at x_{peak}. Non-dimensional pressures were converted to dimensional values using the reference properties of Table IV.

The measured heat transfer coefficients based on gas total temperature, h_T, were converted to the more commonly used coefficient based on adiabadic wall temperature, h_{aw}, as follows:

$$h_{aw} = h_T \frac{(T_o - T_w)}{(T_{aw} - T_w)}$$

For those runs where the undisturbed boundary layer was laminar in the interaction region, it was necessary to determine whether the boundary layer was laminar or turbulent after the interaction, in order to choose the correct T_{aw}. It was not always possible to make this determination by examination of the flow photographs. As a result, plots of amplification in h_T vs amplification in pressure were constructed, similar to those discussed in the following section, and these were used to discern whether the disturbed boundary layer was laminar or turbulent. In general, where the data plots indicated that the disturbed boundary layer was transitional, the laminar adiabatic wall temperature was used to compute h_{aw}. In those cases where the boundary transition was judged to be nearly complete, the turbulent value of adiabatic wall temperature was used to compute h_{aw}. The subscript L or T with the value of h_{aw} denotes whether the laminar or turbulent adiabatic wall temperature was used to compute the coefficient.

For some runs, the pressure or heat transfer distribution would indicate more than one apparent peak in the interaction region. In these cases, the first peak value associated with the primary impingement of the generator shock was selected by comparison of the measured distributions with profile flow photographs. In some cases, secondary peaks could be correlated with reflected shock waves or with the generator lip shock as evidenced in the flow photographs. In a number of cases, however, the selection of a first peak required considerable engineering judgement. In these cases, the secondary peaks are also noted in Table III.

As previously mentioned (Section III-1), the heat transfer data were obtained at wall temperatures significantly lower than for the pressure data. Usually, this disparity produced no clear disagreement in flow fields, as evidenced by the profile flow photographs, pressure and heat transfer distributions. In some cases, however, pressure and heat transfer distributions obtained for identical test configurations showed inconsistent

shapes, number or location of peaks, or other evidence to suggest that there were different boundary layer flows for the pressure and heat transfer runs. Flow photographs (shadowgraphs for heat transfer runs and schlieren photographs for pressure runs) for these runs were also compared. These runs are identified by appropriate comments in Table III.

The phase change paint testing provided useful qualitative information about the distribution of heating over the receiver body. This type of testing is, however, not ideally suited to the determination of peak heating values. When the region of peak heating is small, as was true in our testing, it is extremely difficult to discern the exact time phase change begins, and also to determine the location of the point of peak heating. In addition, paint phase change temperatures were selected to provide information on the distribution over the receiver body in a reasonably short test time. Such a selection, at times, resulted in the occurrence of phase change at the location of peak heating shortly after the model reached the tunnel centerline. This introduces an error in evaluating $h_{T,\,peak}$ because h_T is not constant over the injection period although it is assumed constant in the solution described in Section II. In fact, h_T varies as the model passes through the tunnel boundary layer. As this transient time decreases with respect to the time required for phase change to occur, the error decreases.

As a consequence, the phase change paint data is included in Table III to indicate the general agreement between paint data and thermocouple data. The quantitative data obtained from the phase change paint testing have not been used in the analytical correlations discussed in the following section.

SECTION IV
DATA CORRELATION

1. ANALYTICAL CONSIDERATIONS

Although it is not our intent to perform rigorous analyses of the interaction process, some discussion of a very simple analytical approach provides the insight necessary to organize the test data for correlation. The analytical assumption we will make is that the peak heating after shock impingement can be represented by an ideal zero pressure gradient flat plate film coefficient equation. This may be valid for either of two reasons: (1) the boundary layer may actually have low pressure gradients in the x and y directions at the point of peak heating, since this is some distance downstream of the impingement point; or (2) although pressure gradients exist, resolving the boundary layer into an equivalent flat plate flow may be sufficiently accurate to predict heating. The standard forms of the laminar and turbulent flat plate heating equations are

$$\text{Laminar} \qquad Nu = .332 \quad Re^{.5} \, Pr^{.33} \tag{6}$$

$$\text{Turbulent} \qquad Nu = .0296 \, Re^{.8} \, Pr^{.33} \tag{7}$$

Simple forms of these equations, from handbooks such as Ref. 18 , are

$$h_{LAM} = \frac{.00963 \, (pV)^{.5}}{T_*^{.04} \, x^{.5}} \tag{8}$$

$$h_{TURB} = \frac{.0334 \, (pV)^{.8}}{T_*^{.576} \, x^{.2}} \tag{9}$$

where h is in BTU/ft^2 hr $^\circ$R, p is in LBS/FT^2, V is in ft/sec, T is in $^\circ$R, and x is in feet. These equations result from expressing density by the perfect gas law and by substituting functions of the reference temperature, T_*, for thermal conductivity and viscosity. The reference temperature is defined as

$$T_* = .5 \left[T_w + T_e \right] + .22 \left[T_r - T_e \right]$$

Using subscript 1 for the initial boundary layer, 2 for conditions after the incident shock and 3 for conditions after the reflected shock, we can write three possible equations for the peak heating amplification depending on type of boundary layer.

Case 1. Boundary layer laminar before and after shock impingement.

$$\frac{h_{3_{LAM}}}{h_{1_{LAM}}} = \frac{\dfrac{.00963\ (p_3 V_3)^{.5}}{T_{*_3}^{.04}\ x_3^{.5}}}{\dfrac{.00963\ (p_1 V_1)^{.5}}{T_{*_1}^{.04}\ x_1^{.5}}} = \left(\frac{p_3}{p_1}\right)^{.5} \left(\frac{T_{*1}}{T_{*_3}}\right)^{.04} \left(\frac{V_3}{V_1}\right)^{.5} \left(\frac{x_1}{x_3}\right)^{.5} \qquad (10)$$

Case 2. Boundary layer turbulent before and after impingement.

$$\frac{h_{3_{TURB}}}{h_{1_{TURB}}} = \frac{\dfrac{.0334\ (p_3\ V_3)^{.8}}{T_{*_3}^{.576}\ x_3^{.2}}}{\dfrac{.0334\ (p_1\ V_1)^{.8}}{T_{*_1}^{.576}\ x_1^{.2}}} = \left(\frac{P_3}{P_1}\right)^{.8} \left(\frac{T_{*1}}{T_{*_3}}\right)^{.576} \left(\frac{V_3}{V_1}\right)^{.8} \left(\frac{x_1}{x_3}\right)^{.2} \qquad (11)$$

Case 3. Boundary layer laminar before impingement and turbulent after impingement.

$$\frac{h_{3_{TURB}}}{h_{1_{LAM}}} = \frac{\dfrac{.0334\ (p_3\ V_3)^{.8}}{T_{*_3}^{.576}\ x_3^{.2}}}{\dfrac{.00963\ (p_1\ V_1)^{.5}}{T_{*_1}^{.04}\ x_1^{.5}}} = 3.47\ \frac{(p_1\ V_1)^{.3}}{(T_{*_1})^{.536}} \left(\frac{p_3}{P_1}\right)^{.8} \left(\frac{T_{*_1}}{T_{*_3}}\right)^{.576} \cdot \left(\frac{V_3}{V_1}\right)^{.8} \frac{x_1^{.5}}{x_3^{.2}} \qquad (12)$$

Our testing was performed at M = 8 with a range of shock strengths up to a 15° wedge. Table VII shows the computation, for 5, 10, and 15 deg. wedge shocks of the various flow properties required in equations (10), (11) and (12). In order to simplify the equations, the calculated ratios $\frac{T_{*_1}}{T_{*_3}}$ and $\frac{V_3}{V_1}$ can be approximated, by a curve fit,

as powers of the pressure ratio:

$$\frac{V_3}{V_1} = \left(\frac{p_3}{p_1}\right)^{-.032} \qquad \frac{T_{*_1}}{T_{*_3}} = \left(\frac{p_3}{p_1}\right)^{-.022}$$

Substituting these ratios in equations (10), (11) and (12) and using our Tunnel B values for V_1 and T_{*_1} in equation (12) we get

$$\frac{h_{3_{LAM}}}{h_{1_{LAM}}} = \left(\frac{p_3}{p_1}\right)^{.48} \left(\frac{x_1}{x_3}\right)^{.5} \tag{13}$$

$$\frac{h_{3_{TURB}}}{h_{1_{TURB}}} = \left(\frac{p_3}{p_1}\right)^{.76} \left(\frac{x_1}{x_3}\right)^{.2} \tag{14}$$

$$\frac{h_{3_{TURB}}}{h_{1_{LAM}}} = 1.38\, p_1^{.3}\, x_1^{.5} \left(\frac{p_3}{p_1}\right)^{.76} \frac{1}{x_3^{.2}} \tag{15}$$

where x is in ft and p in lbs/ft^2

In all these equations, x_3, the distance from the apparent start of the boundary layer that exists after impingement must be determined. Since we are assuming that ideal zero pressure gradient boundary layers exist both before and after impingement, we can determine the boundary layer thickness at station 3 if we make some assumption regarding conservation of mass and/or momentum. As a first approach the simplest assumption is that the interaction process does not add mass to the boundary layer, and that the mean boundary layer density and velocity are proportional to the edge velocity and density for boundary layers of the same type.

$$\rho_1 V_1 \delta_1 = \rho_3 V_3 \delta_3 \tag{16}$$

$$\frac{\delta_1}{\delta_3} = \frac{\rho_3 V_3}{\rho_1 V_1} = \frac{p_3 V_3 T_1}{p_1 V_1 T_3} \tag{17}$$

The ratio of boundary layer thicknesses before and after impingement can be evaluated from the flow properties in Table VII. With our simplifying assumption, it is the same for either laminar/laminar or turbulent/turbulent interactions.

$$\left.\begin{aligned} \frac{\delta_1}{\delta_3} &= 2.87 \quad \text{5 deg wedge} \\ &= 5.87 \quad \text{10 deg wedge} \\ &= 8.09 \quad \text{15 deg wedge} \end{aligned}\right\} \text{ for } M_1 = 8$$

It should be noted that we do not claim that these are the actual ratios of boundary layer thickness, only that these are the ratios to be used in an equivalent ideal flat plate heat transfer equation if it is assumed that no mass is added during the interaction. Mass addition would result in lower values of $\delta_1/\ \delta_3$.

The ratios of $\frac{x_1}{x_3}$ to be used in equations (13) & (14) can be determined from standard boundary layer equations using the known value of $\delta_1/\ \delta_3$. These ratios are calculated for the pressure ratios corresponding to 5, 10 and 15 deg wedges and are shown in Fig 94. By curve fitting $\frac{x_1}{x_3}$ as a function of p_3/p_1 (see Figure 94) equations (13) and (14) can be simplified to

$$\frac{h_{3_{LAM}}}{h_{1_{LAM}}} = \left(\frac{p_3}{p_1}\right)^{.73} \tag{18}$$

$$\frac{h_{3_{TURB}}}{h_{1_{TURB}}} = \left(\frac{p_3}{p_1}\right)^{.87} \tag{19}$$

Since our assumption of constant boundary layer mass flow results in the maximum value of $\frac{x_1}{x_3}$, these equations should be somewhat conservative. The available turbulent data support this, since Sayano (Ref 2) and Neumann and Burke (Ref 19) obtained a correlation of $\frac{h_3}{h_1} = \left(\frac{p_3}{p_1}\right)^{.8}$. Holden (Ref 20) and Hains and Keyes (Ref 21) correlated the data as $\left(\frac{p_3}{p_1}\right)^{.85}$. It will be shown later that eqn (18) is also slightly conservative compared to our laminar data.

The case of an initially laminar boundary layer that is turbulent after the shock is not easy to analyze even with our very simplified analysis. Natural transition has been studied for years and is still not well understood, and shock induced transition is much more complex. In our test program we varied the tunnel pressure level and x_i, the location of impingement on the plate. When these two parameters result in a local Reynolds number less than natural transition the question arises as to what shock strength is required to cause transition to fully turbulent flow. The more stable the boundary layer the greater is the shock strength (pressure ratio) required to cause transition. Since boundary layer stability and transition are primarily a function of Reynolds number and Mach number,

for a flat plate without strong heat transfer effects, we can assume that the transition pressure ratio is an inverse function of Reynolds number at our constant Mach number, or

$$\frac{p_T}{p_1} = f\left(\frac{1}{R_{e_1}}\right) \tag{20}$$

In order for eqn (20) to also be valid for natural transition it must satisfy the constraint that as $Re_1 \rightarrow Re_T$, $p_T/p_1 \rightarrow 1$. Natural Transition data on a plate of similar bluntness, tested at M = 8 in the same tunnel is presented in Ref 22 and can be correlated approximately as $Re_T \sim p^{.6}$. In Ref 23 this unit Reynolds number effect was attributed to aerodynamic noise from the tunnel wall boundary layer.

Combining the natural transition constraint and eqn (20) we get

$$\frac{p_T}{p_1} = f\left(\frac{p_1^{.6}}{Re_1}\right) \tag{21}$$

It will be shown later that a functional relation of this form provides a reasonable correlation of our shock induced transition data.

We have now analytically developed the form of the equations to predict laminar or turbulent heating amplifications (eqns 18 & 19) and to predict the pressure ratio required to cause transition (eqn 21). The remaining important parameter is the apparent start of the turbulent boundary layer after transition (x_3) which is required in eqn (15) for laminar/turbulent interactions. Unfortunately, modifications of the simple flat plate approach of equating laminar and turbulent momentum thicknesses at the transition point in order to solve for x_3 did not agree with our data when transition was shock induced. Therefore, later in this section, we will obtain a data correlation for x_3 but an analytical rationale for the equation requires further study.

2. SHARP PLATE/WEDGE TURBULENT INTERACTIONS

Figure 95 presents the peak heating as a function of the measured pressure amplification, p_3/p_1. It is also seen that the measured pressure amplifications agree well with the theoretical amplifications predicted by an inviscid calculation across the incident and reflected shock. The peak heating can be predicted by $\frac{h_3}{h_1} = \left(\frac{p_3}{p_1}\right)^{.8}$ which is consistent with previous experiments.

3. SHARP PLATE/WEDGE INITIALLY LAMINAR INTERACTIONS

Figure 96 shows our wedge test data and best fit correlations. It can be seen that the boundary layer stays laminar for shock strengths up to $p_3/p_1 \approx 4$ to 20 depending on initial Reynolds number. The laminar data correlate as $\left(\frac{h_3}{h_1}\right) = \left(\frac{p_3}{p_1}\right)^{.7}$ which is consistent with our simplified analysis.

The transition regime between laminar/laminar and laminar/turbulent interactions is defined by only a few data points, so our correlations are indicative of the trend but certainly not exact. However, using our correlation from Figure 96 to define the shock strength necessary to have fully turbulent flow, p_T/p_1, we obtain Figure 97. Since we did not obtain natural transition on our plate, two data points from Ref 22 are shown for natural transition at $p_o = 850$ psia with leading edge bluntness of .007 in. and .010 in. Our leading edge is .007 in. thick but is flat-faced instead of cylindrical, thereby probably causing a greater bluntness effect. One of the questions raised by our transition data is that the data of Gulbran et al (Ref 24) taken in the same tunnel, was found by Newman and Burke (Ref 19) to be fully turbulent at $p_3/p_1 = 3$ at $p_o = 200$ psia and $x \approx 20$ in., compared to $p_T/p_1 \approx 8.5$ predicted from our data in Figure 97. Their plate was very sharp, however, with natural transition occuring at $x \approx 3$ ft at $p_o = 850$ psia based on the data of Ref 22. Using our curve fit correlation of $p_T \sim \frac{p_1^{.8}}{e^{.5x_1}}$ we can see from Fig. 97 that transition at $x \approx 20$ in. on a very sharp plate should occur for $\frac{p_T}{p_1} \approx 2.8$ at $p_o = 200$ psia. Therefore we can say that our transition correlation (eqn 22) from Fig. 97 is reasonably consistent with shock-induced data from two experiments, and with natural transition data on plates with slight leading edge bluntness taken in the same wind tunnel.

$$\frac{p_T}{p_1} = \frac{26}{p_1^{.2} e^{.5x_1}} \qquad (22)$$

Also, the correlation is similar to the form that we expected from our simplified analysis since over the .5 to 2.0 ft range of x in our test, $e^{.5x} \sim x^{.5}$. The transition correlation is therefore approximately

$$\frac{p_T}{p_1} \sim \frac{1}{p_1^{.2}\, x_1^{.5}} \qquad \text{or} \qquad \frac{p_T}{p_1} \sim \left(\frac{p_1^{.6}}{p_1 x_1}\right)^{.5}$$

which agrees with eqn (21).

The heating rate amplification data, for a boundary layer that is laminar before the shock and turbulent after, correlates from Fig. 96 as

$$\frac{h_{3_{TURB}}}{h_{1_{LAM}}} = 1.9\, p_1^{.22}\, x_1^{.55} \left(\frac{p_3}{p_1}\right)^{.8} \tag{23}$$

This correlation can be compared to the analytical expression, eqn (15), to obtain an equation for x_3, the apparent start of the turbulent boundary layer, however, a modification of eqn (15) to account for leading edge bluntness should be made first. The ideal, zero pressure gradient, laminar flat plate equation used to derive eqn (15) is $h_{LAM} = .46 \frac{p_1^{.5}}{x_1^{.5}}$ which is obtained from eqn (8) by substituting our tunnel flow conditions. Figure 98 presents our actual laminar baseline data with no shock impingement, which, because of our slight leading edge bluntness, correlates as

$$h_{LAM} = .5 \frac{p_1^{.47}}{x_1^{.59}} \tag{24}$$

Modifying eqn (15) by substituting eqn (24) for h_{LAM} we obtain

$$\frac{h_{3_{TURB}}}{h_{1_{LAM}}} = 1.27\, p_1^{.33}\, x_1^{.59} \left(\frac{p_3}{p_1}\right)^{.76} \frac{1}{x_3^{.2}} \tag{25}$$

Equations (23) and (25) can be equated and solved for x_3

$$x_3^{.2} = .67\, p_1^{.11}\, x_1^{.04} \left(\frac{p_1}{p_3}\right)^{.04} \tag{26}$$

An alternate method of correlating x_3, which eliminates the need to accurately define $h_{1_{LAM}}$ is to solve directly for x_3 from the turbulent heating rate, $h_{3\ TURB.}$ This is done in Figure 99 where the turbulent data (initially laminar) is plotted in the form $.634 \frac{p_3^{.8}}{h_3}$ vs p_1, since $x_3^{.2} = .634 \frac{p_3^{.8}}{h_3}$ is the ideal turbulent flat plate equation, eqn 9, for our tunnel conditions. The correlation obtained in this manner becomes

$$x_3^{.2} = .6\, p_1^{.15}\, x_1^{.10} \tag{27}$$

Since this is a more direct solution than eqn (26) we will use eqn (27) as our data correlation for the apparent start of the turbulent boundary layer.

4. THREE-DIMENSIONAL SHOCK GENERATORS

In order to determine the effect of an incident three-dimensional shock on our basic wedge correlation, we tested a limited number of cone and sphere shock generators. The intersection of these shocks with a plate produces a flow field with pressure gradients away from the peak pressure location in the y direction. Flow in the ± y direction will tend to reduce the peak pressure below that obtained with a two dimensional shock of the same strength. Although the pressure will be lower, the heating should be higher (for a given pressure) due to three-dimensional thinning of the boundary layer. Both of these effects should be more pronounced for sphere generators than for cones since the spherical shock strength decreases with downstream distance. This will cause higher pressure gradients in the y direction than would occur for an equivalent shock strength cone.

a. Turbulent Data

Since the initially laminar test data are complicated by separation shocks and boundary layer transition, it is desirable to look at the turbulent data first to determine 3-D effects. Figure 100 shows the cone data with the wedge correlation of $\frac{h_3}{h_1} = \left(\frac{p_3}{p_1}\right)^{.8}$ for comparison. It can be seen that the peak pressure is less than the theoretical value obtained by an inviscid calculation of a conical shock reflected as an oblique shock. However, as expected, the heating correlation is about 25% above the wedge correlation when based on the measured pressure ratio. An interesting point about the turbulent data is that the 3-D effects compensate, in that the heating can be predicted by $\frac{h_3}{h_1} = \left(\frac{p_3}{p_1}\right)^{.8}$ providing the theoretical pressure ratio is used.

As expected, the sphere data (Fig. 101) exhibits stronger 3-D effects than the cone data. The pressure amplification is considerably below the theoretical prediction so that using $\frac{h_3}{h_1} = \left(\frac{p_3}{p_1}\right)^{.8}_{\text{Theory}}$

would result in predicted heating rates high by as much as a factor of two. On the other hand, using the measured pressure ratio will under predict the heating by a factor up to 40%. In order to determine a correlating equation, it is reasonable to assume that spherical shock heating amplification will approach heating due to a wedge shock as the diameter of the sphere increases or as the height of the sphere off the surface decreases. Figure 102 therefore shows the value of $(h_3/h_1)/(p_3/p_1)^{.8}$ versus $\frac{Z}{D}$ where Z is the height of the sphere centerline above the plate. The result is a correlation for turbulent flow

$$\left(\frac{h_3}{h_1}\right)_{\text{Sphere}} = .68\left(\frac{D}{Z}\right)^{.34}\left(\frac{p_3}{p_1}\right)^{.8}_{\text{Theory}}$$

where p_3/p_1 is the inviscid calculation of the incident spherical shock reflected as an oblique shock. This equation should of course be used with caution since it is based on only four data points. Note that the equation predicts that for a large sphere close to the surface ($Z \approx D/2$) the maximum heating is $\frac{h_3}{h_1} \approx .85 \left(\frac{p_3}{p_1}\right)^{.8}_{\text{Theory}}$

b. Initially Laminar Data

The effect of conical and spherical shocks on an initially laminar boundary layer is considerably more complex than the turbulent case. Figure 103 shows all the sharp plate cone data compared to the correlation previously discussed for the wedge data. The heating amplification data are plotted against the measured (not the theoretical) pressure amplification. Although the data are limited it appears that transition occurs at a lower pressure ratio than for two dimensional shocks and that the turbulent heating level h_3/h_1 is less sensitive to impingement location. Earlier transition might be expected since for a given pressure ratio the incident shock strength must be higher for a 3-D shock. The apparent lesser dependence on x implies that the correlation $x_3^{.2} \sim p_1^{.15} x_1^{.1}$ determined for two-dimensional shocks is different for 3-D shocks. The spherical shock data shown in Fig. 104 is very similar to the conical data. Transition occurs at a lower pressure ratio and the heating seems to be less dependent on x than 2-D shock data.

5. BLUNT PLATE RECEIVER

The blunt plate wedge data are shown in Fig. 105 and compared to the correlation of the sharp plate/wedge data. Although the data are not extensive, some trends are apparent. The heating amplification at 22 inches is similar but somewhat lower than for the sharp plate. At the front of the receiver plate, the generator locations were selected to provide impingement at a nominal 7 in. The lower local Mach number, however, resulted in greater wedge shock angles than would occur at M = 8. In addition the plate bow shock interacted with the wedge on some of the runs, as can be seen in Figures 67 and 71. The net result of these effects is that peak heating occurred at about x = 4 inches for the forward wedge runs. The heating amplification at x = 4 inches is higher on the blunt plate than at x = 5 inches on the sharp plate. Also, the pressure ratio required to cause transition is lower on the blunt plate, which is as expected, since natural transition occurs at a smaller x (see Fig. 59). The blunt plate heating data at x = 22 in. is slightly lower than for the sharp plate, which is consistent with eqn (23) for the following reasons. Although p_1 on the blunt plate is twice the sharp plate value, the average impingement location for the blunt cases was x = 19 in., versus x =22 inches for the sharp plate, so that the term $p_1^{.22} x_1^{.55}$ is approximately the same. However, the constant in eqn. (23) is proportional to $\frac{V_1^{.3}}{T_*^{.536}}$ (see eqn. 12) which is somewhat smaller for the blunt plate due to the reduced local Mach number. At the front of the plate the smaller constant in eqn. (23) is more than offset by the term $p_1^{.22} x_1^{.55}$ since the local blunt plate pressure is about five times the sharp plate value. Therefore, the blunt plate heating amplification data at x = 4 in. is about 25% greater than the sharp plate data at x = 5 in. While the blunt plate data qualitatively agree with the sharp plate equations the data were not complete enough to justify a detailed correlation.

6. BOOSTER RECEIVER

The undisturbed flow field on the booster has some of the characteristics of both the sharp and blunt plates. As shown in Fig. 76, the high pressure, low Mach number flow in the nose region expands around the shoulder. The remainder of the flow over the booster is at nearly the free stream pressure, with a low pressure gradient which is characteristic of a sharp flat plate. The bow shock, however, reduces the local flow velocity and raises the static temperature which results in lower heating at a given x station than occurs on the sharp plate. The booster data could be discussed in terms of h_3/h_1 as we have done for the blunt and sharp plates by deriving an expression for the undisturbed laminar heating rate h_1, but since we are mainly interested in the shock

interaction process it is clearer to discuss h_3 directly. The first step is to determine the type of boundary layer present downstream of the shock. The 10 deg. wedge was tested with the booster at p_o = 850, 200 and 75 psia. On the sharp plate (Fig. 96) only the p_o = 75 psia case with the wedge in the forward location was laminar after a 10^o wedge shock. Since the start of natural transition on the booster at p_o = 850 psia is at x = 12 inches (see Fig. 74) and on the sharp plate at x > 24 inches, we can assume that a 10^o wedge shock will result in a turbulent boundary layer for all booster cases.

As discussed in Section III the theoretical inviscid pressure rise for a 10^o wedge shock is $p_3/p_1 \approx 20$. The pressure ratio should be lower on the booster since the local Mach number is less than 8. In addition, three dimensional effects should result in a lower pressure ratio for impingement on the forward cylindrical cross section (fuselage) than on the aft flat plate section (wing) of the booster. The data (Table III) does show these effects (neglecting the p_o = 850 psia run at the forward location which has an additional pressure amplification due to the reflected booster bow shock).

The turbulent heating after the shock can be predicted from the standard flat plate equation (9) assuming p_3 is known from test data, or from inviscid shock calculations.

$$h_3 = .0334 \frac{V_3^{.8}}{T_*^{.576}} \frac{p_3^{.8}}{x_3^{.2}} \tag{28}$$

The ratio $\frac{V_3^{.8}}{T_*^{.576}}$ is somewhat lower than free stream conditions due both to the lower local Mach number on the booster and the effect of the 10^o wedge shock, as shown in Table VII. Both of the effects are relatively small so we will use free stream conditions

$$h_3 = .634 \frac{p_3^{.8}}{x_3^{.2}} \tag{29}$$

Although natural transition occurs at a smaller x on the booster and may effect the correlation of x_3 we will apply our flat plate correlation to the booster runs.

$$x_3^{.2} = .6\, p_1^{.15}\, x_1^{.10}$$

$$h_3 = 1.06 \frac{p_3^{.8}}{p_1^{.15}\, x_1^{.1}} \tag{30}$$

Using the data from Table III, eqn (30) can be compared to the measured h_3.

10^0 Wedge Data/Booster Receiver

Nominal x Ft	p_1 Lbs/Ft^2	p_3 Lbs/Ft^2	Data h_3 Btu/Hr-Ft^2-^{o}R	Eqn. (30) h_3 Btu/Hr-Ft^2-^{o}R
.5	2.02	23.6	11.6	12.9
.5	4.76	58.4	17.9	23.4
.5	17.1	574.0	106.0	119.0
1.16	1.87	26.6	10.8	13.1
1.16	4.46	63.4	19.9	22.9
1.16	16.13	200.0	53.6	47.7

With the exception of the last data point, eqn. (30) overpredicts the data by 10 - 30%. This is to be expected since the value of $\frac{V_3^{.8}}{T_*^{.576}}$ used in eqn. (30) was for free stream conditions and is lower for local conditions on the booster due to the bow shock. The last data point is at p_o = 850 psia with the wedge located aft on the booster, so that the shock impinges at $x_i \approx 14$ inches. As noted above, the undisturbed heating is transitional at this location on the booster. This may explain why eqn. (30) underpredicts the heating since the correlation of x_3 was based on initially laminar data.

7. DESIGN METHODS

In paragraph IV-1, we postulated relations to define shock induced transition and heating amplification. These relations were not based on rigorous analysis but it was hoped they would indicate the parameters of importance and the approximate form of the equations. In paragraphs IV-2 thru IV-6 we correlated the test data and compared the results to the assumptions of paragraph IV-1 in order to establish the most reasonable design methods. The steps recommended to obtain an engineering estimate to an interference heating problem are as follows:

1) Define the undisturbed flow field including local velocity, pressure and temperature.

2) Specify the natural transition Reynolds number

3) Determine the shock strength p_3/p_1 from an inviscid calculation or test data if available

4) If the initial boundary layer is turbulent $h_3 = h_1 \left(\frac{p_3}{p_1}\right)^{.8}$.

5) If the initial boundary layer is laminar estimate the pressure ratio required to cause transition by

$$\frac{p_T}{p_1} = \frac{C}{p_1^{.2}\, e^{.5x_1}}$$ where C can be determined from the natural transition conditions, $p_1 = p_T$, $x_1 = x_T$ and $p_{T/p_1} = 1$.

6) If $p_3/p_1 < .5 \frac{p_T}{p_1}$ assume the boundary layer after the shock is laminar and predict the heating by $h_3 = h_{1_{LAM}} \left(\frac{p_3}{p_1}\right)^{.7}$

7) If $p_3/p_1 > \frac{p_T}{p_1}$ the resultant boundary layer is assumed to be fully turbulent.

8) Predict the apparent start of the turbulent boundary layer by $x_3^{.2} = .6\, p_1^{.15}\, x_1^{.1}$

9) The turbulent heating is then given by $h_3 = 0.334 \frac{V_3^{.8}}{T_{*3}^{.576}} \frac{p_3^{.8}}{x_3^{.2}}$

10) If p_3/p_1 is between $.5 \frac{p_T}{p_1}$ and $\frac{p_T}{p_1}$ the boundary layer is transitional and the conservative assumption is to use the turbulent heating rate for h_3.

The above approach is applicable to shocks that can be considered two dimensional. Three dimensional shocks appear to result in lower heating (if based on the theoretical 2D pressure rise) but will cause an initially laminar boundary layer to transition to turbulent at a lower shock strength.

It should be noted that these methods are based on correlating data at M = 8 and a Reynolds number range of .4 to 3.7 x 10^6/ft. Caution should be exercised in using these equations for other flow conditions. This is especially true of the expression for x_3, for which no analytical logic has, as yet, been developed.

8. APPLICATION OF METHODS TO ORBITER/BOOSTER

We obtained data on several very interesting orbiter/booster configurations, with complex shock patterns impinging and reflecting off both the orbiter and booster, that can be used to check the recommended design methods in the previous paragraphs. Since this data was obtained very late in the program, a review of only one simple case can be included in this report, although all the data is presented in Table III.

The configuration chosen for discussion is the orbiter located aft at a 10^{o} angle of attack to the booster. The tunnel pressure was p_o = 850 psia, the thermocouple data are from group 403, and the pressure data are from group 452. The data are presented in Figures 82 and 86. Since we are primarily concerned with the analytical prediction of the shock interaction effects, we will assume that the undisturbed flow fields on the orbiter and booster are known, and that we desire a conservative preliminary estimate of the heating amplification due to impingement of the orbiter shock on the booster. Since natural transition on the booster begins to occur at $x \approx 12$ inches and the orbiter shock for this configuration will impinge at $x \approx 16$ inches, we can assume that the orbiter shock is strong enough to separate the boundary layer and cause turbulent heating in the re-attachment region. The undisturbed booster pressure from Table III is $p_1 = 15.8$ lbs/ft^2. As discussed in Section III, Hill's correlation of the laminar separation plateau pressure is $P_{pl} = 1.7\ p_1 = 26.9$ Lbs/Ft^2. The orbiter shock angle is 13^{o}, for the 10^{o} angle of attack. The inviscid pressure rise is $p_3/P_{pl} \approx 11$ at M = 8. Although the local Mach number is less than 8 due to the combined effects of the booster bow shock and the boundary layer separation shock, it is conservative to use the pressure rise for M = 8. Therefore $p_3 = 11 \times P_{pl} = 296$ Lbs/Ft^2. Another conservatism in the prediction of the shock pressure rise is the treatment of the orbiter shock as a wedge shock. The orbiter shock will be somewhat three dimensional, which should result in a lower pressure rise. However, in the case of cone generators we have shown that the lower pressure rise is offset by increased heating due to three dimensional thinning of the boundary layer and the theoretical pressure ratio for a wedge shock should be used to predict heating. Therefore, using $p_3 = 296$ lbs/ft^2, $p_1 = 15.8$ Lbs/Ft^2 and x = 1.33 ft in eqn (30) we obtain

$$h_3 = 1.06 \frac{\left(\frac{p_3}{p_1}\right)^{.8}}{.15\, x_1^{.1}} = 64 \frac{\text{Btu}}{\text{hr-ft}^2\text{-}^{o}\text{F}}$$

which compares with the experimental value of h = 60 Btu/hr-ft^2-^{o}F from Table III. Although this level of accuracy is probably not typical, the sample calculation does illustrate the steps required to obtain an engineering estimate of a shock interference heating rate.

Section V

CONCLUSIONS

Fairly extensive data of pressure and heating amplification due to wedge shocks impinging on sharp flat plate laminar and turbulent boundary layers indicate that a simplified analytical approach to interaction problems is feasible.

1) The shock induced pressure rise can be predicted by an inviscid flow field calculation across the incident and reflected shocks. It is important to include the possible pressure rise due to flow separation and to consider extraneous shocks that may reflect off the shock generator and amplify the pressure rise due to the primary shock. A fairly common cause of shock reflection is the boundary layer separation shock, which is almost always present for laminar boundary layers and for turbulent boundary layer interactions with strong shocks.

2) Heat transfer for laminar interactions can be predicted from the pressure rise by $\left(\frac{h_{peak}}{h_{Und}}\right) = \left(\frac{p_{peak}}{p_{Und}}\right)^{.7}$.

3) Heat transfer for turbulent interactions can be predicted from the pressure rise by $\left(\frac{h_{peak}}{h_{Und}}\right) = \left(\frac{p_{peak}}{p_{Und}}\right)^{.8}$.

4) The prediction of heating for an initially laminar boundary layer that transitions to turbulent, due to the incident shock, requires a method of predicting the apparent start of the resulting turbulent boundary layer. Correlations of the pressure ratio required to cause transition and the apparent start of the turbulent boundary layer are presented in Section IV as well as some logic to explain the form of the pressure ratio correlation. The present simplified analytical approach did not yield an explanation for the correlation of the apparent start of the turbulent boundary layer. This theoretical understanding is necessary before the correlation can be applied with confidence to conditions other than those tested.

Data was also taken with conical and spherical shock generators and blunt plate and booster receivers. While time did not permit a detailed correlation of this data some general conclusions were reached.

5) Pressure rises due to 3D shocks are less than predicted by inviscid calculations assuming the reflected shock is two dimensional. The heating can be conservatively predicted by using the theoretical pressure ratio. The 3D shock appears to cause an initially laminar boundary layer to transition at a lower shock strength than does a 2D shock.

6) The heating correlations for the sharp flat plate are applicable to the blunt plate and booster providing local flow conditions are used where values are significantly different from free stream conditions. The correlation of the pressure ratio required to cause transition must be adjusted for the different natural transition points of the blunt plate and booster.

REFERENCES

1 Ryan, B.M., "Summary of the Aerothermodynamic Interference Literature" Naval Weapons Center TN 4061 - 160, April 1969

2 Sayano, S., "Heat Transfer in Shock Wave-Turbulent Boundary Layer Interaction Regions," Douglas Report No. SM-42567, November 1962

3 Murphy, J.D., "A Critical Evaluation of Analytic Methods for Predicting Laminar Boundary Layer - Shock Wave Interaction, "NASA SP-228, Oct. 1969

4 Rose, W.C. "A Method for Analyzing the Interaction of an Oblique Shock Wave and a Boundary Layer," NASA SP-228, Oct 1969

5 Markarian, C.F. "Heat Transfer in Shock Wave - Boundary Layer Interaction Regions," Naval Weapons Center TP 4485, November 1968

6 Romanowski, R. "Report of AFFDL/Grumman Interference Heating Tests Performed at AEDC Tunnel B, 11/71 to 4/72," Grumman Report AER/T - AEDC/B - 1, May 1972

7 Jones, R.A. and Hunt, J.L. "Use of Fusible Temperature Indicators for Obtaining Quantitative Aerodynamic Heat Transfer Data," NASA TR - R - 230, February 1966

8 Chapman, D.R., Kuehn, D.M. and Larson, H.K., "Investigation of Separated Flows in Supersonic and Subsonic Streams with Emphasis on the Effect of Transition," NACA Report 1356, 1958

9 Eckert, E.R.G., "Engineering Relations for Friction and Heat Transfer to Surfaces in High Velocity Flow," Jour. Aero Sci Readers Forum, Vol. 22, No. 8, August 1955

10 Korkegi, R.H., "Effect of Transition on Three-Dimensional Shock - Wave/Boundary - Layer Interaction," AIAA Journal, Vol. 10, No. 3, March 1972

11 Hama, F.R., "Estimation of the Strength of Lip Shock," A1AA Journal, Vol. 4, No. 1, January 1966

12 Hill, W.G. Jr., "A Comparison of Theory and Experiment for Laminar Separation ahead of a Compression Corner at Supersonic and Low Hypersonic Speeds," Grumman Research Report RE-401, December 1970

13 Ames Research Staff, Equations, Tables, and Charts for Compressible Flow, NACA Report 1135, 1953

14 Eckstrom, D.J., "Engineering Analysis of Boundary Layers and Skin Friction on Bodies of Revolution at Zero Angle of Attack," Lockheed Missiles and Space Co. Rept. LMSC/805162, May 1965

15 Lukasiewicz, J., "Blast-Hypersonic Flow Analogy Theory and Application," ARS Jr, pp 1341-1346, September 1962

16 Edney, B.E., "Anomalous Heat Transfer and Pressure Distributions on Blunt Bodies at Hypersonic Speeds in the Presence of an Impinging Shock," FFA Report 115, Sweden, February 1968

17 Kaufman, L.G. II, Korkegi, R.H., and Morton, L.C., "Shock Impingement Caused by Boundary Layer Separation Ahead of Blunt Fins," Grumman Research Report RE-428, July 1972 (to be published also as an ARL Report).

18 Harms, R.J., et al, "A Manual for Determining Aerodynamic Heating of High Speed Aircraft, Volume I," Bell Aircraft Corp. Report No. 7006-3352-001, June 1959

19 Neumann, R & Burke G., "The Influence of Shock Wave-Boundary Layer Effects on the Design of Hypersonic Aircraft," AFFDL TR-68-152, March 1969

20 Holden M., "Shock Wave - Turbulent Boundary Layer Interaction in Hypersonic Flow", AIAA Paper 72-74, January 1972

21 Hains, F.D. & Keyes, J.W., "Shock Interference Heating in Hypersonic Flows," AIAA Paper 72-78, January 1972

22 Whitfield, J. & Potter, J.L., "The Influence of Slight Leading Edge Bluntness on Boundary Layer Transition at a Mach Number of Eight," AEDC TDR-64-18, March 1964

23 Pate, S.R. & Schueler C.J. "Radiated Aerodynamic Noise Effects on Boundary-Layer Transition in Supersonic and Hypersonic Wind Tunnels," AIAA Journal, March 1969

24 Gulbran, et al "Heating in Regions of Interfering Flow Fields, Part III," AFFDL-TR-65-49, March 1967

Table I Run Schedule Overview

Entry	Date	Occupancy	Receiver	Generators	Type of Testing
1	11/30/71 12/9/71	48 hours	Flat Plate (Blunt & Sharp)	Wedges, Cones, Hemispheres, Orbiter Vehicle (uninstrumented)	Thermocouple
			Booster Vehicle	Wedges, Cones, Hemispheres, Orbiter Vehicle (uninstrumented)	Thermocouple
			Booster Vehicle	Wedges, Cones, Hemispheres, Orbiter Vehicle (uninstrumented)	Phase Change Paint
1A	2/18/72	8 hours	Flat Plate (Sharp)	Wedge, Cones	Thermocouple
2	2/24/72 3/3/72	56 hours	Flat Plate (Blunt & Sharp)	Wedge, Cones, Hemisphere, Orbiter Vehicle (uninstrumented)	Pressure
			Booster Vehicle	Wedge, Cones, Hemisphere, Orbiter Vehicle (uninstrumented)	Pressure
3	3/29/72 4/4/72	32 hours	Flat Plate (Sharp)	Wedge, Cones, Hemispheres	Phase Change Paint
			Booster Vehicle	Orbiter Vehicle (instrumented)	Thermocouple
			Booster Vehicle	Orbiter Vehicle (instrumented)	Pressure
			Booster Vehicle	Orbiter Vehicle	Phase Change Paint

Nominal test conditions are listed below.

Mach Number: 8				
Tunnel Total Pressure, Po (PSIA)	850	400	200	75
Tunnel Total Temperature, T_o(°R)	1341	1286	1245	1200
Reynolds number per foot:	3.7×10^6	1.9×10^6	1.0×10^6	$.4 \times 10^6$

Table II Data Obtained on Flat Plate with Sharp Leading Edge

p_o (psia)	x_i (in.)	Wedge Angles					Cone Half Angles				Hemispheres	
		0 T	1.5° p T	5° p T	10° p T	15° p T	2.5° p T P	7.5° p T P	7.5° L T	12.5° p T P	0.5" p T P	2.0" p T P
850	5		• •	• •	• •	• •		•			•	
	11		• •	• •	• •	• •						
	22		•	•	• •	• •						
trip	22	*	•	* *	* *	* *	• • •	• * •	*	• •	* * •	* * •
400	5		• •	• •	• •	• •		• •			• •	
	11		• •	• •	• •	• •		• •			• •	
	22		• •	• •	• •	• •		• •			• •	
200	5		• •	• •	• •	• •		• •			• •	
	11		• •	• •	• •	• •						
	22		• •	• *	• •	• •	• •	• •		• •	• *	•
75	5		• •	• •	• •	• •	• •	• • •	•	• • •	• * •	• •
	11		• •	• •	• •	• •						
	22		• •	• •	• •	* *	• •	• • •		• •	• *	• •

* Data obtained for two or more heights of shock generator above plate.

p - Pressure T - Thermocouple P - Paint

Table III Data Summary (Sheet 1 of 11)
a. Sharp Flat Plate Initially Laminar BL – No Trip

WEDGE GENERATORS				HEAT TRANSFER										PRESSURE									NOTE
								PEAK			UNDISTURBED								PEAK		UNDIST.			
P_o psia	α deg	Nom x_i, in.	Z_m in.	Grp No.	x_i Plt in.	x_i BL in.	x_{PK} in.	$\frac{h_T}{h_{REF}}$	h_T †	h_{aw_L} †	$\frac{h_T}{h_{REF}}$	h_T †	h_{aw} †	$\frac{h_{aw,PK}}{h_{aw,\,Und}}$	Grp No.	x_i Plt in.	x_i BL in.	x_{PK} in.	$\frac{P}{P_\infty}$	P psia	$\frac{P}{P_\infty}$	P psia	$\frac{P_{PK}}{P_{Und}}$	
75	1.5	5	.8	119	4.0	3.0	4.5	.051	1.76	2.34L	.026	.90	1.20	1.95	328	4.3	2.6	5.3	4.3	.037	1.5	.0129	2.9	
		11	.8	118	9.0	7.1	9.0	.051	1.76	2.34L	.0175	.60	.80	2.92	327	9.0	7.1	9.0	5.2	.0449	1.37	.0118	3.8	(1)
		11	.8	242	9.0	7.5	10.	.036	1.24	1.65L	.016	.55	.73	2.26										(2)
		22	.8	117			19.5	.022	.76	1.00L	.0105	.36	.48	2.08	329			19.8	4.2	.036	1.2	.0104	3.5	(3)
	5	5	.8	94	3.5	2.9	5.5	.065	2.24	2.98L	.024	.828	1.10	2.71	325	4.0	2.9	5.5	8.0	.069	1.58	.0136	5.1	
		11	.8	239	10.8	8.3	11.5	.078	2.69	3.58L	.015	.518	.689	5.20	326	10.8	8.3	11.8	14.5	.125	1.25	.011	11.4	(4)
		22	.8	93			23	.21	7.25	8.77T	.0094	.324	.431	20.2	324	21.2		22.6	13	.110	1.15	.0099	11.1	
	10	5	.8	95	5.2	3.5	5.8	.155	5.35	7.12L	.0235	.811	1.08	6.59	321	5.2	3.5	4.8	26.	.224	1.55	.013	17.2	
		11	.8	240	10.6	8.0	11.2	.44	15.2	18.2T	.015	.518	.689	26.4	322	10.6	8.0	10.6	45.	.388	1.3	.011	35.3	
		22	.8	90	21.5	18.6	21.5	.43	14.8	17.8T	.01	.345	.459	38.7	323	21.5		20.8	31.	.268	1.15	.0099	27.1	
	15	5	.8	96	5.2	4.4	5.2	.9	31.1	37.3T	.024	.828	1.10	33.9	317	4.9	4.0	4.8	61	.526	1.55	.0134	39.4	
		11	.8	241	10.8	8.6	10.6	.88	30.4	36.5T	.0155	.535	.712	51.3	318	10.8	8.6	10.6	78	.673	1.3	.0112	60.	
		22	.8	87	22.2	19.7	22.2	.67	23.1	27.7T	.0097	.335	.446	62.2										(5)
		22	.8	88	22.2	19.7	22.2	.72	24.8	29.8T	.0097	.335	.446	66.8										(5)
		22	.8	89	22.2	19.7	22.2	.68	23.5	28.2T	.0097	.335	.446	63.2	319	21.2		21.5	52	.449	1.12	.0097	46.5	(6)
		22	1.0	243	22.2	19.7	22.2	.70	24.2	29.0T	.0097	.335	.446	65.0										(6)
		22	1.2	244	22.5	20.4	22.8	.75	25.9	31.1T	.0094	.324	.431	72.2	320	22.5	20.4	23.2	68	.587	1.12	.0097	60.7	(6)
200	1.5	5	.8	229	4.5	3.1	5.4	.045	2.511	3.315L	.022	1.228	1.621	2.05	305	4.5	3.1	5.0	3.5	.0767	1.5	.033	2.33	(7)
		11	.8	231	10.0	8.5	11.0	.038	2.120	2.798L	.012	.670	.884	3.17	306	10.0	8.5	11.	3.7	.081	1.25	.027	2.96	
		22	.8	232	21.0	18.9	21.6	.014	.781	1.031L	.0088	.491	.648	1.59	307	20.3	18.0	21.6	3.2	.0701	1.1	.024	2.9	
	5	5	.8	236	4.5	2.9	5.6	.085	4.743	6.261L	.022	1.228	1.621	3.86	310	4.0	2.9	5.6	6.2	.1358	1.40	.031	4.43	
		11	.8	237	11.4	9.0	11.4	.085	4.743	6.261L	.012	.670	.884	7.08	309			11.4	9.5	.208	1.25	.027	7.6	
		22	.8	84	22	19	23.2	.34	18.972	22.577T	.0086	.480	.634	35.61	308	22.0	19.0	23.0	14.8	.324	1.1	.024	13.5	(8)
		22	.5	238	22.5	18.6	22.2	.105	5.859	6.972T	.0085	.474	.626	11.14										
	10	5	.8	83	5.1	3.7	5.8	.26	14,508	17.265_T	.021	1.172	1.547	11.16	311	5.1	3.7	6.0	18.0	.394	1.4	.031	12.9	
		11	.8	233	11.5	9.0	11.6	.44	24.552	29.217_T	.012	.670	.884	33.05	312	11.5	9.0	11.4	4.3	.942	1.25	.027	34.4	
		22	.8	85	21.9	18.8	22.	.44	24.552	29.217_T	.0086	.480	.634	46.08	313	21.3	19.0	21.4	30.	.657	1.15	.025	26.1	

† $\frac{BTU}{HR\text{-}FT^2\text{-}^oF}$ L – Laminar T – Turbulent

NOTES

(1) Gen Reflects Plate LE Shock. 2nd peak h/h at X=13 due to refl of wedge shock (Ref - Shadowgraph for GRP 118)

(2) GRP 242 is repeat of 118 with Gen moved Aft 1" to prevent LE shock from striking Gen.

(3) 2nd h/h peak at X = 24"; (h_T, peak/h_T, und) = 4
2nd press. peak at X = 23", but p at 23 < p_{peak}

(4) Generator reflects plate LE shock

(5) Groups 87 & 88 (h) plate at neg α

(6) These three runs examined effect of BL occupying space between gen. & plate. For Z_m = .8 space is all BL. For Z_m = 1.2 gen should be out of BL.

(7) 2nd P/P_∞ peak at X = 8 P/P_{und} = 3.7
2nd h/h peak at X = 8.6 ($h_T/h_{T,\,und}$) = 4.65

(8) Shadowgraph for group 84 shows wave from gen trailing edge striking plate upstream of X_{peak}. For Group 238, gen moved down 0.3" & aft 1.0" to move X_{peak} upstream of wave while keeping $X_{peak} \approx$ constant.

Table III Data Summary (Sheet 2 of 11)
a. Sharp Flat Plate Initially Laminar BL – No Trip

WEDGE GENERATORS				HEAT TRANSFER										PRESSURE									NOTE
								PEAK			UNDISTURBED							PEAK		UNDIST.			
P_o psia	α deg	Nom x_i, in.	Z_m in.	Grp No.	x_i Plt in.	x_i BL in.	x_{PK} in.	$\frac{h_T}{h_{REF}}$	h_T †	h_{aw} †	$\frac{h_T}{h_{REF}}$	h_T †	h_{aw_L} †	$\frac{h_{aw,PK}}{h_{aw,Und}}$	Grp No.	x_i Plt in.	x_i BL in.	x_{PK} in.	$\frac{P}{P_\infty}$	P psia	$\frac{P}{P_\infty}$	P psia	$\frac{P_{PK}}{P_{Und}}$	
200	15	5	.8	235	4.8	3.8	4.8	.70	39.06	46.48_T	.0235	1.311	1.731	26.9	316	5.0		5.2	42	.92	1.5	.033	34.6	
		11	.8	234	11.0	9.0	11.0	.90	50.22	59.76_T	.012	.670	.884	67.6	315	10.3	9.3	11.3	87.	1.91	1.25	.027	69.5	
		22	.8	86	22.7	20.9	22.6	.80	44.64	53.12_T	.0086	.480	.634	83.8	314	22.0	20.0	22.6	56.	1.23	1.1	.024	51.0	
400	1.5	5	.8	228	5.0	3.2	5.6	.044	3.45	4.52_L	.024	1.88	2.46	1.84	288	6.0	3.5	5.6	2.8	.118	1.35	.057	2.08	
		11	.8	227	10.0	8.6	11.	.038	2.98	3.90_L	.014	1.09	1.44	2.71	287	10.0	8.6	11.0	3.5	.148	1.20	.051	2.91	
		22	.8	226	22.6	19.5	22.	.0135	1.06	1.39_L	.0084	.659	.863	1.61	286	23.5	19.5	24.2	4.7	.199	1.08	.046	4.35	(9)
	5	5	.8	224	5.0	3.0	5.2	.083	6.51	8.52_L	.024	1.88	2.46	3.46	285	5.0	3.0	6.5	7.3	.309	1.3	.055	5.63	(10)
		11	.8	223	11.5	9.4	12.	.105	8.23	10.8_L	.0135	1.06	1.39	7.77	284	11.5	9.4	12.2	9.9	.419	1.2	.051	8.25	
		22	.8	225	22.8	19.7	22.6	.060	4.70	6.16_L	.0083	.651	.852	7.23	283	23.3	22.6	23	11.5	.486	1.1	.047	10.5	(11)
	10	5	.8	6	5.1	4.	5.4	.32	25.1	29.9_T	.0235	1.84	2.41	12.4	281	5.6	4.6	6.2	19.	.804	1.3	.055	14.6	
		11	.8	62			11.2	.42	32.9	39.2_T	.014	1.09	1.44	27.2	280	11.3	10.2	11.8	36.	1.52	1.2	.051	30.0	
		22	.8	63	22	19.9	22.2	.51	39.9	47.6T	.0084	.659	.863	55.2	282	21.7	20.1	22.2	31.	1.31	1.1	.047	28.2	
	15	5	.8	221	4.6	3.9	4.8	.77	60.4	71.8_T	.024	1.88	2.46	29.2	278	4.6	3.9	5.2	41	1.73	1.37	.058	30	
		11	.8	222	11.0	9.3	11.0	1.15	90.2	$107._T$	.014	1.09	1.44	74.3	279	11.0	9.3	11.3	85	3.60	1.2	.051	71	
		22	.8	219	22.7	20.4	22.4	1.0	78.4	93.3_T	.0083	.651	.852	109.	277	22.0	20.8	22.8	68	2.88	1.1	.047	61.9	(12)
		22	.8	220	22.5	20.4	22.4	1.0	78.4	93.3_T	.0083	.651	.852	109.										(12)
850	1.5	5	.8	110			3.8	.038	4.31	5.61_L	.025	2.84	3.69	1.52	272	4.4	3.1	5.5	2.7	.233	1.4	.121	1.92	(13)
		11	.8	115	10.	8.	10.2	.048	5.45	7.08_L	.0145	1.65	2.14	3.31	271	10.0	8.0	11.4	4.1	.354	1.3	.112	3.15	(14)
		11	.8	215	10.3	8.5	11.	.032	3.63	4.72_L	.014	1.59	2.07	2.28	270	10.3	8.5	11.8	4.0	.348	1.3	.112	3.08	(15)
		22	.8	116	19.6	18.9	21.	.0155	1.76	2.29_L	.0086	.976	1.27	1.80	269			21.0	2.5	.26	1.05	.090	2.38	
	5	5	.8	111	4.7	3.3	5.4	.080	9.08	11.8_L	.023	2.61	3.39	3.48	265	6.5	4.3	6.6	6.6	.57	1.2	.104	5.5	(16)
		5	.8	214	5.0	2.7	5.6	.083	9.42	12.2_L	.022	2.50	3.25	3.75	264	5.9	3.8	5.8	6.0	.518	1.2	.104	5.0	(17)
		11	.8	114	11.2	8.9	11.2	.17	19.3	22.8_T	.0138	.157	2.04	11.2										
		22	.8	213	22.7	19.4	23.2	.115	13.1	15.4_T	.008	.908	1.18	13.1	262	23.3	19.9	23.6	6	.518	1.05	.091	5.7	(18)

† $\frac{BTU}{HR\text{-}FT^2\text{-}^oF}$ L – Laminar T – Turbulent

NOTES

(9) Heat transfer & pressure data not consistent. Schlieren & shadowgraph show different BL flows.

(10) At X = 6.6 (h/h) = .105/.023 = 4.6
At X = 6.8 $(P/P_\infty/P/P_{\infty,und})$ = 8.2/1.30 = 6.3.

(11) More than one h/h peak possible. Correct choice of 1st peak for h/h is uncertain. Do not use for correlation.

(12) Groups 219 & 220 are repeats.

(13) Group 110: 1st data point on plot is assumed to be $(h/h)_{peak}$

(14) Group 215 repeats group 115, but gen. moved aft 1.0" gen will not reflect LE shock.

(15) At X = 14.4 $(h/h)_{peak}/(h/h)_{und}$ = .074/.011 = 6.84
At X = 14.6 $(P/P_\infty)_{pk}/(P/P_\infty)_{und}$ = 5./1.1 = 4.55

(16) Plate LE shock is refl by gen trailing edge & strikes plate in X max region. At X = 7.6 $(h/h)_{peak}/(h/h)_{und}$ = .090/.020 = 4.5
At X = 7.5 $(P/P_\infty)_{peak}/(P/P_\infty)_{und}$ = 8.5/1.18 = 7.2

(17) Repeat of groups 111 & 265 with gen. moved fore 0.6" & no refl at X = 6.8 $(h/h)_{peak}/(h/h)_{und}$ = .125/.020 = 6.3
At X = 5.8 $(P/P_\infty)_{peak}/(P/P_\infty)_{und}$ = 9/1.2 = 7.5

(18) At X = 24.5 $(h/h)_{peak}/(h/h)_{und}$ = .2/.0077 = 26
At X = 24.4 $(P/P_\infty)_{peak}/(P/P_\infty)_{und}$ = 8.8/1.02 = 8.6

Table III Data Summary (Sheet 3 of 11)
a. Sharp Flat Plate Initially Laminar BL – No Trip

WEDGE GENERATORS				HEAT TRANSFER										PRESSURE									
								PEAK			UNDISTURBED							PEAK		UNDIST.				
p_0 psia	α deg	Nom x_i, in.	Z_m in.	Grp No.	x_i Plt in.	x_i BL in.	x_{PK}	$\frac{h_T}{h_{REF}}$	h_T †	h_{aw} †	$\frac{h_T}{h_{REF}}$	h_T †	h_{aw_L} †	$\frac{h_{aw,PK}}{h_{aw,Und}}$	Grp No.	x_i Plt in.	x_i BL in.	x_{PK} in.	$\frac{p}{p_\infty}$	p psia	$\frac{p}{p_\infty}$	p psia	$\frac{P_{PK}}{P_{Und}}$	NOTE
850	10	5	.8	30	5.6	4	5.8	.51	57.9	68.3_T	.022	2.50	3.25	21.0	266	5.6	4.0	6.4	20.	1.73	1.2	.104	16.7	
		11	.8	216	11.2	9.5	11.2	.59	66.9	79.0_T	.014	1.59	2.07	38.2	267	11.5	9.5	12.0	33.	2.85	1.15	.099	28.7	
		22	.8	217	21.4	20.1	23.	.62	70.4	83.0T	.008	.908	1.18	70.3	268	22.0	19.8	22.6	32.	2.76	1.05	.091	30.5	
	15	5	.8	112	5.1	4.2	6.0	.85	96.5	$114._T$	.021	2.38	3.10	36.8	273	5.5	4.4	6.4	47.	4.06	1.2	.104	39.2	
		11	.8	113	11.2	10.2	11.2	1.00	114.0	$135._T$	.014	1.59	2.07	65.2	274	11.2	10.2	11.8	86.	7.43	1.15	.099	74.8	
		22	.8	218	23.2	21.0	23.2	1.05	119.0	140.T	.008	.908	1.18	119.	275	23.2	21.0	23.2	79.	6.83	1.05	.091	75.5	
CONE GENERATORS																							
p_0 psia	α deg	Nom x_i, in.	Z_m in.																				
75	2½	5	.8	102			6	.030	1.14	1.52_L	.022	.759	1.01	1.36	332			5	1.95	.017	1.56	.013	1.31	
		20	.8	124			20.6	.02	.69	$.92_L$	.01	.345	.459	2.0	331			22*	1.4	.012	1.12	.010	1.2	(19)
		22	.8	103			21	.018	.62	$.82_L$	.01	.345	.459	1.79										(20)
	7½Lg	5	.8	99	4.7	3.8	5.2	.084	2.90	3.85_L	.024	.83	1.1	3.5										(21)
	7½	5	.8	100	4.7	3.5	5.6	.093	3.21	4.27_L	.023	.794	1.06	4.03	334	4.7	3.0	5.4	4.5	.039	1.52	.013	3.0	
		5	1.0	127	5.2	4.	5.4	.08	2.76	3.67_L	.023	.794	1.06	3.46										
				383P				.065	2.24	3.0_L														
		22	.8	101		19.8	22.8	.067	2.31	2.77_T	.0094	.324	.431	6.42	333			21.4	4.2	.036	1.14	.010	3.6	
				384P				.065	2.25	2.7T														
	12½	5	.8	121	5.1	4.4	5.8	.22	7.59	9.11_T	.022	.759	1.01	9.02	335	6.1	5.7	5.8	11.6	.10	1.51	.013	7.69	
				385P				.23	6.7	8.0_T														
		22	.8	120			23	.20	6.90	8.28_T	.011	.38	.505	16.4	336	23.2	22.5	22.8	15	.13	1.12	.010	13.0	(22)
200	2.5	22	.8	78			21	.0145	.809	1.07_L	.0086	.48	.633	1.69	302		20.8	21 - 22	1.35	.030	1.11	.024	1.25	(23)
	7.5	5	.8	75	5.9	4.9	6.4	.11	6.14	7.30_T	.018	1.00	1.33	5.49	303	6.5	5.1	6.4	4.4	.096	1.42	.031	3.10	
		22	.8	76	22.5	20.5	22.4	.042	2.34	3.08_L	.0084	.47	.62	4.97	304	22.5	20.5	22.8	4	.088	1.11	.024	3.60	(24)
	12.5	22		77	23.1	21.5	23.2	.21	11.7	13.9_T	.0084	.469	.619	22.5	301	23.1	20.8	23	13.5	.30	1.11	.024	12.5	

† $\frac{BTU}{HR\text{-}FT^2\text{-}^oF}$

L – Laminar
T – Turbulent
P – Paint Run
Lg – 2½ dia. Base

NOTES

(19) Peak (h/h) is on same order as noise. Press. data begins at X = 22" - peak X may be at X<22"

(20) Peak (h/h) is on same order as noise.

(21) At $X = 6.2\ (h/h)_{peak}/(h/h)_{und} = .11/.022 = 5$

(22) In undisturbed region h/h was slightly higher than $(h/h)_{und}$ so at X_{peak}, the value (h/h) used was corrected up.

(23) h_T data noisy at X_{max}

(24) At $X = 23.4\ (h/h)_{peak}/(h/h)_{und} = .078/.0084 = 9.3$ Plot of h_T seems inconsistent with press. Plot Schlieren & shadowgraph show inconsistent BL flows.

Table III Data Summary (Sheet 4 of 11)
a. Sharp Flat Plate Initially Laminar BL — No Trip

CONE GENERATORS				HEAT TRANSFER											PRESSURE									NOTE
								PEAK			UNDISTURBED								PEAK		UNDIST.			
p_o psia	α deg	Nom x_i, in.	Z_m in.	Grp No.	x_i Plt in.	x_i BL in.	x_{Pk} in.	$\frac{h_T}{h_{REF}}$	h_T †	h_{aw} †	$\frac{h_T}{h_{REF}}$	h_T †	h_{aw_L} †	$\frac{h_{aw,PK}}{h_{aw,Und}}$	Grp No.	x_i Plt in.	x_i BL in.	x_{PK} in.	$\frac{P}{P_\infty}$	P psia	$\frac{P}{P_\infty}$	P psia	$\frac{P_{PK}}{P_{Und}}$	
400	7.5	5	.7	56	5.4	4.2	6	.12	9.41	11.2_T	.02	1.57	2.05	5.46	289	6.2	5.4	6.8	4.3	.182	1.30	.055	3.31	(25)
		5	.7	57	5.4	4.2	6	.12	9.41	11.2_T	.02	1.57	2.05	5.46										
		11	.7	55		10.	11.8	.12	9.41	11.2_T	.0125	.98	1.28	8.75	290	11.4	10.0	12	5.9	.25	1.18	.05	5.0	
		22	.7	54	22.5	20.2	22.8	.085	6.66	7.93_T	.008	.627	.822	9.65	291	22.5	20.2	22.8	4.4	.186	1.08	.046	4.04	
850	7.5	5	.7	29	5.4	4.2	6.2	.115	13.1	15.5_T	.0197	2.24	2.91	5.30										
SPHERE GENERATORS																								
p_o psia	Nom x_i, in.	dia. in.	Z_m in.																					
75	5	½	.8	122	6.1	5.2	6.2	.095	3.28	3.93_T	.022	.759	1.01	3.89	338	6.1	5.2	6.4	4.2	.036	1.5	.013	2.77	
		½	1.3	128	7.6	6.1	7.0–8.0	.044	1.52	2.02_L	.0195	.673	.895	2.26										(26)
		2	1.0	125	6	5.3	6	.45	15.5	18.6_T	.022	.759	1.01	18.4										
				382P				.47	16.2	19.5_T														
	22	½	.8	123	22.1	21.3	22.4	.073	2.52	3.35_L	.0095	.328	.436	7.68	337	22.1	21.3	22	3.9	.034	1.14	.010	3.40	
		½	1.3	129	23.5	21.3	24	.032	1.10	1.46_L	.009	.311	.414	3.53										(26)
		2	1.0	126	22.3	21.6	22.6	.40	13.8	16.6_T	.0094	.324	.431	38.5										
				381P				.41	14.	16.8_T														
200	5	½	.8	79	6.2	5.5	6.2	.12	6.70	7.97_T	.019	1.06	1.40	5.69	299			6.8	3.9	.085	1.41	.031	2.74	
	22	½	.8	80	22.5	21.7	23.2	.078	4.35	5.18_T	.0084	.469	.619	8.37	298	22.5	21.7	22.6	3.6	.079	1.11	.024	3.29	
		½	1.3	81	23.5	22.2	24	.035	1.95	2.57_L	.0083	.463	.611	4.21										(27)
		2	1.0	82	22.8	21.9	22.8	.45	25.1	29.9_T	.0084	.469	.619	48.3										
400	5	½	.8	58	6.5	5.6	6.5	.13	10.2	12.1_T	.019	1.49	1.95	6.21	292	6.5	5.6	7.	3.85	.163	1.3	.055	2.96	
	11	½	.8	59		11.3	12.2	.10	7.84	9.33_T	.0125	.98	1.28	7.29	293	12.3	11.3	12.4	4.1	.173	1.18	.05	3.46	
	22	½	.8	60	22.7	22	23.4	.083	6.51	7.75_T	.008	.627	.821	9.44	294	22.7	22.0	23	3.8	.161	1.08	.046	3.56	(28)
850	5	½	.8	28	6.3	5.3	6.6	.115	13.1	15.5_T	.019	2.16	2.54	6.10										

† $\frac{BTU}{HR\text{-}FT^{2.0}F}$

L — Laminar
T — Turbulent
P — Paint Run

NOTES

(25) Groups 56 & 57 are repeatability checks Note $X_{max;h} < X_{max;p}$

(26) Lots of scatter at X_{max}

(27) X_{max} is at end of data plot. h_{peak} may be aft of last data pt. Significant data scatter at $> X_{max}$.

(28) X_{peak} is in region where undist. BL separated with no generator

Table III Data Summary (Sheet 5 of 11)
b. Sharp Flat Plate Initially Turbulent BL – Trip

WEDGE GENERATORS				HEAT TRANSFER											PRESSURE									NOTE
								PEAK			UNDISTURBED								PEAK		UNDIST.			
P_o psia	α deg	Nom x_i, in.	Z_m in.	Grp No.	x_i Plt in.	x_i BL in.	x_{PK} in.	$\frac{h_T}{h_{REF}}$	h_T †	h_{aw_T} †	$\frac{h_T}{h_{REF}}$	h_T †	h_{aw_T} †	$\frac{h_{aw,PK}}{h_{aw,Und}}$	Grp No.	x_i Plt in.	x_i BL in.	x_{PK} in.	$\frac{P}{P_\infty}$	P psia	$\frac{P}{P_\infty}$	P psia	$\frac{P_{PK}}{P_{Und}}$	
850	0	22	.2	13		16.9	18.6	.064	7.26	8.57	.041	4.65	5.49	1.56										(29)
	0		.4	14			18.6	.067	7.60	9.00	.041	4.65	5.49	1.64										(29)
	5		.8	9	21.	20.	22.4	.16	18.2	21.4	.039	4.43	5.22	4.10	249	21.8	21.2	23.4	6.5	.562	1.1	.095	5.92	(30)
			.8	10	21.	20.	22.4	.16	18.2	21.4	.039	4.43	5.22	4.10										
			.4	11	20.7	19.6	22.4	.16	18.2	21.4	.039	4.43	5.22	4.10										(31)
			.2	12		18.9	21.0	.16	18.2	21.4	.040	4.54	5.36	4.00										(32)
			1.0	212	20.	18.9	23	.15	17.0	20.1	.039	4.43	5.22	3.85	261	23.	22.	24.	6.5	.562	1.1	.095	5.92	(33)
	10		.8	7	21.7	20.4	22.8	.41	46.5	54.9	.0395	4.48	5.29	10.4	250	21.	20.	23.2	21.0	1.81	1.1	.095	19.1	(34)
			.8	8	21.7	20.4	22.8	.41	46.5	54.9	.0395	4.48	5.29	10.4										(34)
			1.0	211			23.2	.41	46.5	54.9	.039	4.43	5.22	10.5	260	23.	22.	23.5	20.	1.73	1.1	.095	18.2	(35)
	15		.6	5	22.4–23.2	20.6	23.0	.70	79.5	93.8	.038	4.31	5.09	18.4	251			22.4	95.	8.21	1.1	.095	86.4	(36)
			.6	6	22.2	20.6	23.0	.70	79.5	93.8	.038	4.31	5.09	18.4										(36)
			1.0	210			23.6	.64	72.6	85.7	.038	4.31	5.09	16.8	259	24.2	23.5	23.8	44	3.80	1.1	.095	40.0	(37)
CONE GENERATORS																								
P_o psia	α deg	Nom x_i, in.	Z_m In.																					
850	2½	22	.8	17	–	–	24.5	.055	6.24	7.37	.038	4.31	5.09	1.45	253			24.	1.35	.117	1.1	.095	1.23	(38)
				376P				.048	5.4	6.4														
			.8	18	–	–	24.5	.055	6.24	7.37	.038	4.31	5.09	1.45										(38)

† $\frac{BTU}{HR\text{-}FT^2\text{-}^oF}$ L – Laminar; T – Turbulent; P – Paint Run

NOTES

(29) "Choked" runs. Generators submerged into boundary layer.

(30) From group 9 & 10 shadowgraphs - there appears to be a 2nd compr wave leaving gen trailing edge & striking plate at X = 23. The resulting 2nd peaks are:
$(h/h)_{peak}/(h/h)_{und}$ = .55/.039 = 14.1 at X = 23
$(P/P_\infty)_{peak}/(P/P_\infty)_{und}$ = 10.5/1.1 = 9.55 at X = 23.8
Note: Groups 9 & 10 are repeats

(31) At X = 24.2 $(h/h)_{peak}/(h/h)_{und}$ = .38/.038 = 10.
Shock from gen trailing edge strikes plate at X = 24.1

(32) At X = 23.6 $(h/h)_{peak}/(h/h)_{und}$ = .36/.036 = 9.5
"Choked" flow with gen trailing edge well into plate BL

(33) At X = 24.6 $(h/h)_{peak}/(h/h)_{und}$ = .26/.0385 = 6.75
At X = 24.6 $(P/P_\infty)_{peak}/(P/P_\infty)_{und}$ = 10.5/1.1 = 9.55

(34) Groups 7 & 8 are repeats. Shadowgraph show shock from gen trailing edge strikes plate at X = 23.3
At X = 23.3 $(h/h)_{peak}/(h/h)_{und}$ = .59/.039 = 15.1
At X = 23.4 $(P/P_\infty)_{peak}/(P/P_\infty)_{und}$ = 24./1.1 = 21.8

(35) At X = 24. $(h/h)_{peak}/h/h)_{und}$ = .5/.038 = 13.2 &
$(P/P_\infty)_{peak}/(P/P_\infty)_{und}$ = 23/1.1 = 20.9

(36) Groups 5 & 6 are repeats
At X = 23.4 $(h/h)_{peak}/(h/h)_{und}$ = .78/.038 = 20.5
Although h_T plot shows 2nd peak & Schlieren (Gr 251) shows shock from gen trailing edge, no 2nd peak from press. plot. Shadowgraph shows 2nd shock strikes plate at X = 23.7

(37) At X = 24 $(h/h)_{peak}/(h/h)_{und}$ = .74/.038 = 19.4
At X = 24.2 $(P/P_\infty)_{peak}/(P/P_\infty)_{und}$ = 54.5

(38) At X = 24 $(h/h)_{peak}/(h/h)_{und}$ = .74/.038 = 19.4
At X = 24.2 $(P/P_\infty)_{peak}/(P/P_\infty)_{und}$ = 60/1.1 = 54.5

Table III Data Summary (Sheet 6 of 11)
b. Sharp Flat Plate Initially Turbulent BL – Trip

CONE GENERATORS				HEAT TRANSFER										PRESSURE								NOTE
								PEAK			UNDISTURBED							PEAK		UNDIST.			
p_0 psia	α deg	Nom x_i in.	Z_m in.	Grp No.	x_i Plt in.	x_i BL in.	x_{PK} in.	$\frac{h_T}{h_{REF}}$	h_T	h_{aw_T} †	$\frac{h_T}{h_{REF}}$	h_T †	h_{aw_T} †	$\frac{h_{aw\ PK}}{h_{aw,\ Und}}$	Grp No.	x_i Plt In.	x_i BL in.	x_{PK} In.	$\frac{P}{P_\infty}$	P psia	$\frac{P}{p_\infty}$	P psia	$\frac{P_{PK}}{P_{Und}}$	
850	7½	22	.6	19	21.6	19.6	22.6	.16	18.2	21.4	.0395	4.48	5.29	4.05	248			22.6	4.8	.415	1.1	.095	4.37	(39)
				378P				.17	19.5	23														
			.6	20	21.6	19.6	22.6	.16	18.2	21.4	.0395	4.48	5.29	4.05										(39)
			.8	21	21.5	19.8	22.5	.14	15.9	18.8	.04	4.54	5.36	3.51										
				377P				.14	16	18.9														
			1.0	22	2.19	20.3	22.5	.13	14.8	17.4	.04	4.54	5.36	3.25										
	7½	22	.5	23	20.2	19.2	21.4	.15	17.0	20.1	.04	4.54	5.36	3.75										(40)
			.6	208			21.6	.13	14.8	17.4	.04	4.54	5.36	3.25										(41)
			.8	209			23.2	.145	16.5	19.4	.038	4.31	5.09	3.81										(42)
	12½	22	.5	15	21.8	20.4	22.4	.44	49.9	58.9	.0395	4.48	5.29	11.1	256	21.8		22.6	18	1.56	1.1	.095	16.4	(43)
			.5	16	21.8	20.4	22.4	.44	49.9	58.9	.0395	4.48	5.29	11.1										(43)
SPHERE GENERATORS																								
p_0 psia	Nom. x_i in.	dia in.	Z_m in.																					
850	22	½	.8	25	22.6	21.5	22.7	.16	18.2	21.4	.039	4.43	5.22	4.10	252	22.	21.5	23.4	3.5	.302	1.1	.095	3.18	
				375P				.17	19	22.4														
			1.3	26	23.1	21.6	24	.095	10.8	12.7	.038	4.31	5.09	2.50	247	24.	22.	24.2	2.4	2.07	1.1	.095	2.18	(44)
		2	.5	24	22.1	21.6	22	.90	102.	121.	.039	4.43	5.22	23.2	257	22.6	21.6	22.2	41.	3.54	1.1	.095	37.3	
			1.0	27	22.8	21.9	22.7	.60	68.1	80.4	.039	4.43	5.22	15.4	258	23.7	21.9	23	27.	251	1.1	.095	24.6	

† $\frac{BTU}{HR\text{-}FT^2\text{-}^\circ F}$

L – Laminar
T – Turbulent
P – Paint Run
Lg – 2½ dia. Gase

NOTES

(39) At X = 24 $(h/h)_{peak}/(h/h)_{und}$ = .74/.038 = 19.4
At X = 24.2 $(P/P_\infty)_{peak}/(P/P_\infty)_{und}$ = 60/1.1 = 54.5

(40) At X = 23.2$(h/h)_{peak}/(h/h)_{und}$ = .22/.039 = 5.6

(41) At X = 23.6$(h/h)_{peak}/(h/h)_{und}$ = .19/.038 = 5.0

(42) At X = 24 $(h/h)_{peak}(h/h)_{und}$ = .165/.038 = 4.3

(43) At X = 24$(h/h)_{peak}(h/h)_{und}$ = .165/.038 = 4.3

(44) At X = 24 there is a measured P/P_∞ = 3. which appears to be a bad measurement

Table III Data Summary (Sheet 7 of 11)

c. Blunt Flat Plate – No Trip

WEDGE GENERATORS				HEAT TRANSFER											PRESSURE									NOTE
								PEAK			UNDISTURBED								PEAK		UNDIST.			
P_0 psia	α deg	Nom x_i in.	Z_m in.	Grp No.	x_i Plt In.	x_i BL in.	x_{PK} in.	$\frac{h_T}{h_{REF}}$	h_T †	h_{aw} †	$\frac{h_T}{h_{REF}}$	h_T †	h_{aw} †	$\frac{h_{aw,PK}}{h_{aw,Und}}$	Grp No.	x_i Plt In.	x_i BL in.	x_{PK} in.	$\frac{P}{P_\infty}$	P psia	$\frac{P}{P_\infty}$	P psia	$\frac{P_{PK}}{P_{Und}}$	
75	5	7	.8	134	3.5	3.4	4.6	.275	.949	11.4_T	.038	1.31	1.74_L	6.55	358	3.8	3.5	4.6	33.	.28	5.4	.047	6.1	
	10	7	.8	135	≈3.2		3.8	.6	20.7	24.8_T	.042	1.45	1.93_L	12.8	357			4.2	53.	.457	5.7	.049	0.33	
		22	.8	137	–	–	19	.25	8.63	10.4_T	.014	.483		16.2	356			19.4	22.	.19	2.6	.022	8.64	(45)
			.8	138	18.5	16.9	19	.25	8.63	10.4_T	.014	.483	$.64_L$	16.2										
	15	7	.8	136	≈3		4.2	.58	20.0	24.0_T	.04	1.38	1.84_L	13.0	359			5	65.	.561	5.2	.045	12.5	(46)
			.8	.8											360			6	66	.57	4.8	.041	13.9	
400	10	7	.8	70	3.4	3	3.8	.71	55.7	66.3_T	.045	3.53	4.62 L	14.4	351	3.4	3.0	4	53.	2.24	5.7	.241	9.29	
		22	.8	64	18.5	18	20	.26	20.4	24.3_T	.0122	.056	1.25L	19.4	352			20.2	29.	1.23	2.55	.108	11.4	
850	5	7	.5	48	≈2.6		3.2	.68	77.2	91.1_T	.042	4.77	6.20_L	14.7										(47)
	10	7	.5	46	–	–	3.2	.82	93.1	$110._T$	.042	4.77	6.20_L	17.7	345			3.6	62	5.36	5.8	.501	10.7	(48)
															346			3.6	62	5.36	5.8	.501	10.7	
		22	.8	45	18.5	18.2	19.2	.23	26.1	30.8_T	.022	2.50	2.95_T	10.4	347			10.6	16.5	1.43	2.53	.219	6.53	(49)
	15	7	.5	47	–	4.2	.71	80.6	80.6	95.1_T	.04	4.54	5.90_L	16.1										
CONE GENERATORS																								
P_0 psoa	α deg	Nom x_i, in	Z_m in																					
75	2½	7		141	–	–	–	–	–	–				–										(50)
	7½	7		139	3.5-4		5	.075	259	3.44_L	.036	1.24	1.65_L	1.57	361	4.5	4.0	5	8.5	.073	5.2	.045	1.62	
		22		140	–	–	21.4	.043	14814	197_L	.0132	.45	$.606_L$	2.44	362			21	4.	.035	2.5	.022	1.59	
400	7½	7		66	4.4		5.2	.062	4.86	6.37_L	.035	2.74	3.59_L	1.77										
		22		65	19		21	.033	2.59	3.39_L	.0120	.94	123_L	2.76										
850	2½	7		35	–	–	3.6	.05	5.68	7.38_L	.042	4.77	6.20_L	1.19										
	7½	7	.5	34	3.3	–	4.	.085	9.65	12.5_L	.04	4.54	5.90_L	212	344	3.7		4.2	9.	.778	5.6	.484	1.61	
		22		33	–	–	21	.055	6.24	7.37_T	.023	2.61	3.08_T	2.39	342			21.8	4.2	.363	2.56	.213	1.70	
	12½	7		36	4.15	–	4.8	.18	20.4	24.1_L	.037	4.20	5.46_L	4.41										

† $\frac{BTU}{HR\text{-}FT^2\text{-}°F}$ L – Laminar T – Turbulent

(45) Groups 137 & 138 are repeats

(46) Group 360 is a repeat of 359 with the gen moved aft 1.0"

(47) The first data point on the h_T plot corresponds to peak, ∴ the actual peak may be missing

(48) Groups 345 & 346 are repeats

(49) BL is transitional at X_{PK}, $h_{aw,PK} / h_{aw,Und}$ = 16.3 for $h_{aw,Und}$ based on extrapolated value for a fam. undist. BL at x_{PK}

(50) Heating amplification is indistinguishable from noise. Shock is too weak to be seen on shadowgraph

Table III Data Summary (Sheet 8 of 11)

c. Blunt Flat Plate – No Tip

SPHERE GENERATORS				HEAT TRANSFER										PRESSURE								NOTE
								PEAK			UNDISTURBED							PEAK		UNDIST.			
P_o psia	Nom. X_i, in.	dia. in.	Z_m in.	Grp No.	x_i Plt in.	x_i BL in.	x_{PK} in.	$\frac{h_T}{h_{REF}}$	h_T †	h_{aw} †	$\frac{h_T}{h_{REF}}$	h_T †	h_{aw} †	$\frac{h_{aw,PK}}{h_{aw,Und}}$	Grp No.	x_i Plt in.	x_i BL in.	x_{PK} in.	$\frac{P}{P_\infty}$	P psia	$\frac{P}{P_\infty}$	P psia	$\frac{P_{PK}}{P_{Und}}$	
75	7	½	.8	142	6.8	–	7.2	.062	2.14	2.84_L	.027	.093	1.24_L	2.30									
		½	1.3	148	–	–	7.0	.049	1.69	2.25_L	.028	.097	1.28_L	1.76	340	6.6		7	6.5	.056	4.5	.039	1.44	
	22	½	.8	143	–	–	22.2	.032	1.10	1.47_L	.013	.05	0.60	2.42										
400	7	½	.8	67	7.0	–	7.2	.088	6.90	9.04_L	.023	1.8	2.36_L	3.83										
	22	½	.8	68	22.	21.6	22.4	.043	3.37	4.41_L	.0119	9.3	1.22_L	3.61										
850	7	½	.8	38	7.0		7.4	.10	11.4	14.8_L	.024	2.7	3.54_L	4.18										
		½	1.3	39	6.3		6.8	.07	7.95	10.4_L	.027	3.06	4.01_L	2.59										
		2	1	40	6.59		7.2	.60	68.1	80.3_T	.025	2.8	3.69_L	21.8										
	22	½	.8	37	22.2		21.7	.09	10.2	12.1_T	.024	2.72	3.21_T	3.77										
ORBITER GENERTAORS																								
P_o psia	α deg	Nom x_i in.	Z_m in.																					
75	0	7	.8	144	6.6		7.0	.071	2.45	3.26_L	.028	.966	1.28_L	2.55										
			1.3	147	–	–	7.	.049	1.69	2.25_L	.028	.966	1.28_L	1.76										
	5	7	.8	145	6.3		7.2	.054	1.86	2.48_L	.027	.932	1.24_L	2.00										
			1.3	146	5.4		6	.149	5.14	6.84_L	.032	.10	1.47_L	4.65										
400	0	7	.8	69	6.7		7.0	.105	8.23	10.8_L	.028	2.20	2.88_L	3.75										
850	0	7	.8	44	6.7		7.0	.15	17.0	22.1_L	.026	4.95	3.84_L	5.76										
			1.3	41	6.25		6.8	.085	9.65	12.5_L	.028	3.18	4.13_L	3.03	341	6.7		7	6.5	.562	4.5	.389	1.44	
	5	7	.8	43	6.55		7.2	.08	9.08	11.8_L	.025	2.84	3.69	320										
			1.3	42	5.6		6.0	.40	45.3	53.6_T	.032	8.63	4.72_L	11.4										

† $\frac{BTU}{HR\text{-}FT^2\text{-}F}$

L – Laminar
T – Turbulent

Table III Data Summary (Sheet 9 of 11)
d. Booster – No Trip

WEDGE GENERATORS				HEAT TRANSFER														PRESSURE					NOTE
								PEAK			UNDISTURBED							PEAK		UNDIST.			
P_0 psia	α deg	Nom x_i, in.	Z_m in.	Grp No.	x_i Plt in.	x_i BL in.	x_{PK} in.	$\frac{h_T}{h_{REF}}$	h_T †	h_{aw} †	$\frac{h_T}{h_{REF}}$	h_T †	h_{aw} †	$\frac{h_{aw,PK}}{h_{aw,Und}}$	Grp No.	x_i Plt in.	x_i BL in.	x_{PK} in.	$\frac{P}{P_\infty}$	P psia	$\frac{P}{P_\infty}$	P psia	$\frac{P_{PK}}{P_{UND}}$	
75	10	6	.7	178	5.6	–	6.	.28	9.66	11.6_T	.016	.552	$.734_L$	15.8	374	5.4	–	5.8	19.	.164	1.68	.014	11.7	(51)
		15	.7	179	–	–	14.6	.26	8.97	10.8_T	.008	.276	$.367_L$	29.4	373	–	–	14.6	21.4	.185	1.54	.013	14.2	
200	10	6	.7	171	6.2	–	6.	.27	15	17.9_T	.015	.837	1.10_L	16.3	370	5.8	–	5.8	18.5	.405	1.52	.033	12.3	(52)
		15	.7	172	–	–	14.	.30	16.7	19.9_T	.0066	.368	$.486_L$	40.9	369			14.6	20.	.44	1.4	.031	14.3	
850	10	6	.7	152			6.6	.79	89.7	$106._T$	.014	1.59	2.07_L	51.2	365			6.96	45.	3.98	1.38	.119	33.4	(53)
			.7	195 P	–	–	–	–																
	10	15	.7	153	–	–	13.6	.4	45.5	53.6_T	.0053	.60	$.782_L$	68.5	364			14.	16.	1.39	1.3	.112	12.4	
			.7	196P																				
CONE GENERATORS																							
P_0 psia	α deg	Nom x_i, in.	Z_m in.																				
75	7½	6	.7	180	6	–	6.4	.24	8.28	9.94_T	.015	.52	$.69_L$	14.3										(54)
		15	.7	181	–	–	15.8	.048	1.66	1.99_T	.0074	.255	$.31_L$	6.5										
200	7½	6	.7	169	6.	–	6.4	.24	13.4	15.9_T	.0148	.826	1.09_L	14.6										(54)
		15	.7	170	–	–	16.	.046	2.57	3.06_T	.0056	.312	$.412_L$	7.43										
850	7½	6	.7	154			6.4	.26	29.5	34.8_T	.0142	1.61	2.10_L	16.6	366	–	–	6.3	12.7	1.10	1.41	.122	9.02	(54)
				197P	–	–		339	33.	38.9_T														
		15		155	–	–	16.	.051	5.79	6.83_T	.007	.80	$.944_T$	7.24	367	–	–	15.6	3.58	.309	1.30	.112	2.76	
				198P	–	–	–	–																
SHPERE GENERATORS																							
P_0 psia	Nom x_i, in.	dia. in.	Z_m in.																				
75	6	½	1.3	182	–	–	15.	.04	1.38	1.66_T	.0079	.273	$.362_L$	4.59										(55)
	15	½	1.3	183	–	–	17.	.016	.55	$.732_T$	.0068	.235	$.312_L$	2.35										
200	6	½	1.3	168	6.7	–	7.6	.046	2.57	3.39_L	.013	.725	$.958_L$	3.54										
	15	½	1.3	166	–	–	15.8	.014	.78	$.928_T$	.0057	.318	$.42_L$	2.21										
850	6	½	1.3	156	8.5	–	8.8	.038	4.13	4.87_T	.0093	1.06	1.37_L	3.55										(56)
		½	1.3	199P	–	–		.035	4.	4.72_T														
	15	½	1.3	157	–	–	16.	.014	1.59	1.88_T	.007	.795	1.03_L	1.83										(57)
		½	1.3	200P	–	–		.018	2.	2.36_T														

NOTES

† $\frac{BTU}{HR\text{-}FT^2\text{-}°F}$

L – Laminar
T – Turbulent
P – Paint Run

(51) Gen. reflected bow shock impinges at X = 6.5
At X = 6.6 – $(P/P_\infty)_{peak}/(P/P_\infty)_{und}$ = 37/1.6 = 23.1
At X = 6.8 - $(h/h)_{peak}/(h/h)_{und}$ = .43/.014 = 30.7

(52) Gen. reflected bow shock impinges at X = 6.5
At X = 6.6 - $(P/P_\infty)_{peak}/(P/P_\infty)_{und}$ = 41/1.49 = 27.5
At X = 6.8 – $(h/h)_{peak}/(h/h)_{und}$ = .46/.0137 = 33.6

(53) Generator shock & reflected bow shock merge.

(54) $(h/h)_{peak}$ is caused by reflected bow shock.
Generator shock impinges downstream of X_{peak} or merges with reflected bow shock.

(55) 1st $(h/h)_{peak}$ may be in region of no instrumentation.
$(h/h)_{peak}$ shown may be reflected bow shock.

(56) $(h/h)_{peak}$ is next to last data point. Actual $(h/h)_{peak}$ may be missing.

(57) At X = 16.6 $(h/h)_{peak}/(h/h)_{und}$ = .018/.0074 = 2.43

Table III Data Summary (Sheet 10 of 11)

d. Booster – No Trip

ORBITER GENERATORS				HEAT TRANSFER												PRESSURE					
								PEAK			UNDISTURBED					PEAK		UNDIST.			
P_o psia	α deg	Nom x_i, in.	Z_m in.	Grp No.	x_i Plt in.	x_i BL in.	x_{PK} in.	$\frac{h_T}{h}$ REF	h_T †	h_{aw} †	$\frac{h_T}{h}$ REF	h_T †	h_{aw} †	$\frac{h_{aw,PK}}{h}$ aw, Und	Grp No.	x_i Plt in.	x_i Bl in.	x_{PK} in.	$\frac{P}{P_\infty}$	P psia	$\frac{P}{P_\infty}$	P psia	$\frac{P_{PK}}{P}$ Und	NOTE
75	0	F	.5	409	2.8	–	3.0	.165	5.69	7.57_L	.05	1.73	2.29	3.31	442	–	–	3	10.2	.088	4.7	.041	2.15	(58)
				467P	–	–	–	.197	6.8	9.04_L														
		F	1.	415	5.	–	5.6	.088	3.04	3.64_T	.016	.55	.73	4.99	444	5.2	–	5.2	5.2	.045	1.77	.015	3.00	
				468P	–	–	–	–																
		A	2.	412	–	–	–	–																(59)
	5	F	.7	188	5.8	–	6.4	.13	4.49	5.38_T	.015	.52	.69	7.80										
		F	1.	418	5.1	–	5.2	.115	3.97	4.76_T	.017	.59	.78	6.10	445	5.2	–	5.4	8.5	.073	1.72	.015	4.87	
				469P	–	–	–	.120	4.13	4.96_T														
		A	.7	191	12.4	–	13.2	.06	2.07	2.48_T	.0093	.32	.43	5.77										(60)
			.7	193	12.4	–	14.	.065	2.24	2.69_T	.0085	.29	.39	6.90										(60)
		A	1.	421	13.	–	13.6	.09	3.11	3.73_T	.009	.31	.41	9.10	446	13.		14.2	7.	.06	1.54	.013	4.62	
				470P	–	–	–	.068	2.4	2.68_T														
		A	1.3	185	12.3	–	12.2	.027	.93	1.24_T	.01	.35	.46	2.70										(61)
		A	1.3	186,187	8.3	–	–	–																(59)
	10	F	1.	427	7.5	–	7.8	.18	6.21	7.45_T	.013	.45	.60	12.4										
				472P	–	–	–	.14	4.8	5.76_T														
		A	1.	424	–	–	16.4	.20	6.90	8.28_T	.007	.24	.32	25.9	447	–	–	16.8	15.	.13	1.47	.013	10.0	
				471P	–	–	–	.21	7.2	8.64_T														
200	5	F	.7	162,163	8.7	–	–																	(59)
		A	.7	173	–	–	13.6	.069	3.85	4.58_T	.0068	.38	.50	9.2										
		A	.7	164,165	11.6	–	–																	(59)
850	0	F	.5	388	2.8	–	3.0	.20	22.7	26.8_T	.045	5.11	6.64	4.03	450	–	–	3.	14.	1.21	4.0	.35	3.46	(62)
				458P	–	–	2.2	–																
		F	.7												368	4.8	–	5.6	8.5	.73	1.44	.12	6.08	
		F	1.	394	4.6	–	4.8	.075	8.51	10.0_T	.015	1.74	2.26	4.44	451	4.5	–	4.6	4	.35	1.59	.14	2.50	(63)
				459P	–	–	4.	.088	10.	12.0_T														
		A	2.	391	9.3	–	–																	(59)

† $\frac{BTU}{HR\text{-}FT^2 - {}^oF}$

L – Laminar
R – Turbulent
P – Paint Run
F– Forward Impingement
A – Aft Impingement

(58) 2nd peak due to reflected booster bow shock impinging at X = 4.8.
At X = 5.2 $(h/h)_{peak}/(h/h)_{und}$ = .16/.018 = 8.89
$(P/P)_{\infty\ peak}/(P/P)_{\infty\ und}$ = 9/1.77 = 5.08

(59) $(h/h)_{peak}$ is in region of no insturmentation.

(60) Groups 191 & 193 are repeats. X_i is approximate.

(61) 2nd peak probably due to reflected booster bow shock
At X = 14.5 $(h/h)_{peak}/(h/h)_{unf}$ = .09/.008 = 11.3

(62) 2nd peak due to reflected booster bow shock
At X = 5.4 $(P/P_\infty)_{peak}/(P/P_\infty)_{und}$ = 9.5/1.45 = 6.55

(63) At X = 6 $(h/h)_{peak}/(h/h)_{und}$ =.07/.0145 = 4.83
At X = 5.2 $(P/P_\infty)_{peak}/(P/P_\infty)_{und}$ = 5/1.47 = 3.40

Table III Data Summary (Sheet 11 of 11)
d. Booster – No Trip

ORBITER GENERATORS				HEAT TRANSFER													PRESSURE					NOTE
								PEAK			UNDISTURBED				PEAK				UNDIST.					
P_0 psia	α deg	Nom x_i, in.	Z_m in.	Grp No.	x_i Plt in.	x_i BL in.	x_{PK} in.	$\frac{h_T}{h_{REF}}$	h_T †	h_{aw} †	$\frac{h_T}{h_{REF}}$	h_T †	h_{aw} †	$\frac{h_{aw,PK}}{h_{aw,Und}}$	Grp No.	x_i Plt in.	x_i BL in.	x_{PK} in.	$\frac{P}{P_\infty}$	P psia	$\frac{P}{P_\infty}$	P psia	$\frac{P_{PK}}{P_{Und}}$	
850	5	F	1.	397	4.8	–	5.2	.062	7.04	8.31T	.015	1.70	2.21_L	3.76										
				460P	–	–	5.	.061	6.9	8.14_T														
		A	.7	161	9.4	–	–	–																(64)
				202P	–	–		.26	30.	35.4_T														
		A	1.	400	13.4	–	13.6	.23	26.1	30.8_T	.0054	.61	$.79_L$	39.0										(65)
				461_P	–	–	13.	.24	27	31.9_T														
		A	1.3	159	–	–	14.8	.27	30.6	36.1_T	.0064	.73	$.95_L$	38.0										
				201P	–	–		.30	34.	40.1_T														
	10	F	1.	406	8.8	–	–								453	8.5	–	–	–					(64)
		A	1.	403	–	–	16	.45	51.1	60.3_T	.0071	.81	1.05_L	57.4	452	–	–	168	17.	1.47	1.28	.11	13.4	
				462P	–	–	16	.54	61	72.0_T														

† $\frac{BTU}{HR. - FT^2 - {}^oF}$

L – Laminar
T – Turbulent
P – Paint Run
F – Forward Impingement
A – Aft Impingement

(64) $(h/h)_{peak}$ is in region of no instrumentation.

(65) Orbiter shock and reflected booster shock merge before striking booster.

Table IV Reference Conditions for Heat Transfer Data

Stagnation Pressure, psia	75	200	400	850
h_{REF}–Btu/hr–ft^2°R	34.5	55.8	78.4	113.5
M_∞	7.8	7.92	7.96	8.01
P_∞ – psfa	1.21	3.07	5.93	12.1
T_o – °R	1200.	1245.	1286.	1341.
$T_{aw\ L}$ – °R	1035.	1073.	1107.	1154.
$T_{aw\ T}$ – °R	1090.	1130.	1167.	1216.
T_∞ – °R	89.9	92.0	94.0	96.9
T_w – °R	535.	535.	535.	535.
$T_{*_{LAM}}$ – °R	520.	529.	537.	549.
$T_{*_{TURB}}$ – °R	533.	542.	551.	562.
$(T_o - T_w) / (T_{aw\ L} - T_w)$	1.33	1.32	1.31	1.30
$(T_o - T_w) / (T_{aw\ T} - T_w)$	1.2	1.19	1.19	1.18
Re/ft	4.09 + 05	1.01 + 06	1.88 + 06	3.70 + 06
V_∞ – ft/sec	3653.	3722.	3772.	3864.
ρ_∞ – lb$_m$/ft^3	8.10 – 06	2.00 – 05	3.77 – 05	7.47 – 05
μ_∞ – lb/ft–sec	7.24 – 08	7.40 – 08	7.57 – 08	7.80 – 08

Table V

Data Obtained on Flat Plate with Blunt Leading Edge

p_o	x_i	Wedge Angles 5° p	5° T	10° p	10° T	15° p	15° T	Cone Half Angles 2.5° T	7.5° p	7.5° T	12.5° T	Hemispheres 0.5" p	0.5" T	2.0" T	Orbiter α 0° p	0° T	5° T
850	7		•	•	•		•	•		• •	•	•	*	•	•	*	*
	22			•	•					• •			•				
400	7.			•	•					•			•			•	
	22			•	•					•			•				
75	7	•	•	•	•	•	•	•		• •			*			*	*
	22			•	•					•							

* Data obtained for two or more heights of shock generator above plate surface.

p — Pressure T — Thermocouple

Table VI

Data Obtained on Booster and Booster-Orbiter Configurations

p_o	x_i	GENERATORS 10° Wedge p	T	P	7.5° Cone p	T	P	0.5" Hemisph T	P	ORBITER α = 0 p	T	P	α = 5° p	T	P	α = 10° p	T	P
850	FORE	•	•	•	•	•	•	•	•	*	*	*		•	•		•	•
	AFT	•	•	•	•	•	•	•	•		•			•	•		•	• •
200	FORE	•	•			•		•										
	AFT	•	•			•		•										
75	FORE	•	•			•		•		*	*	*		•	•		•	
	AFT	•	•			•		•		•	•			•	•		•	•

* Data obtained for two heights of orbiter above booster surface.

p — Pressure T — Thermocouple P — Paint

Table VII

Flow Properties For Heat Transfer Equations

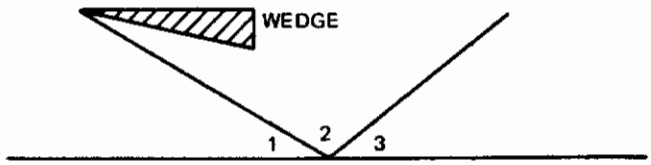

Approximate Free Stream Conditions, AEDC Tunnel B

Total Temperature To = 1310°R
Mach Number M = 8
Free Stream Temperature T_1 = 94.8°R
Viscosity $u_1 = 7.6 \times 10^{-8}$ LB_m – Sec/Ft^2
Free Stream Velocity V_1 = 3820 ft/sec
Laminar Reference Temperature $T_{1\ REF_L}$ = 556°R
Turbulent Reference Temperature $T_{1\ REF_T}$ = 569°R

Calculated Properties Due to Shock Impingement

Wedge Angle δ	5°	10°	15°
Shock Angle† Θ_1	11°	15.5°	21°
Pressure Rise P_2/P_1	2.6	5.2	9.4
Mach No. M_2	6.6	5.7	4.6
Shock Angle Θ_2	12.5°	18.2°	25.2°
Pressure Rise P_3/P_2	2.2	3.5	4.4
Pressure Rise P_3/P_1	5.7	18.5	41.1
Mach No. M_3	5.6	4.4	3.3
Temperature T_3	181° R	274° R	414° R
Temp. Ratio T_1/T_3	.53	.35	.23
Velocity V_3	3670 FT/Sec	3510 FT/Sec	3270 FT/Sec
Velocity Ratio V_3/V_1	.96	.92	.86
Reference Temp T_{REF_3}	578° R	605° R	644° R
Ref Temp Ratio T_{*_1}/T_{*_3}	.98	.94	.88
Viscosity Ratio μ_1/μ_3	.53	.35	.25

†Neglecting Boundary Layer Thickness

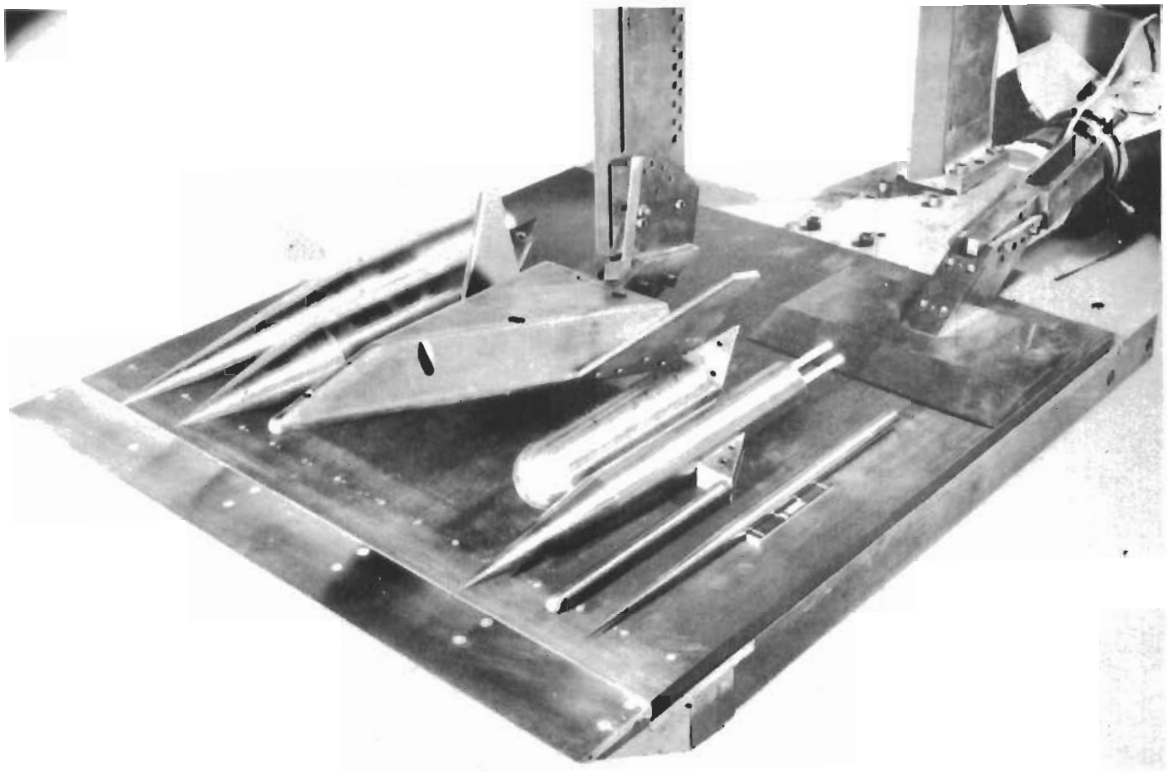

Fig. 1 Shock Generators and Sharp Flat Plate Receiver

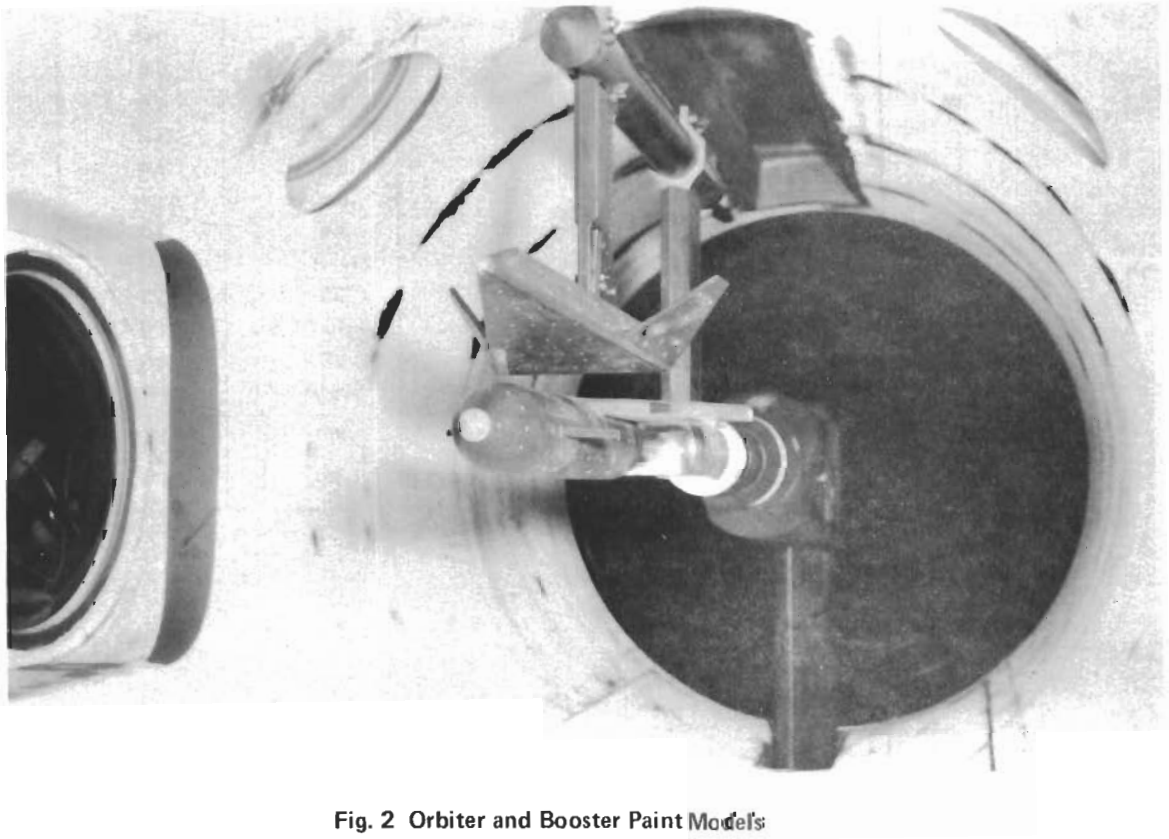

Fig. 2 Orbiter and Booster Paint Models

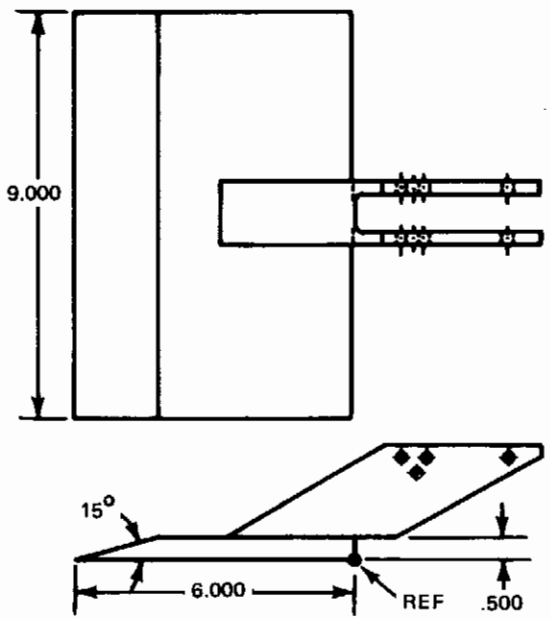

Fig. 3 Wedge Shock Generator

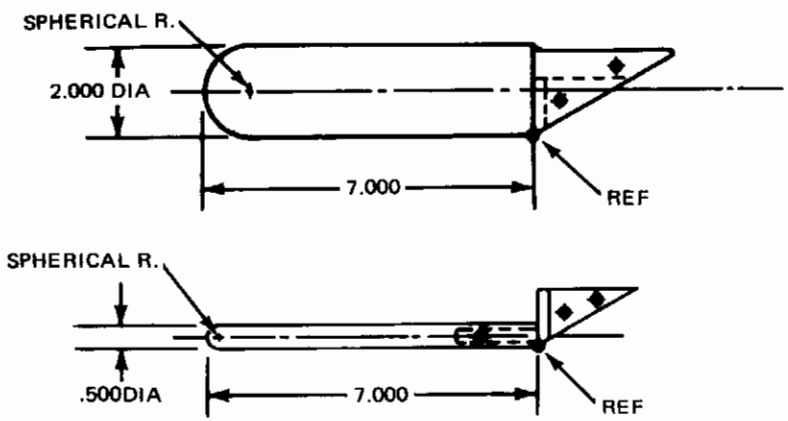

Fig. 4 Hemisphere-Cylinder Shock Generators

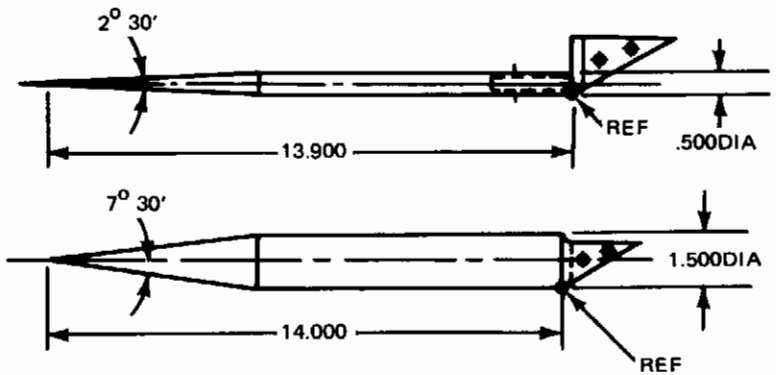

Fig. 5 Cone-Cylinder Shock Generators (2.5°, 7.5°)

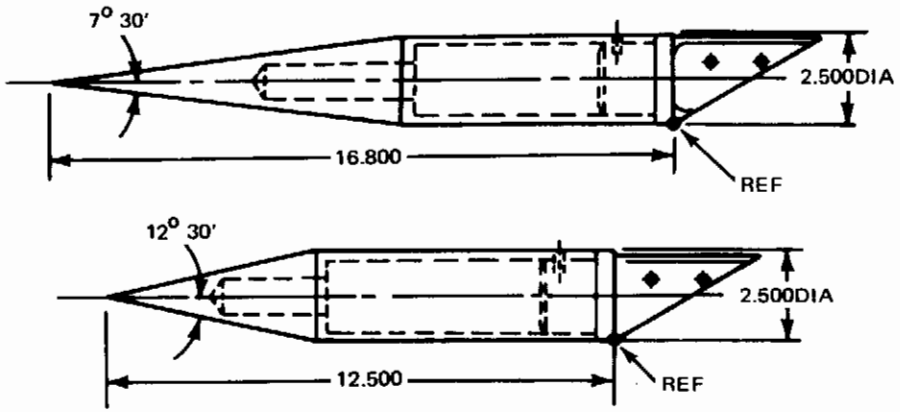

Fig. 6 Cone-Cylinder Shock Generators (7.5°, 12.5°)

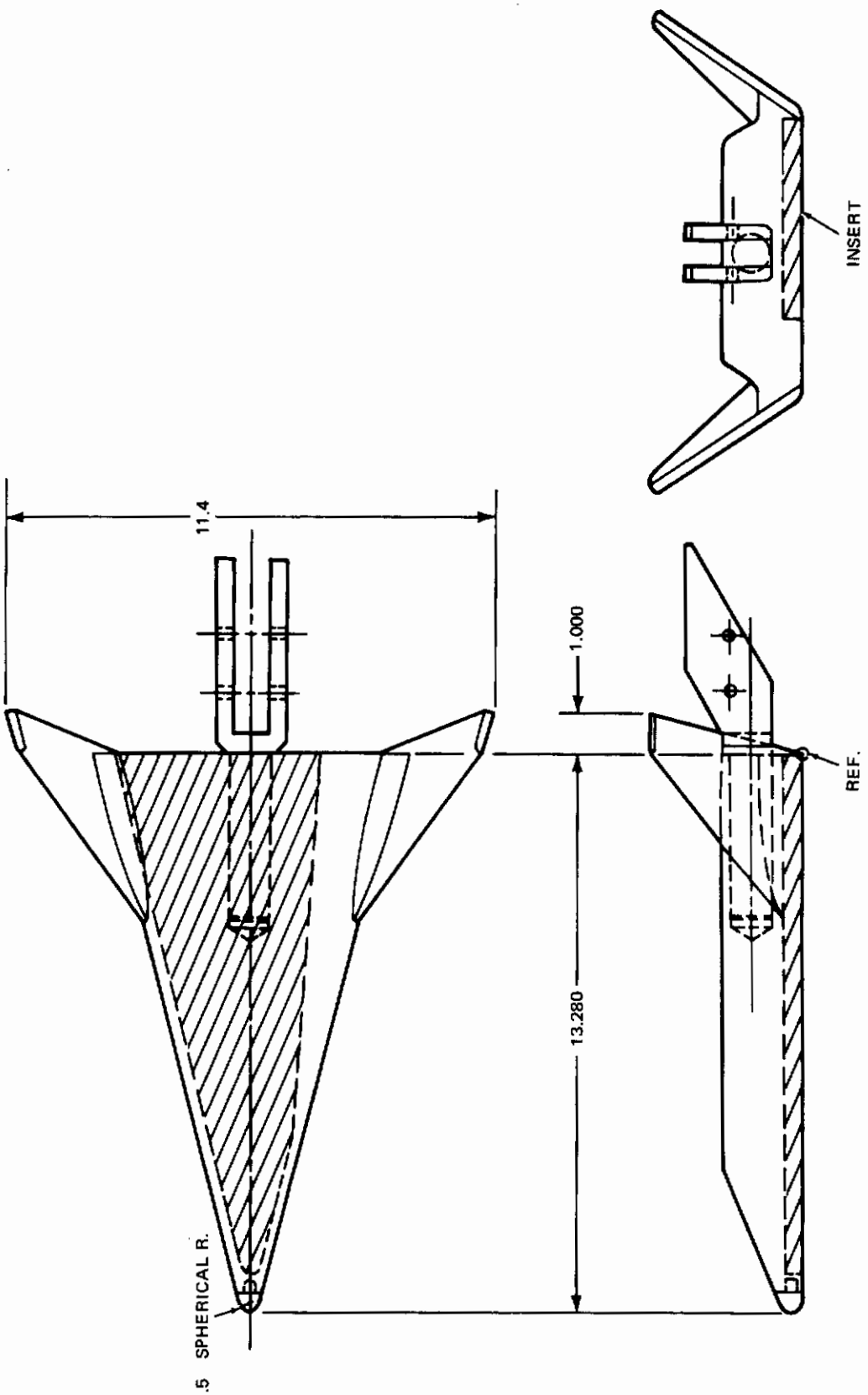

Fig. 7 Orbiter Vehicle Shock Generator

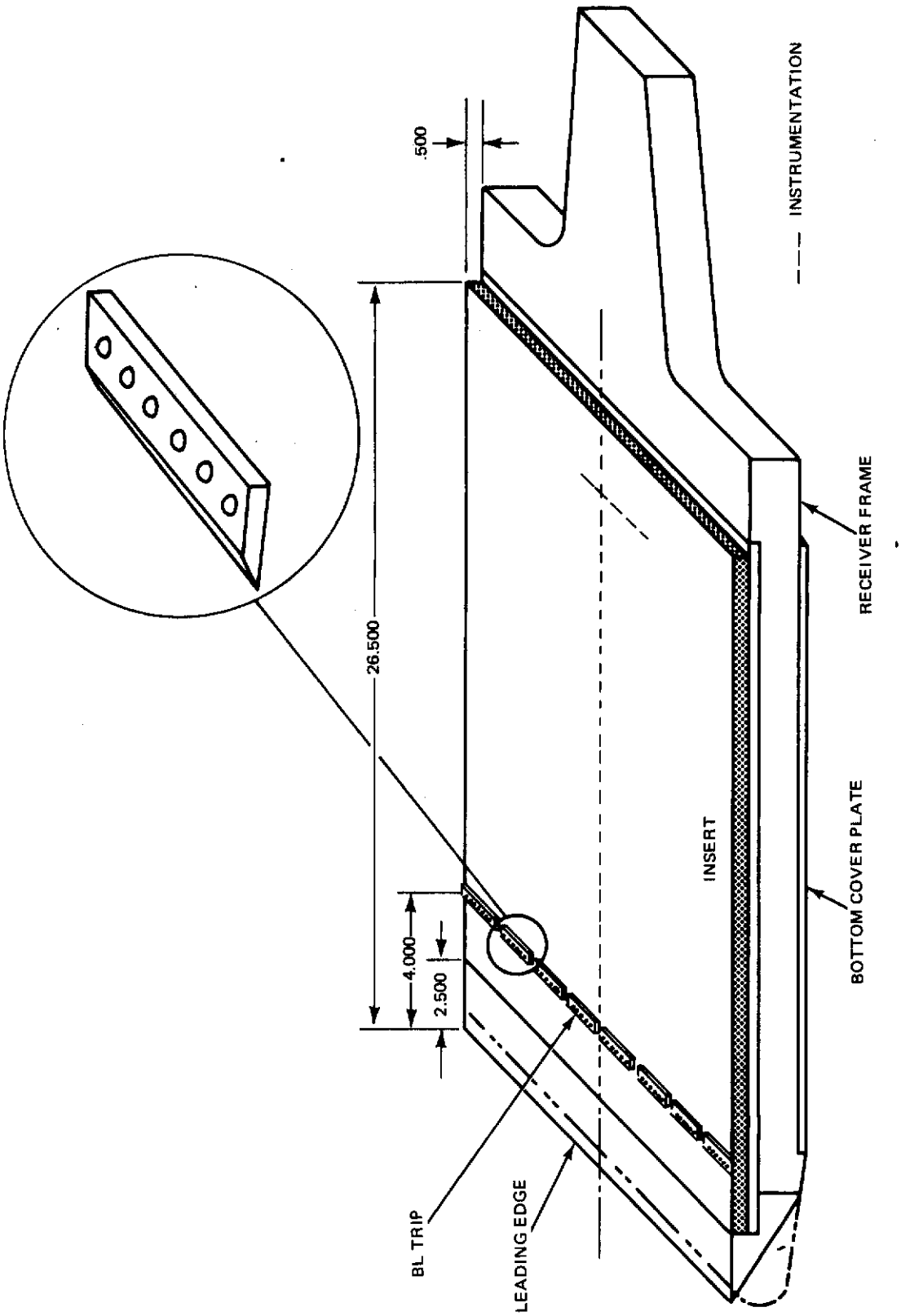

Fig. 8 Flat Plate Shock Receiver

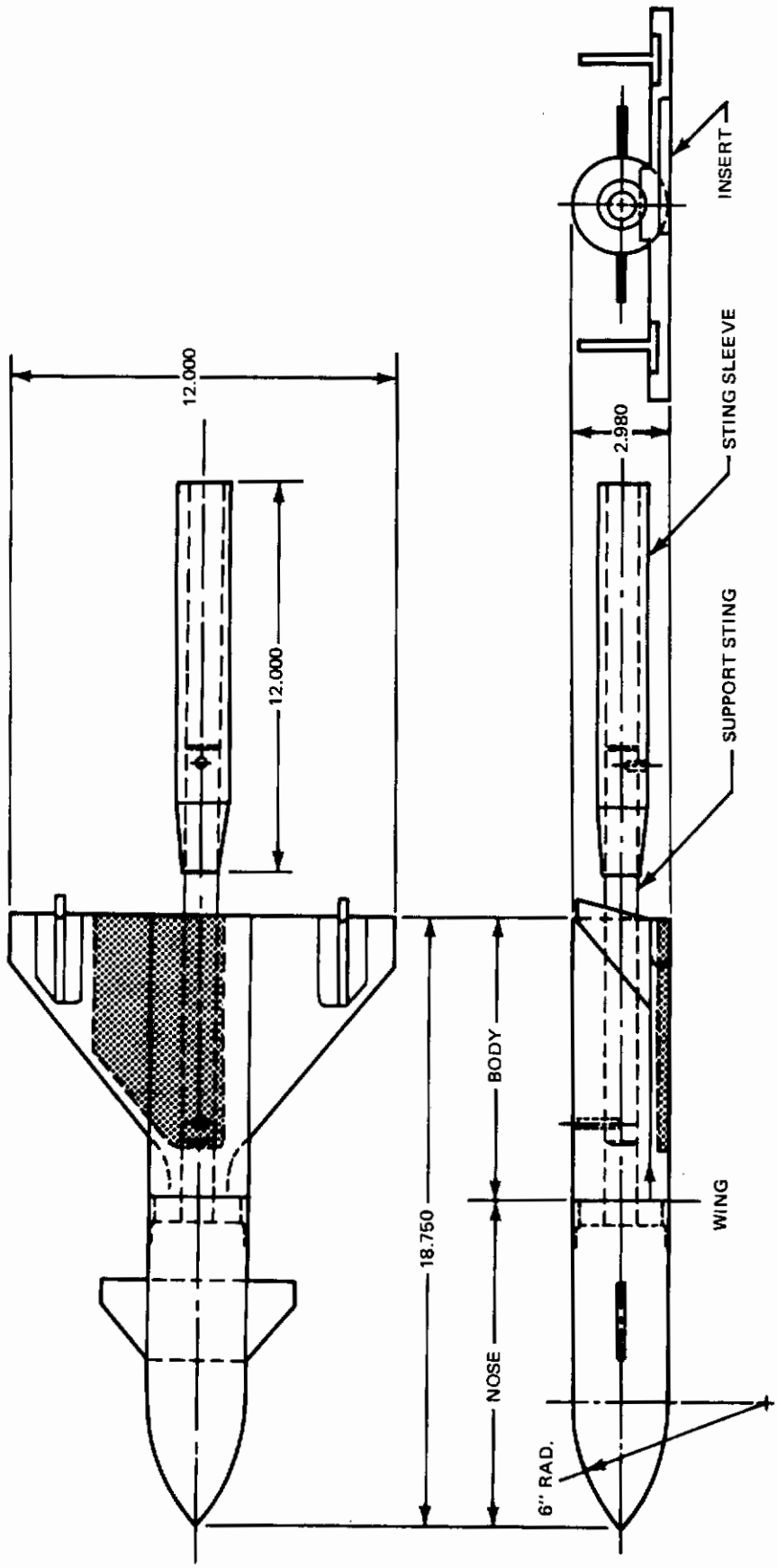

Fig. 9 Booster Vehicle Shock Receiver

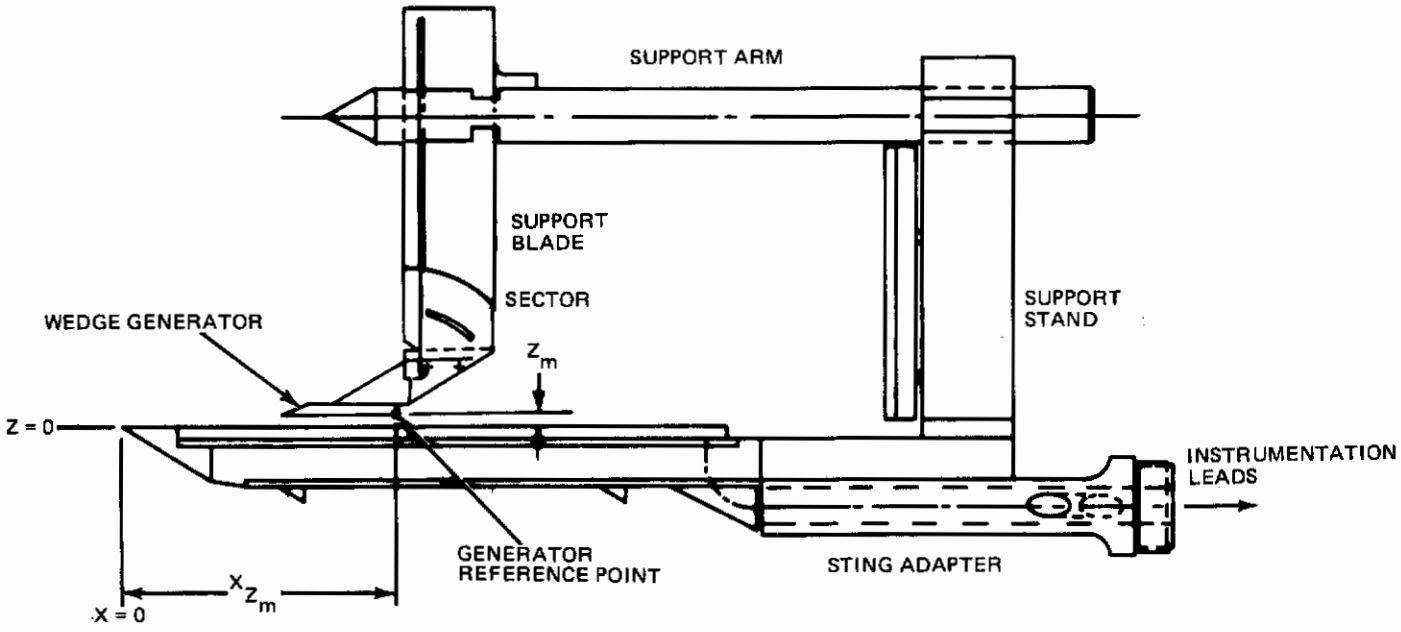

Fig. 10 Wedge Generator Installed in Forward Position with Sharp Flat Plate Receiver

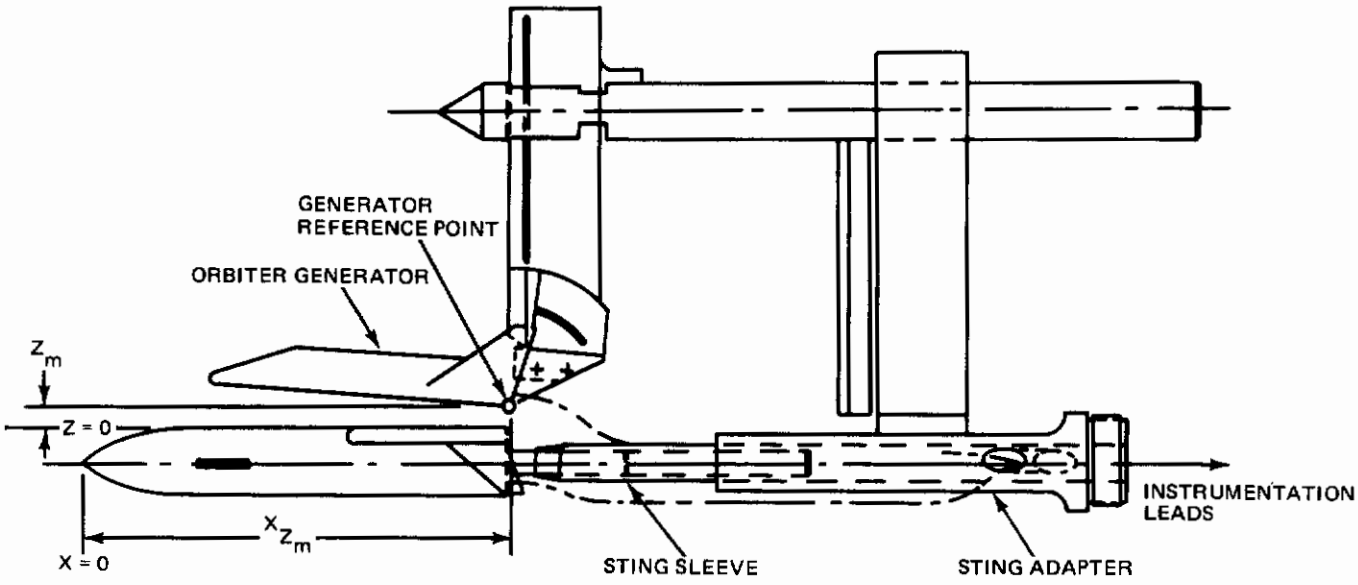

Fig. 11 Orbiter Generator Installed with Booster Receiver

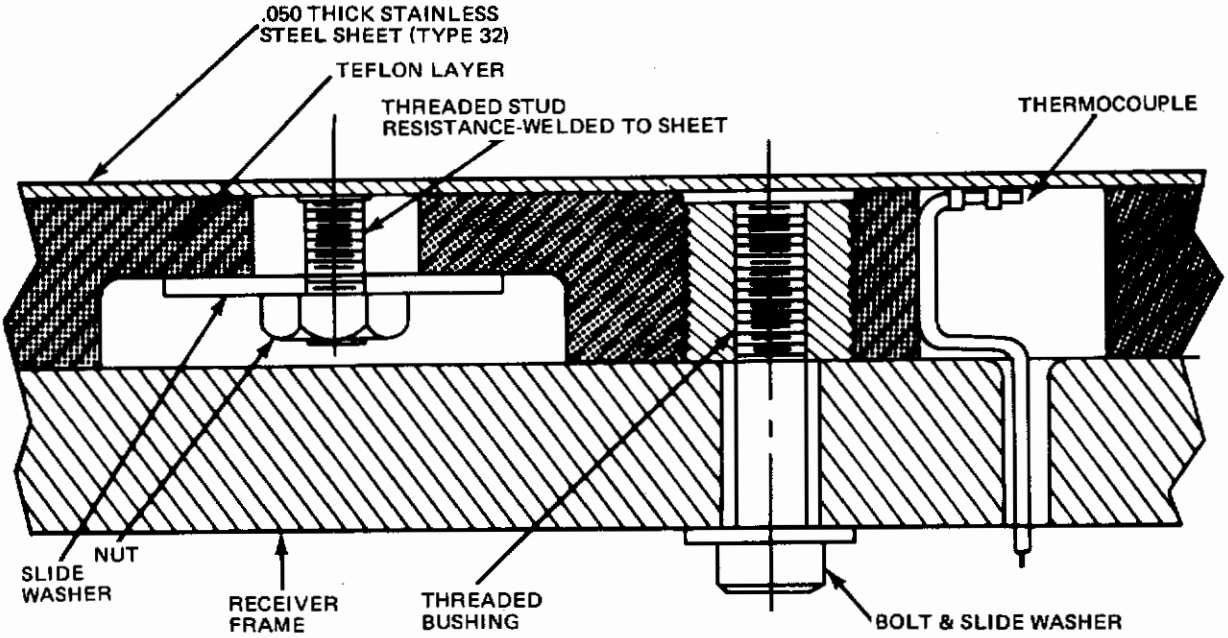

a. TYPICAL SECTION - THIN SKIN FLOATING PANEL

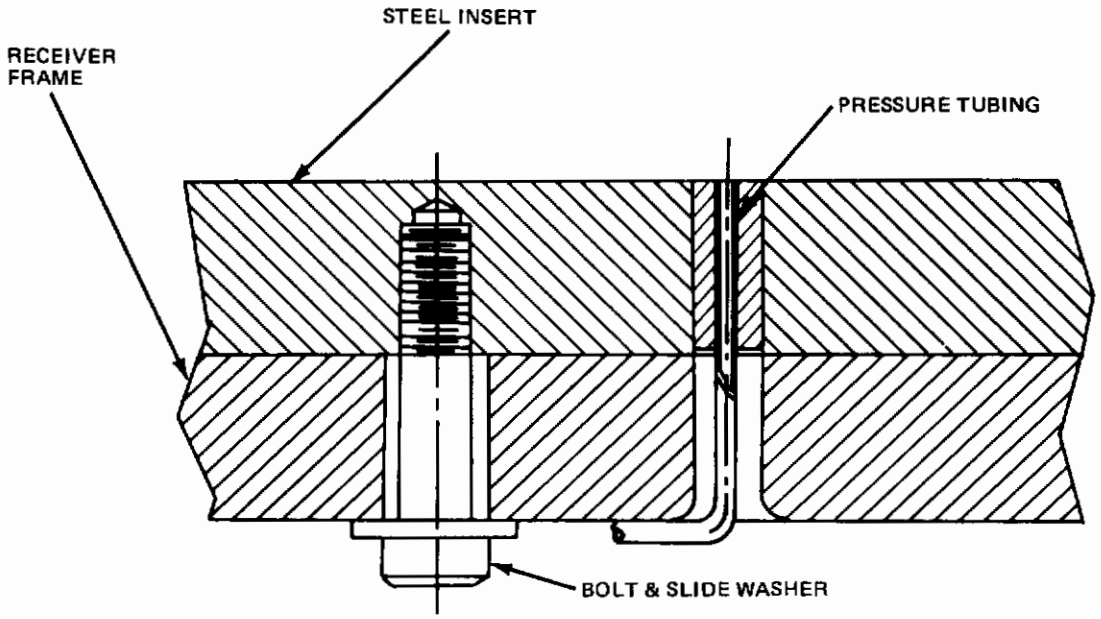

b. TYPICAL SECTION - PRESSURE PANEL

Fig. 12 Typical Thin Skin and Pressure Insert Cross-Sections

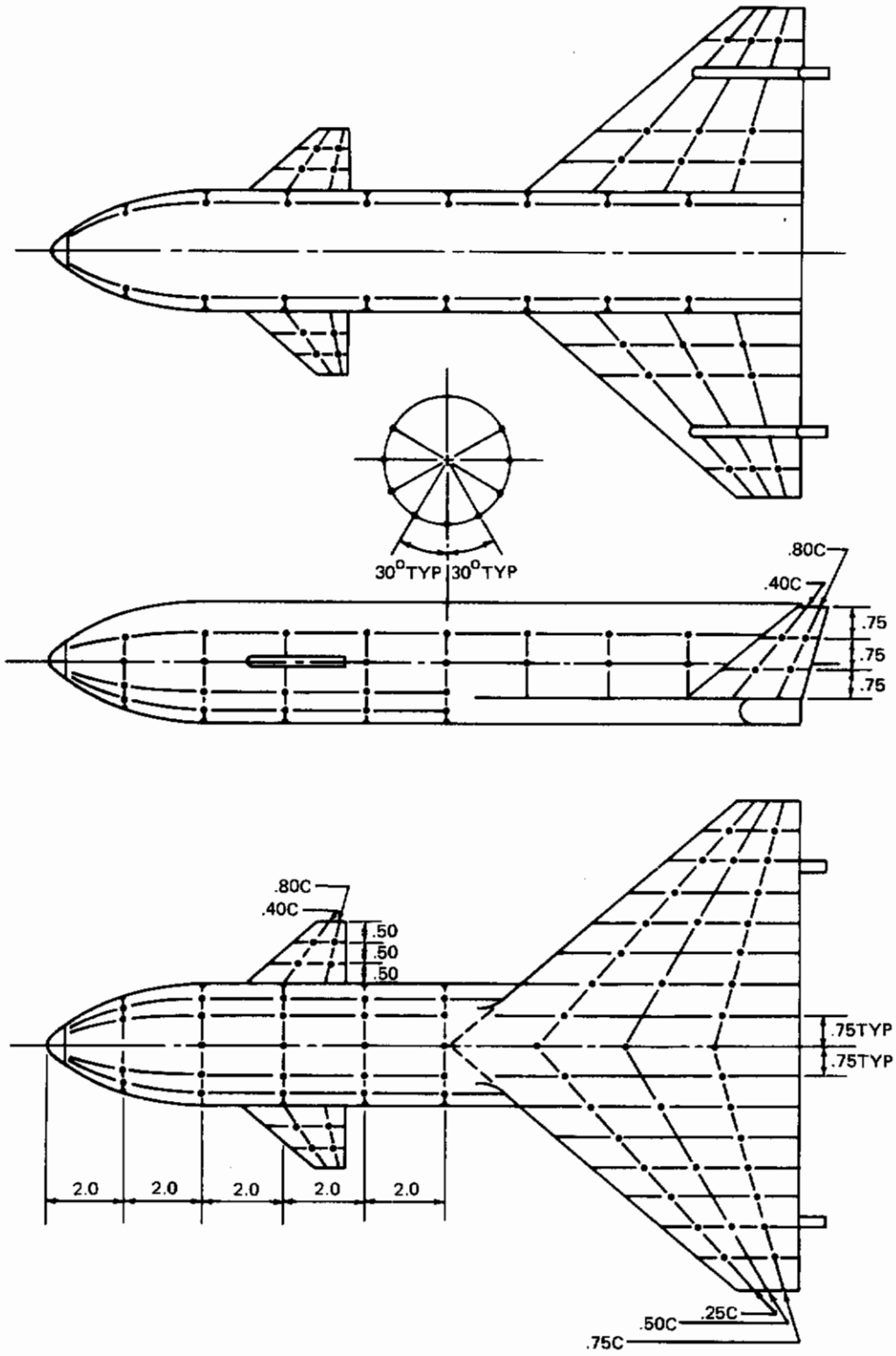

Fig. 13 Reference Grid-Teflon Booster

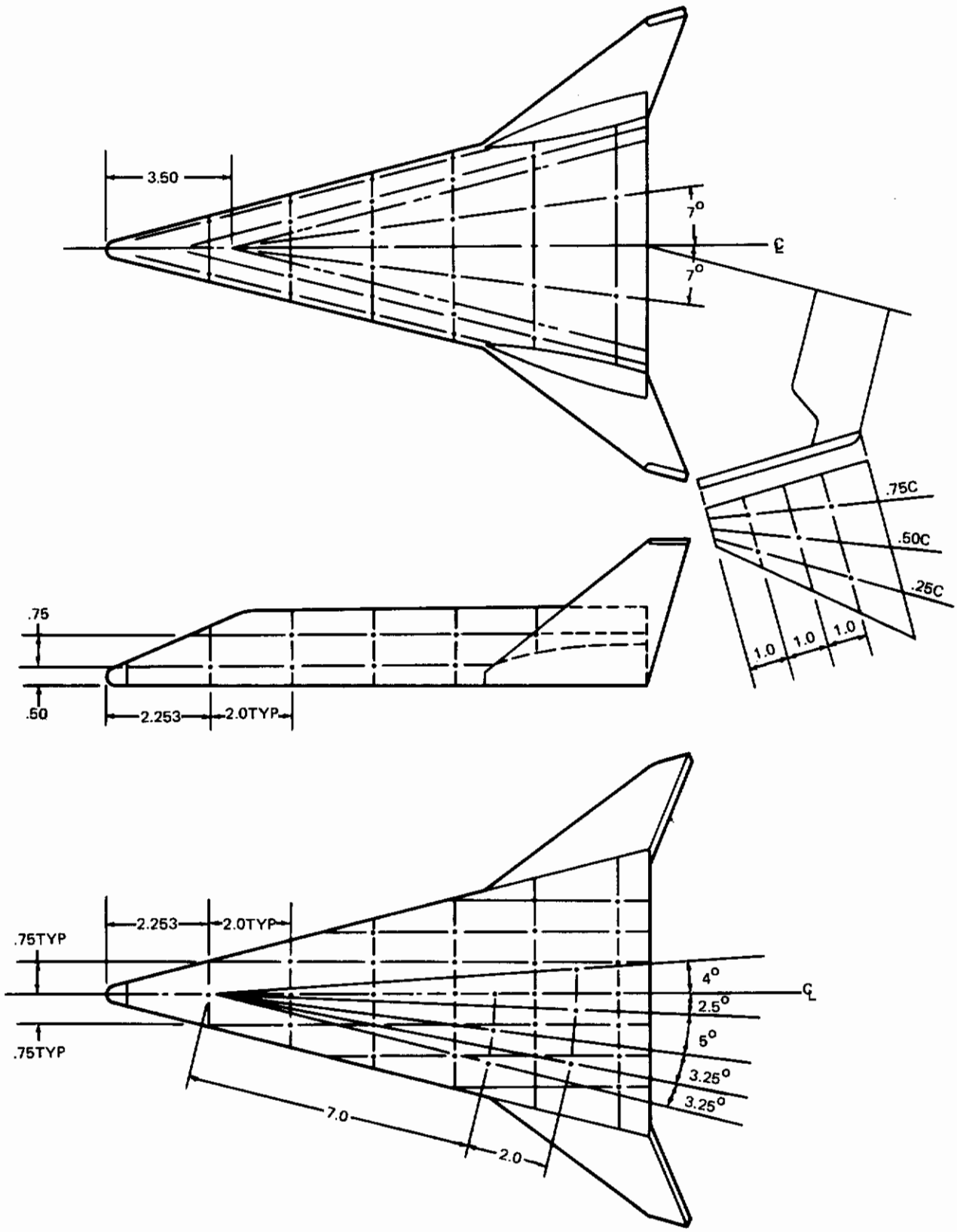

Fig. 14 Reference Grid-Teflon Orbiter

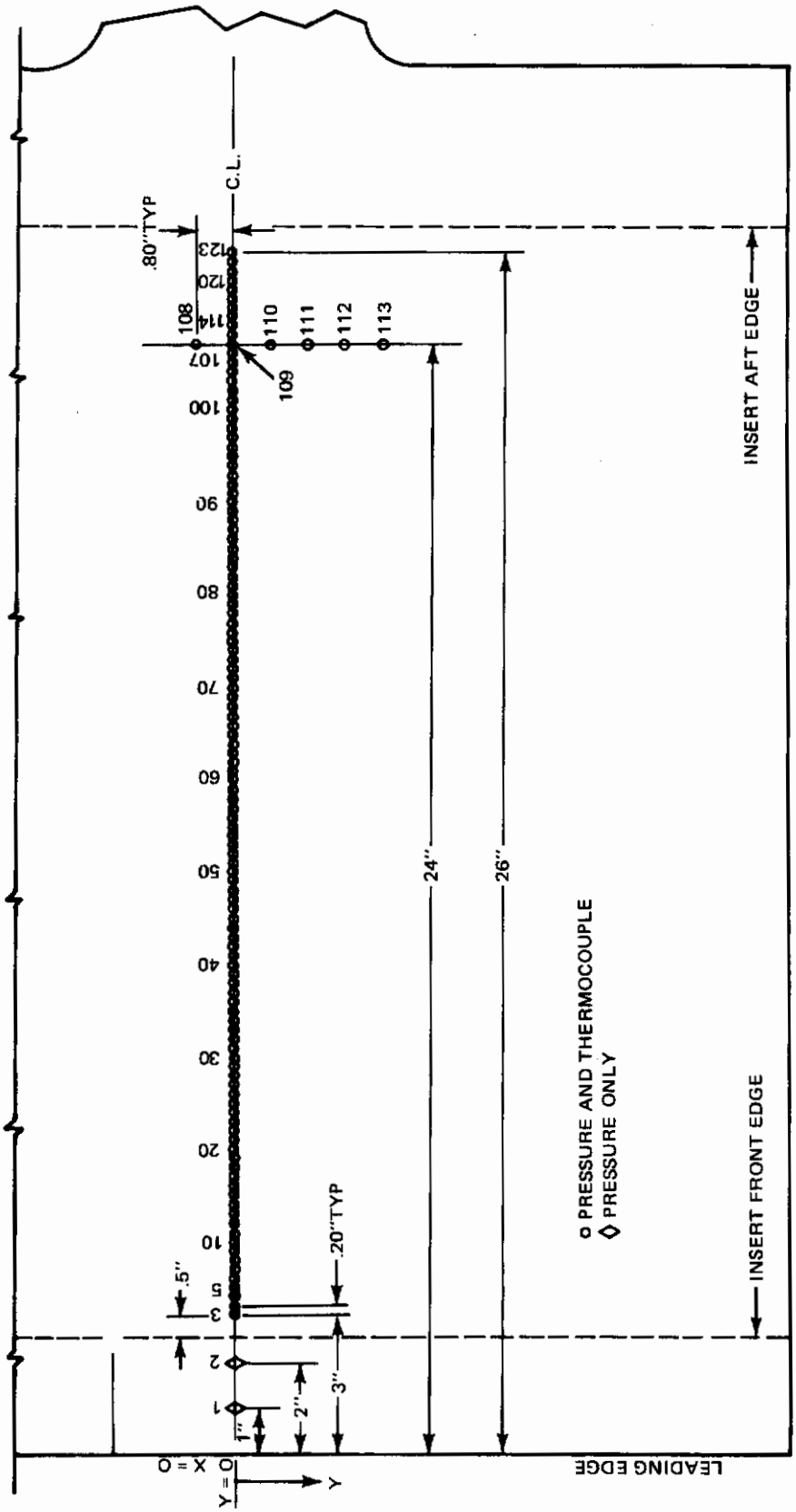

Fig. 15 Planar Model Pressure Tap and Thermocouple Locations

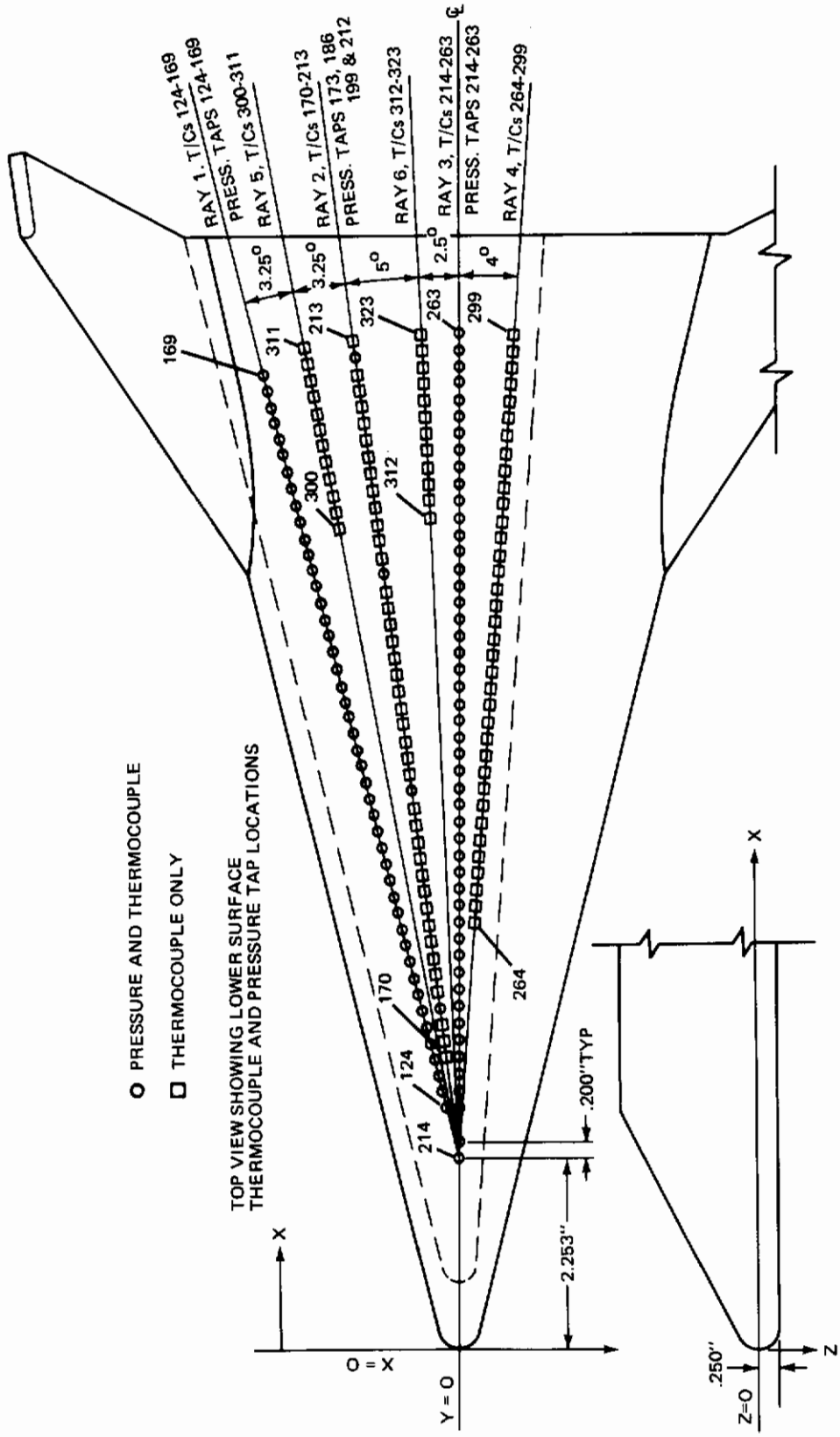

Fig. 16 Orbiter Model Pressure Tap and Thermocouple Locations

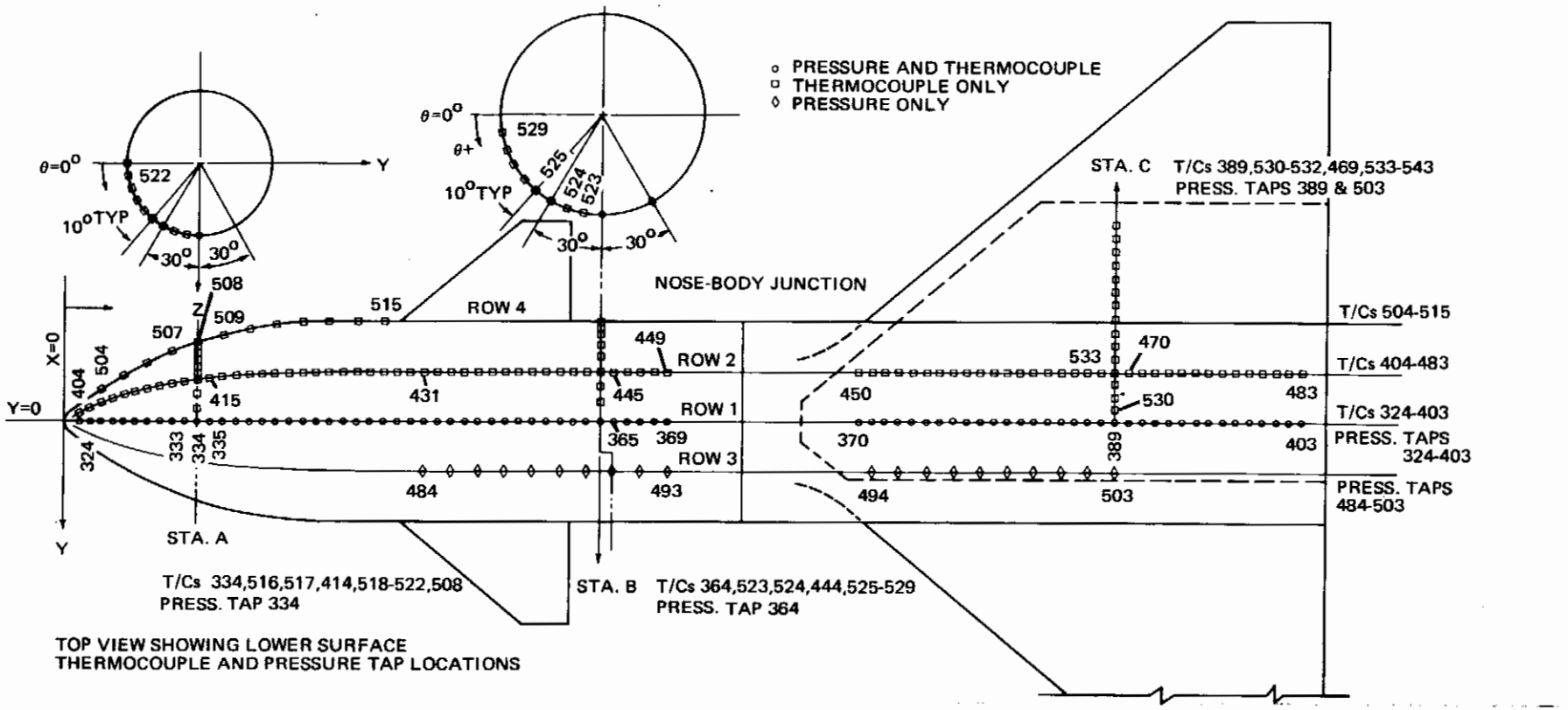

TOP VIEW SHOWING LOWER SURFACE
THERMOCOUPLE AND PRESSURE TAP LOCATIONS

Fig. 17 Booster Model Pressure Tap and Thermocouple Locations

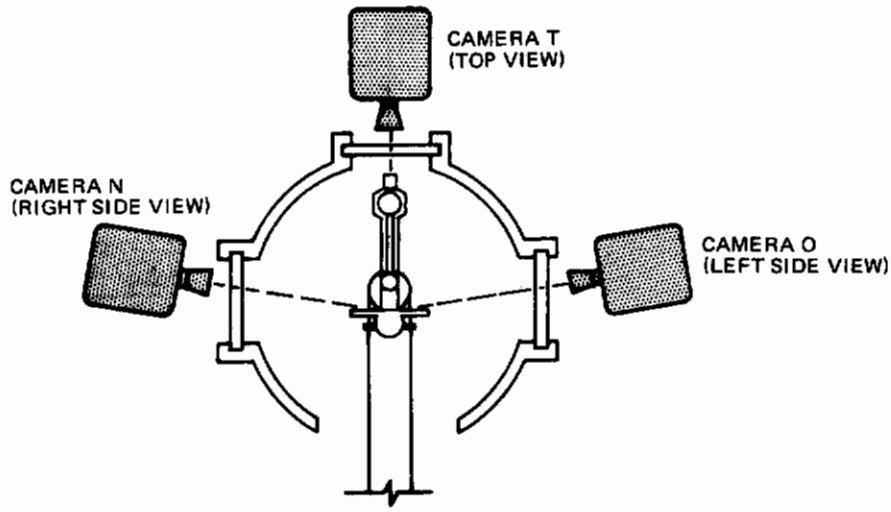

a. CAMERA SET-UP FOR TEFLON RECEIVERS (FLAT PLATE, BOOSTER) AND STEEL GENERATORS. (GROUPS 194-202, 375-387)

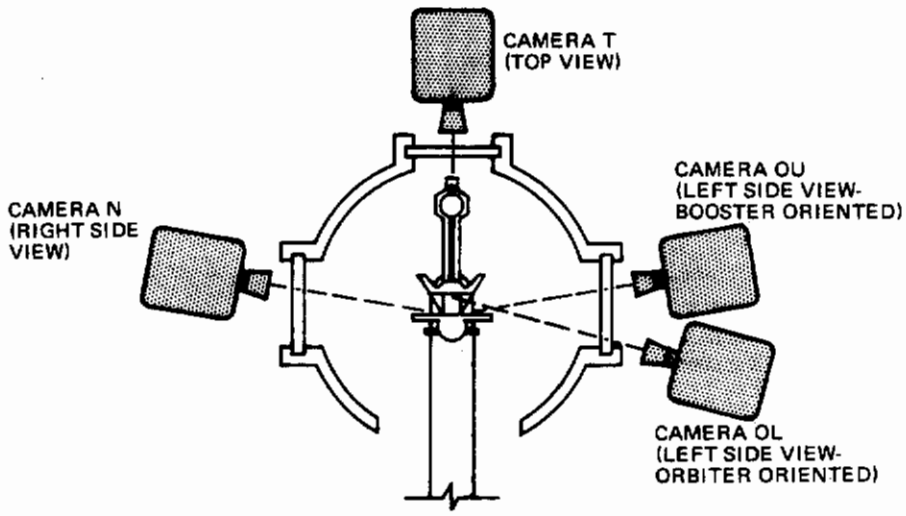

b. CAMERA SET-UP FOR TEFLON BOOSTER WITH TEFLON ORBITER (GROUPS 454-472)

Fig. 18 Tunnel Cross-Section Showing Camera Set-Up for Phase Change Paint Tests

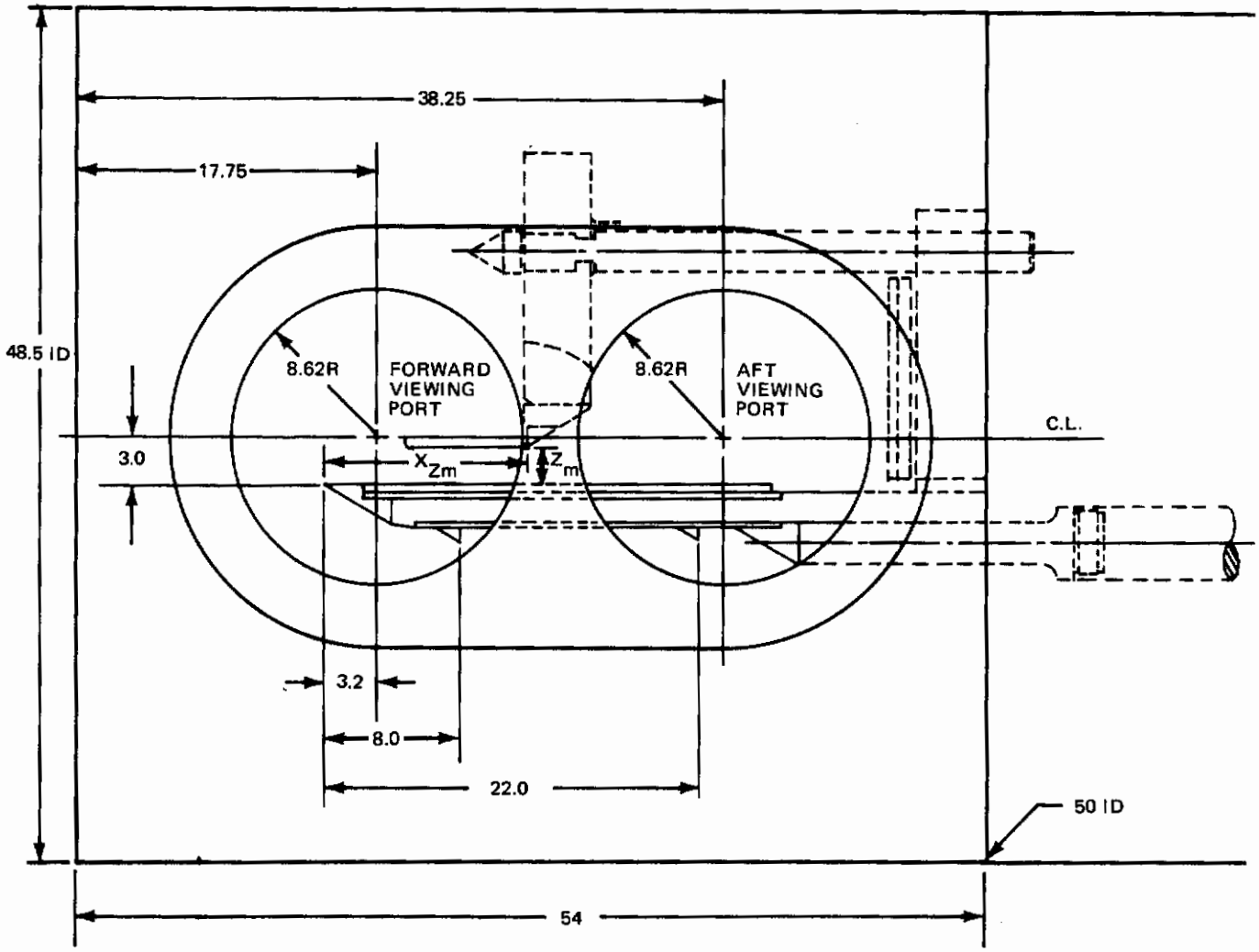

Fig. 19 Position of Flat Plate Model in Test Section

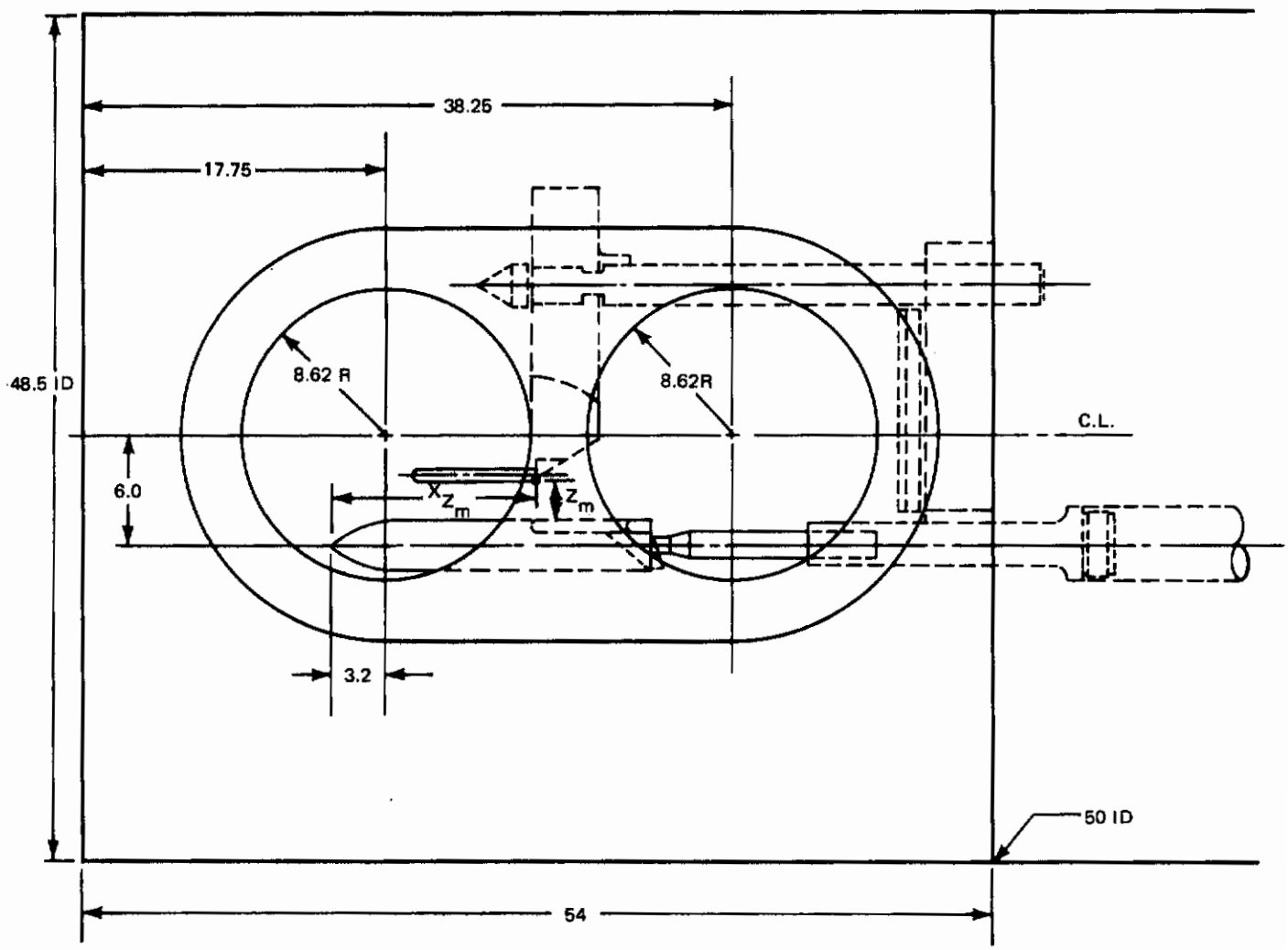

Fig. 20 Position of Booster Model in Test Section

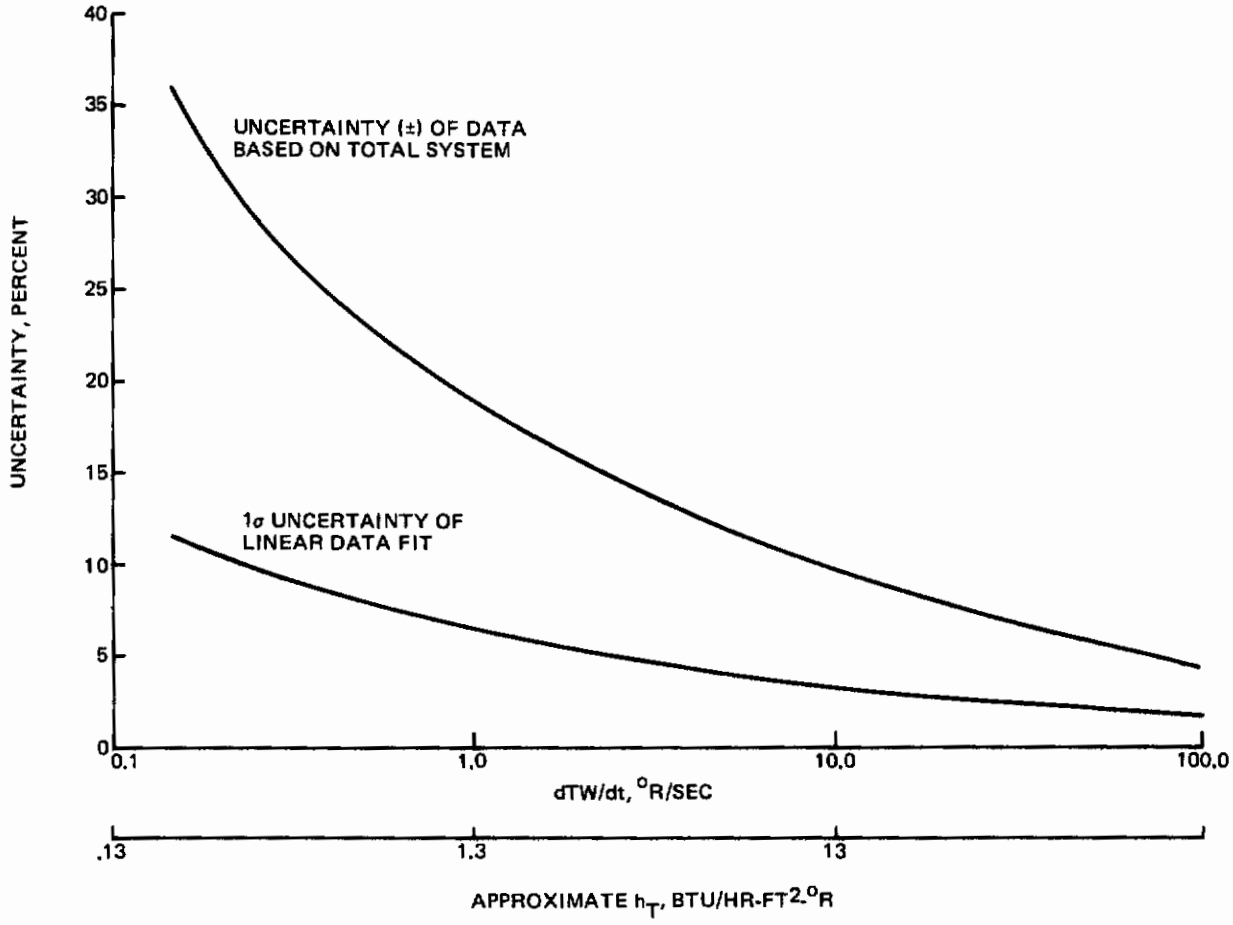

Fig. 21 Data Uncertainty

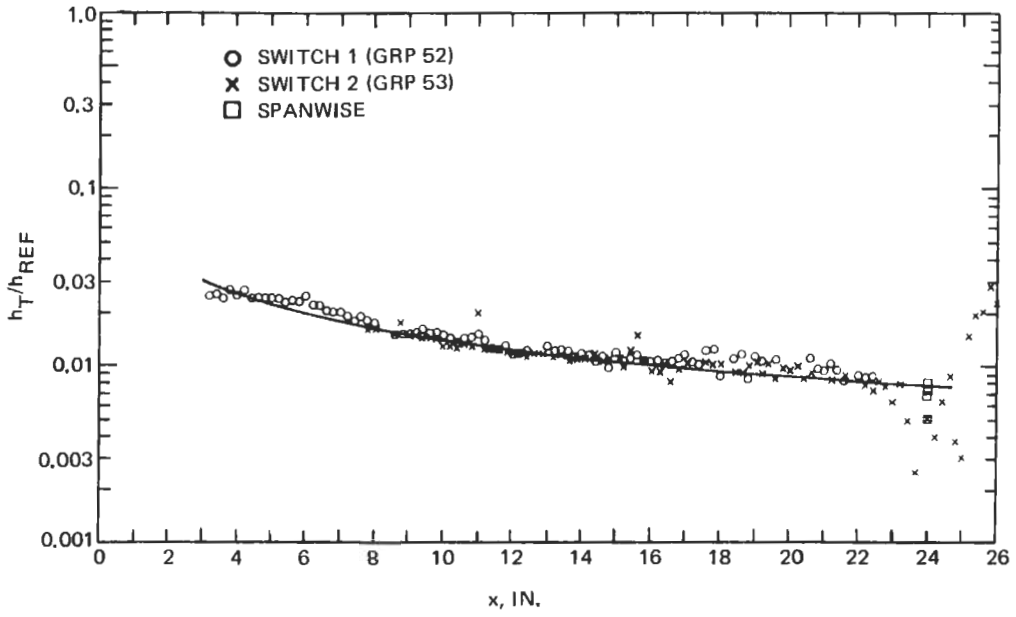

Fig. 22 Undisturbed Heating Distribution on Sharp LE Plate, p_o = 400 psia (Groups 52 & 53)

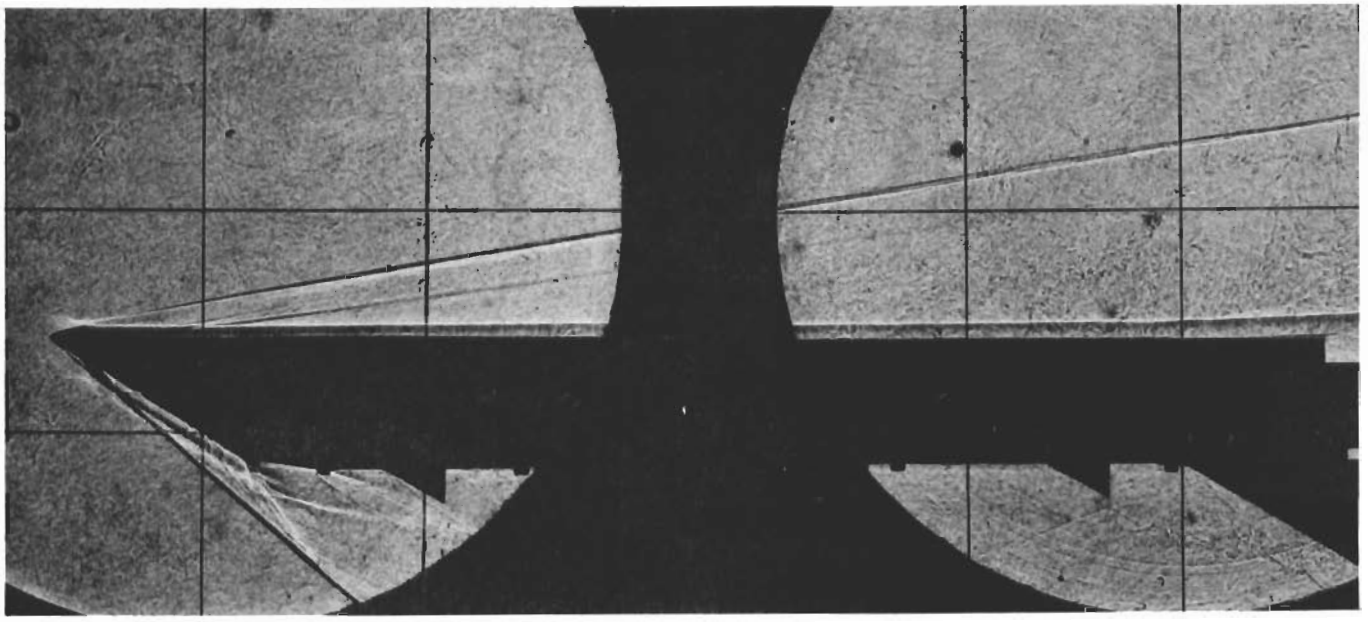

Fig. 23 Shadowgraph Photographs of Undisturbed Flow on Sharp LE Plate; p_o = 400 psia (Group 52)

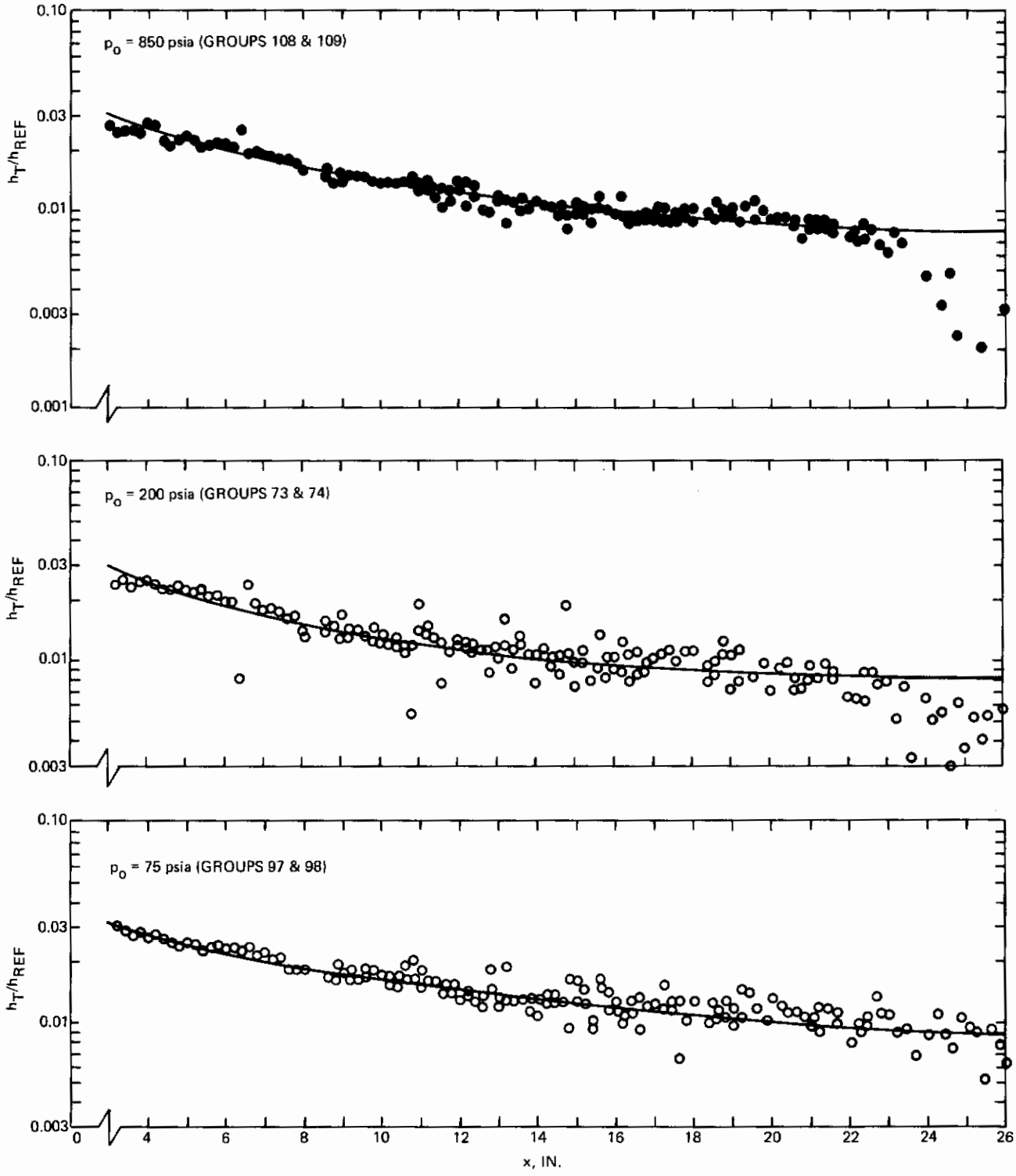

Fig. 24 Distributions of Undisturbed Heating Rates on Sharp L.E. Flat Plate

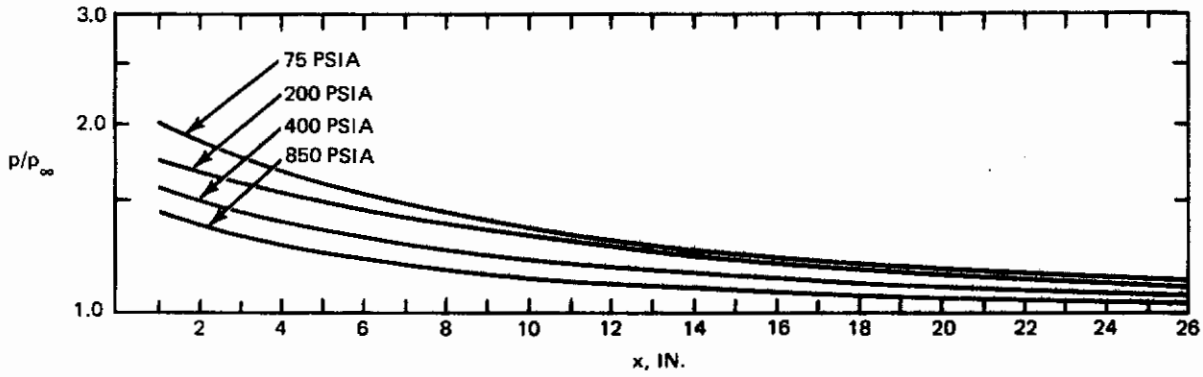

a. FAIRED PRESSURE DISTRIBUTIONS

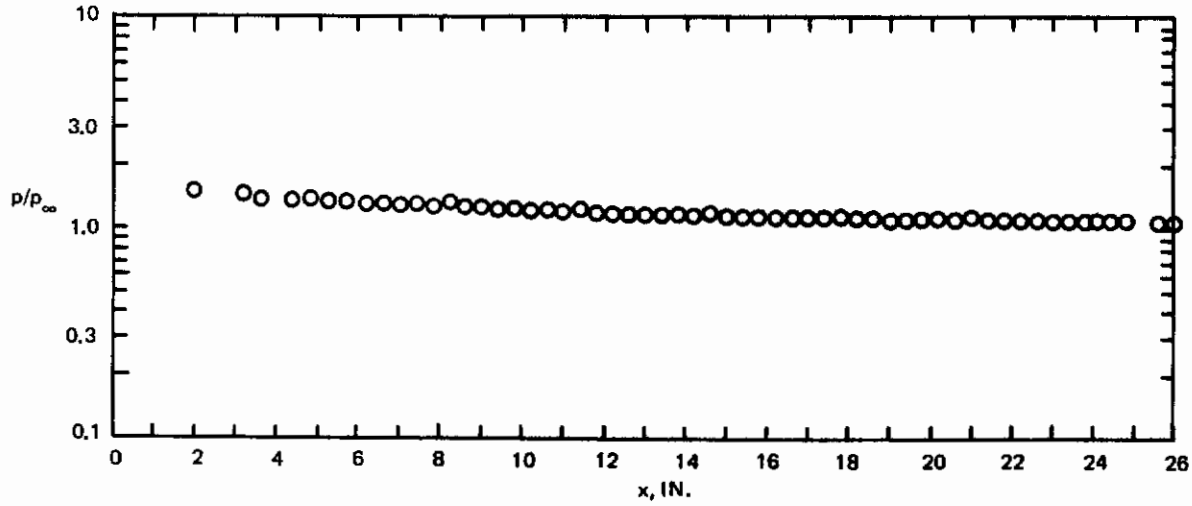

b. MEASURED PRESSURE, p_o = 400 PSIA, GROUP 295

Fig. 25 Distributions of Undisturbed Pressures on Sharp LE Flat Plate

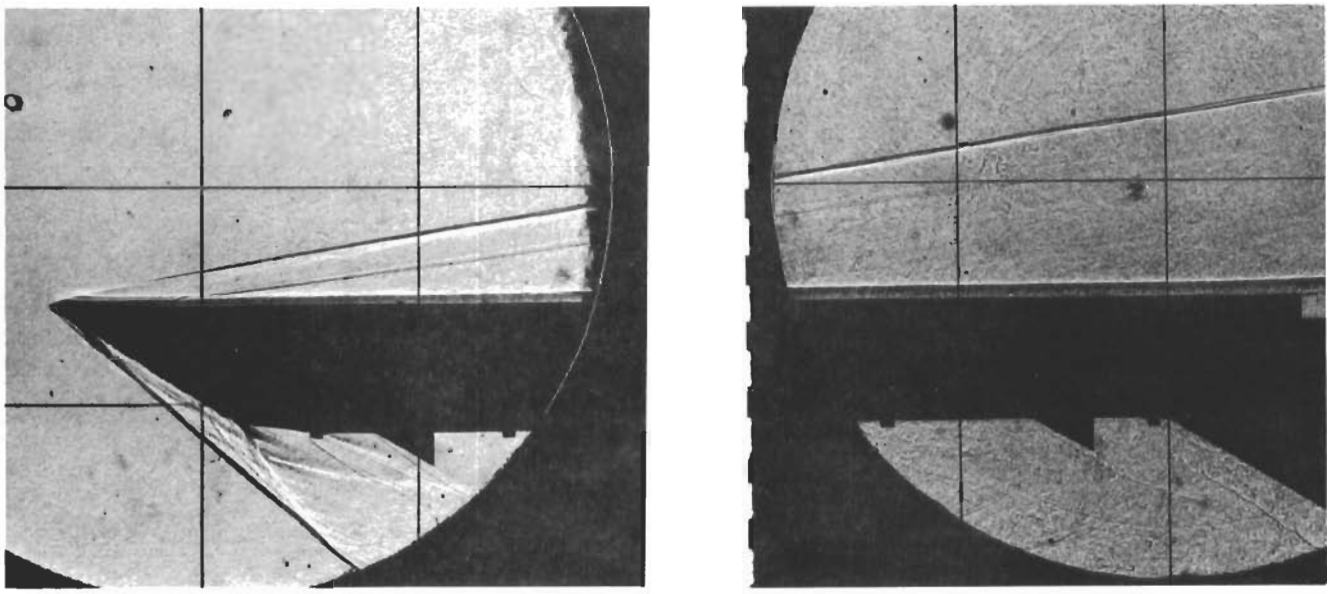

a. SHADOWGRAPHS

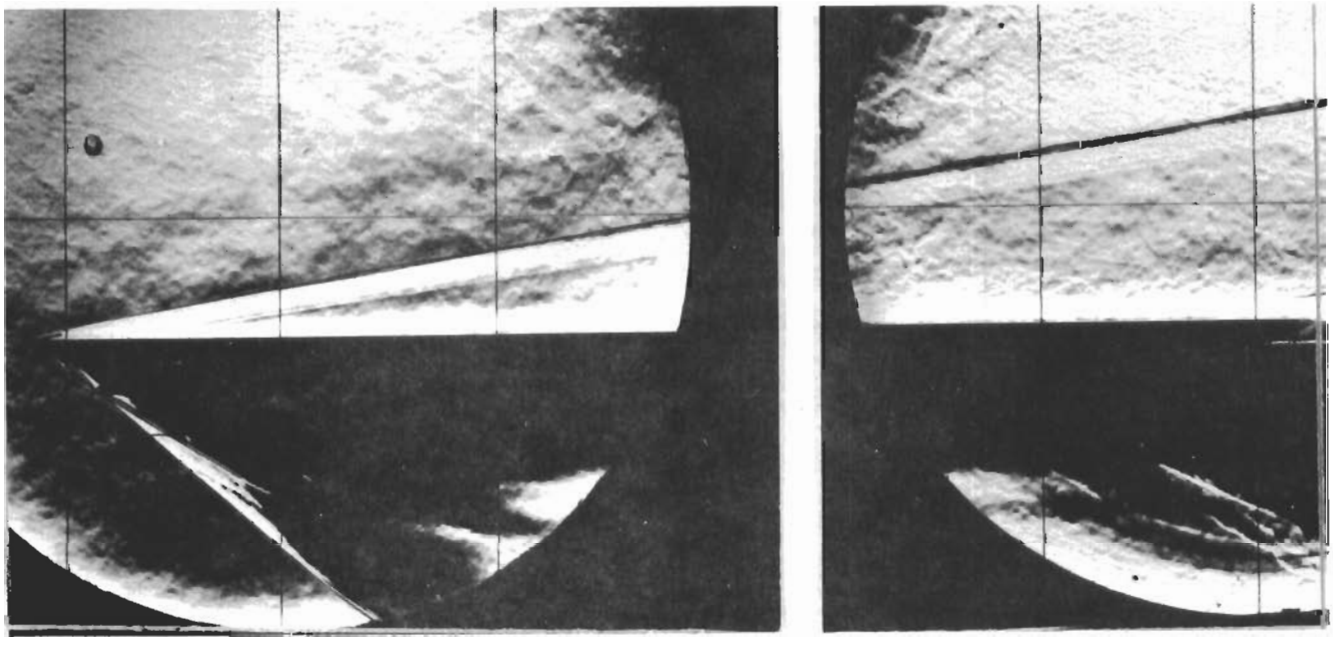

b. SCHLIERENS

Fig. 26 Shadowgraph and Schlieren Photographs of Undisturbed Flows on Sharp LE Plate; p_o = 850 psia (Groups 108 & 254)

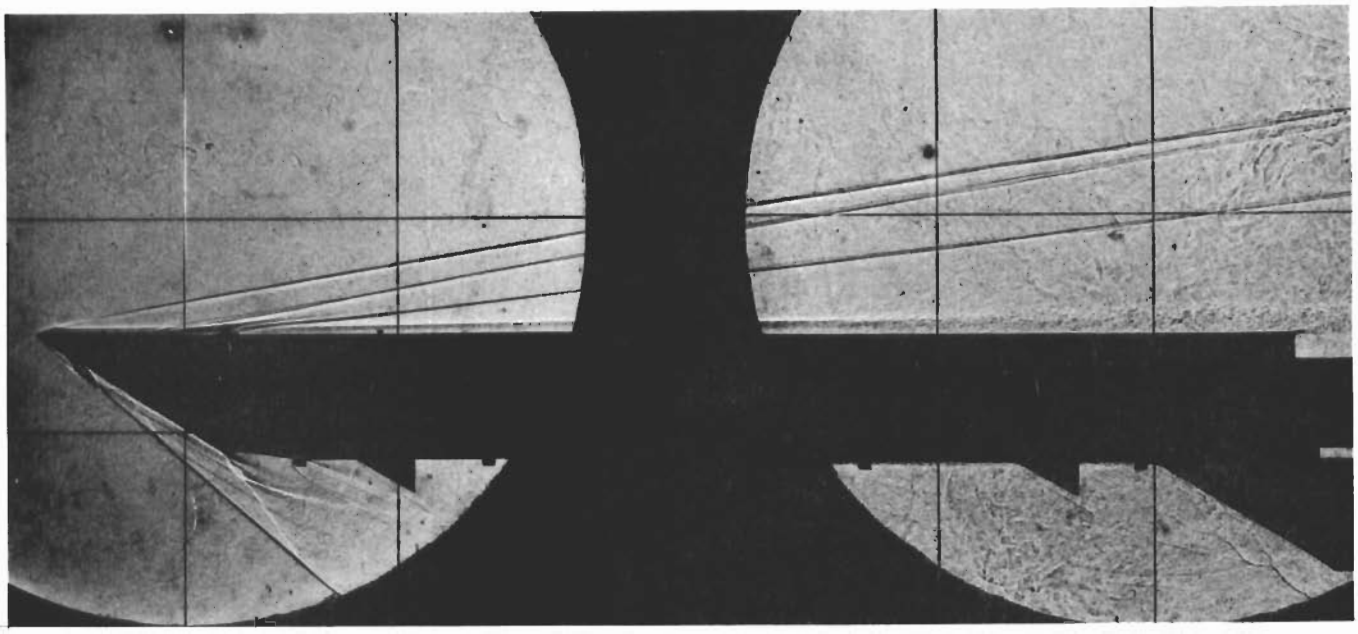

a. SHADOWGRAPHS

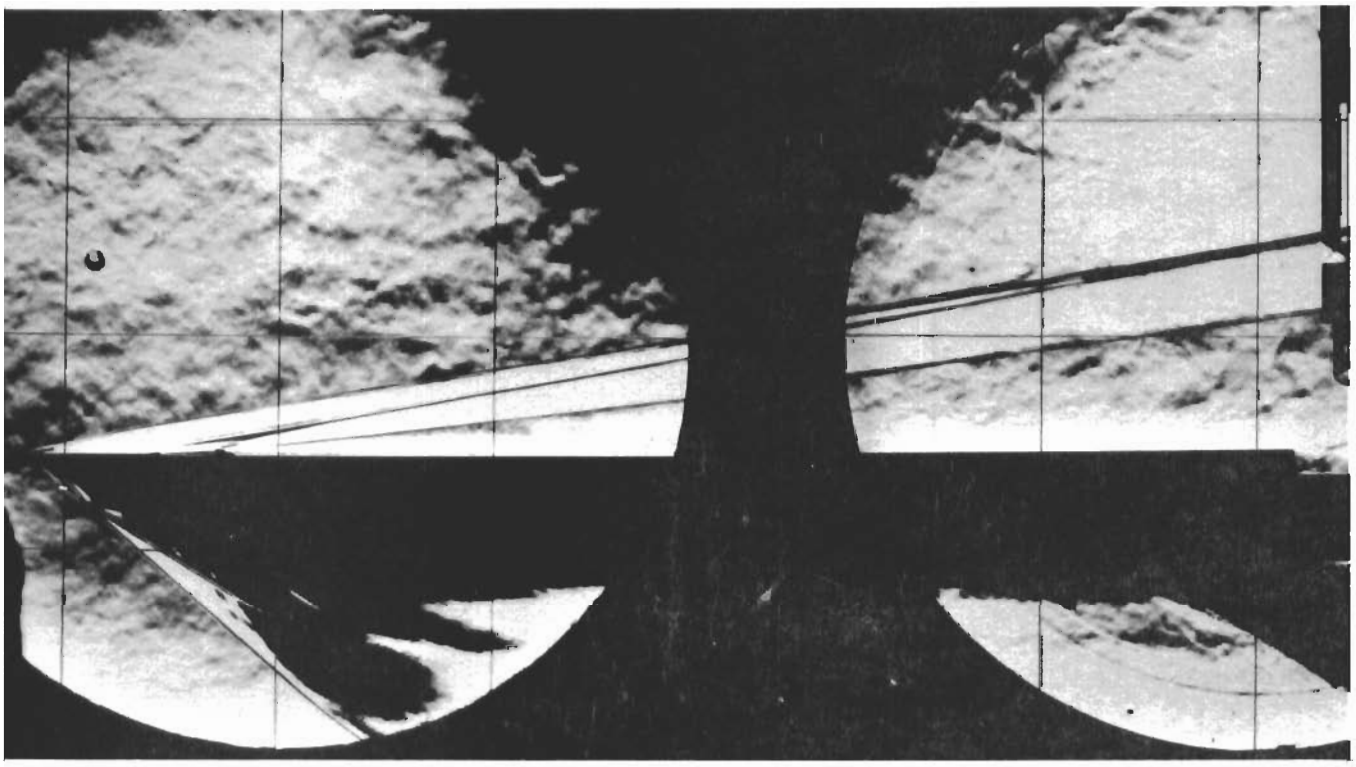

b. SCHLIERENS

Fig. 27 Shadowgraph and Schlieren Photographs of Tripped Boundary Layers on Sharp LE Plate; p_o = 850 psia (Groups 3 & 246)

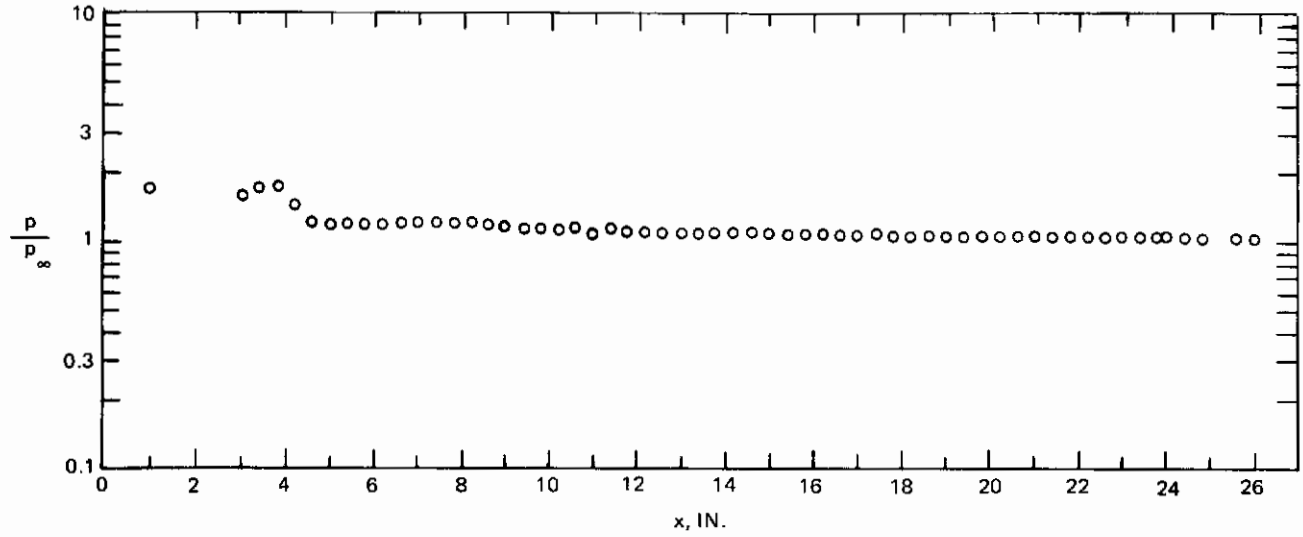

a. PRESSURE (GROUP 246)

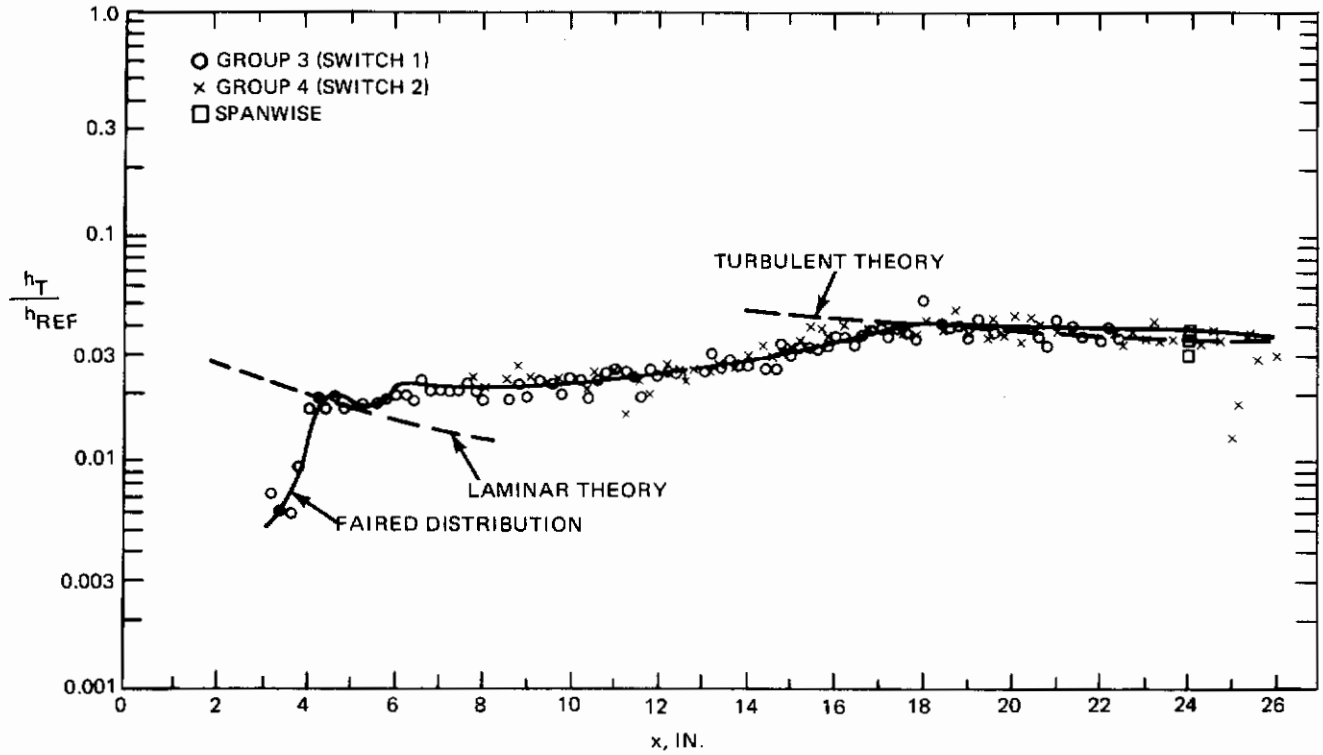

b. HEAT TRANSFER (GROUPS 3&4)

Fig. 28 Undisturbed Pressure and Heating Distributions for Tripped Boundary Layers on Sharp LE Plate; p_o = 850 psia (Groups 246; 3 & 4)

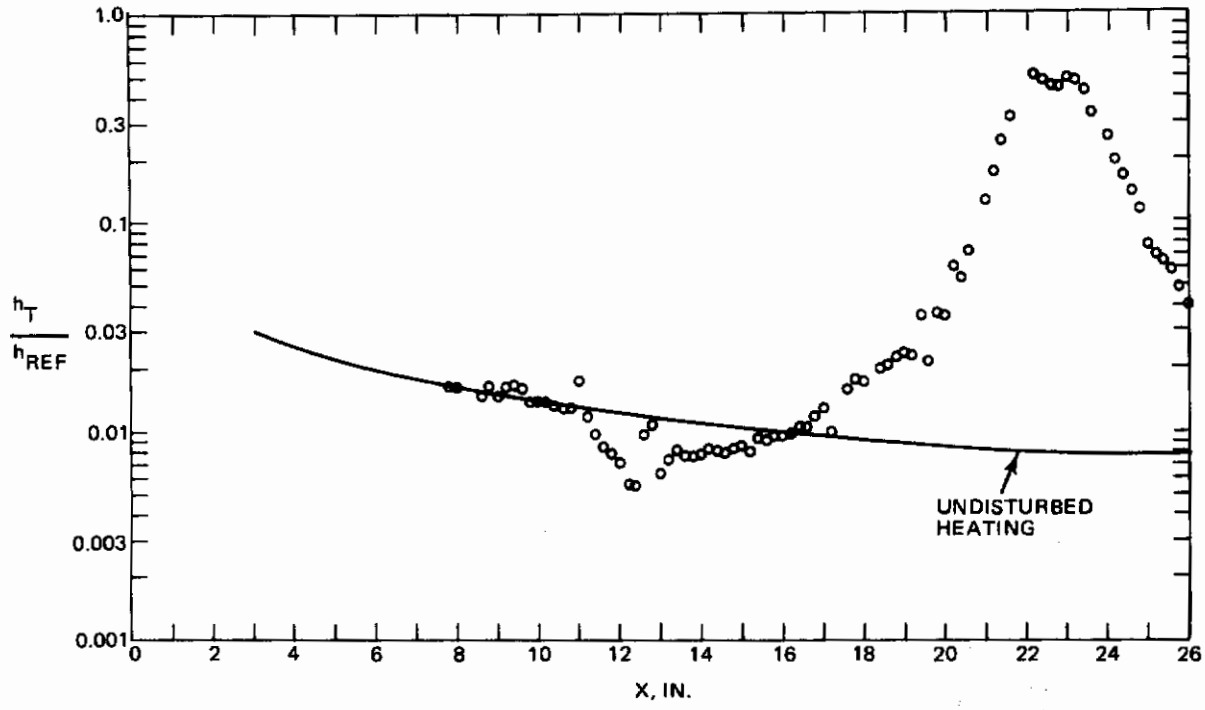

a. HEAT TRANSFER

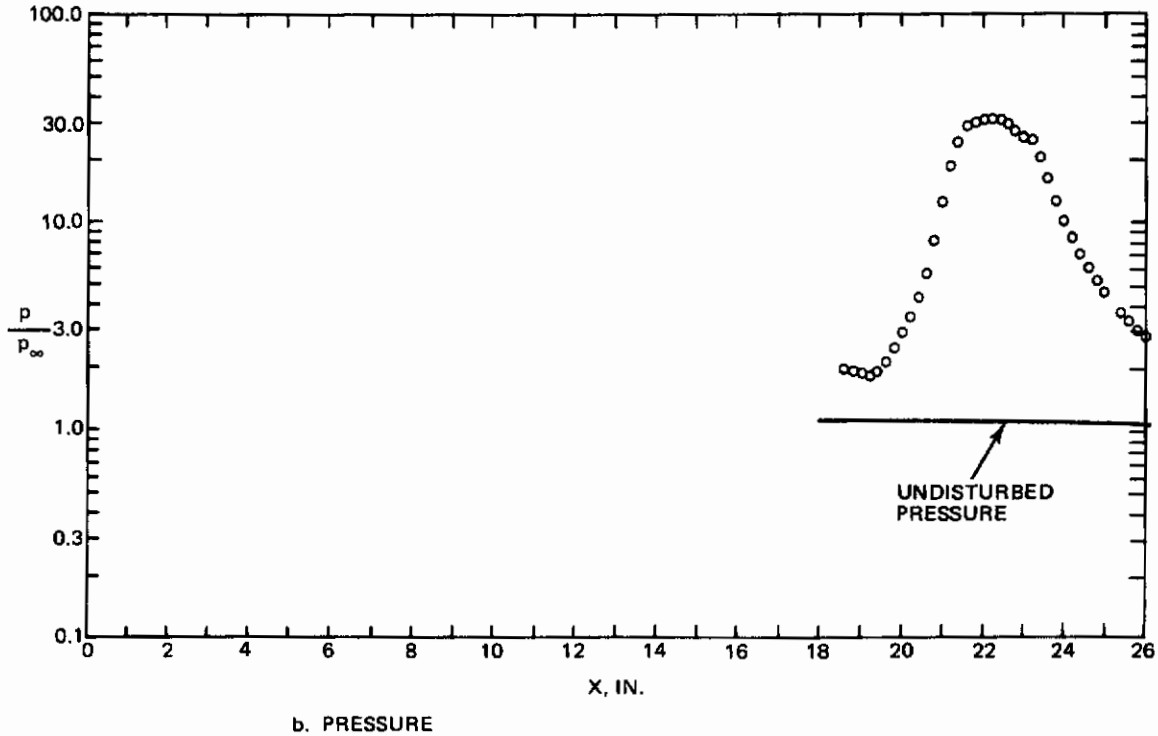

b. PRESSURE

Fig. 29 Heating and Pressure Distributions on Sharp Plate Caused by 10° Wedge Shock; p_o = 400 psia, x_i = 22 in. (Groups 63 & 282)

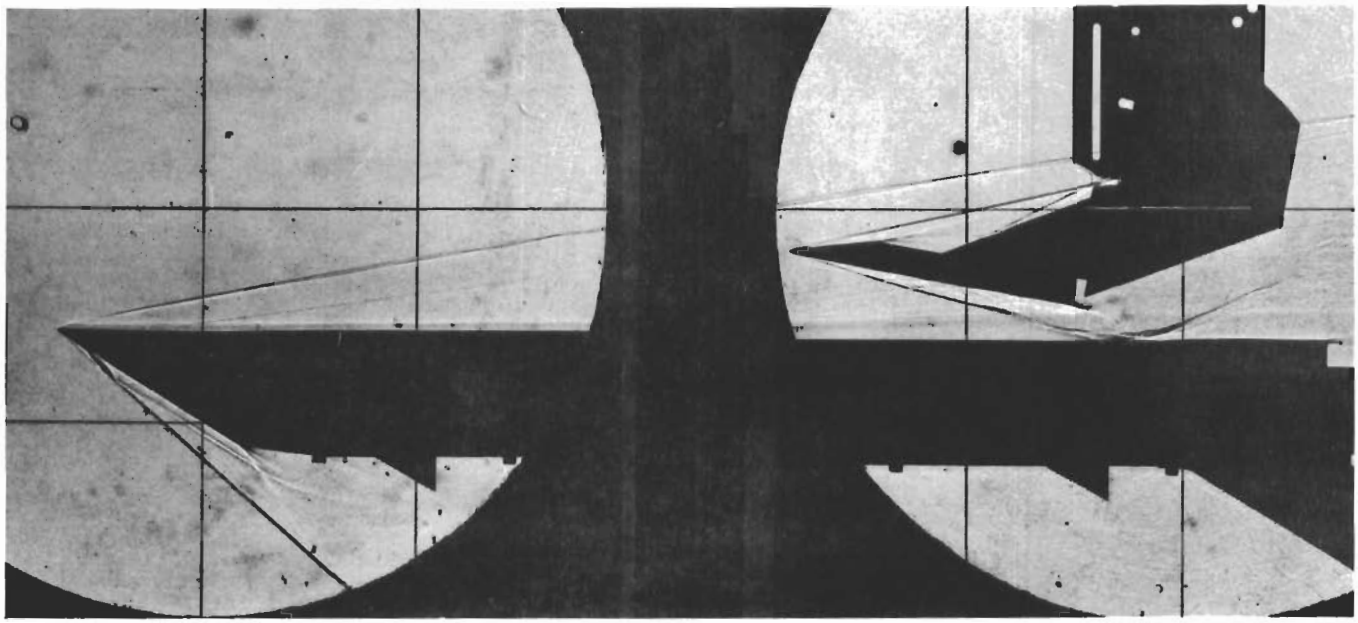

a. SHADOWGRAPHS

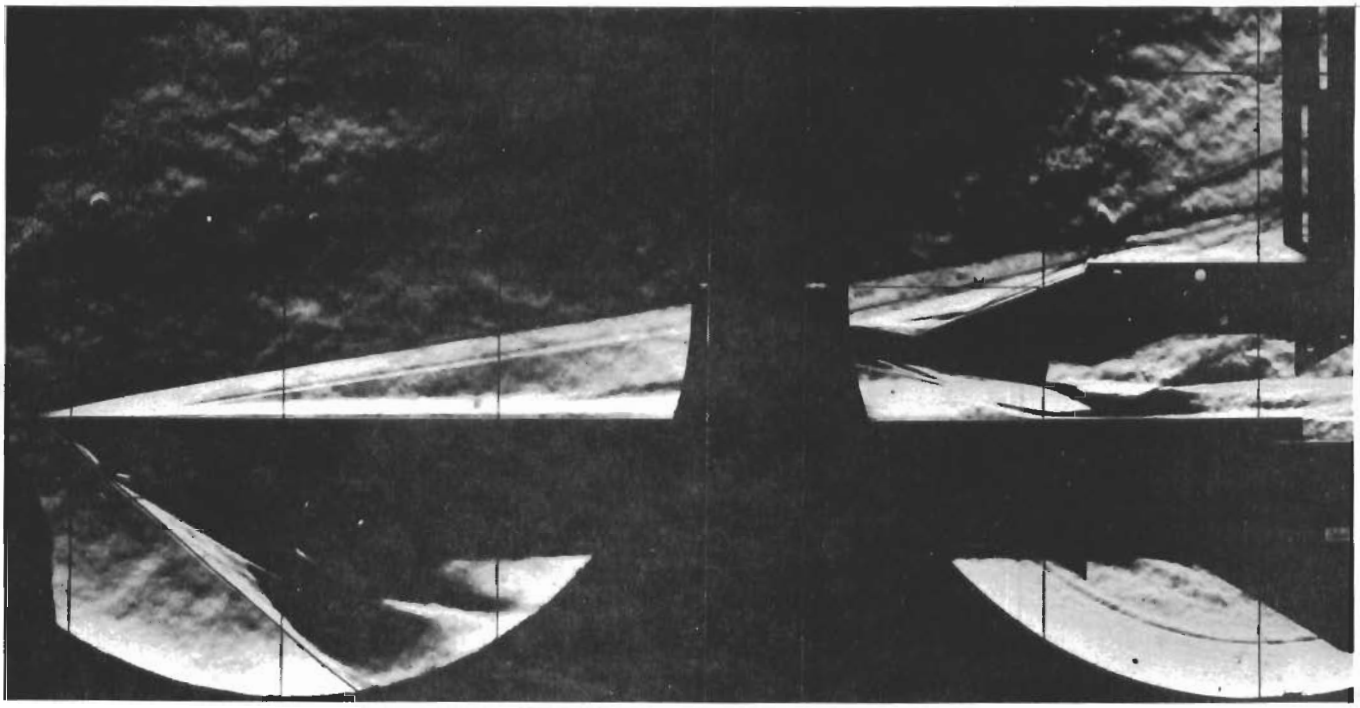

b SCHLIERENS

Fig. 30 Shadowgraph and Schlieren Photographs of Interaction Caused by 10^{o} Wedge Shock; p_o = 400 psia, x_i = 22 in. (Groups 63 & 282)

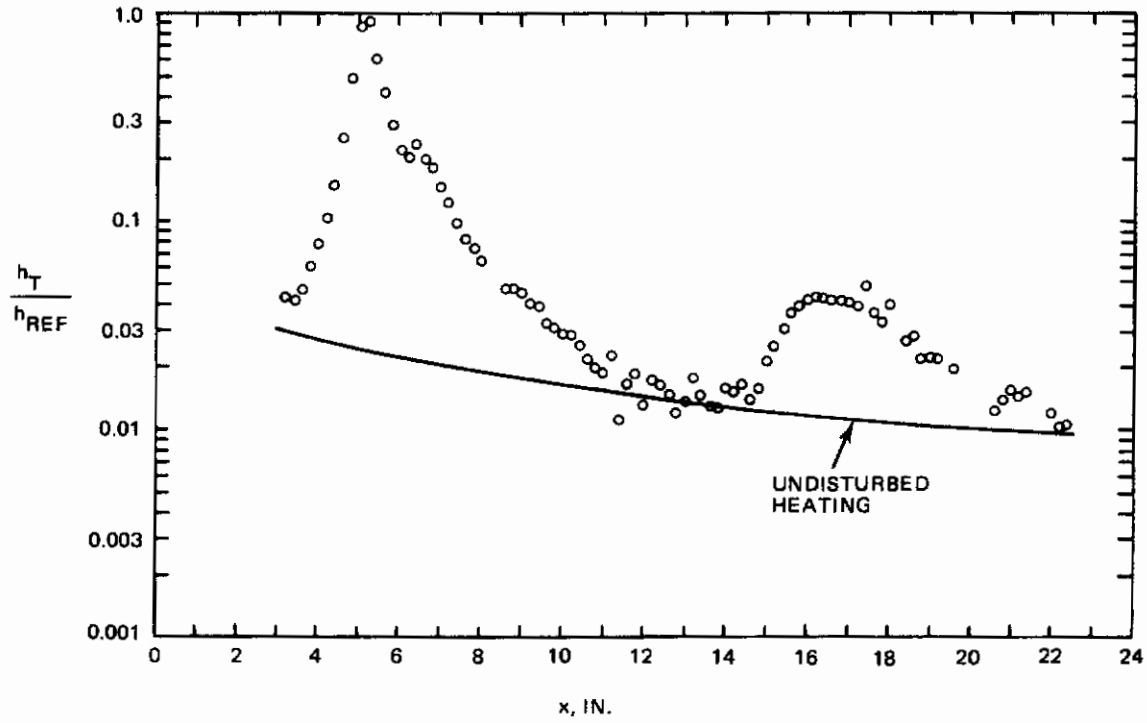

a. HEAT TRANSFER

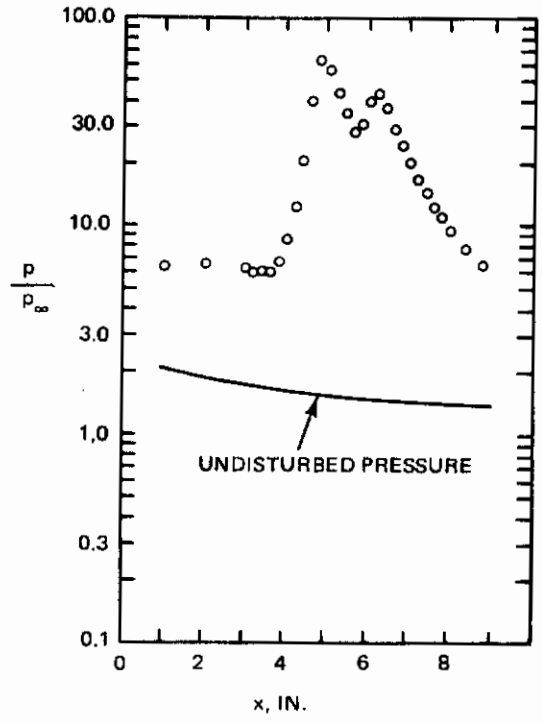

b. PRESSURE

Fig. 31 Heating and Pressure Distributions on Sharp Plate caused by 15° Wedge Shock; p_o = 75 psia, x_i = 5 in. (Groups 96 & 317)

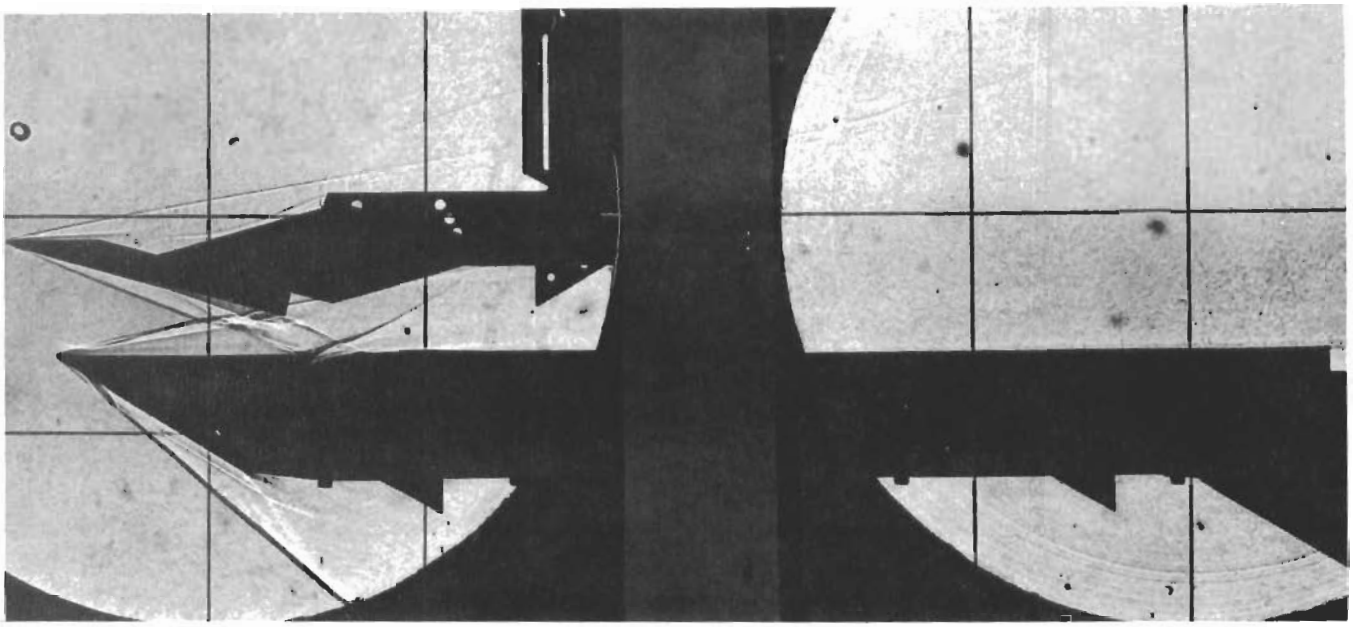

a. SHADOWGRAPHS

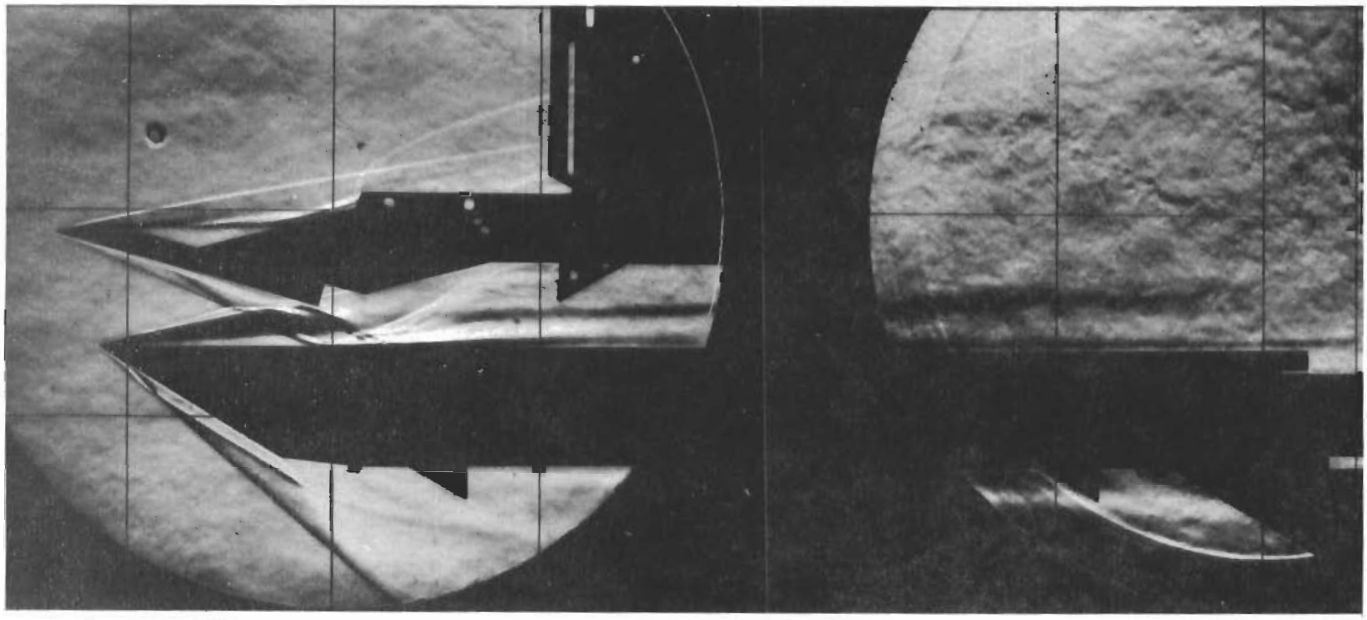

b. SCHLIERENS

Fig. 32 Shadowgraph and Schlieren Photographs of Interaction Caused by 15° Wedge Shock; p_o = 75 psia, x_i = 5 in. (Groups 96 & 317)

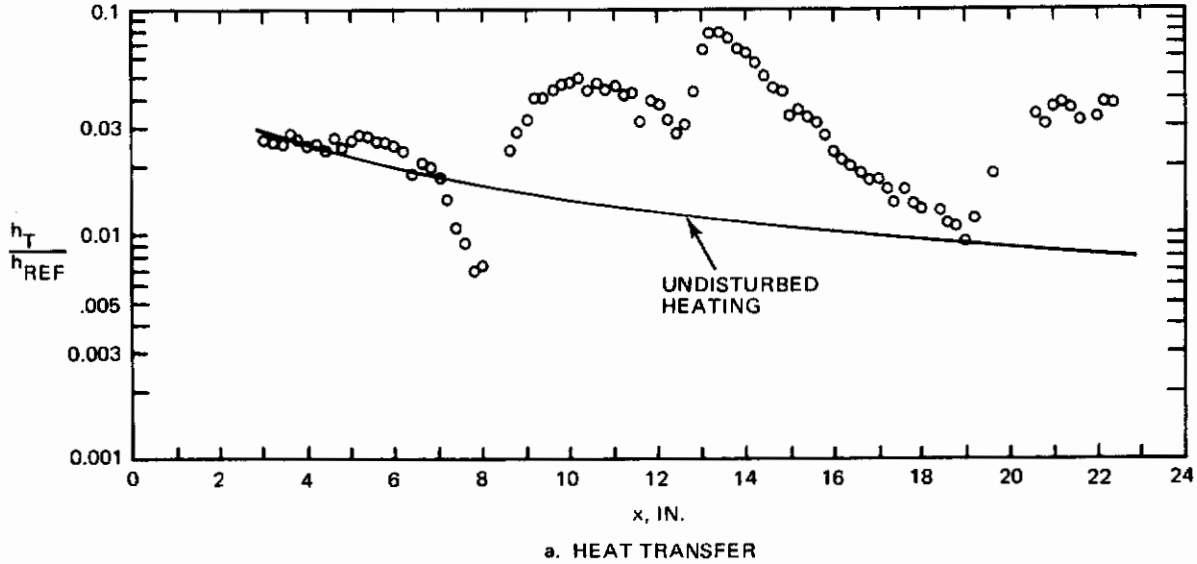

a. HEAT TRANSFER

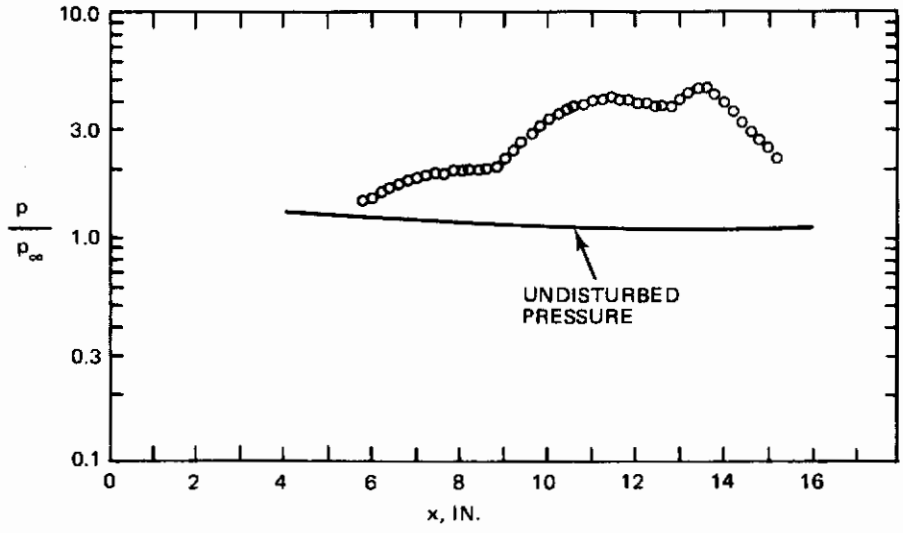

b. PRESSURE

Fig. 33 Heating and Pressure Distributions on Sharp Plate Caused by 1½° Wedge Shock; p_o = 850 psia, x_i = 11 in. (Groups 115 & 271)

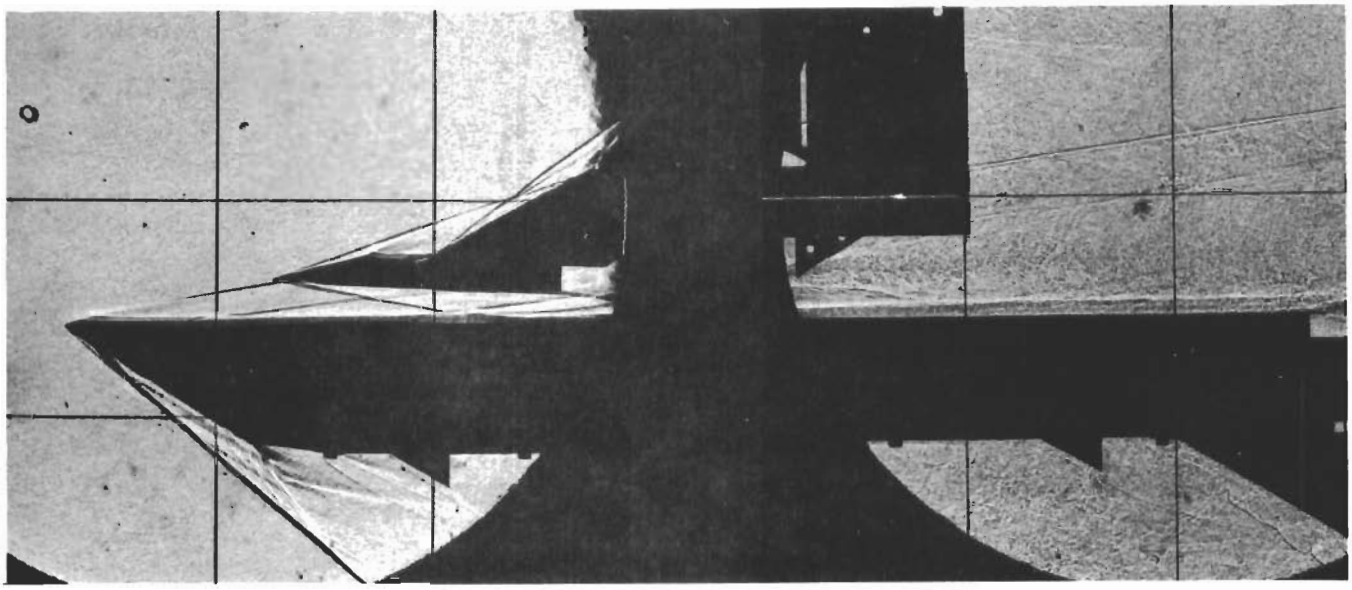

a. SHADOWGRAPHS

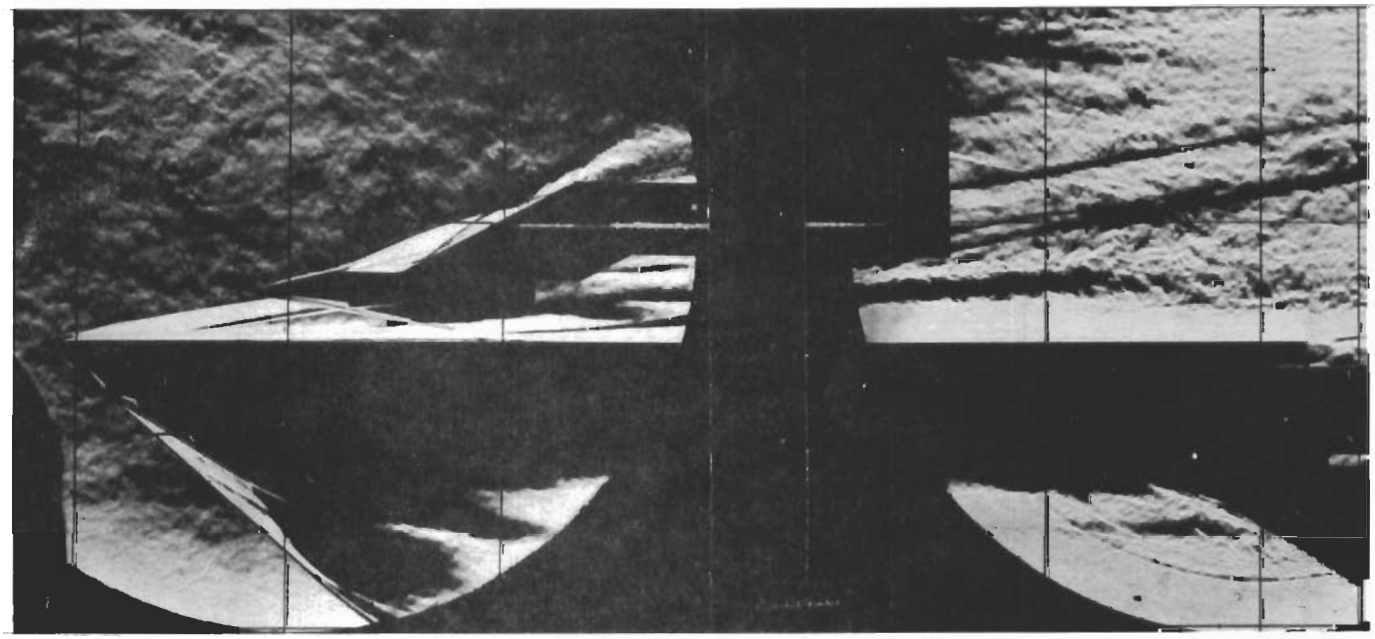

b. SCHLIERENS

Fig. 34 Shadowgraph and Schlieren Photographs of Interaction Caused by 1 1/2° Wedge Shock; p_o = 850 psia, x_i = 11 in. (Groups 115 & 271)

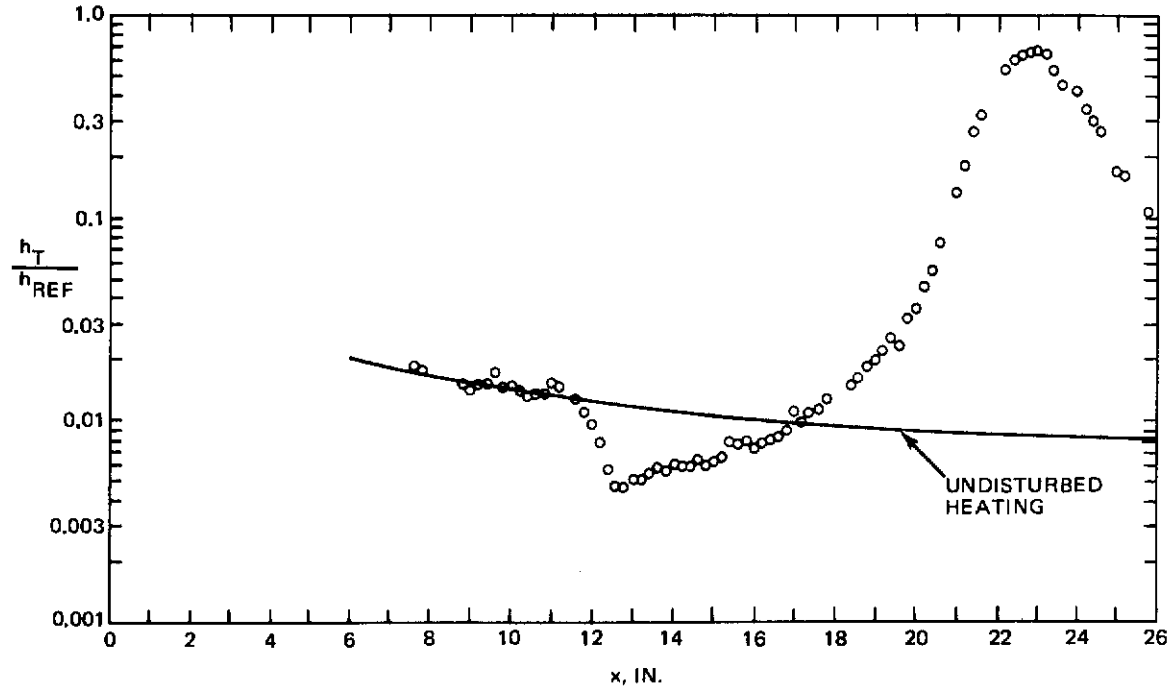

a. HEAT TRANSFER

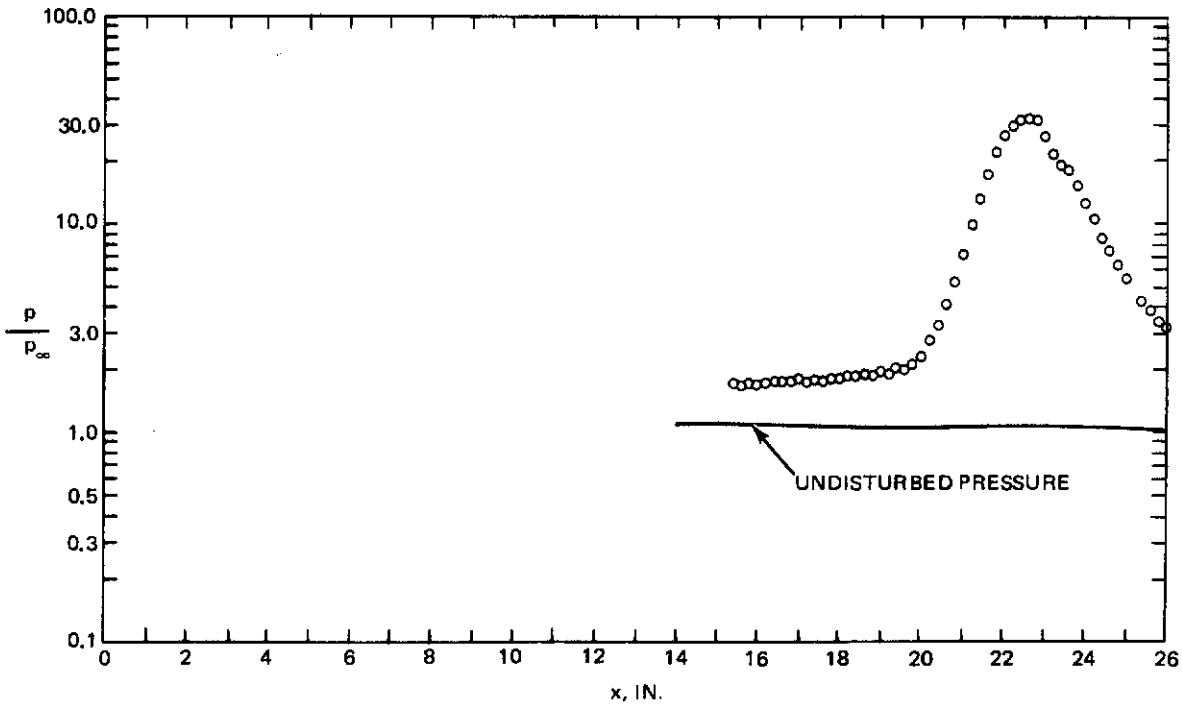

b. PRESSURE

Fig. 35 Heating and Pressure Distributions on Sharp Plate Caused by 10° Wedge Shock; p_o = 850 psia, x_i = 22 in. (Groups 217 & 268)

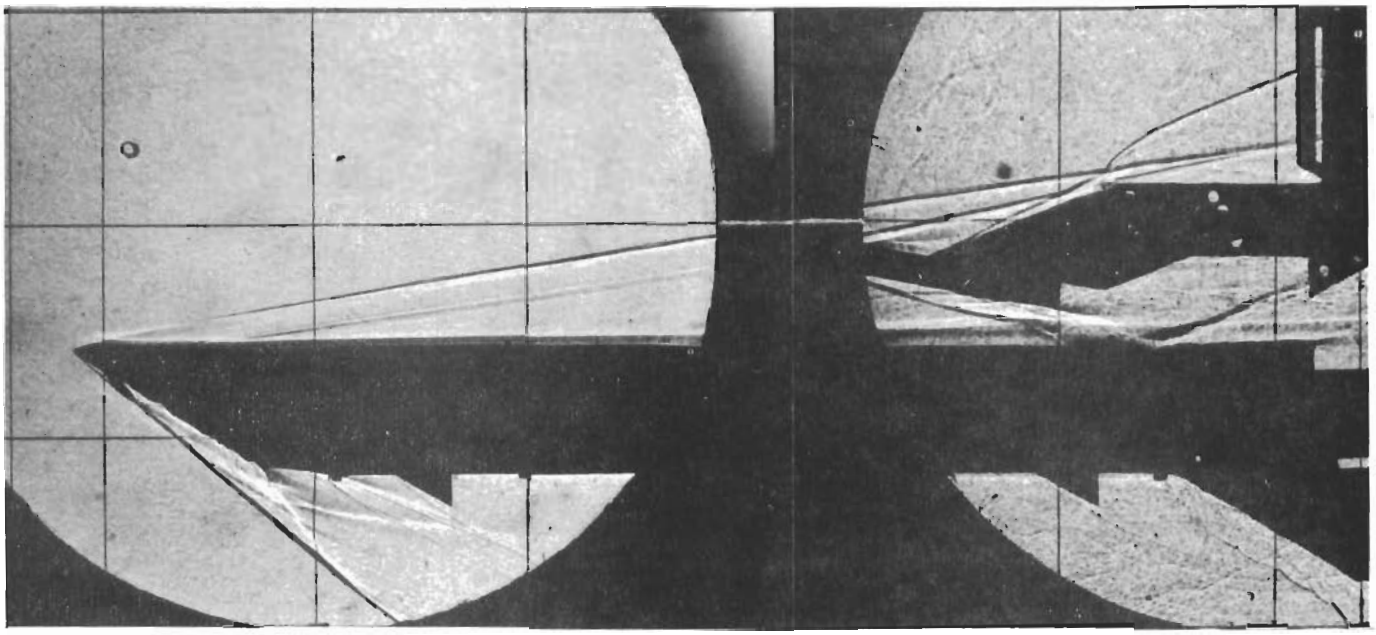

a. SHADOWGRAPHS

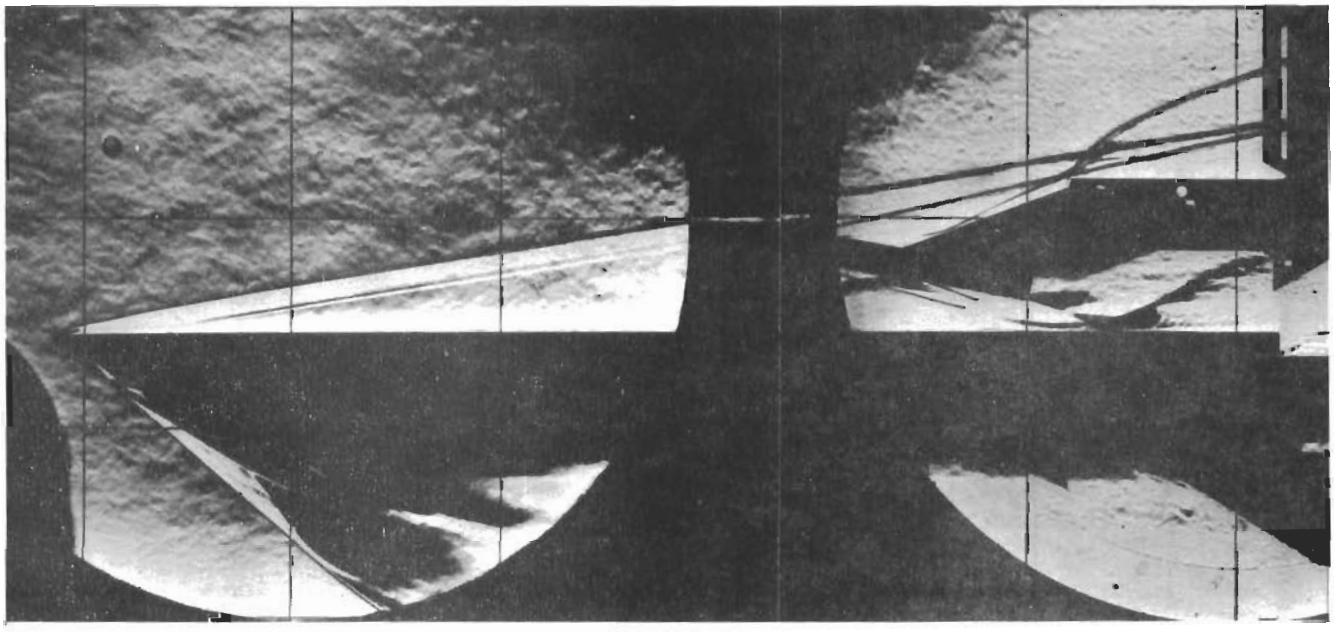

b. SCHLIERENS

Fig. 36 Shadowgraphs and Schlieren Photographs of Interaction Caused by 10° Wedge Shock; p_o = 850 psia, x_i = 22 in. (Groups 217 & 268)

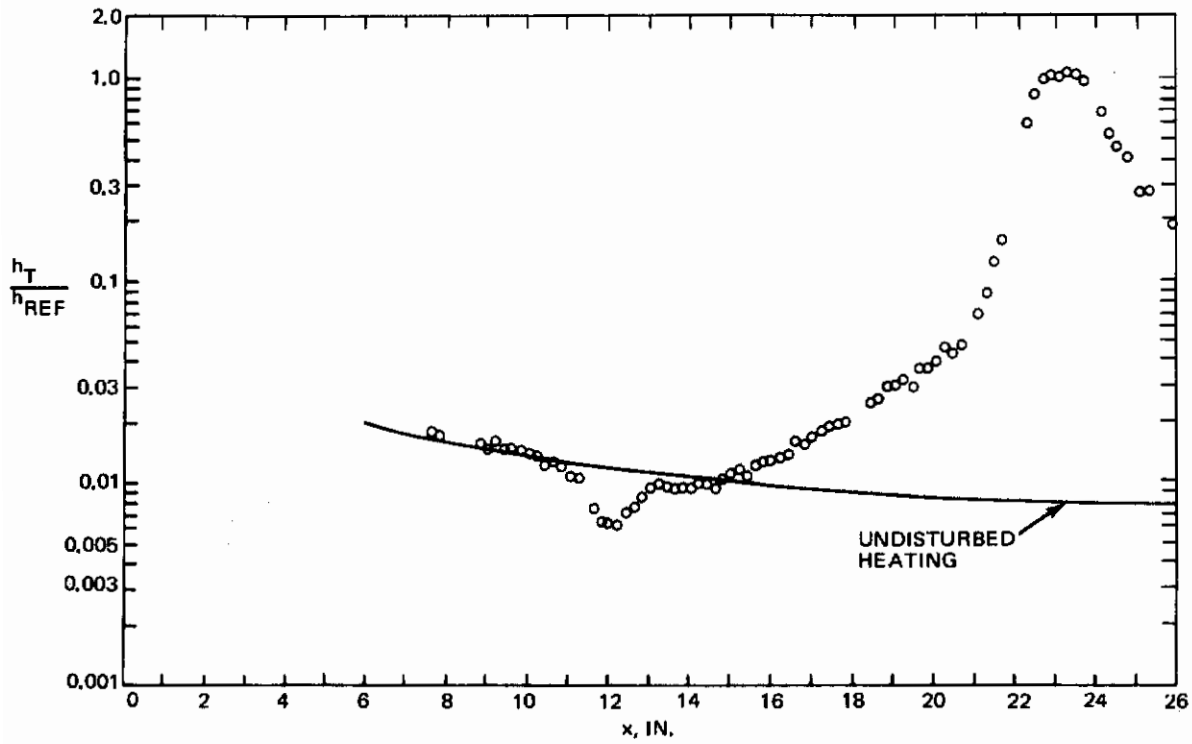

a. HEAT TRANSFER

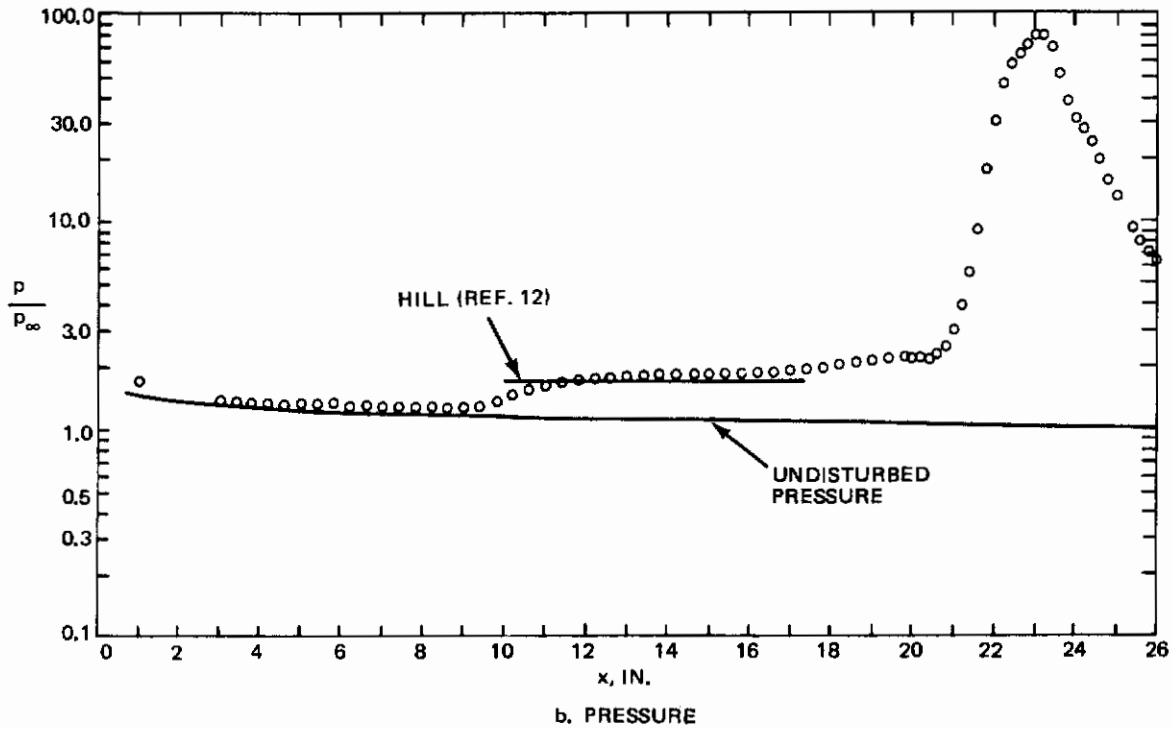

b. PRESSURE

Fig. 37 Heating and Pressure Distributions on Sharp Plate Caused by 15° Wedge Shock; p_o = 850 psia, x_i = 22 in. (Groups 218 & 275)

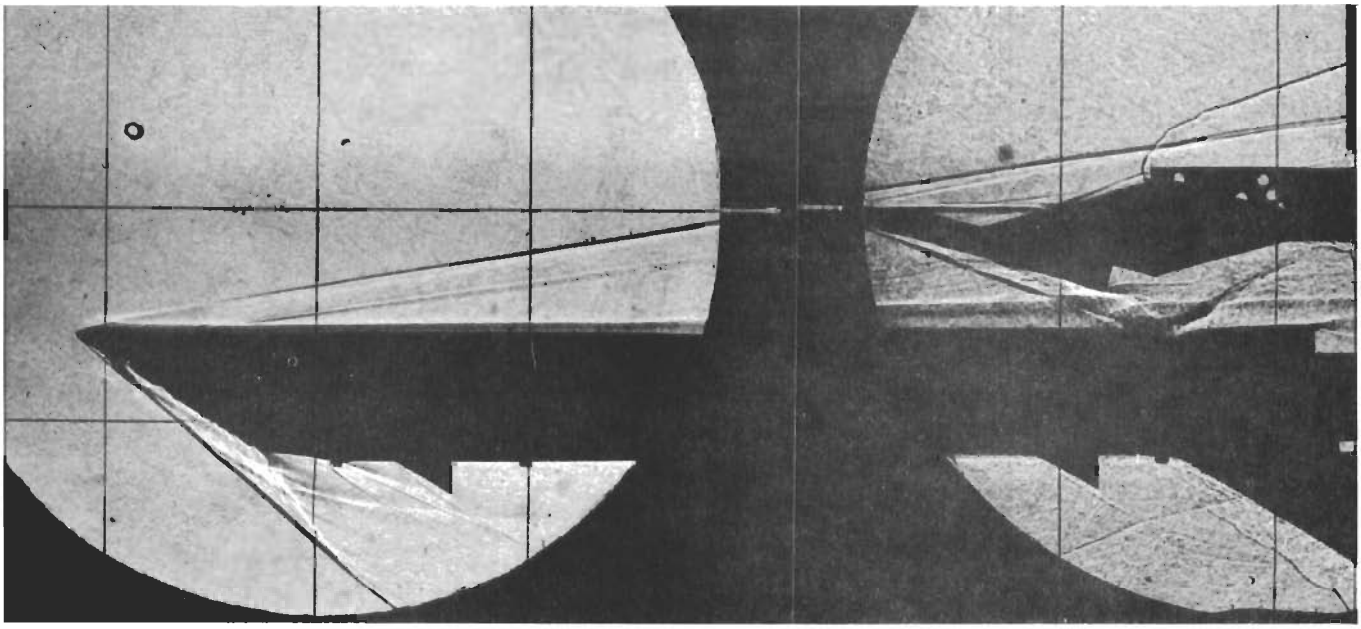

a. SHADOWGRAPHS

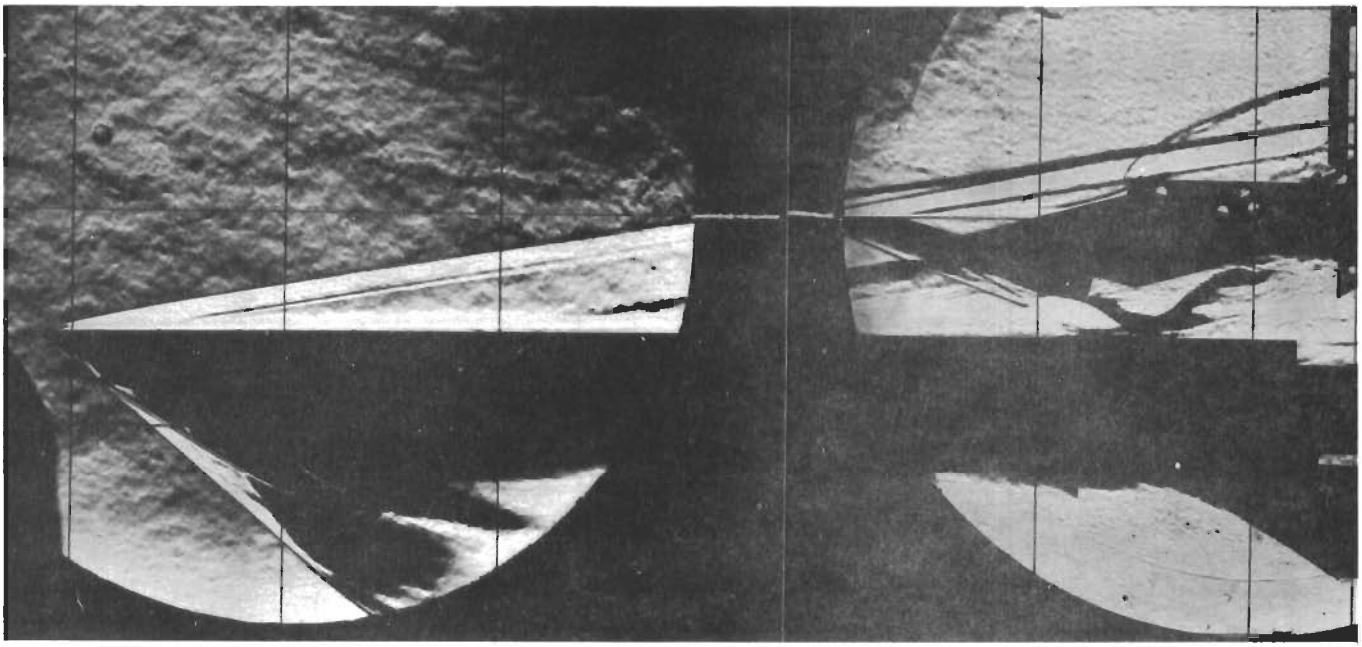

b. SCHLIERENS

Fig. 38 Shadowgraph and Schlieren Photographs of Interaction Caused By 15^{o} Wedge Shock; p_o = 850 psia, x_i = 22 in. (Groups 218 & 275)

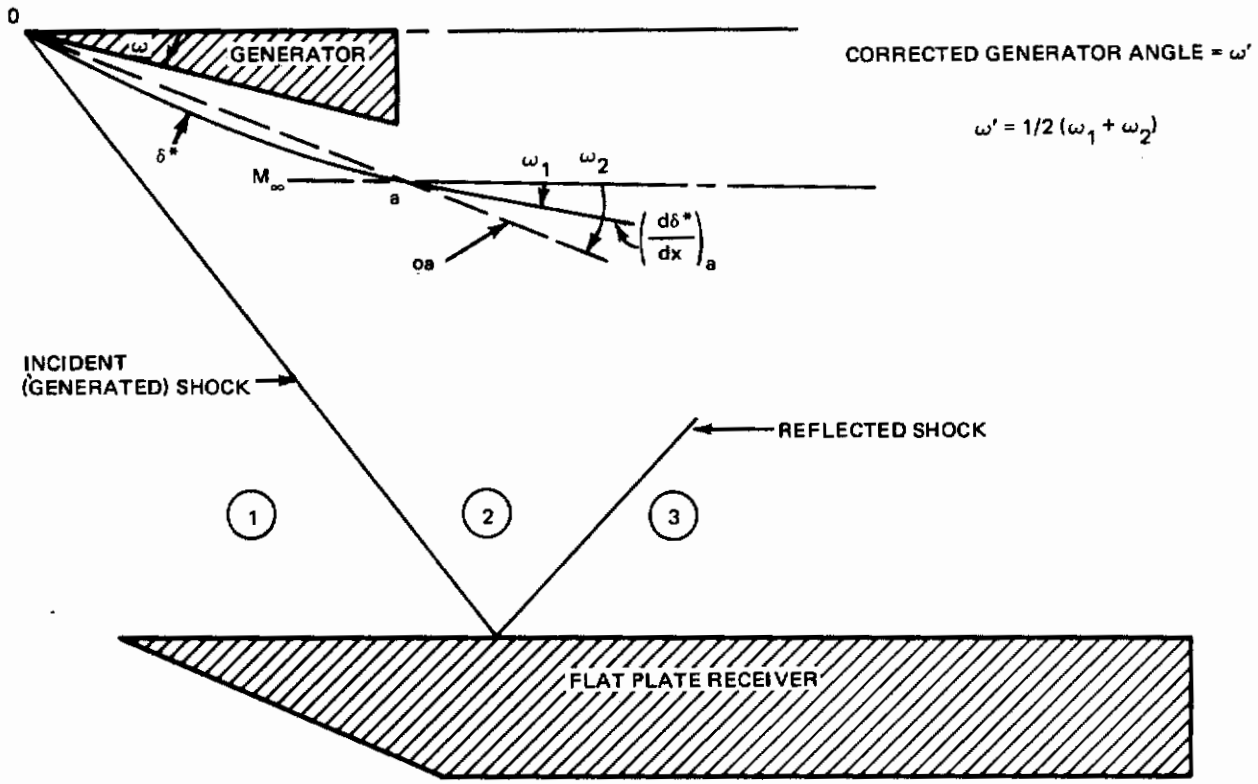

Fig. 39 Boundary Layer Correction for Wedge and Cone Generator Shock Strength Calculations

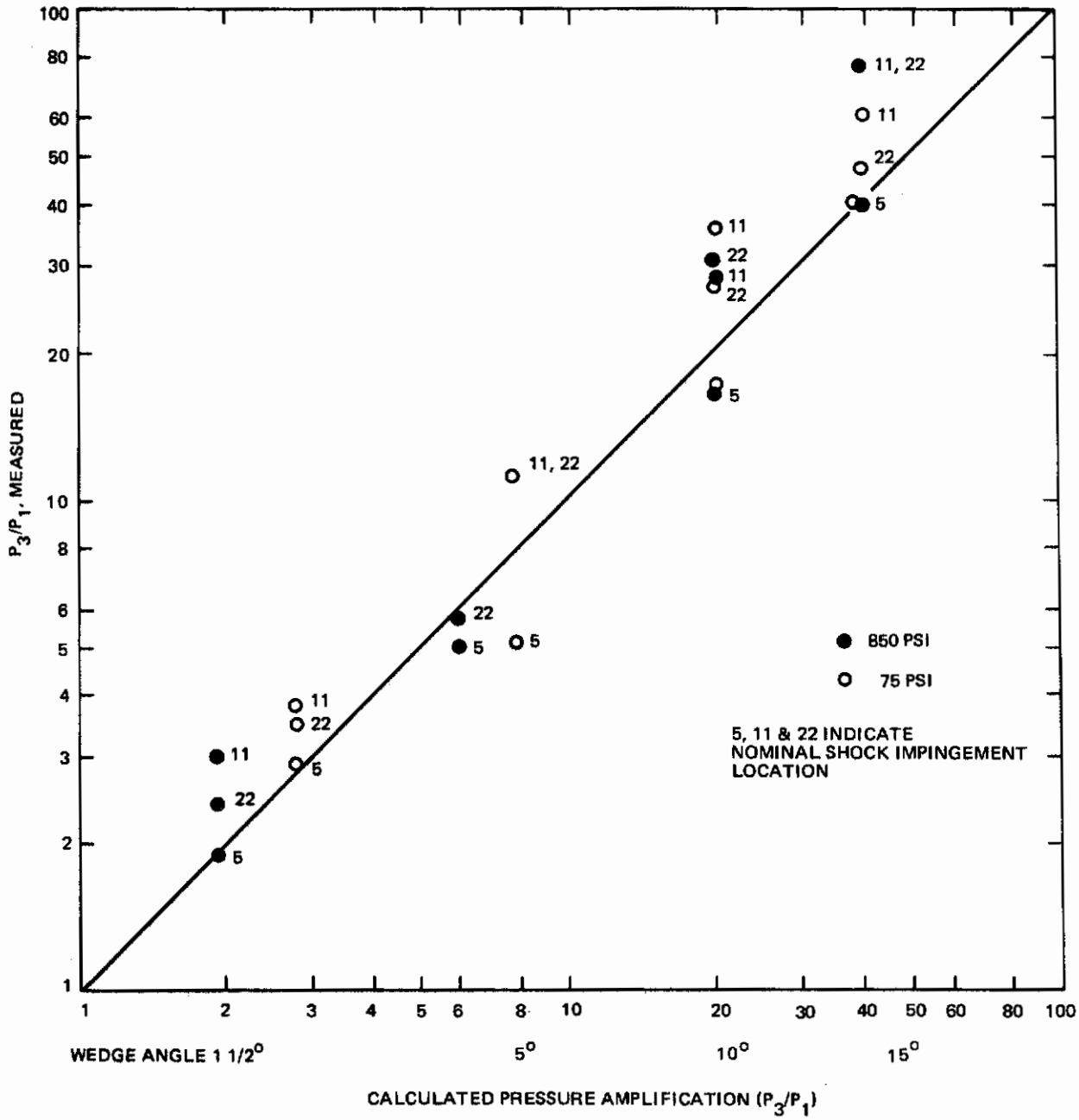

Fig. 40 Pressure Amplification for the Wedge Generators and the Sharp Flat Plate (No Trip)

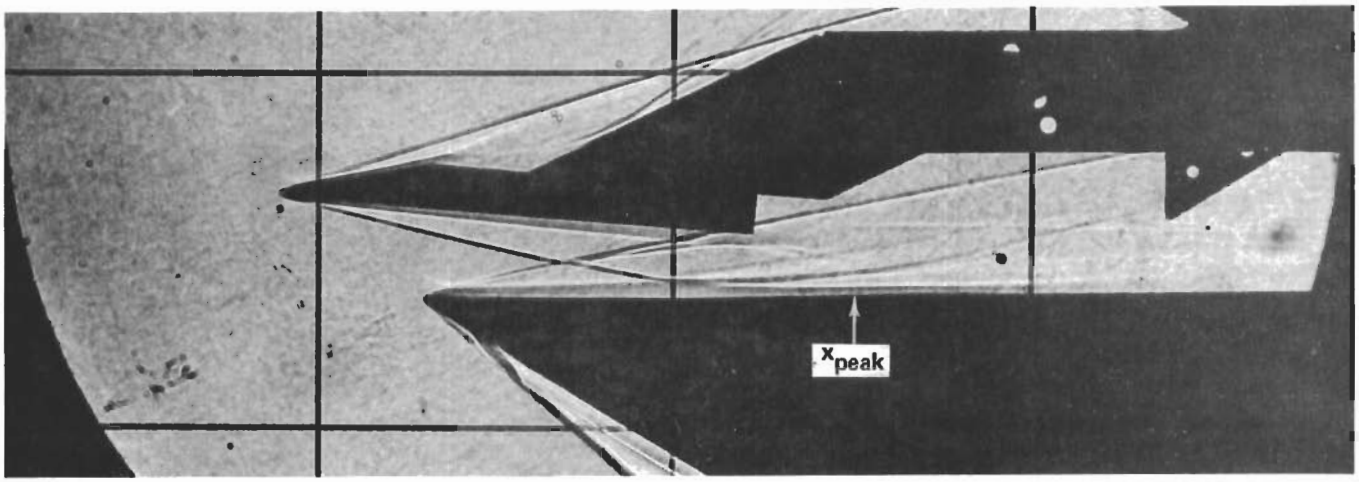

Fig. 41 5^{o} Wedge, x_i = 5" p_o = 75 psia (Group 94)

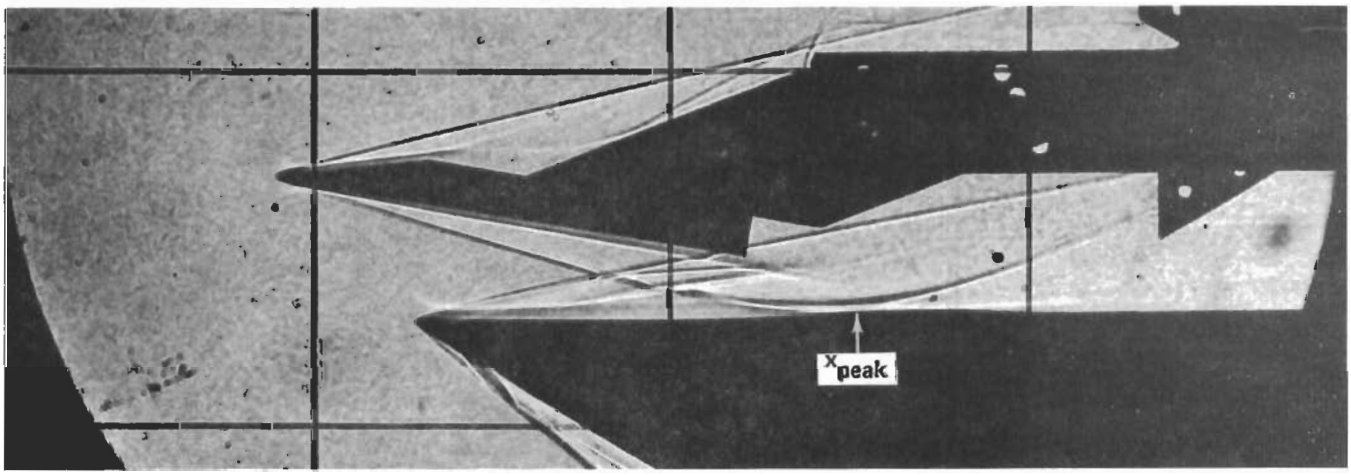

Fig. 42 10^{o} Wedge x_i = 5" p_o = 75 psia (Group 95)

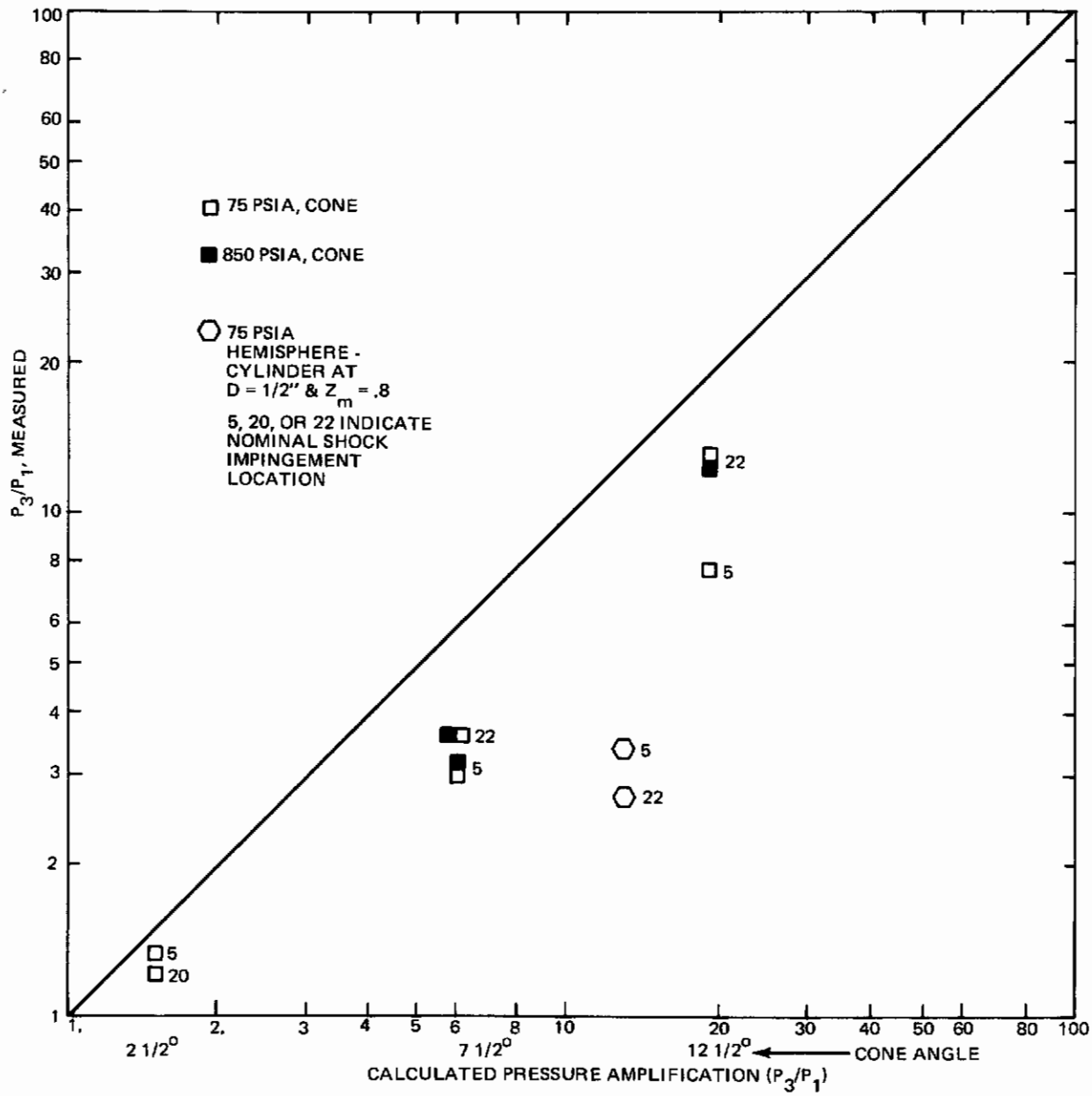

Fig. 43 Pressure Amplification for Cone and Hemisphere-Cylinder Generators Sharp Flat Plate (No Trip)

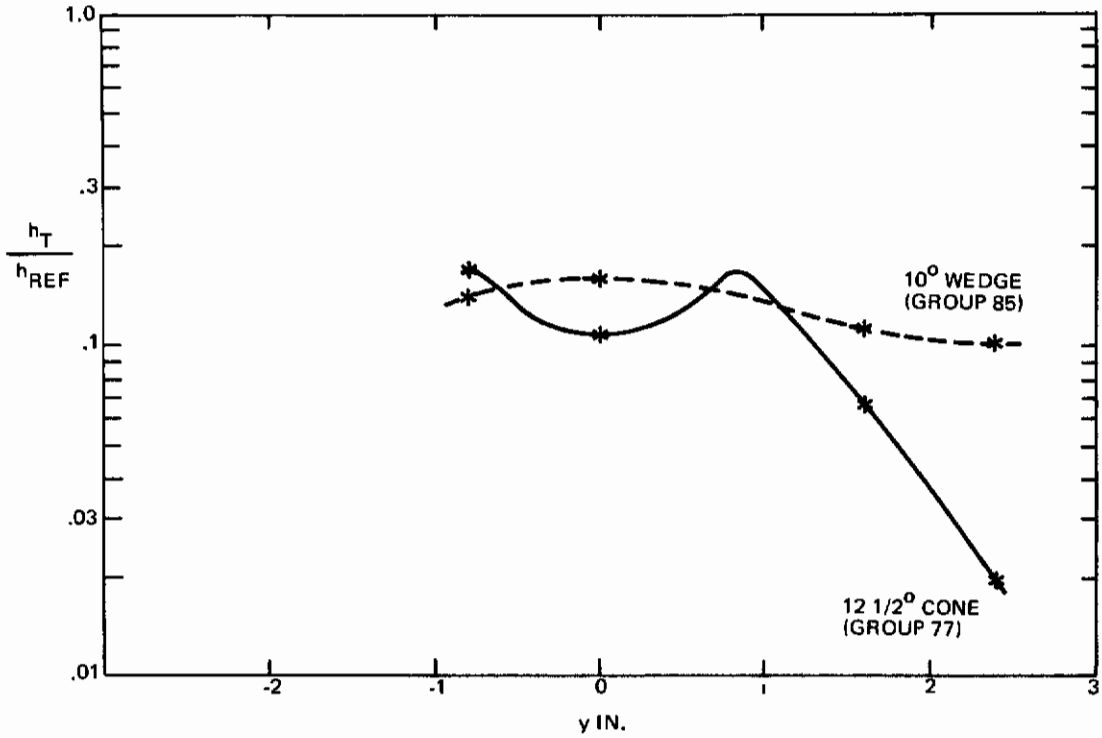

a) HEAT TRANSFER

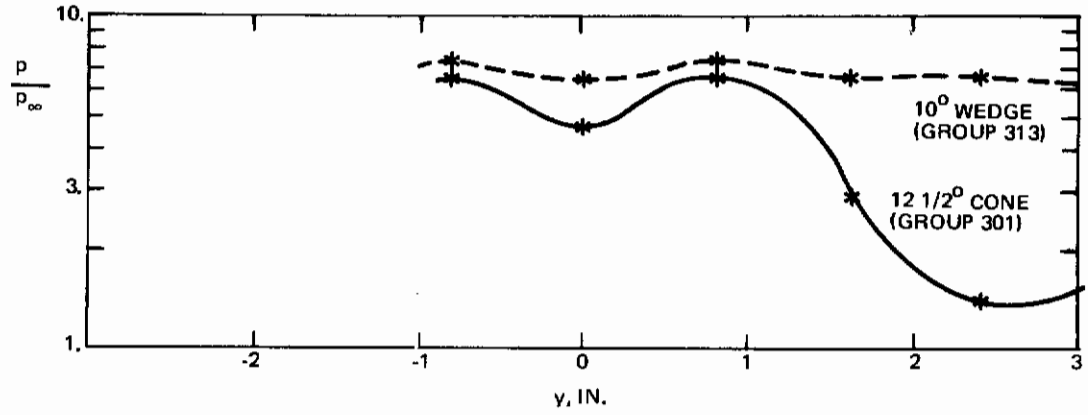

b) PRESSURE

Fig. 44 Lateral Heat Transfer and Pressure Distributions for p_o = 200 psia & Nominal Impingement Location at 22" on Sharp Flat Plate (No Trip)

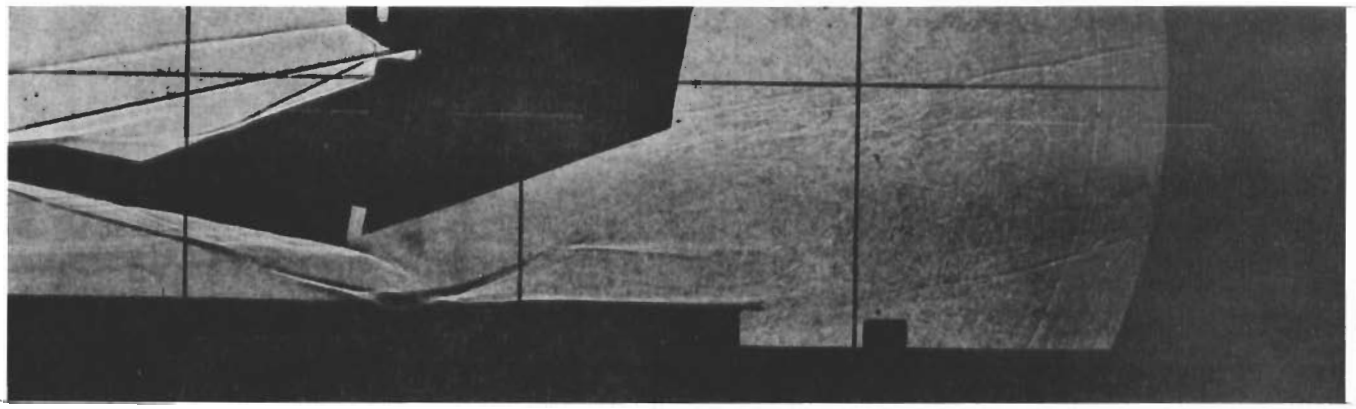

a. GROUP 85, 10° WEDGE

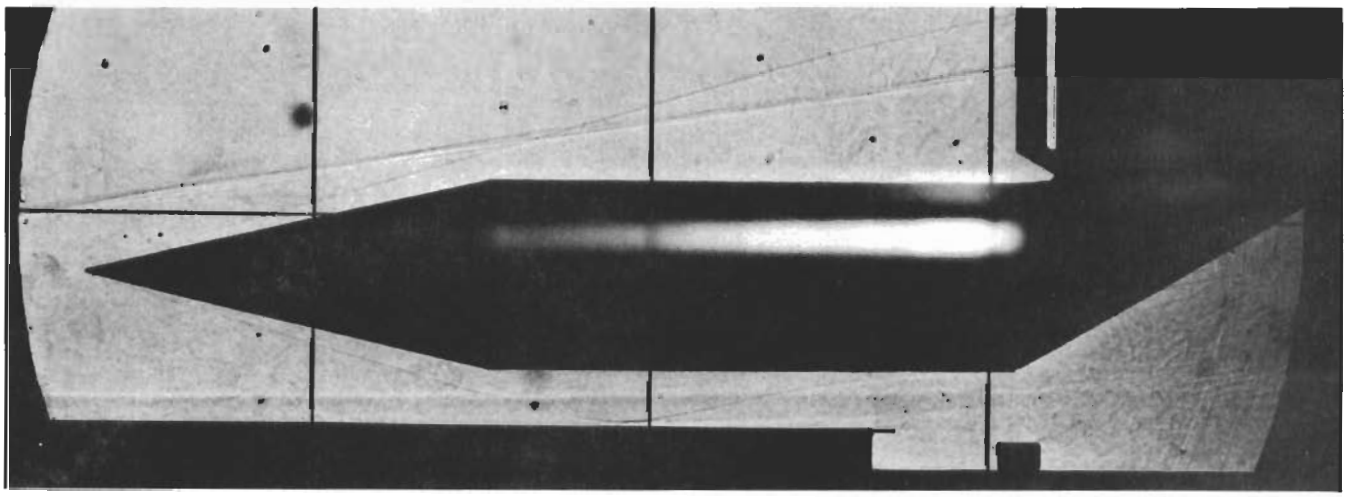

b. GROUP 77, 12° CONE

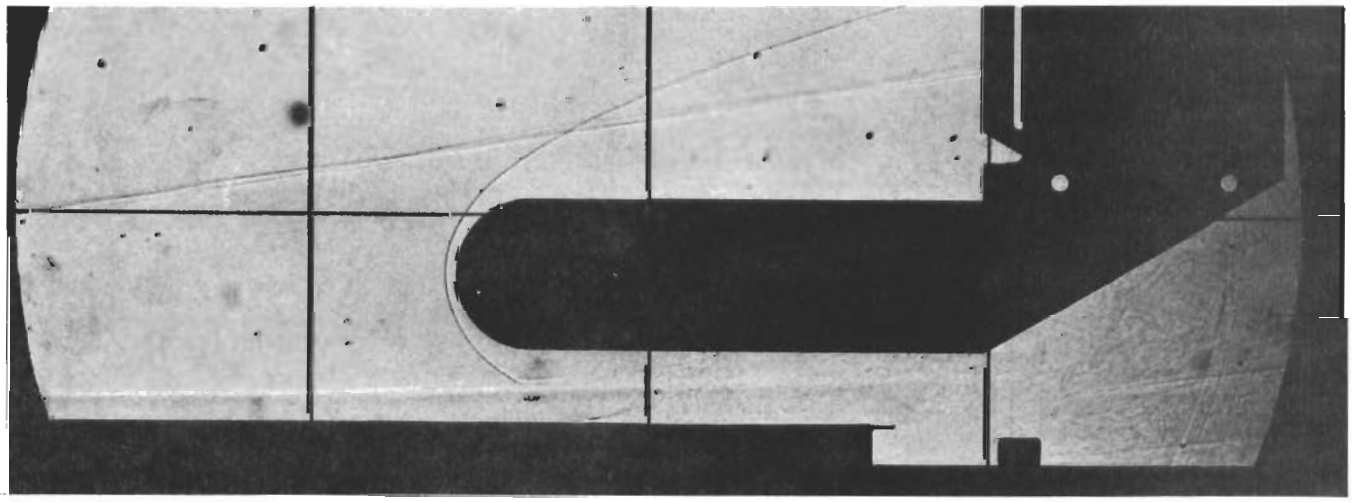

c. GROUP 82, 2" DIA HEMISPHERE - CYL, Z_m = 1"

Fig. 45 Interactions at x_i = 22", p_o = 200 psia

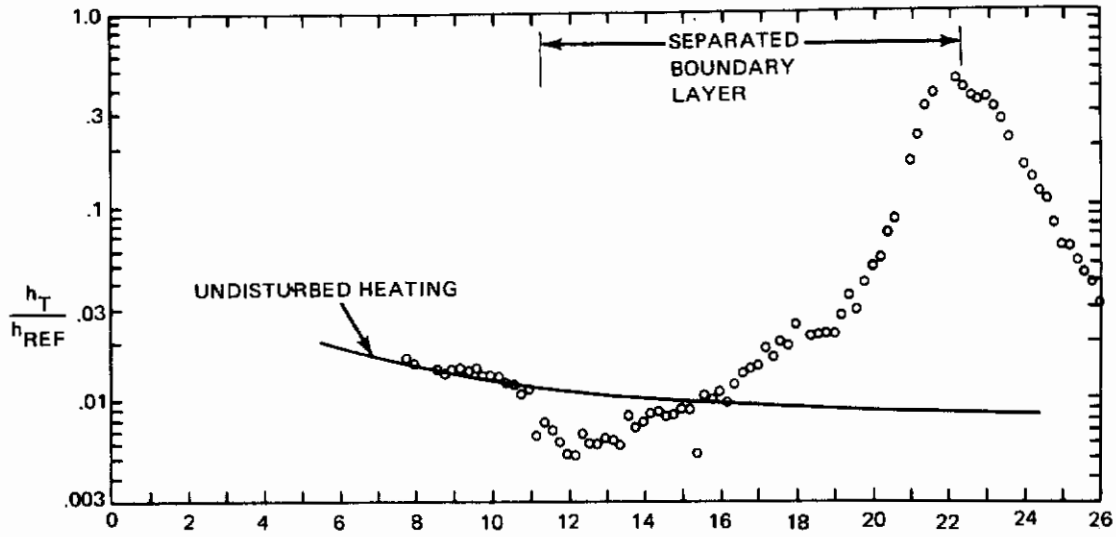

a. 10° WEDGE

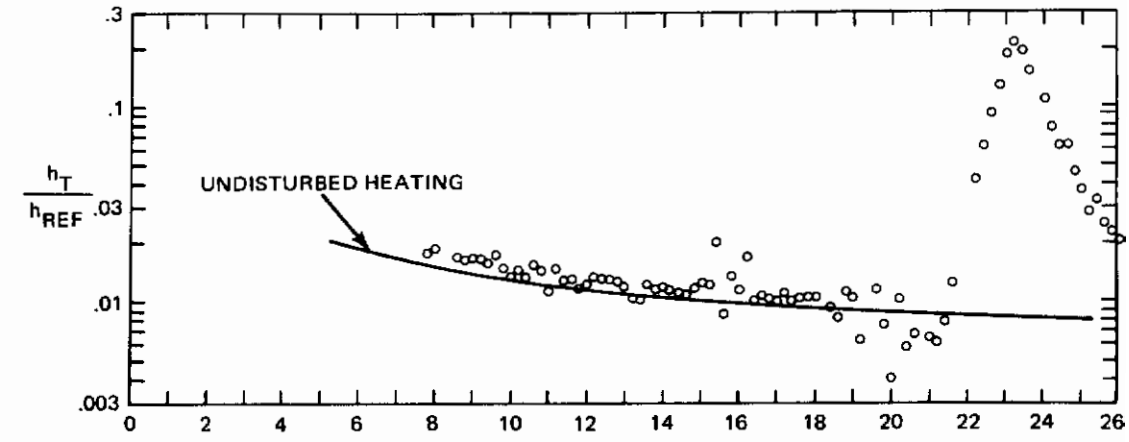

b. 12½° CONE (GROUP 77)

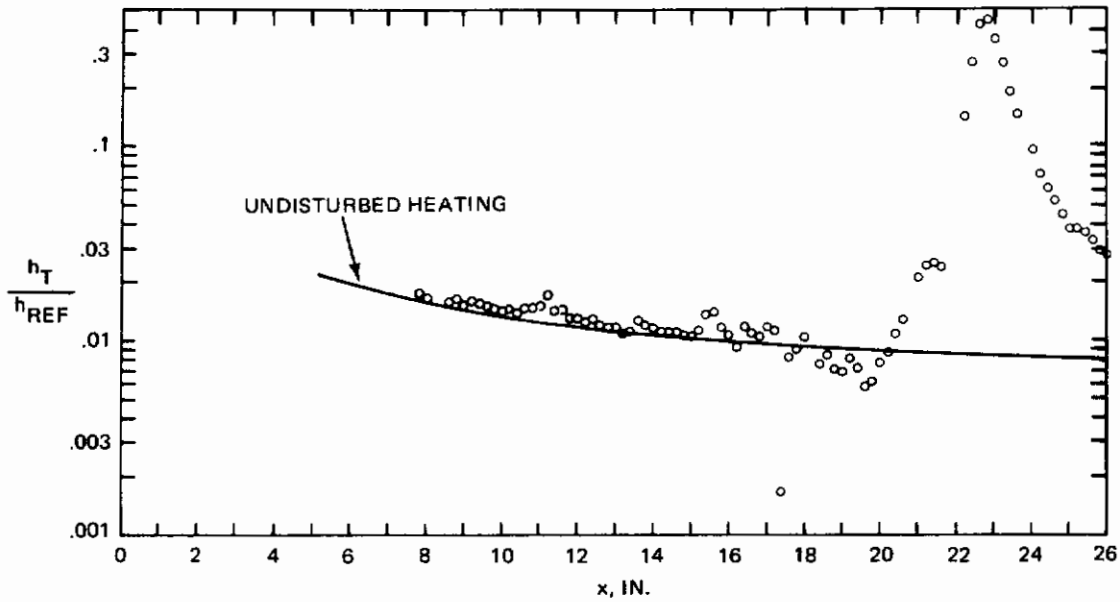

c. 2" DIA HEMISPHERE CYLINDER AT Z_m = 1.0" (GROUP 82)

Fig. 46 Interaction at x_i = 22", p_o = 200 psia

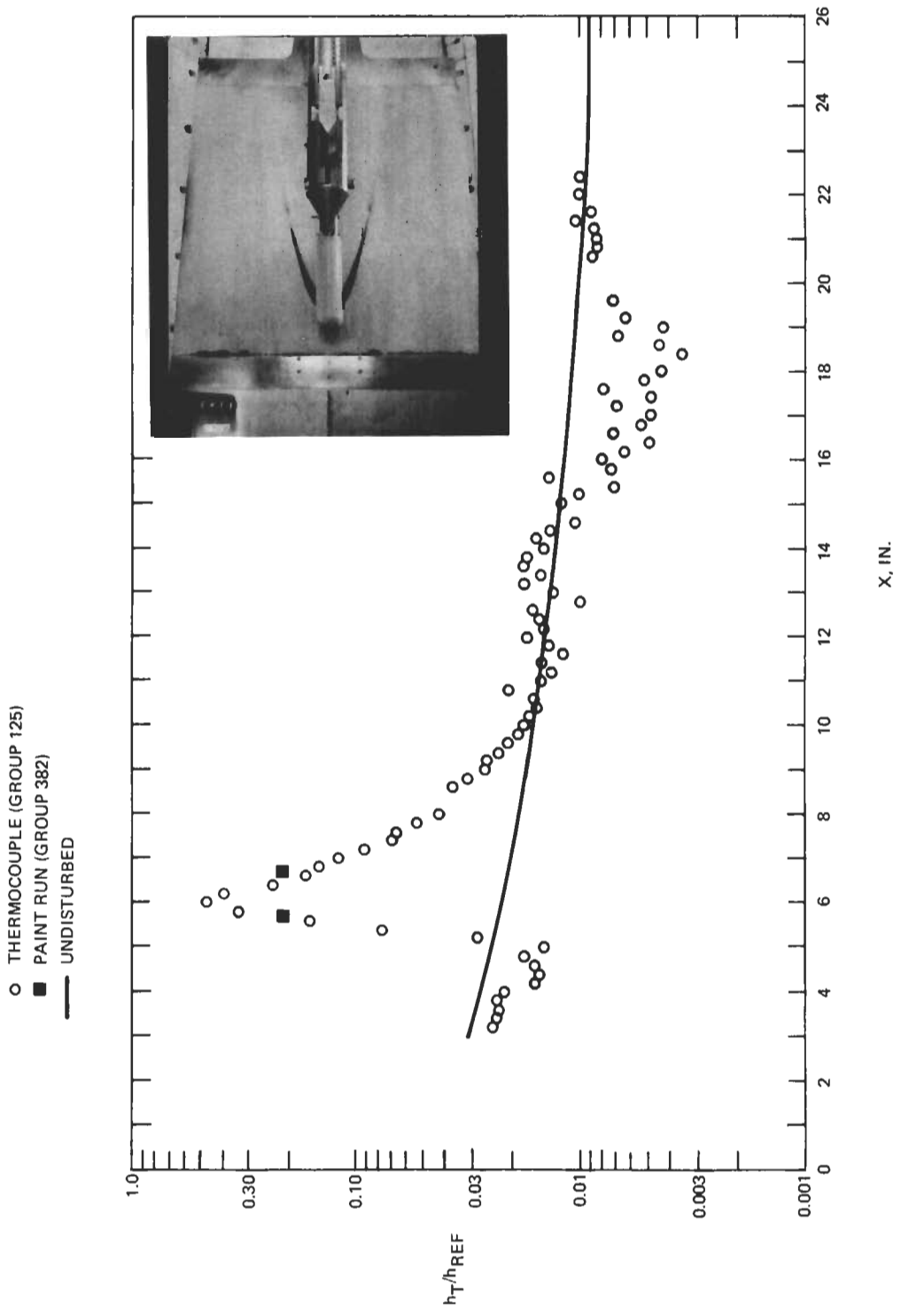

Fig. 47 Heating Distribution on Sharp L.E. Plate Caused by 2.0 inch Hemisphere-Cylinder, P_o = 850 psia, x_i = 5 in. (Groups 125 and 382)

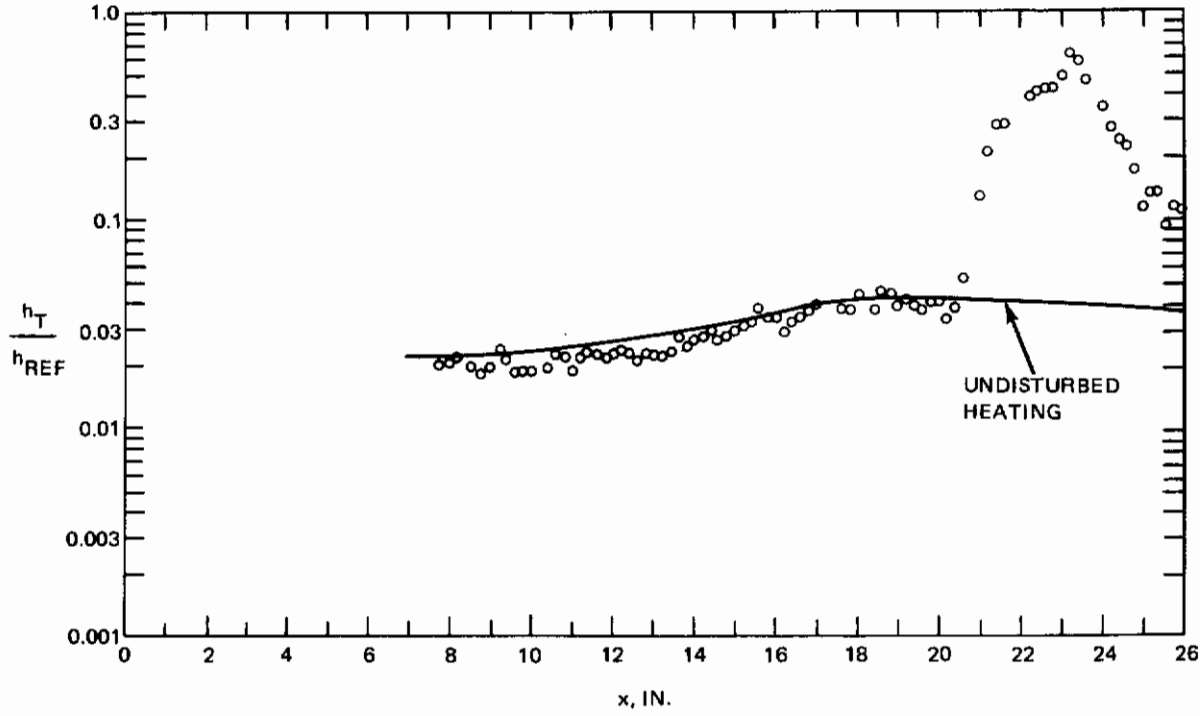

A. HEAT TRANSFER

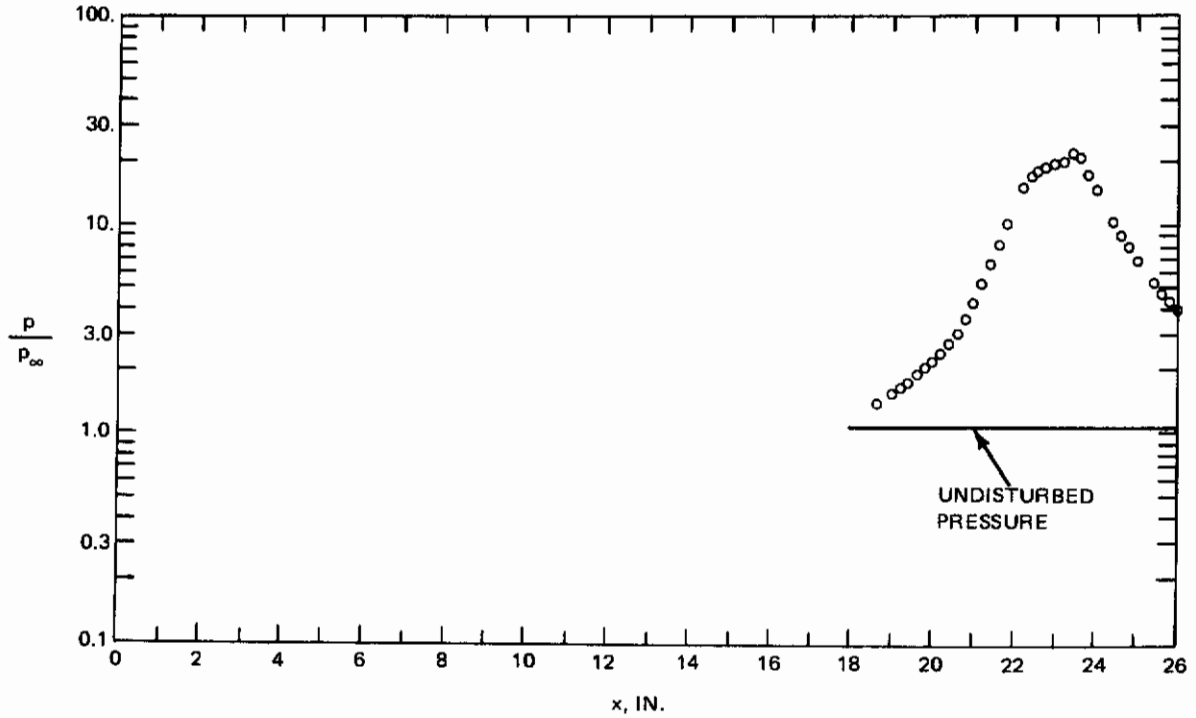

b. PRESSURE

Fig. 48 Heating and Pressure Distributions on Plate with BL Trip, Caused by 10° Wedge Shock; p_o = 850 psia, x_i = 22 in. (Groups 8 & 250)

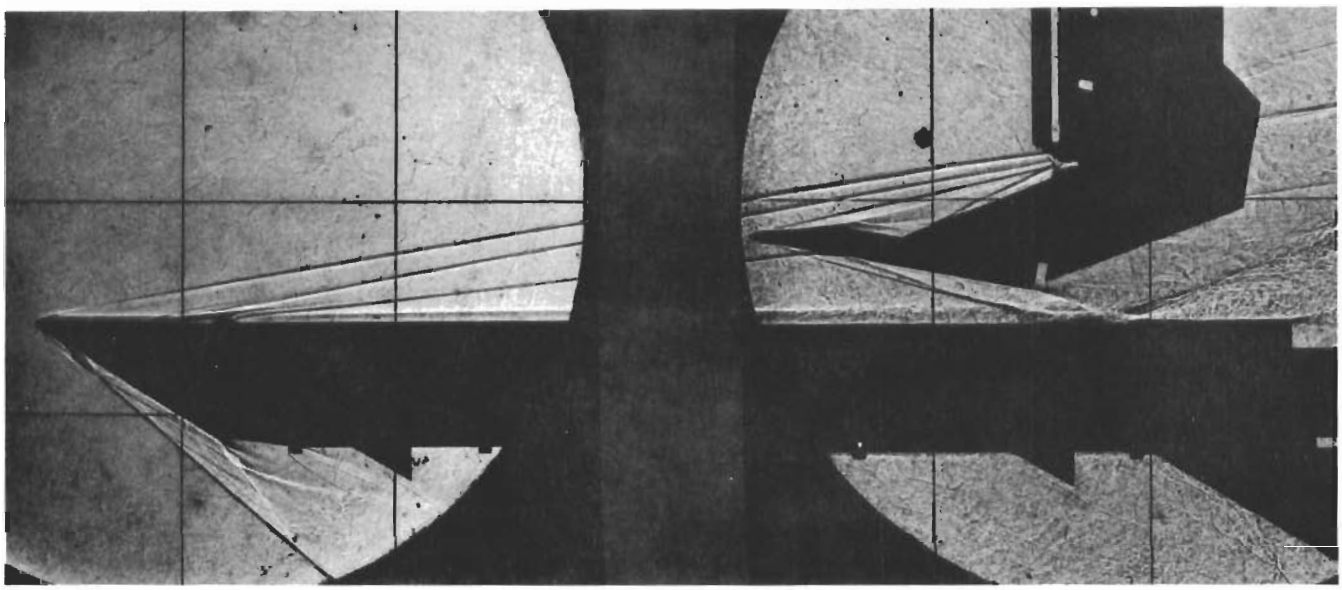

a. SHADOWGRAPHS

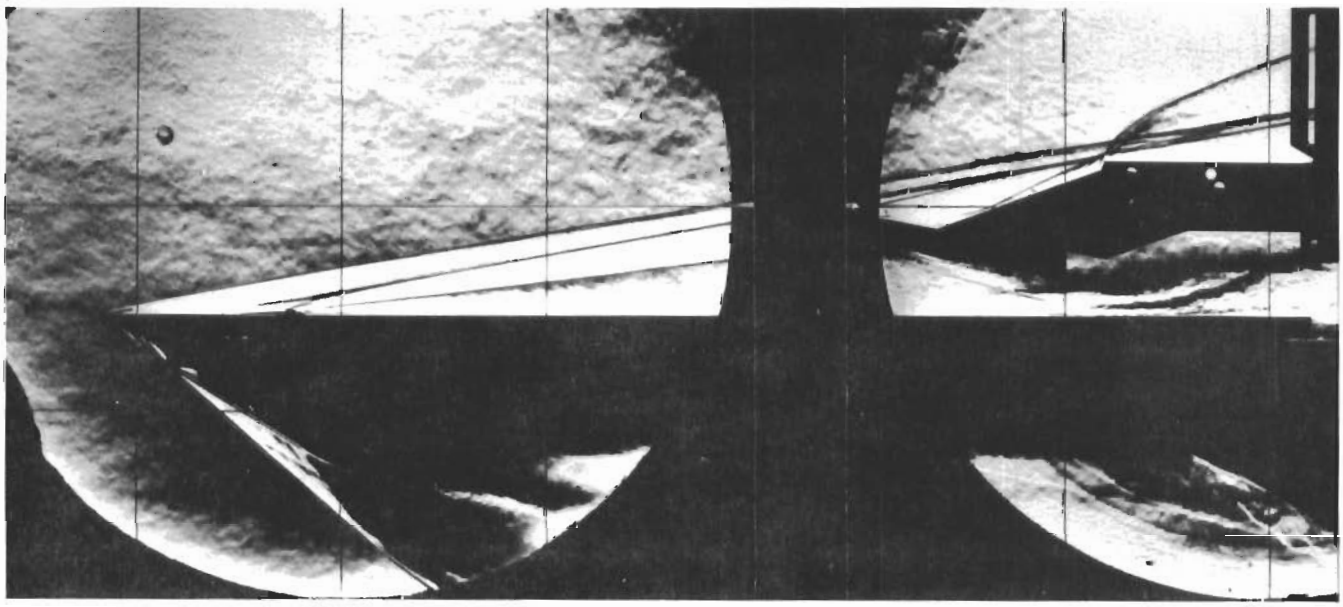

b. SCHLIERENS

Fig. 49 Shadowgraph and Schlieren Photographs of 10^{o} Wedge Shock Interacting with Tripped Boundary Layer, p_o = 850 psia, x_i = 22 in. (Groups 8 & 250)

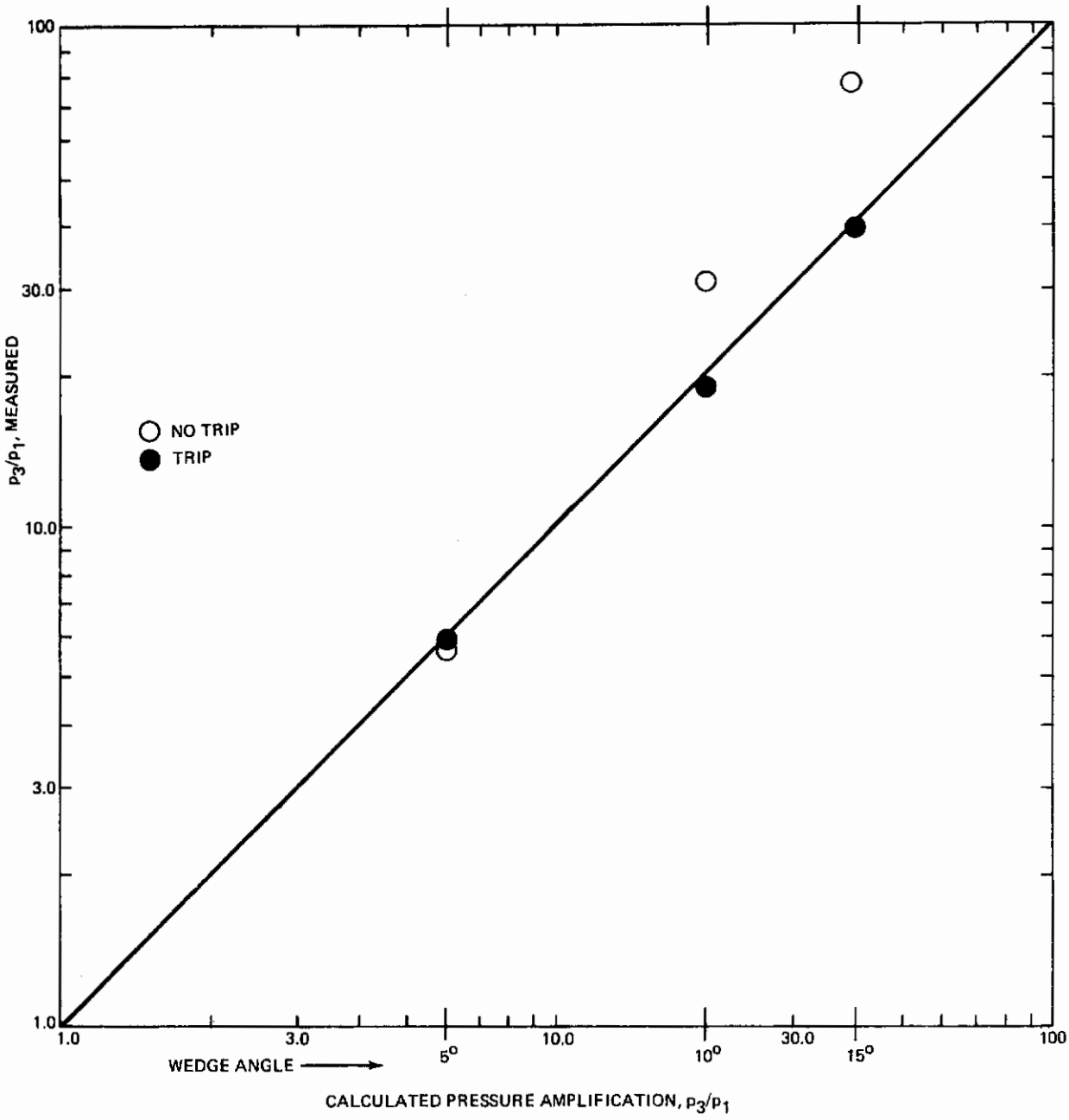

Fig. 50 Comparison of Measured Pressure Ratios for Wedge Generators with Tripped and Untripped Boundary Layers at p_0 = 850 psia and x_i = 22 in.

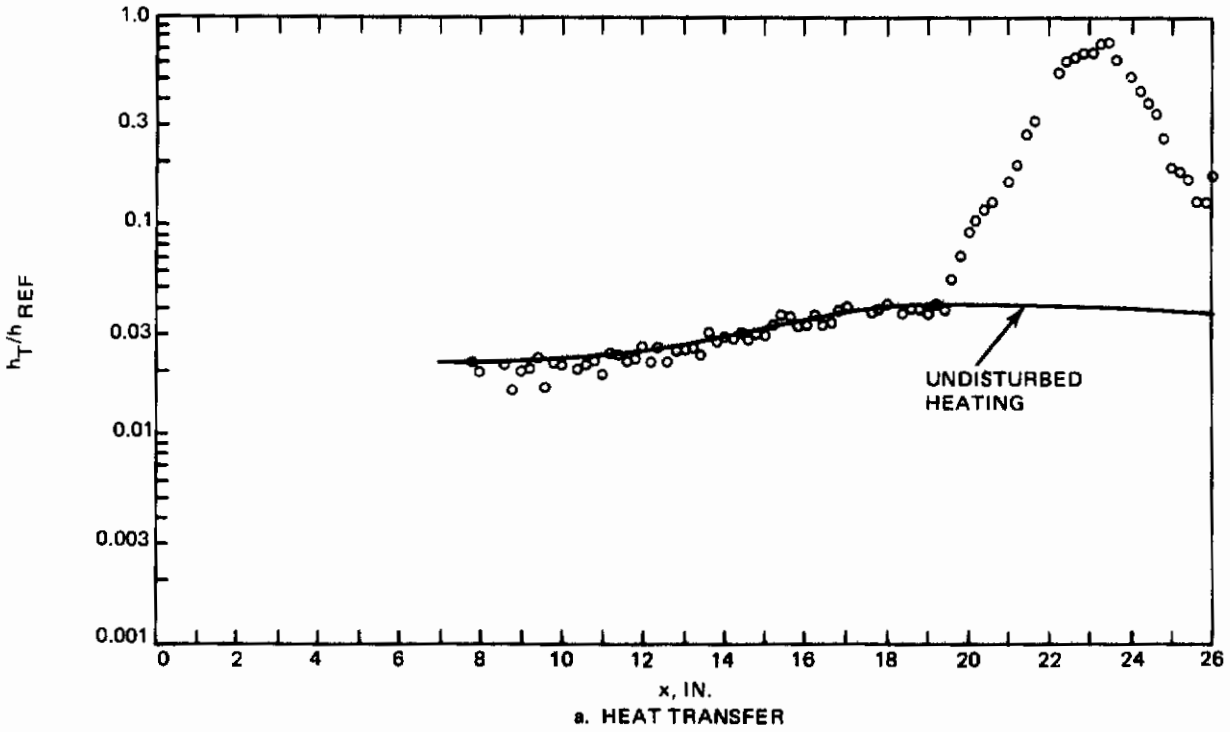

a. HEAT TRANSFER

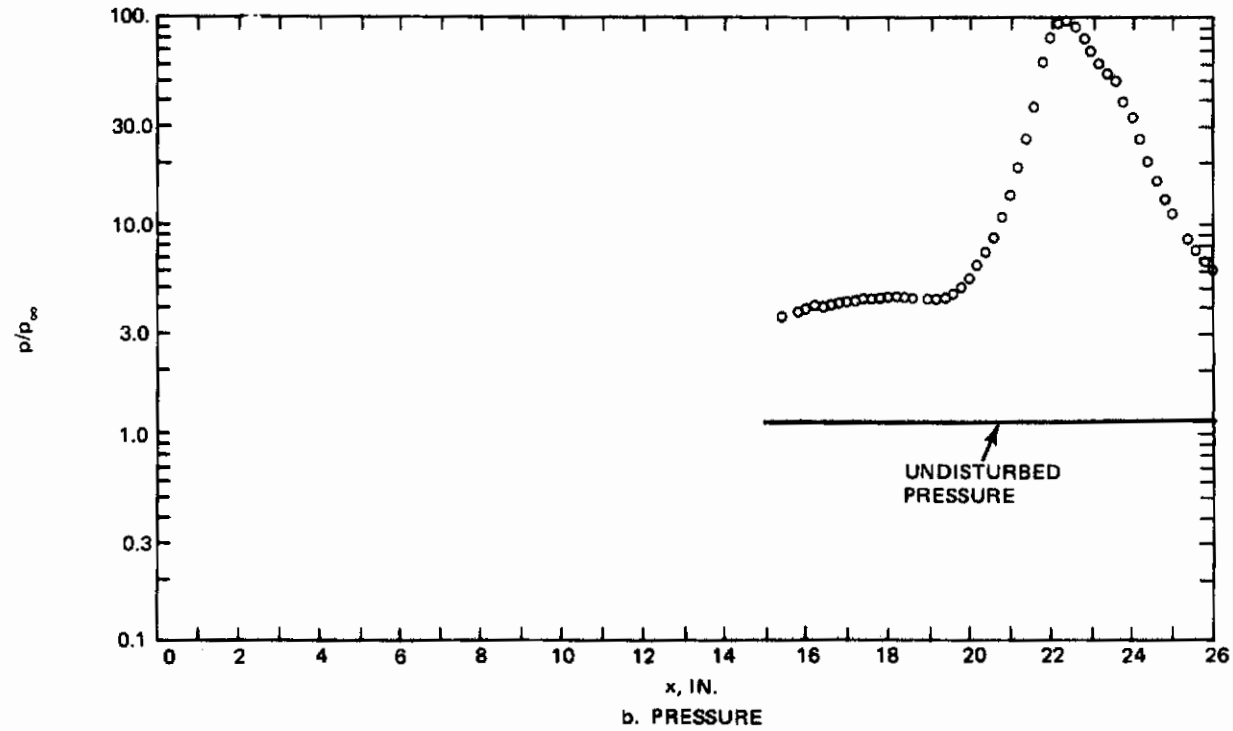

b. PRESSURE

Fig. 51 Heating and Pressure Distributions, on Plate with BL Trip, Caused by 15° Wedge Shock; p_o = 850 psia, x_i = 22 in. (Groups 6 & 251)

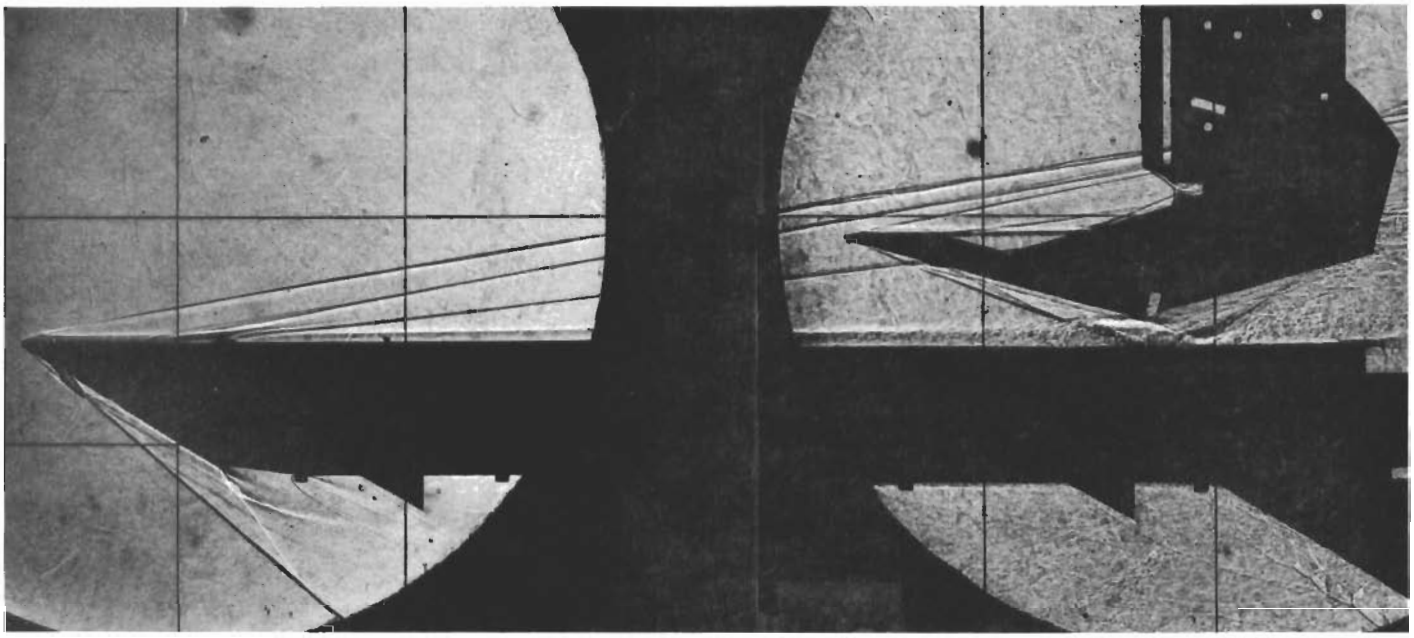

a. SHADOWGRAPHS

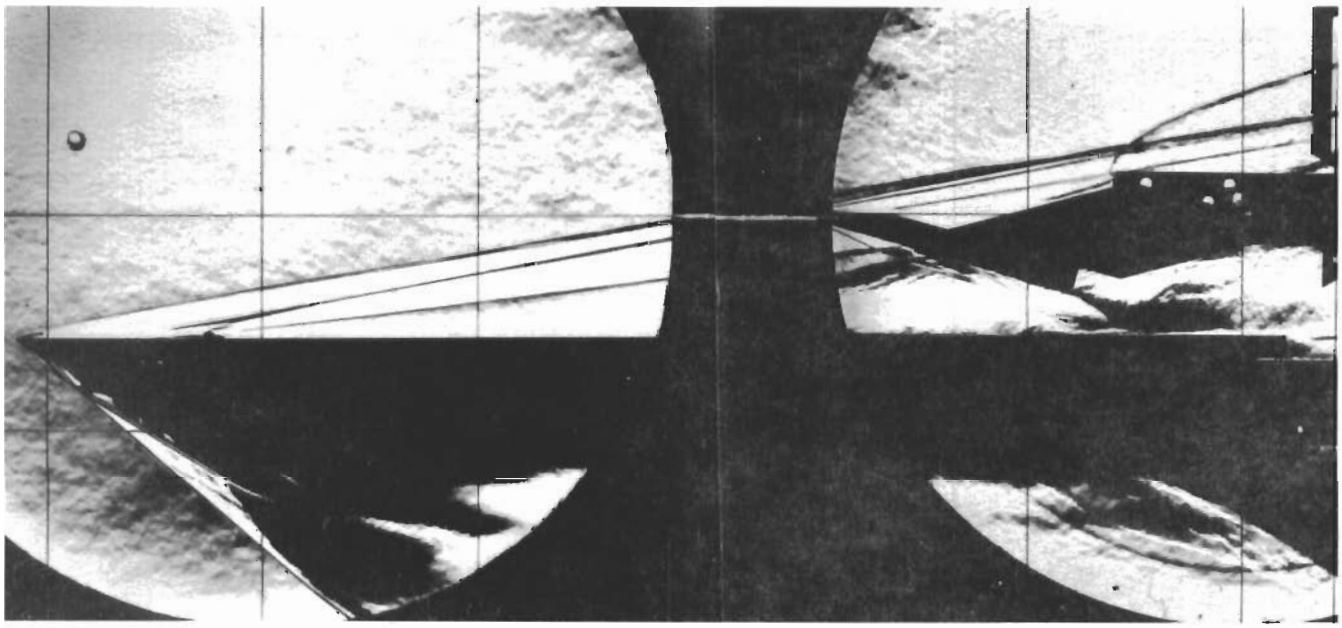

b. SCHLIERENS

Fig. 52 Shadowgraph and Schlieren Photographs of 15° Wedge Shock Interacting with Tripped Boundary Layer; p_o = 850 psia, x_i = 22 in. (Groups 6 & 251)

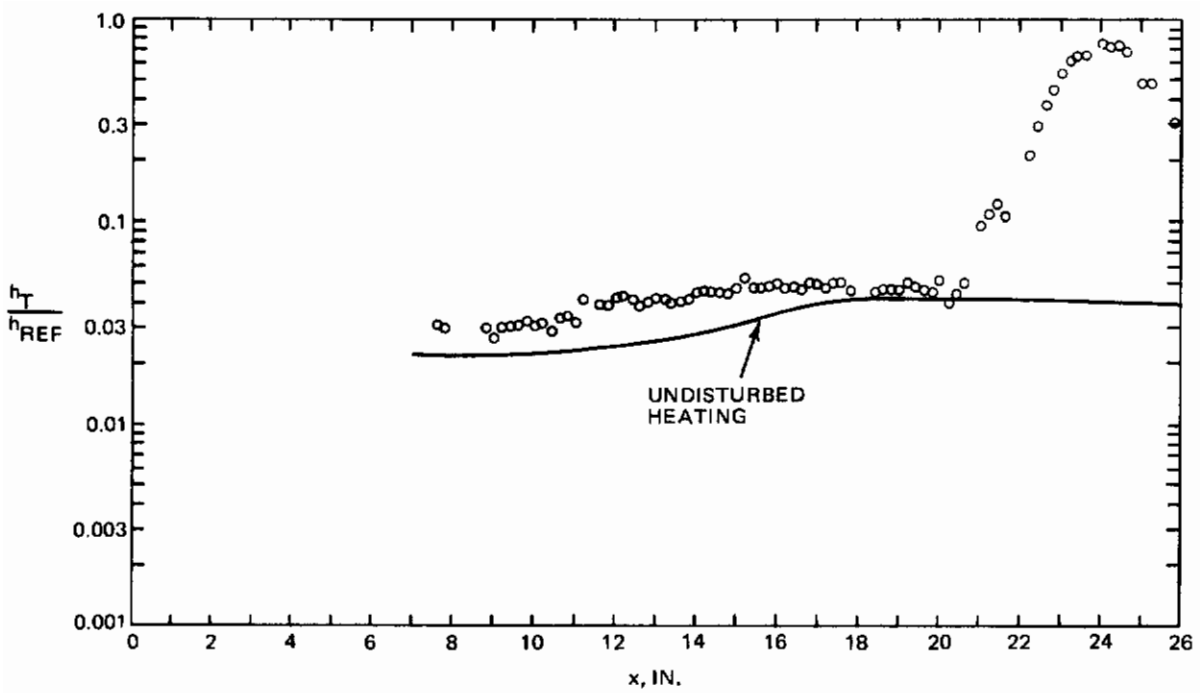

a. HEAT TRANSFER

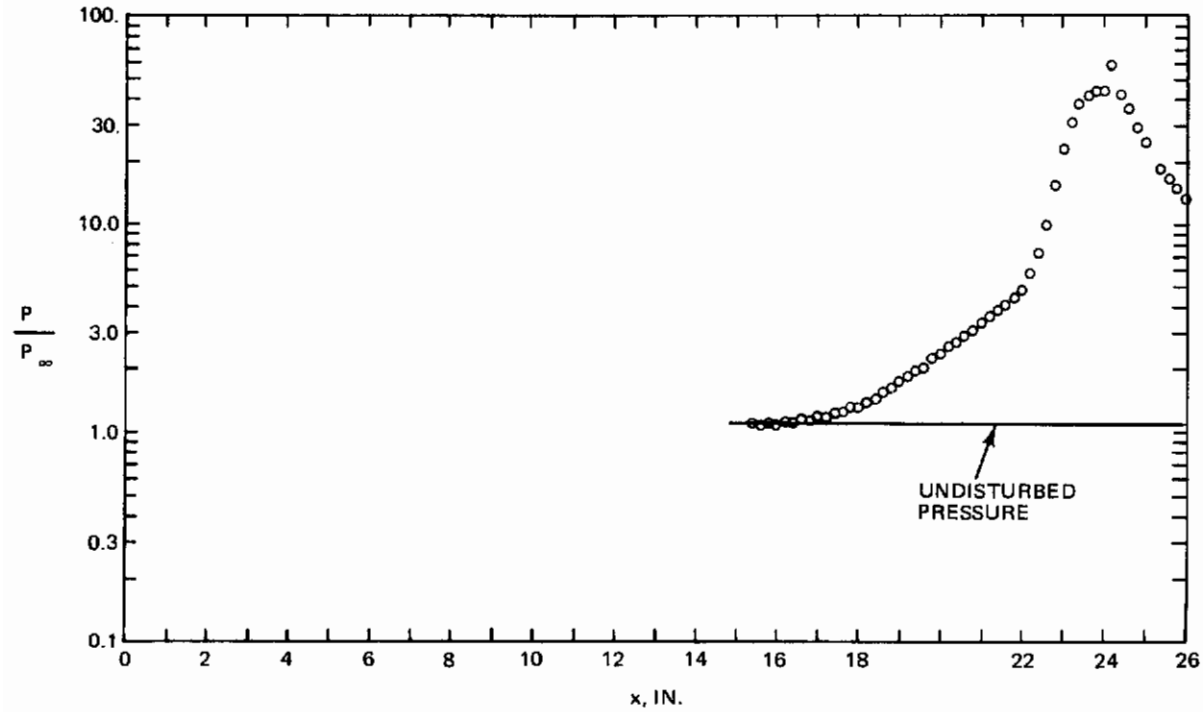

b. PRESSURE

Fig. 53 Heating and Pressure Distributions, on Plate with BL Trip, Caused by Raised 15° Wedge Shock; p_o = 850 psia, x_i = 22 in. (Groups 210 & 259)

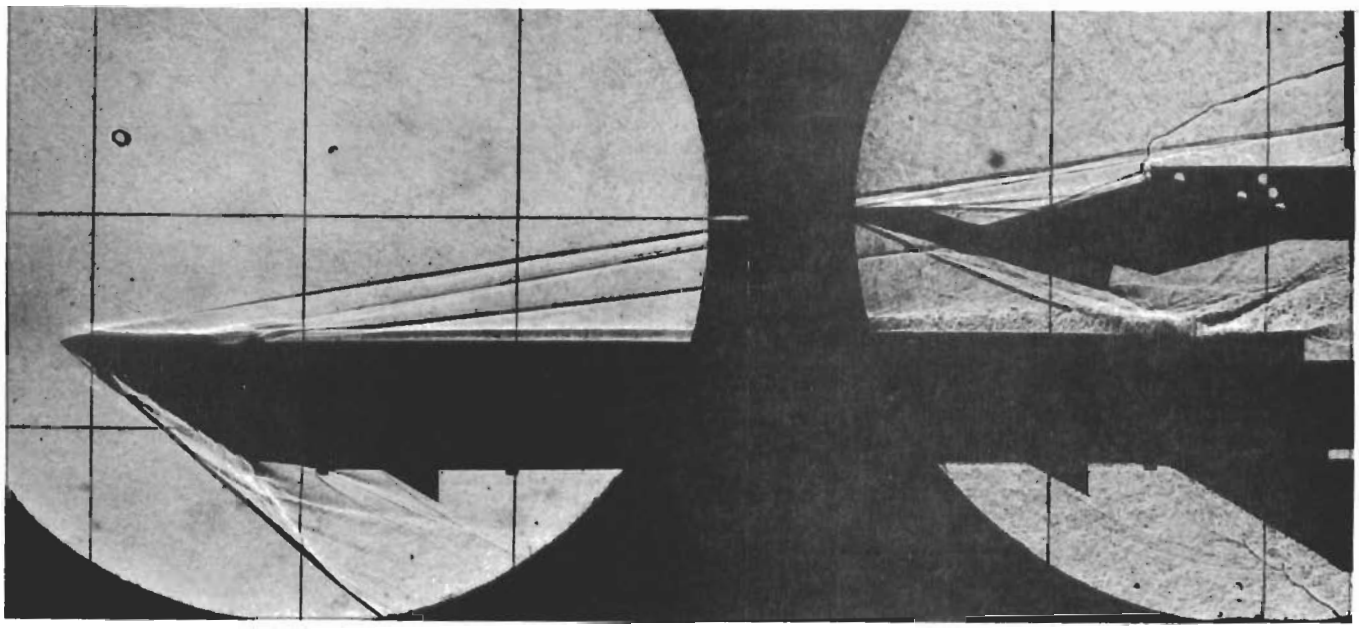

a. SHADOWGRAPHS

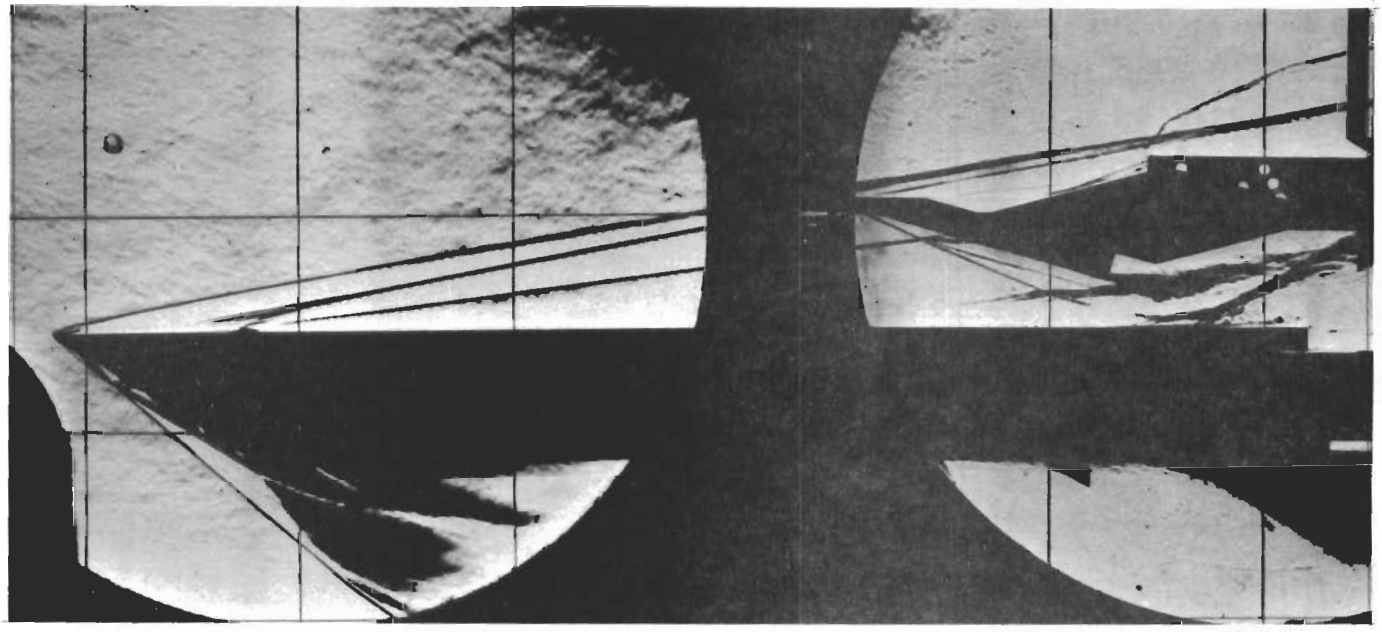

b. SCHLIERENS

Fig. 54 Shadowgraph and Schlieren Photographs of Raised 15° Wedge Shock Interacting with Tripped Boundary Layer; p_o = 850 psia x_i = 22 in. (Groups 210 & 259)

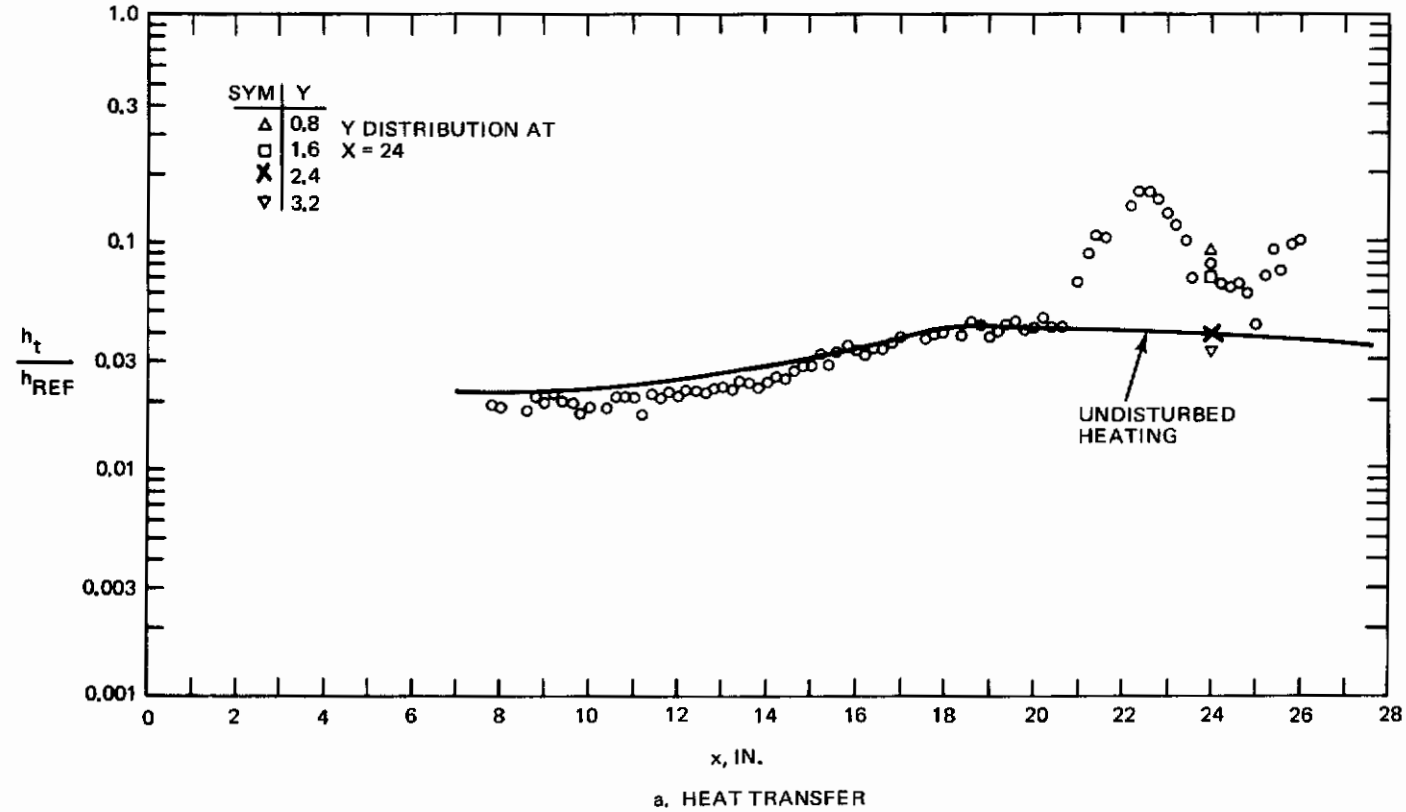

a. HEAT TRANSFER

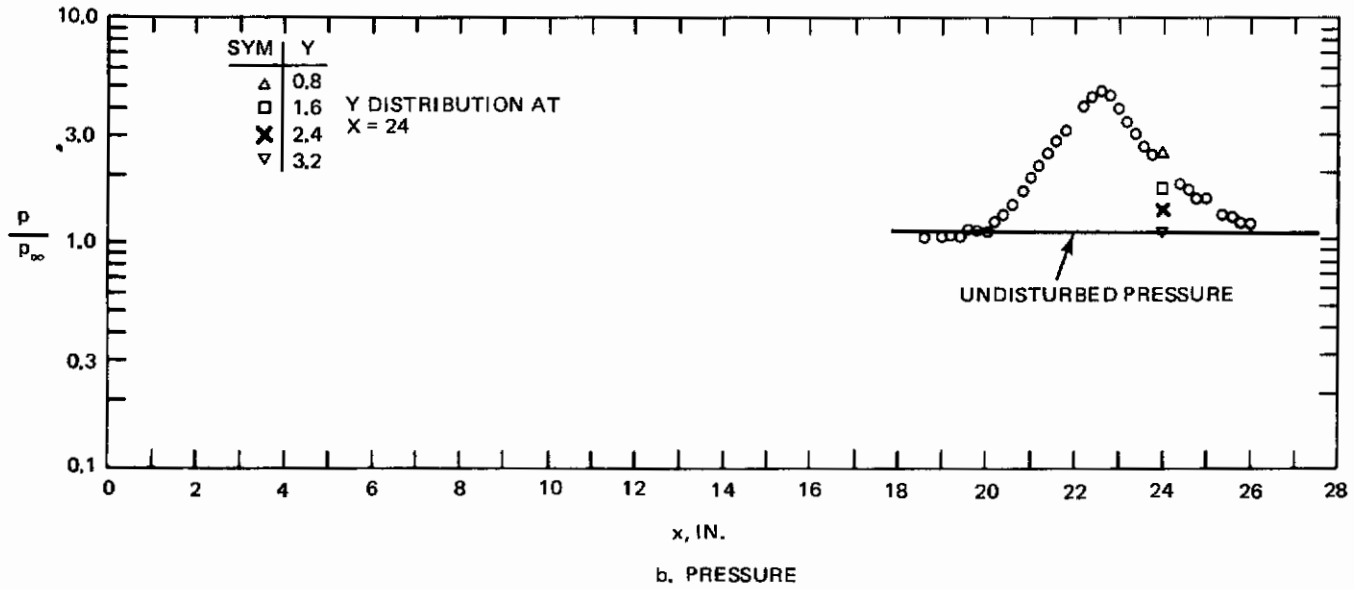

b. PRESSURE

Fig. 55 Heating and Pressure Distributions, on Plate with BL Trip, Caused by 7 1/2° Cone Shock; p_0 = 850 psia, x_i = 22 in. (Groups 19 & 248)

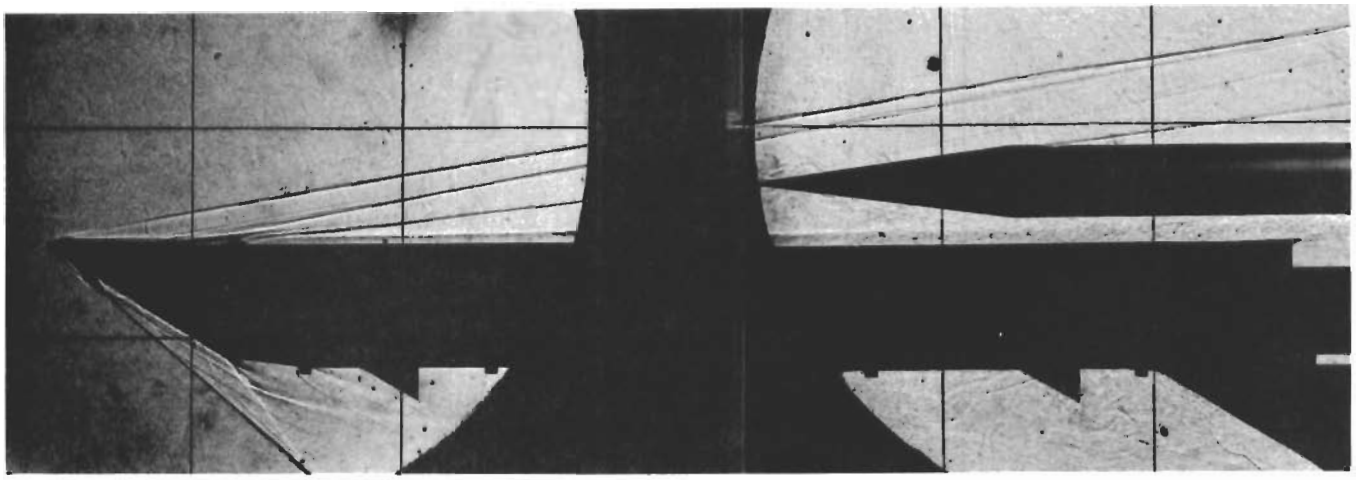

a. SHADOWGRAPHS

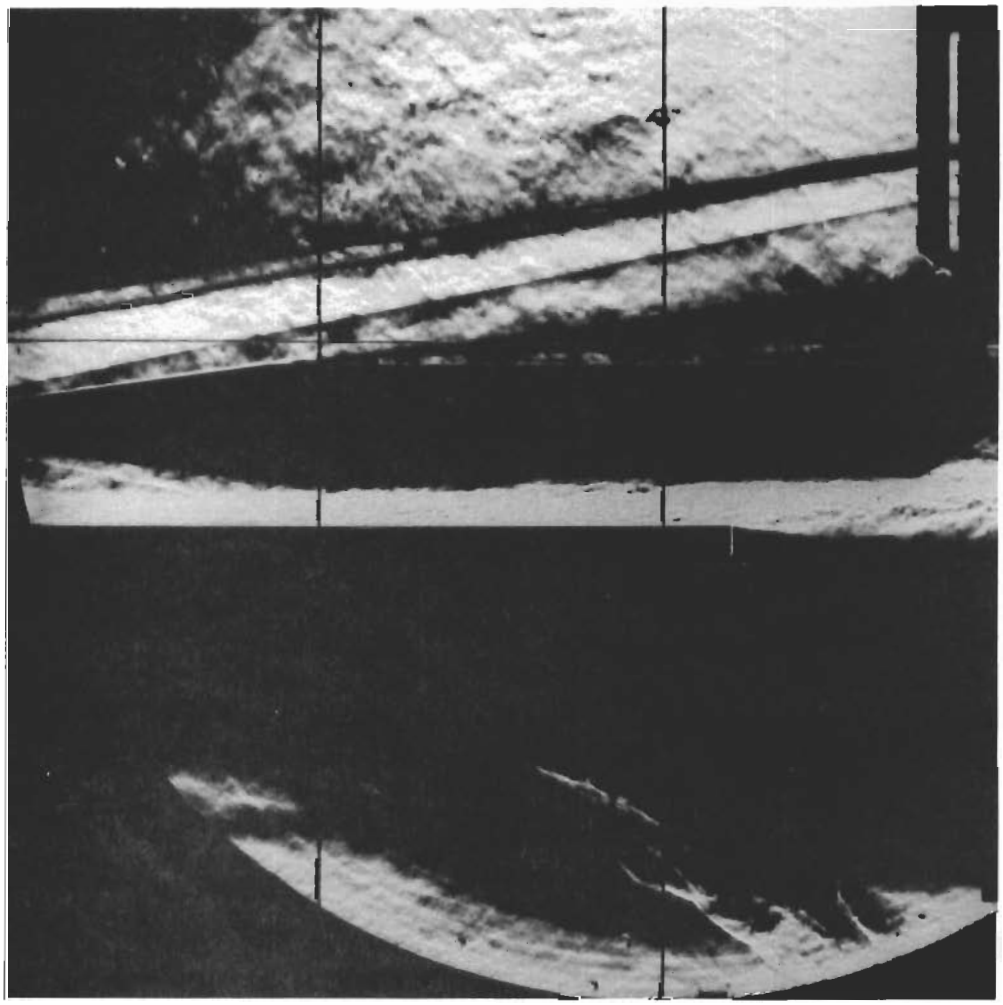

b. SCHLIEREN

Fig. 56 Shadowgraph and Schlieren Photographs of 7½° Cone Shock Interacting with Tripped Boundary Layer; p_o = 850 psia x_i = 22 in. (Groups 19 &248)

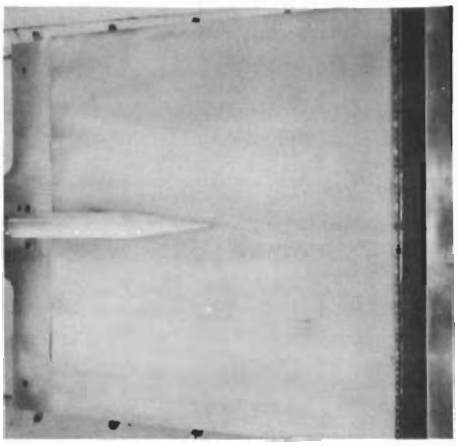

t (SEC) 3.58

h_T (BTU/FT^2 HR ^oR) 14.81

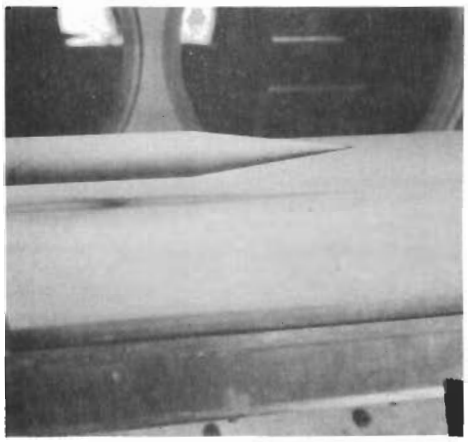

(a)

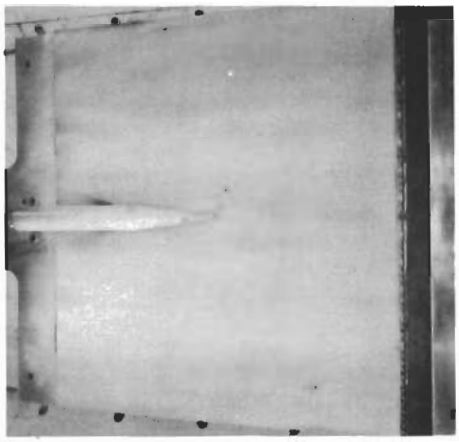

4.78

12.82

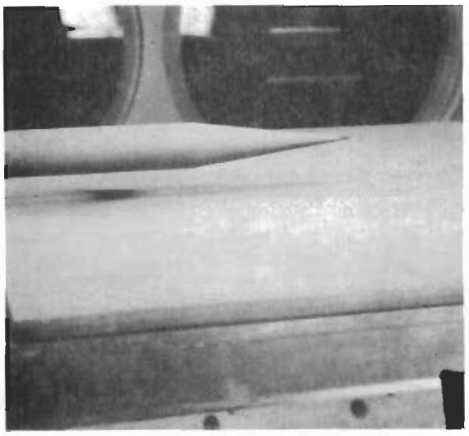

(b)

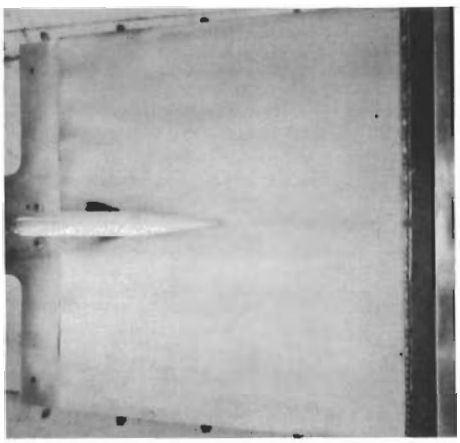

6.53

10.97

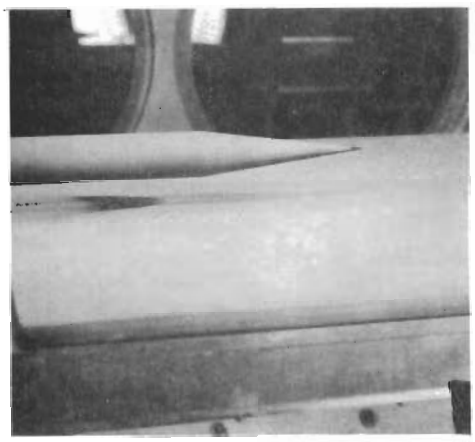

(c)

Fig. 57 Frames from Motion Pictures Taken During Temperature-Sensitive Paint Run for 7 1/2° Cone Shock Interacting with Tripped Boundary Layer; p_o = 850 psia, x_i = 22 in. (Group 377), (Sheet 1 of 2)

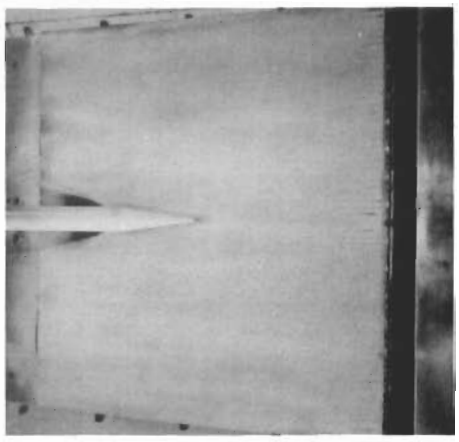

t (SEC)	h_T (BTU/FT^2 HR ^oR)
8.88	9.40

(d)

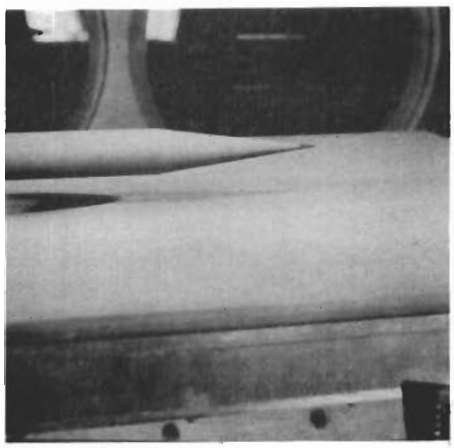

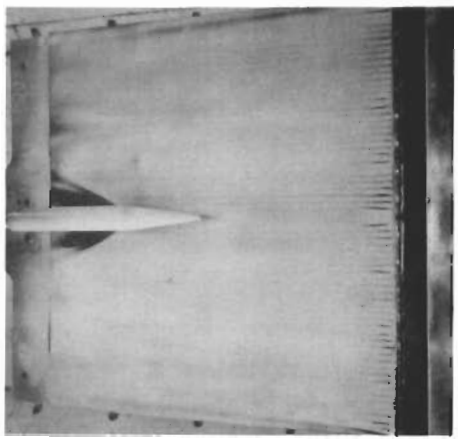

t (SEC)	h_T (BTU/FT^2 HR ^oR)
14.43	7.38

(e)

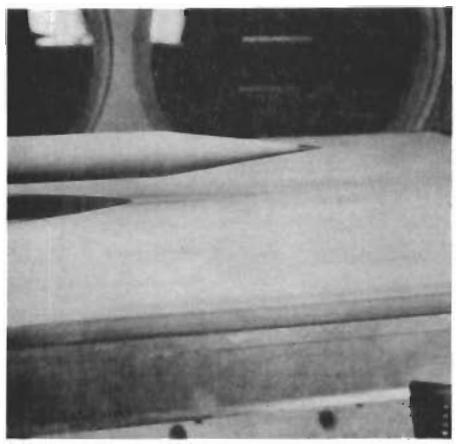

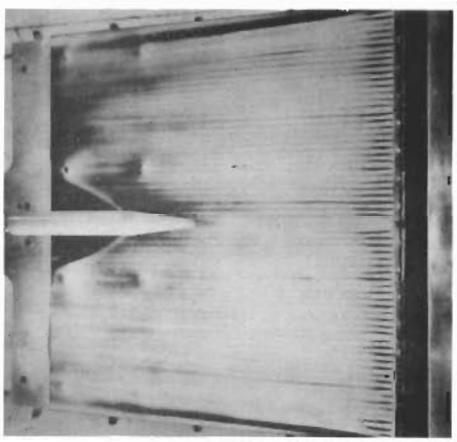

t (SEC)	h_T (BTU/FT^2 HR ^oR)
23.23	5.81

(f)

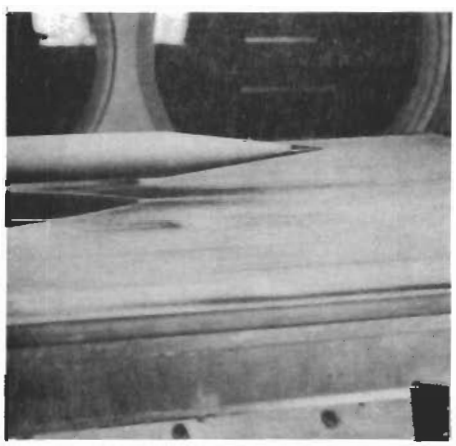

Fig. 57 Frames from Motion Pictures Taken During Temperature - Sensitive Paint Run for 7 1/2° Cone Shock Interacting with Tripped Boundary Layer; p_o = 850 psia, x_i = 22 in. (Group 377), (Sheet 2 of 2)

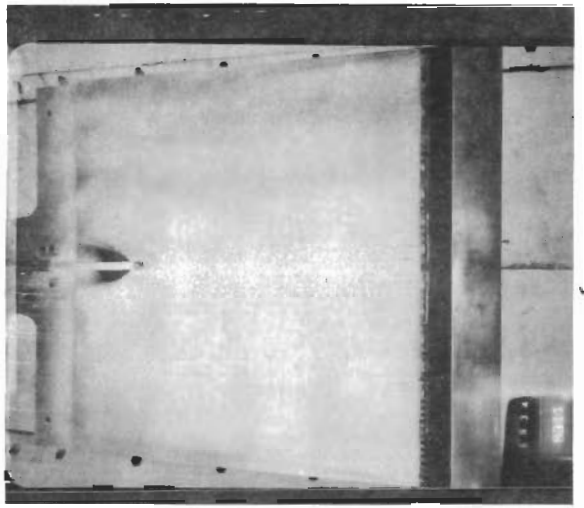

t = 25.15 SEC

$h_T = 7.10 \frac{BTU}{FT^2\ HR - {}^oR}$

$\frac{h_T}{h_{REF}} = 0.0627$

$T_{PC} = 735^oR$
GROUP 375

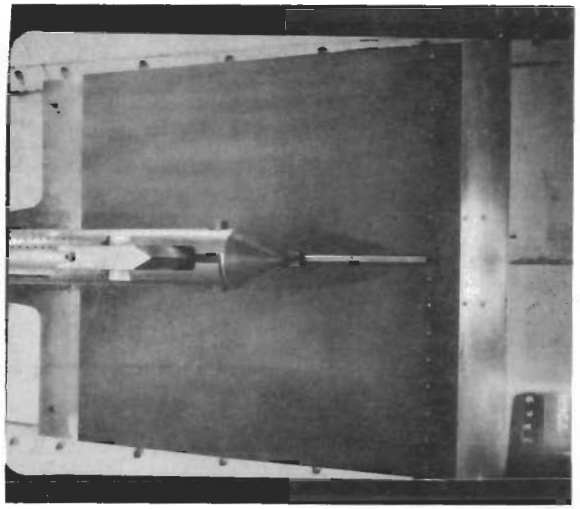

t = 9.87 SEC

$h_T = 1.51 \frac{BTU}{FT^2\ HR - {}^oR}$

$\frac{h_T}{h_{REF}} = 0.0438$

$T_{PC} = 573^oR$
GROUP 387

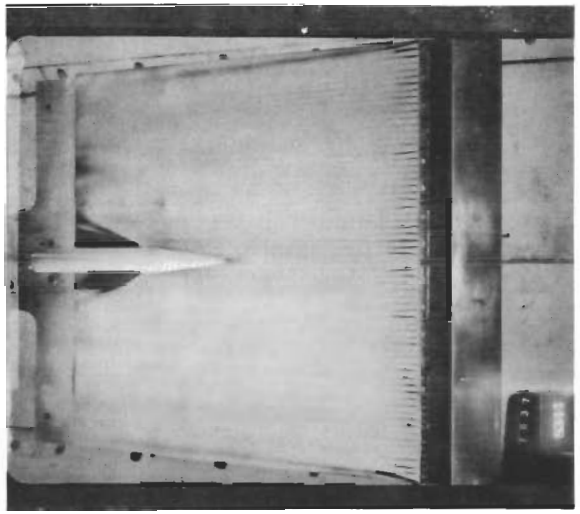

t = 15.53 SEC

$h_T = 7.11 \frac{BTU}{FT^2\ HR - {}^oR}$

$\frac{h_T}{h_{REF}} = 0.0626$

$T_{PC} = 710^oR$
GROUP 377

a) p_o = 850 PSIA, x_i = 22 IN., WITH B L TRIP

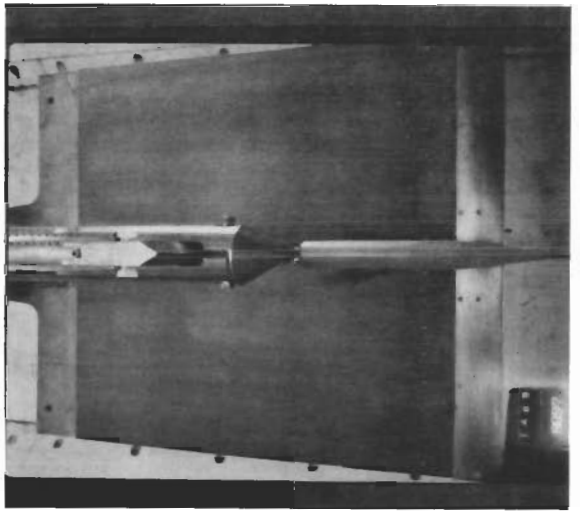

t = 14.09 SEC

$h_T = 1.52 \frac{BTU}{FT^2\ HR\ {}^oR}$

$\frac{h_T}{h_{REF}} = 0.0438$

$T_{PC} = 573^oR$
GROUP 383

b) p_o = 75 PSIA, x_i = 5 IN., NO BL TRIP

Fig. 58 Comparisons of Heating Distributions on Sharp L.E. Plate Caused by 0.5 in. Hemisphere and 7.5° Cone for Turbulent and Laminar Boundary Layers

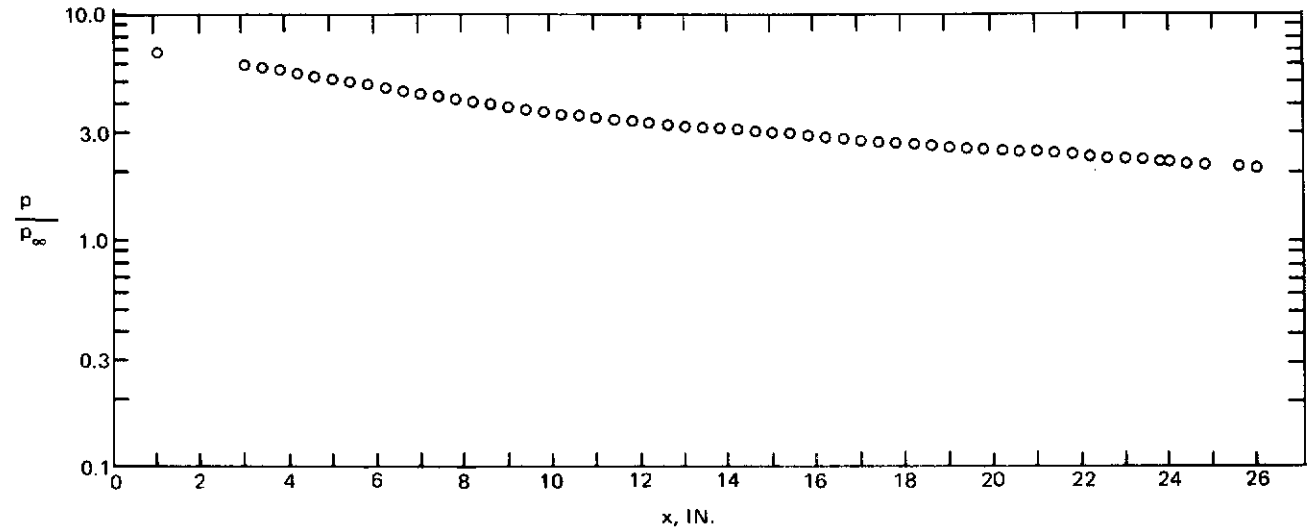

a) PRESSURE

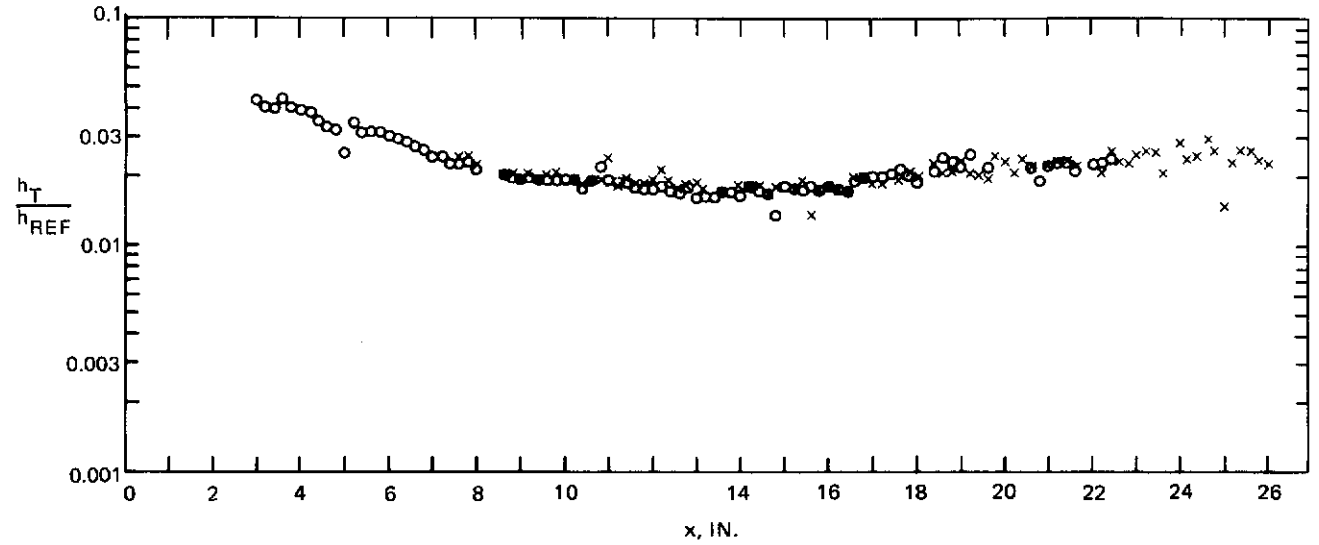

b) HEATING

Fig. 59 Undisturbed Pressure and Heating Distributions on Blunt Plate; p_0 = 850 psia (Groups 348, 104, & 105)

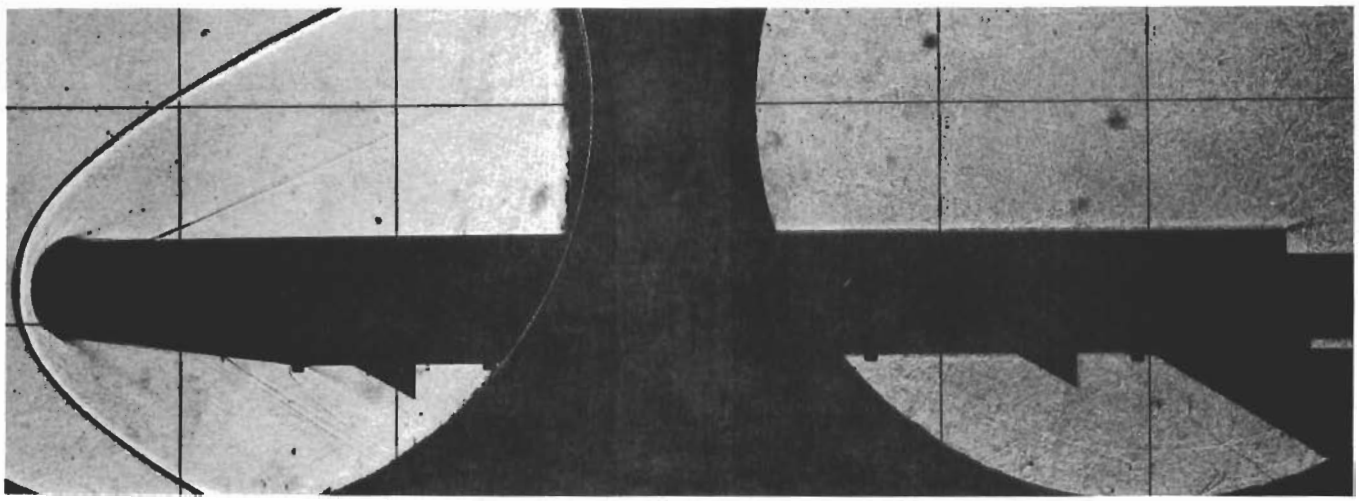

a. SHADOWGRAPHS

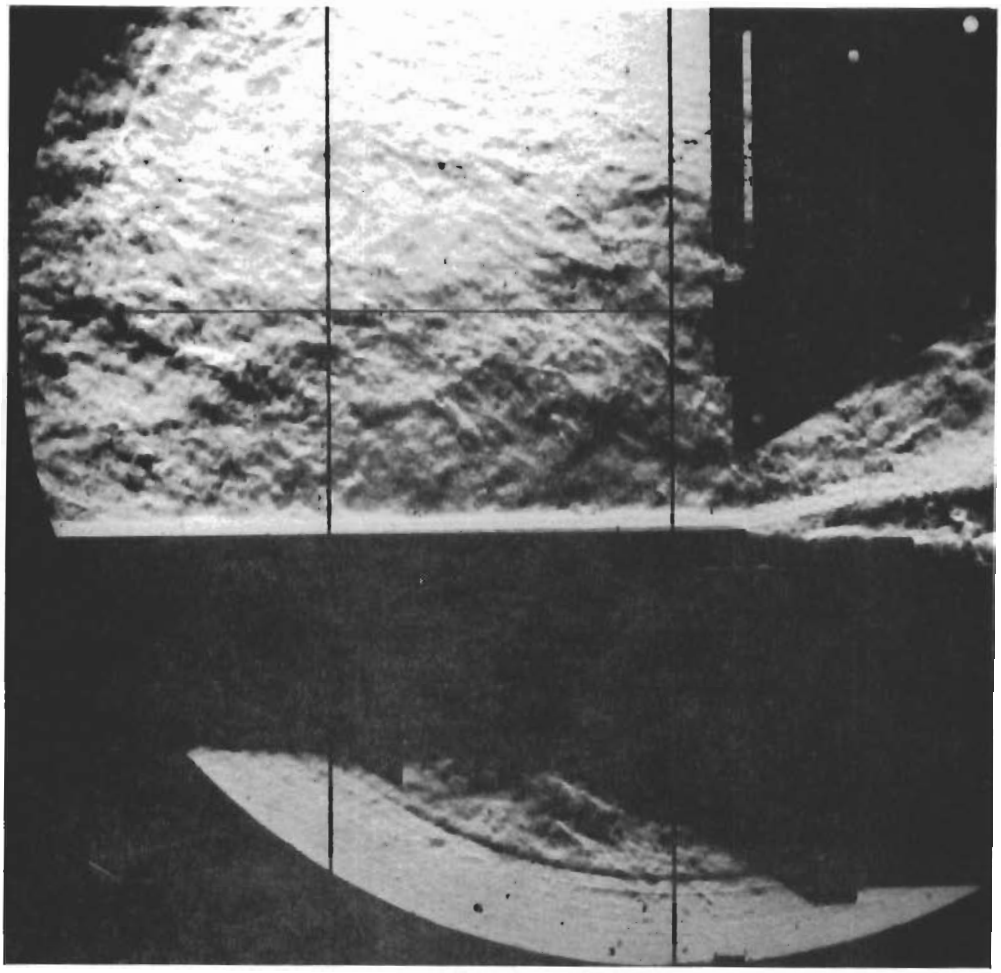

b. SCHLIEREN

Fig. 60 Shadowgraph and Schlieren Photographs of Undisturbed Flows on Blunt LE Plate; p_o = 850 psia (Groups 104, 105, and 348)

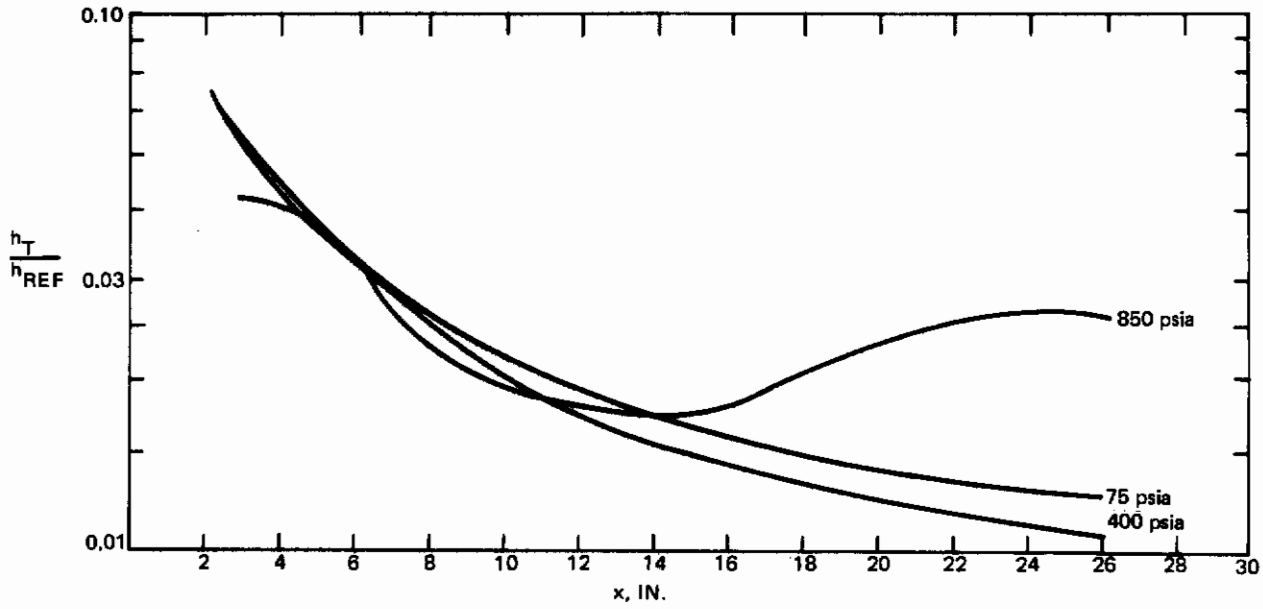

a.. HEAT TRANSFER

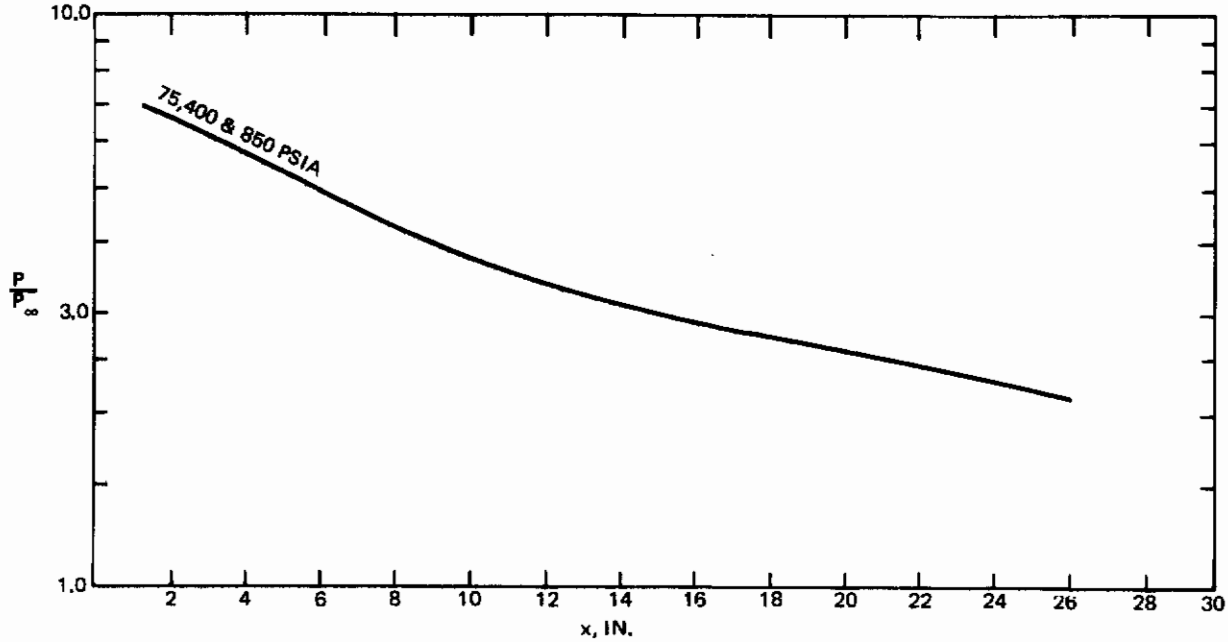

b. PRESSURE

Fig. 61 Faired Distributions of Undisturbed Heating Rates and Pressures on Blunt LE Plate

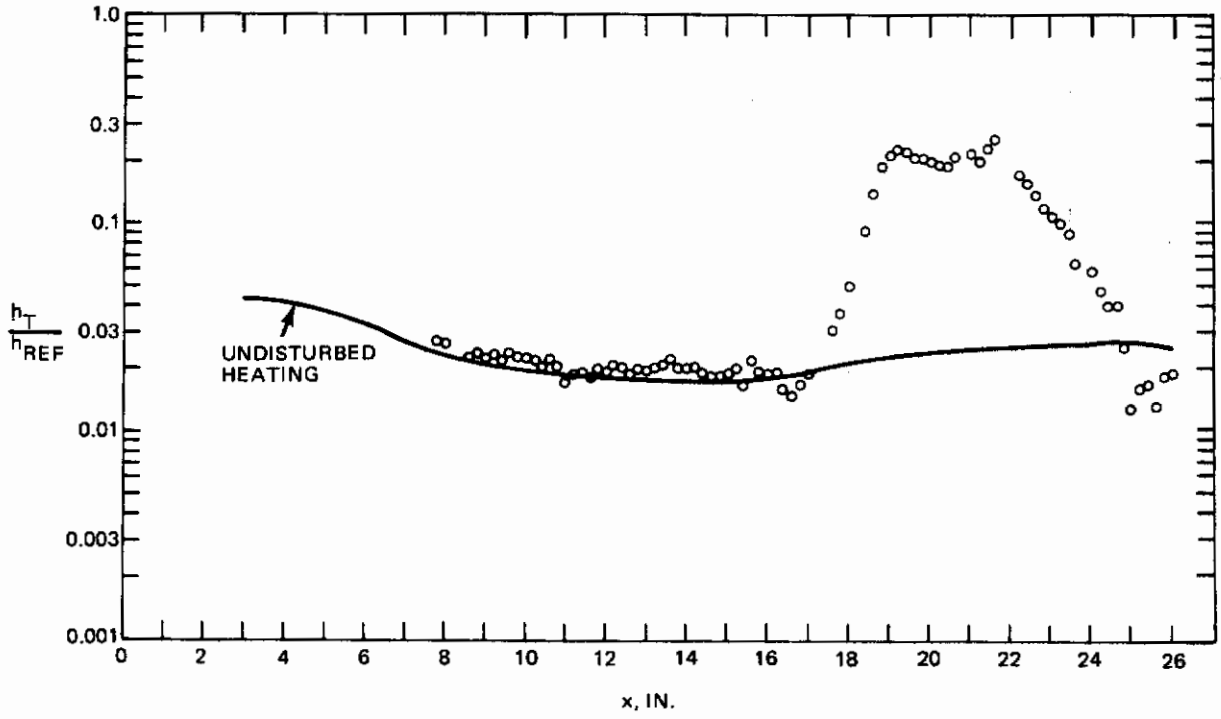

a. HEAT TRANSFER

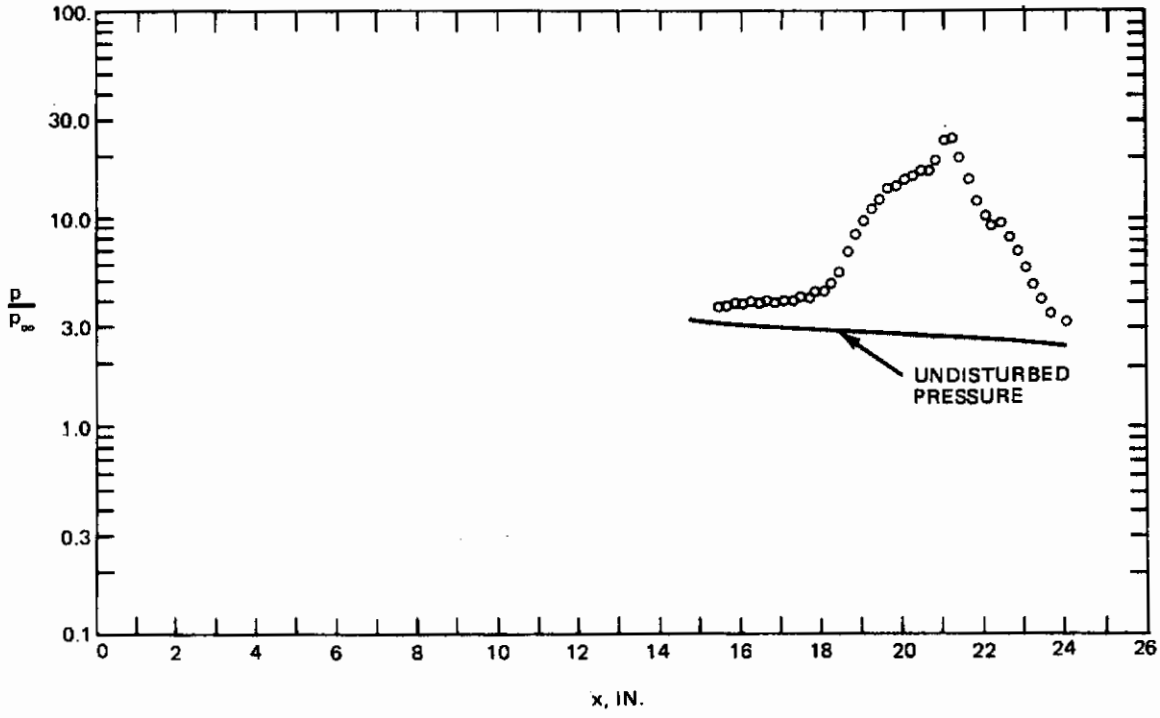

b. PRESSURE

Fig. 62 Heating and Pressure Distributions on Blunt Plate caused by 10° Wedge Shock; p_o = 850 psia, x_i = 22 in. (Groups 45 & 347)

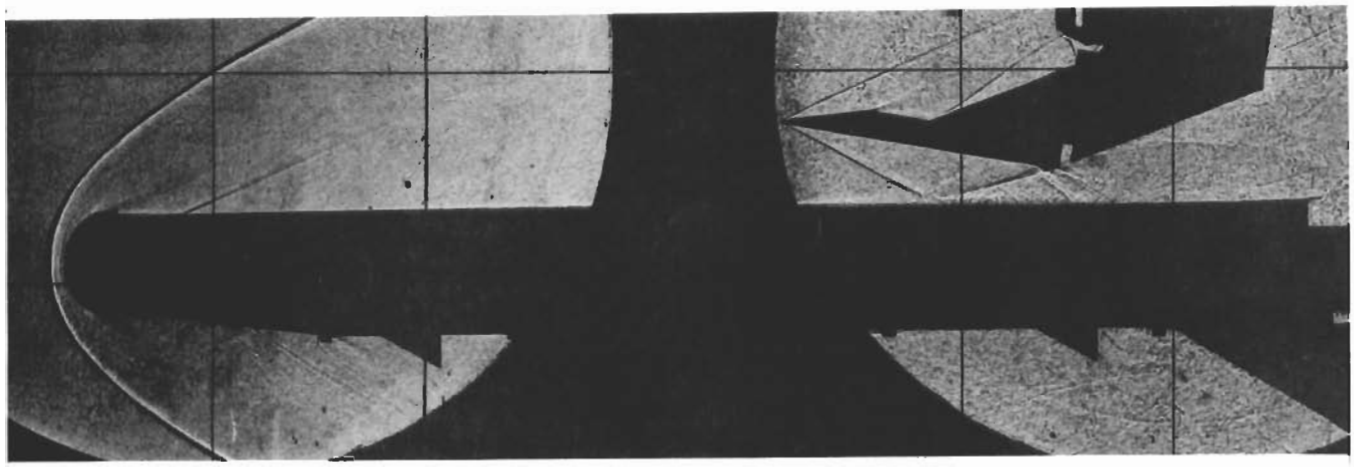

a. SHADOWGRAPHS (GROUP 45)

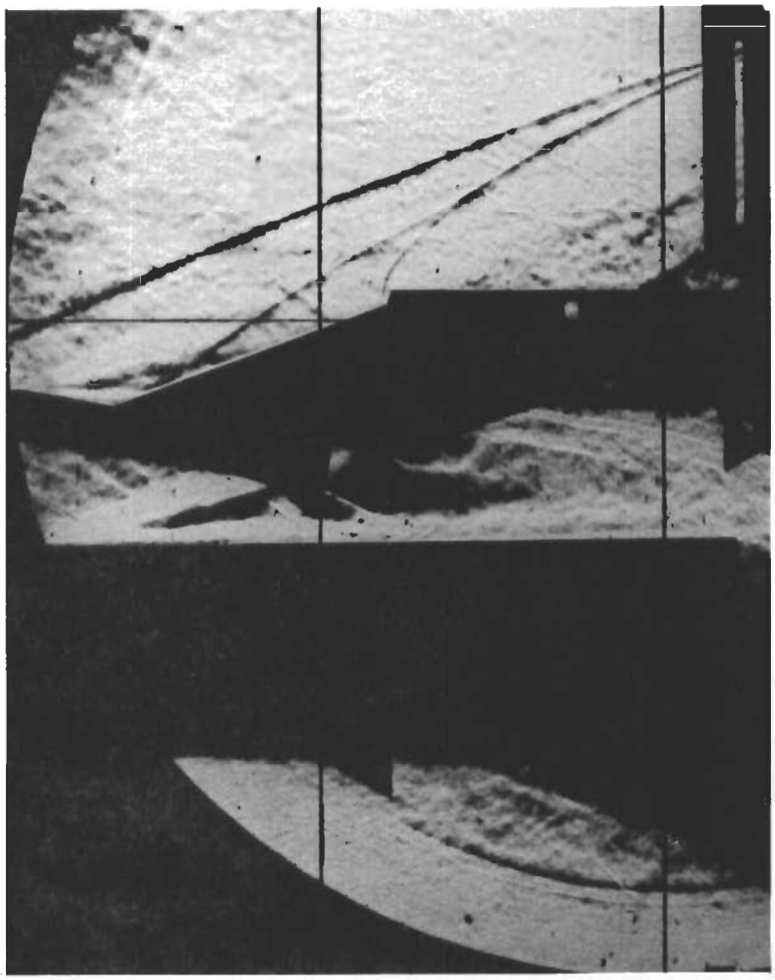

b. SCHLIEREN (GROUP 347)

Fig. 63 Shadowgraph and Schlieren Photographs of 10^{o} Wedge Shock Interacting with Blunt Plate Boundary Layer; p_o = 850 psia, x_i = 22 in. (Groups 45 & 347)

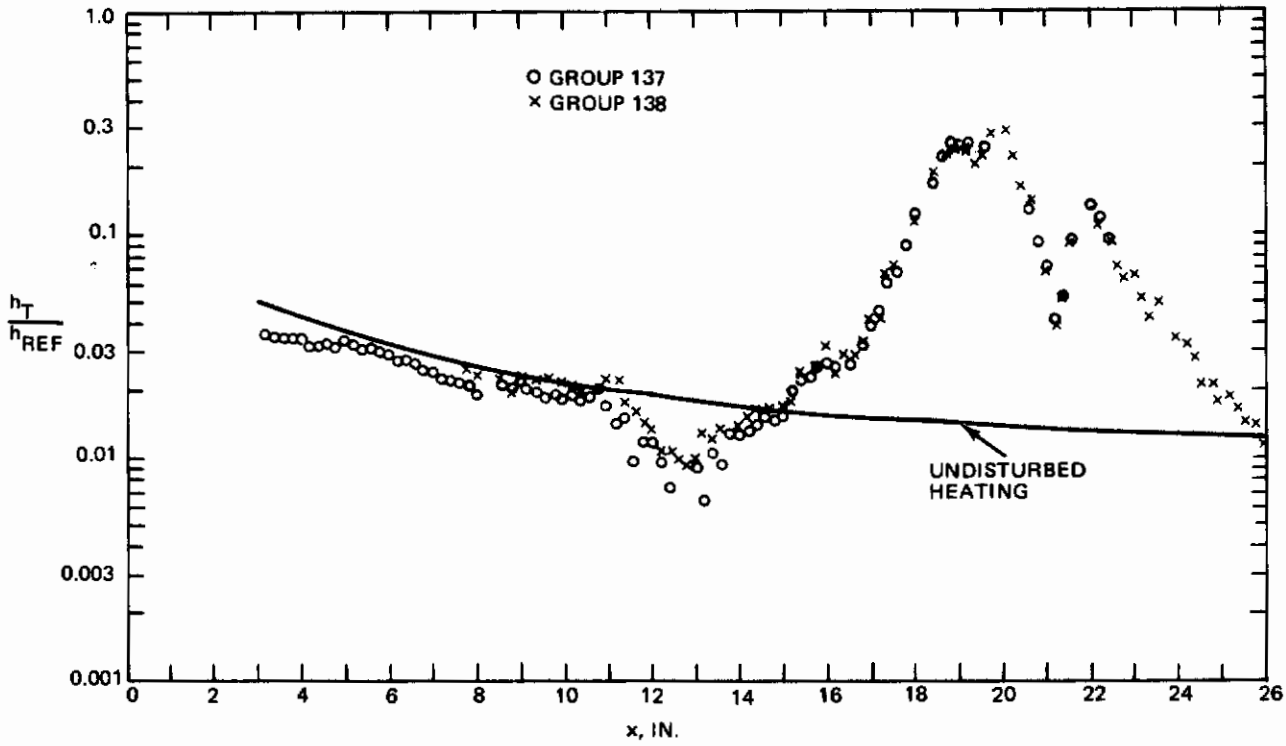

a. HEAT TRANSFER

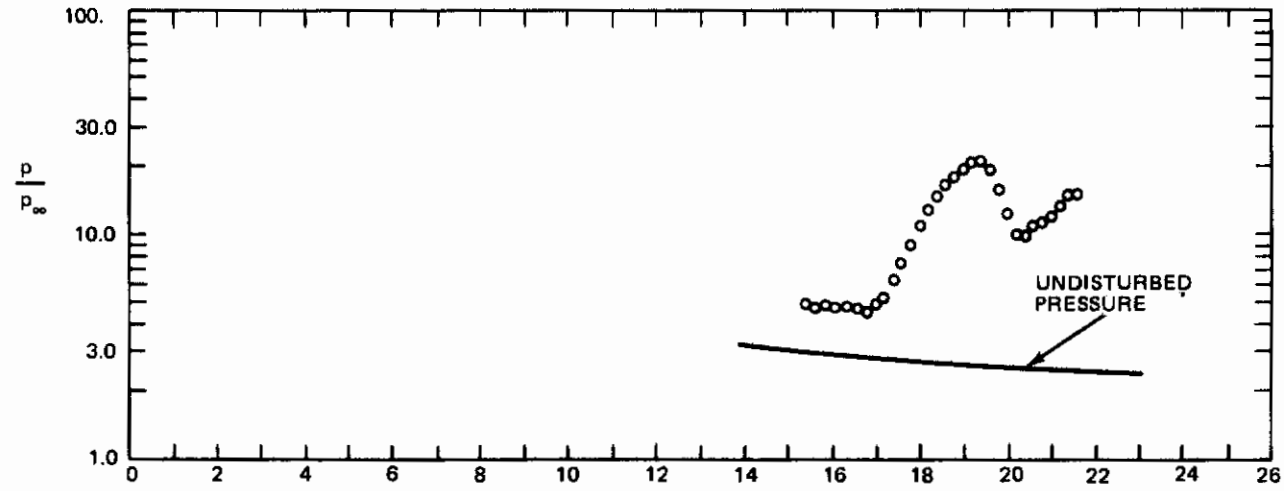

b. PRESSURE

Fig. 64 Heating and Pressure Distributions on Blunt Plate Caused by 10° Wedge Shock; p_o = 75 psia, x_i = 22 in. (Groups 137, 138 & 366)

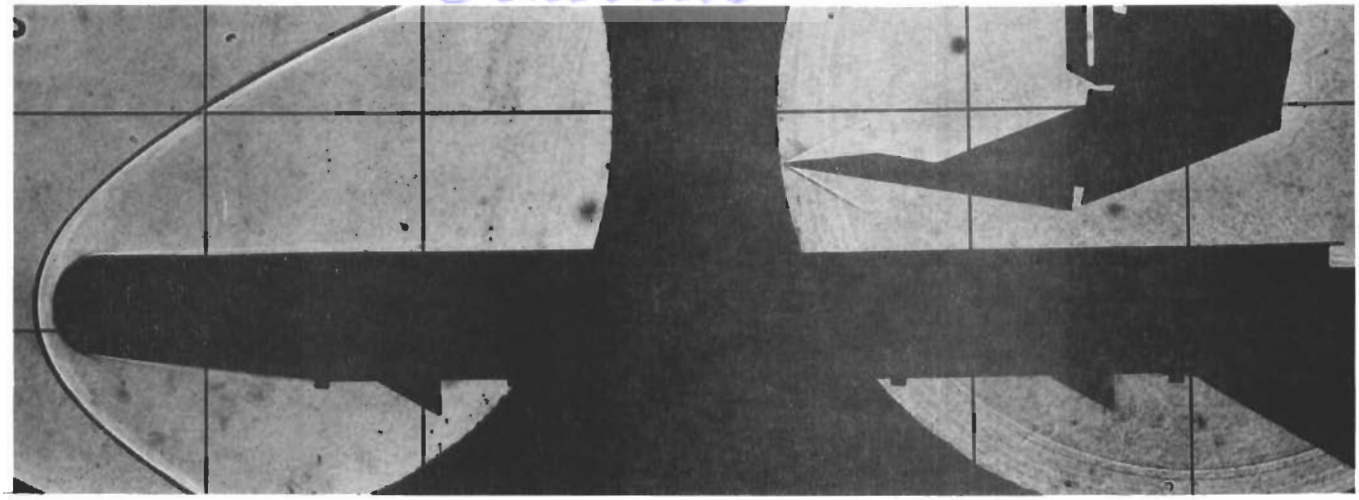

a. SCHLIERENS (GROUP 138)

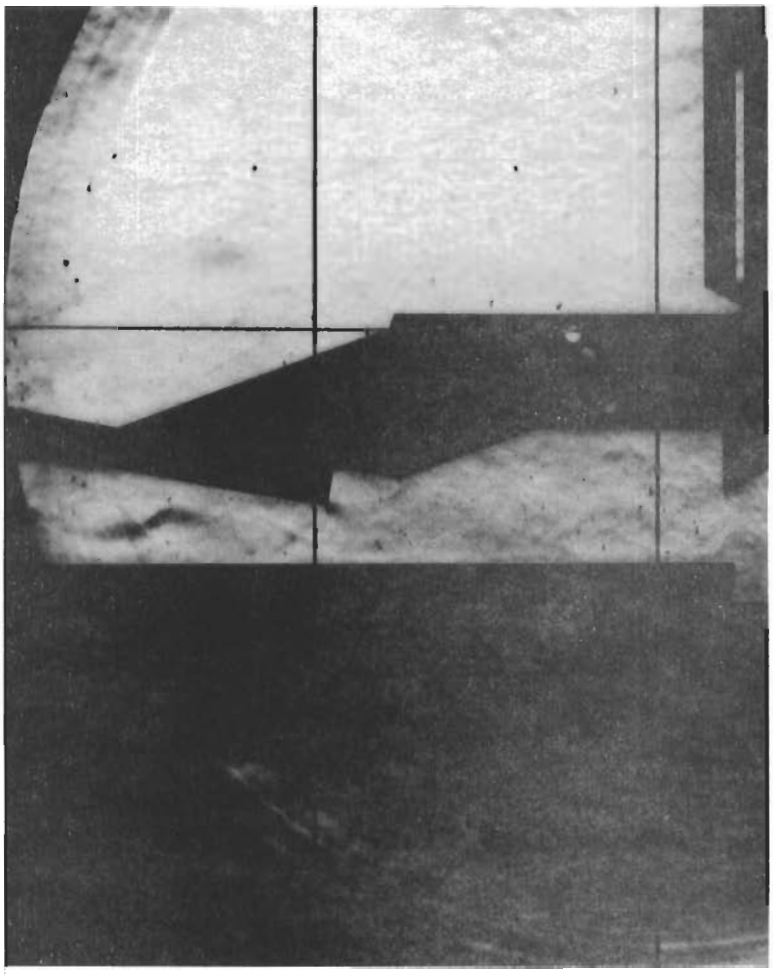

b. SCHLIEREN (GROUP 356)

Fig. 65 Shadowgraph and Schlieren Photographs of 10^{o} Wedge Shock Interacting with Blunt Plate Boundary Layer; p_o = 75 psia, x_i = 22 in. (Groups 137, 138 and 356)

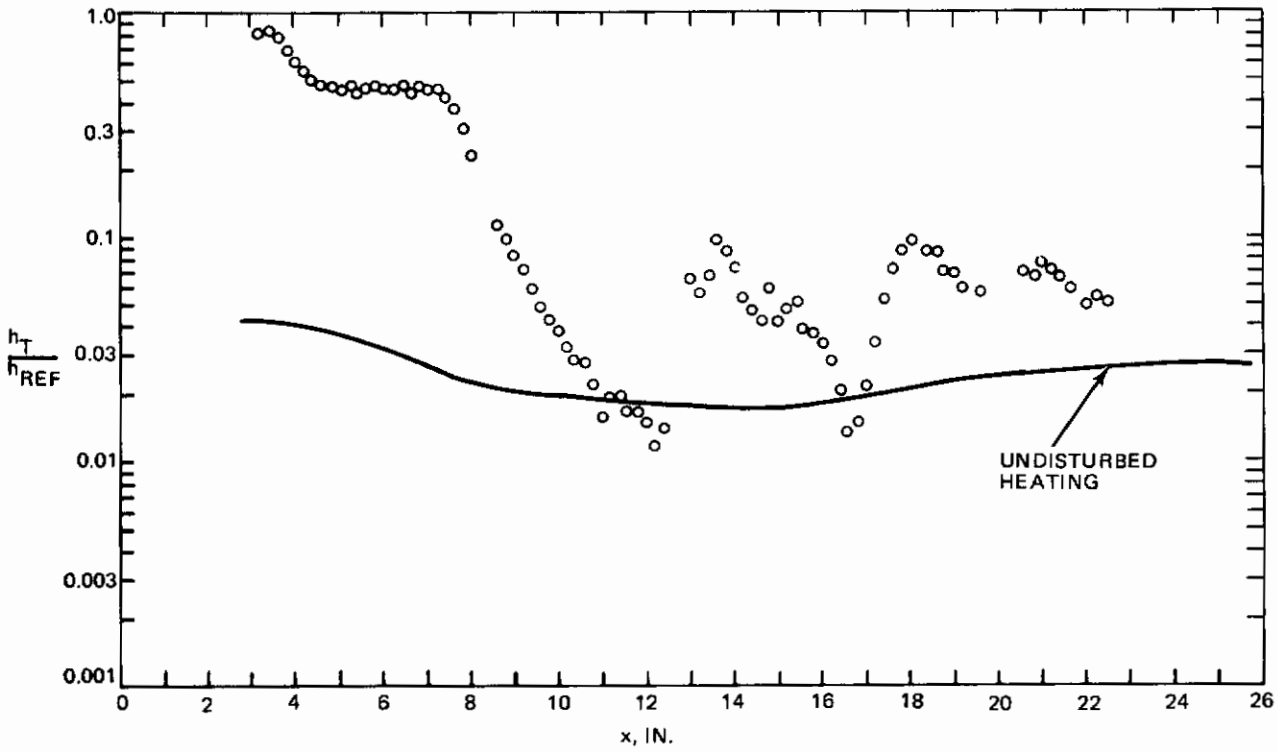

a. HEAT TRANSFER

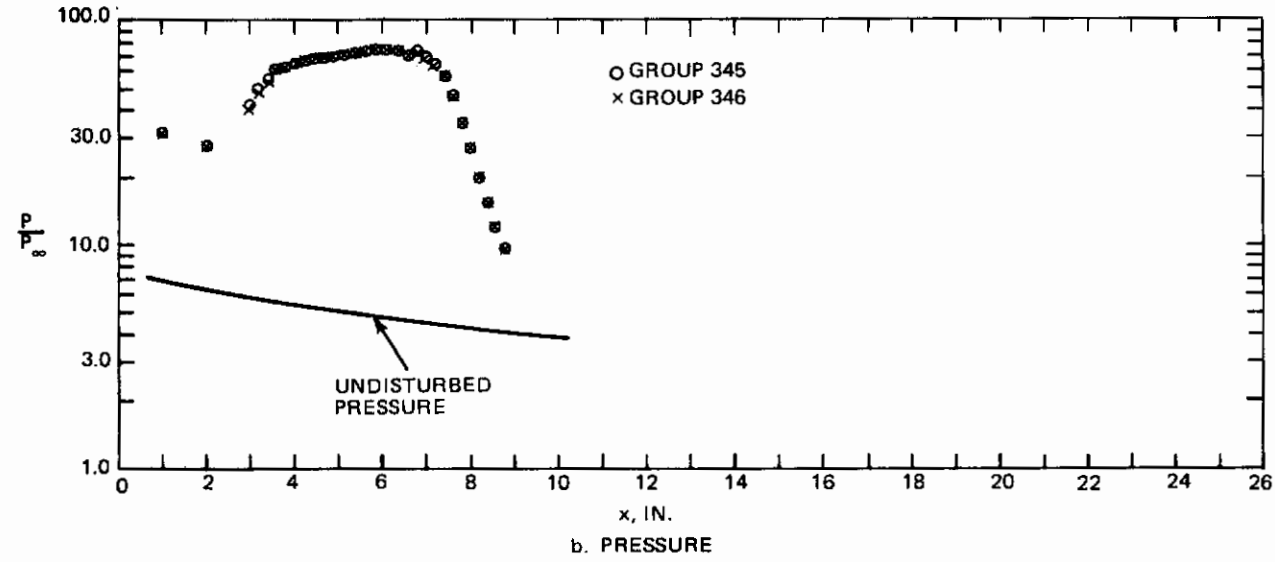

b. PRESSURE

Fig. 66 Heating and Pressure Distributions on Blunt Plate caused by 10° Wedge Shock; p_o = 850 psia, x_i = 7 in. (Groups 46, 345 & 346)

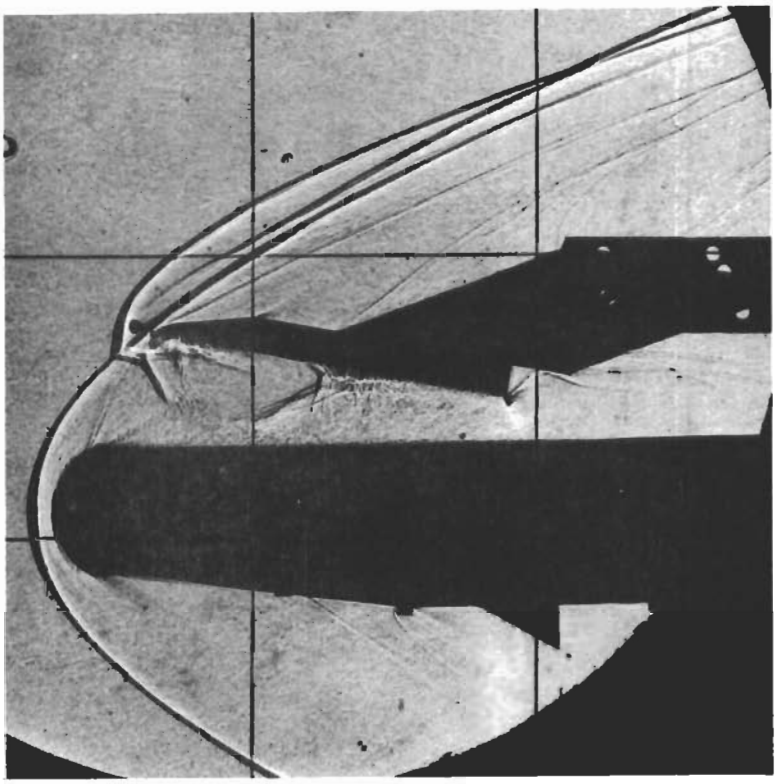

a. SHADOWGRAPH (GROUP 135)

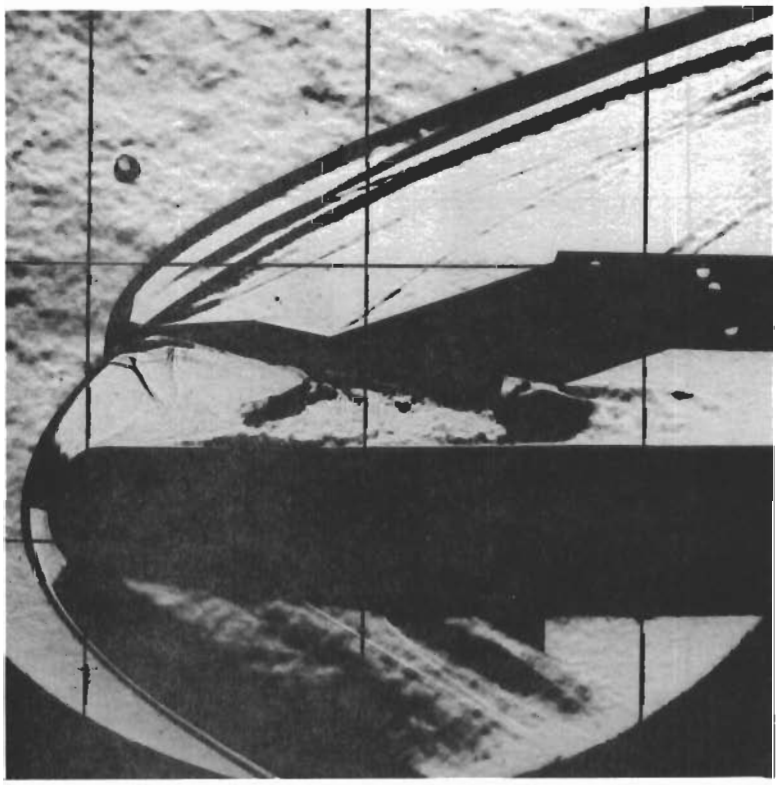

b. SCHLIEREN (GROUP 357)

Fig. 67 Shadowgraph and Schlieren Photographs of 10° Wedge Shock Interacting with Blunt Plate Boundary Layer; p_o =850 psia, x_i = 7.0 in. (Groups 46, 345 & 346)

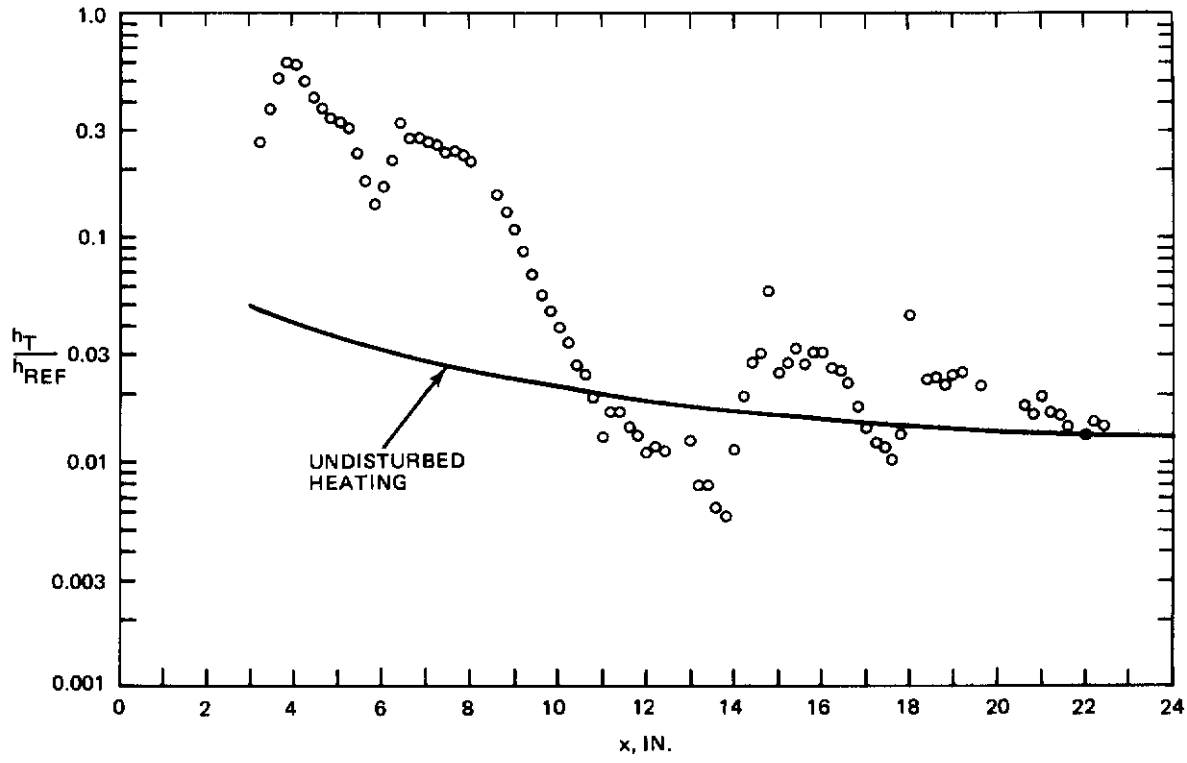

a. HEAT TRANSFER

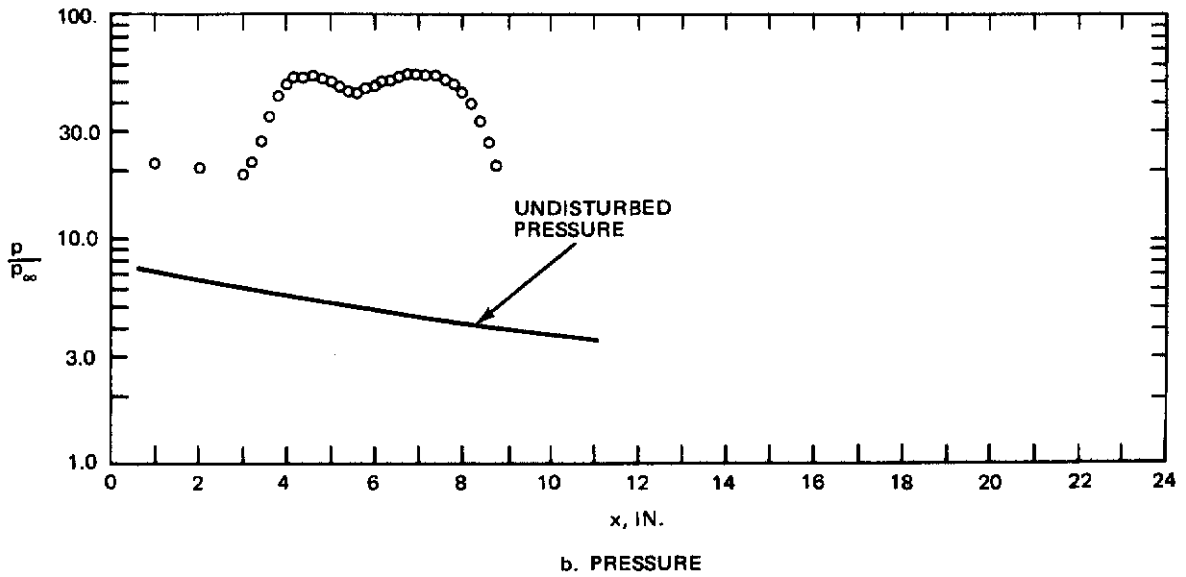

b. PRESSURE

Fig. 68 Heating and Pressure Distributions on Blunt Plate Caused by 10° Wedge Shock; p_o = 75 psia, x_i = 7.0 in. (Groups 135 & 357)

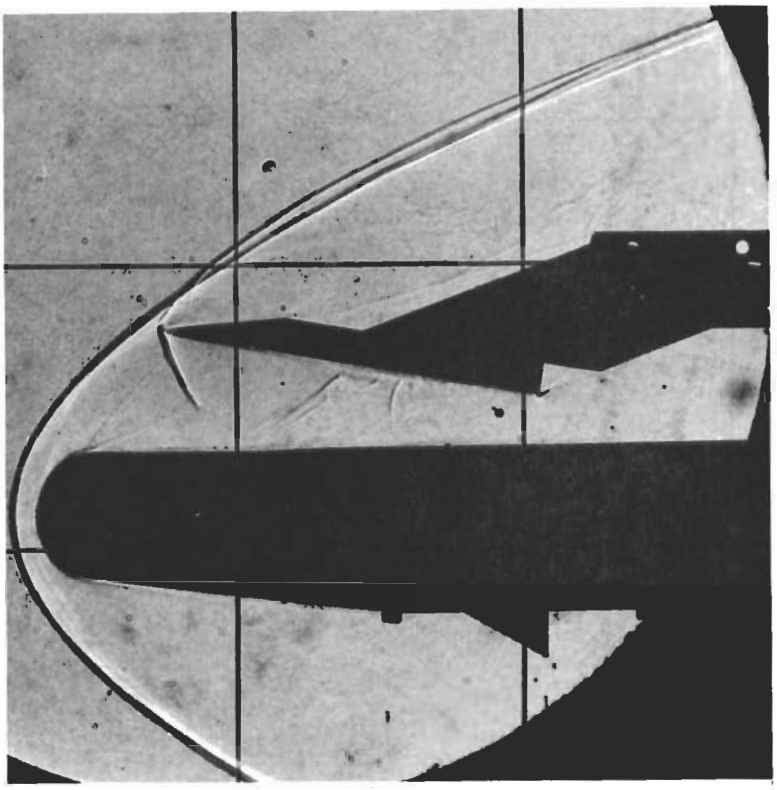

a. SHADOWGRAPH (GROUP 46)

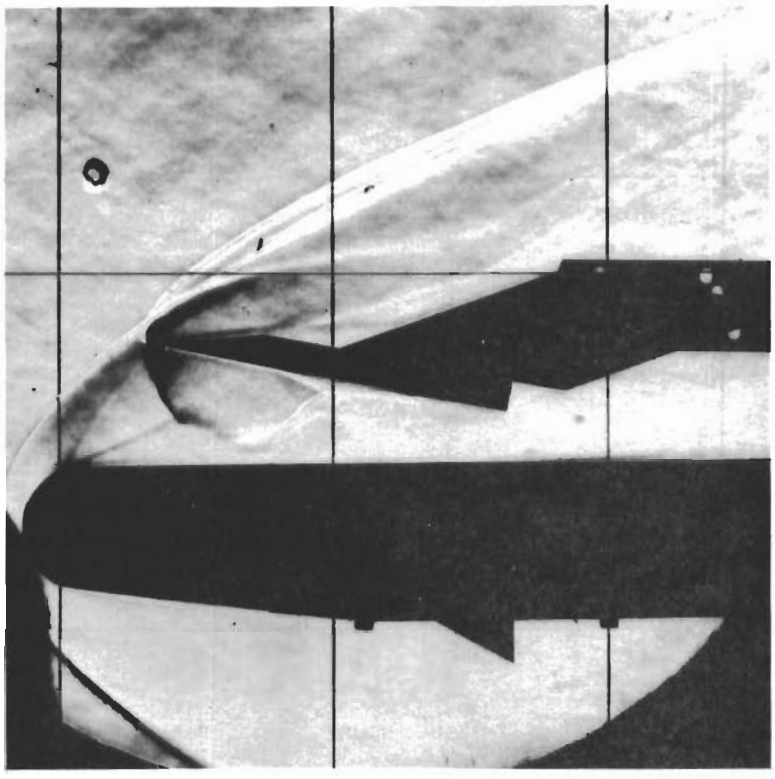

b. SCHLIEREN (GROUP 345)

Fig. 69 Shadowgraph and Schlieren Photographs of 10^{o} Wedge Shock Interacting with Blunt Plate Boundary Layer; p_o = 75 psia, x_i = 7.6 in. (Groups 135 & 357)

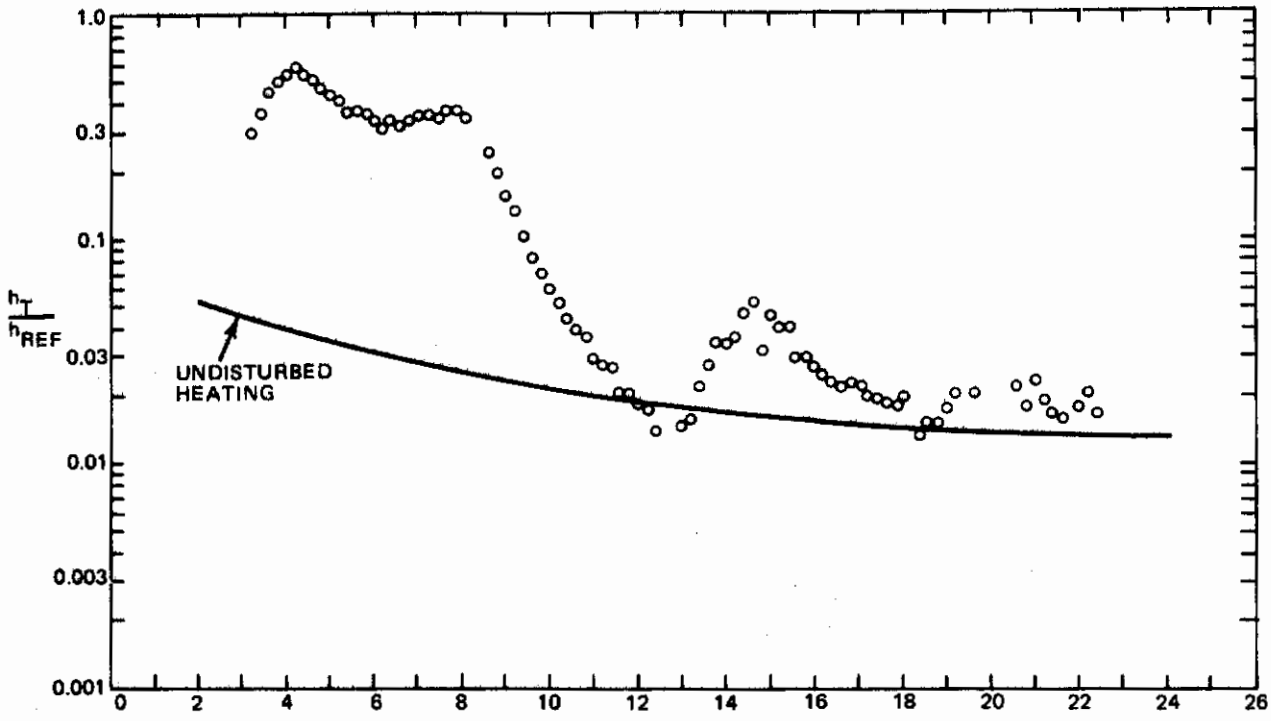

a. HEAT TRANSFER

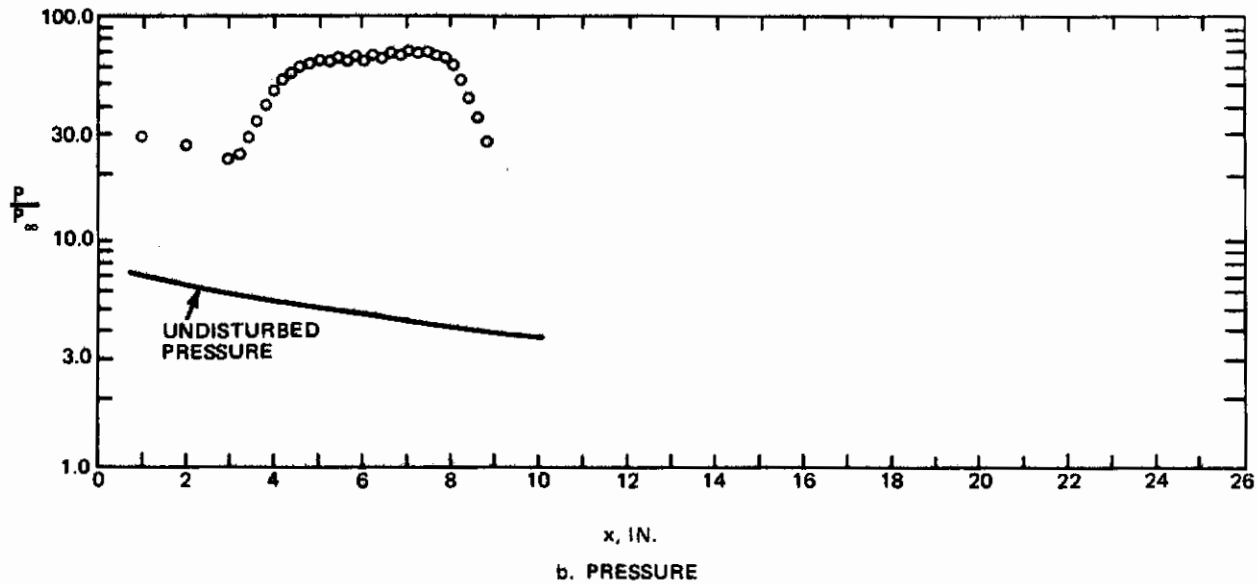

b. PRESSURE

Fig. 70 Heating and Pressure Distributions on Blunt Plate caused by 15° Wedge Shock; p_o = 75 psia, x_i = 7 in. (Groups 136 & 359)

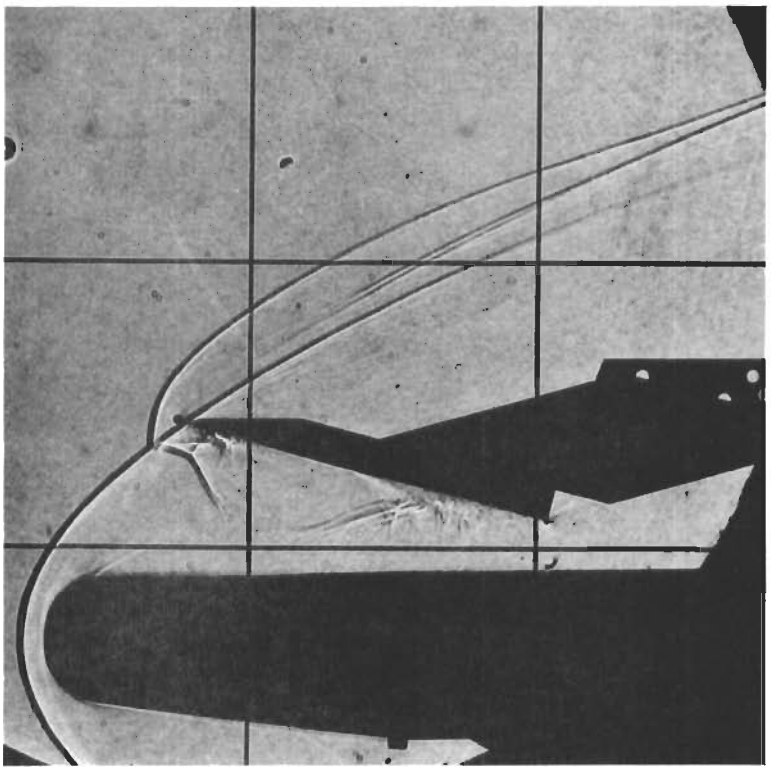

a. SHADOWGRAPH (GROUP 136)

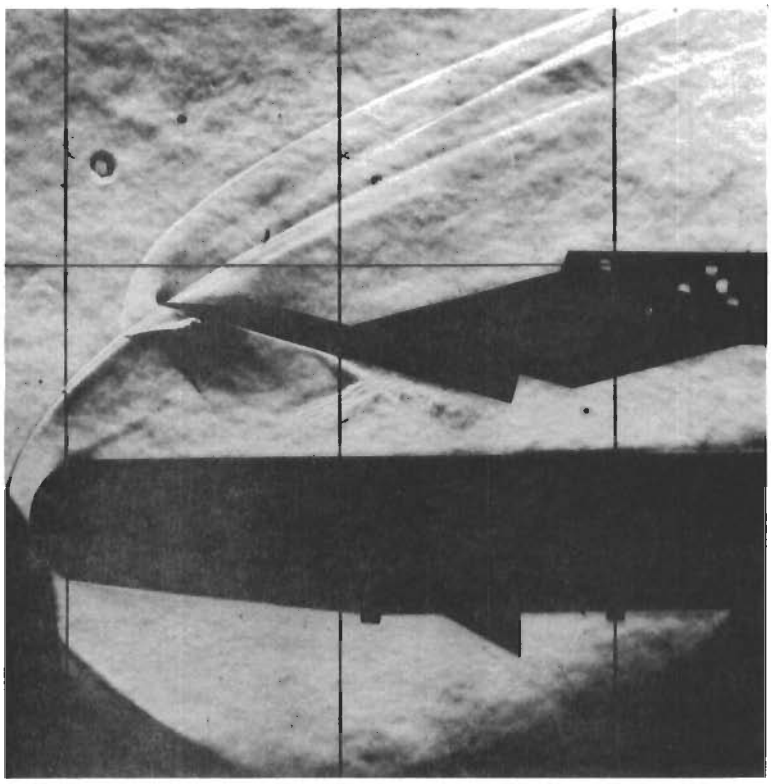

b. SCHLIEREN (GROUP 359)

Fig. 71 Shadowgraph and Schlieren Photographs of 15° Wedge Shock Interacting with Blunt Plate Boundary Layer; p_o = 75 psia, x_i = 7 in. (Groups 136 & 359)

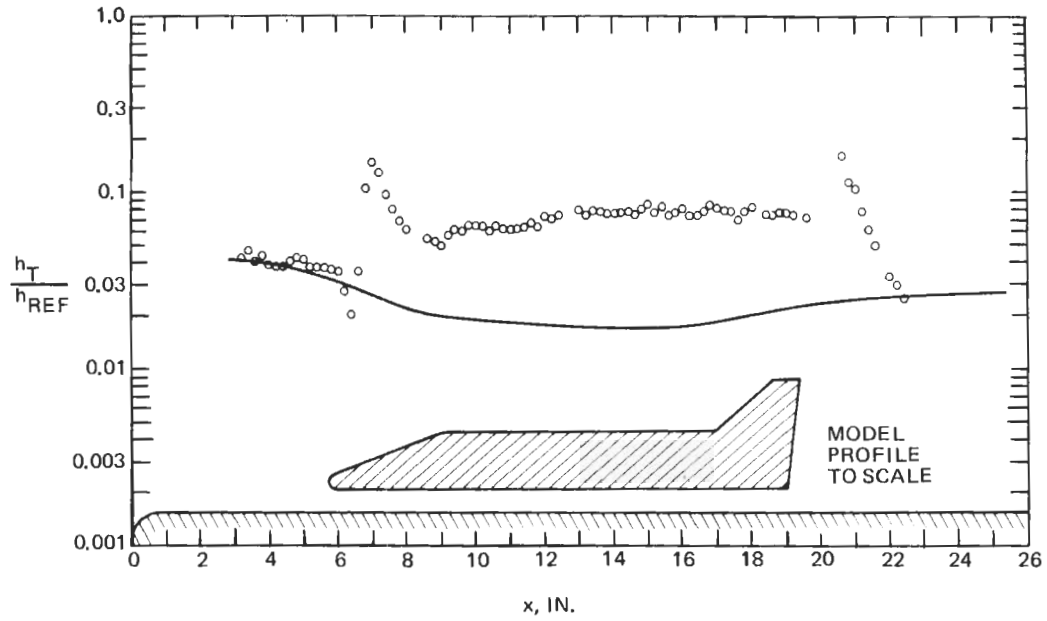

Fig. 72 Heating Distribution on Blunt Plate Caused by $\alpha = 0^o$ Orbiter Shock; p_o = 850 psia, x_i = 7 in. (Group 44)

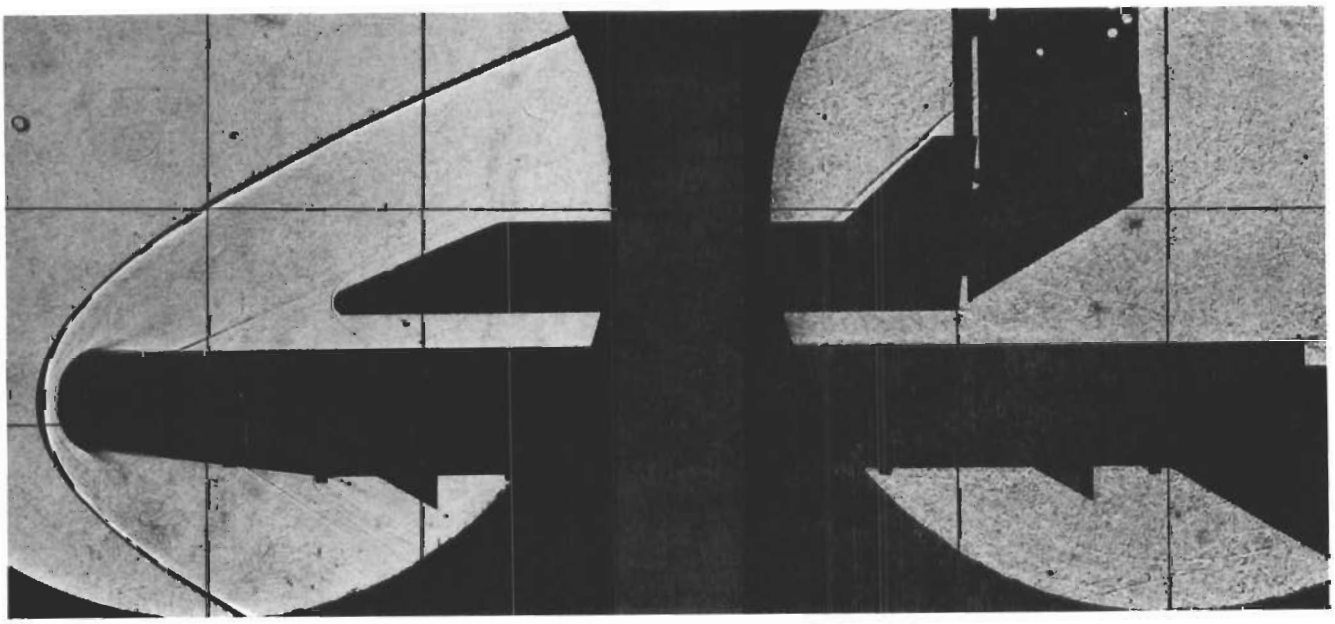

Fig. 73 Shadowgraph Photographs of $\alpha = 0$ Orbiter Shock Interacting with Blunt Plate Boundary Layer, p_o = 850 psia, x_i = 7 in. (Group 44)

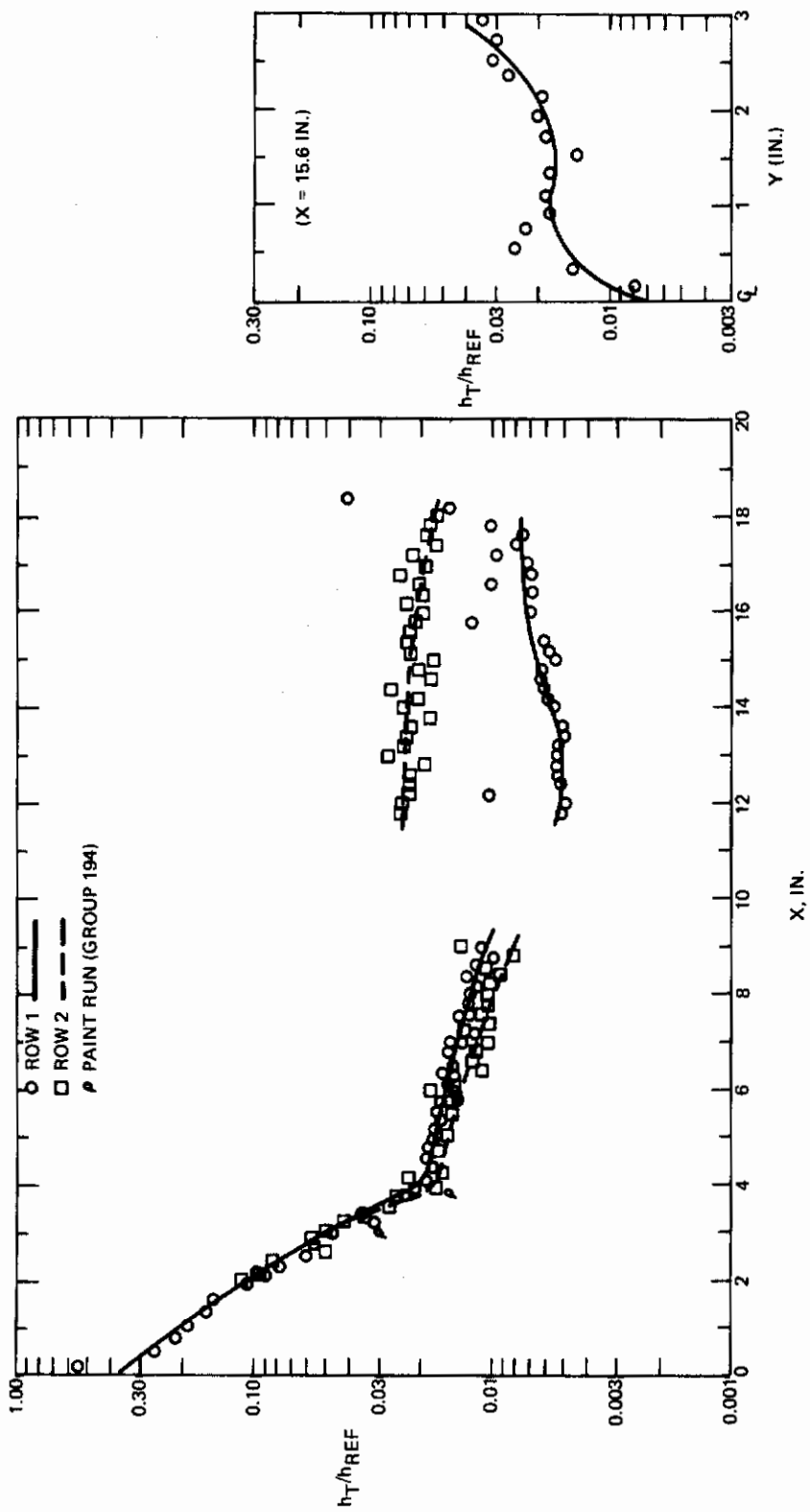

Fig. 74 Undisturbed Heating Distributions on Booster, p_o = 850 psia (Groups 150 & 151)

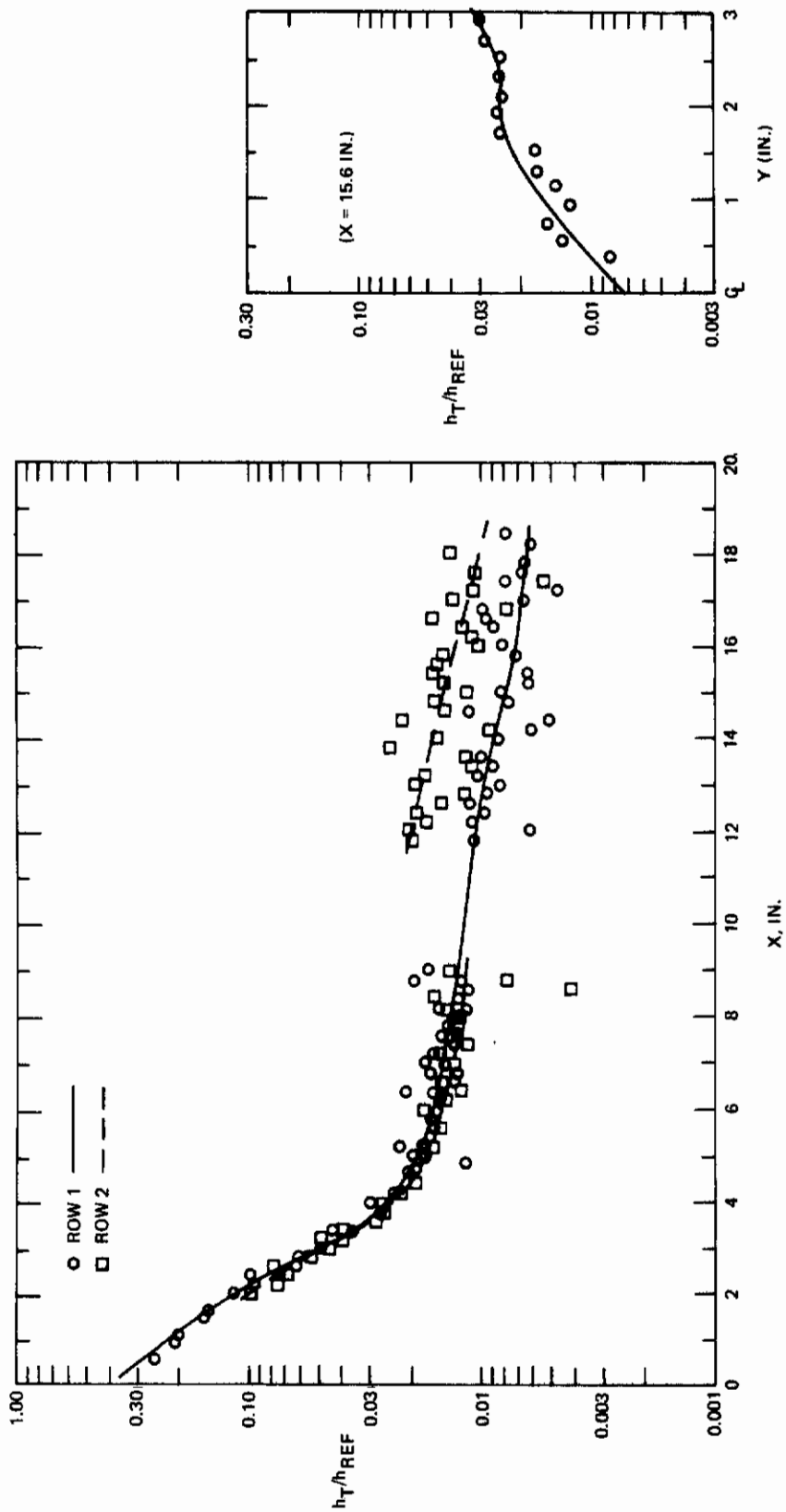

Fig. 75 Undisturbed Heating Distributions on Booster, P_o = 75 psia (Groups 176 & 177)

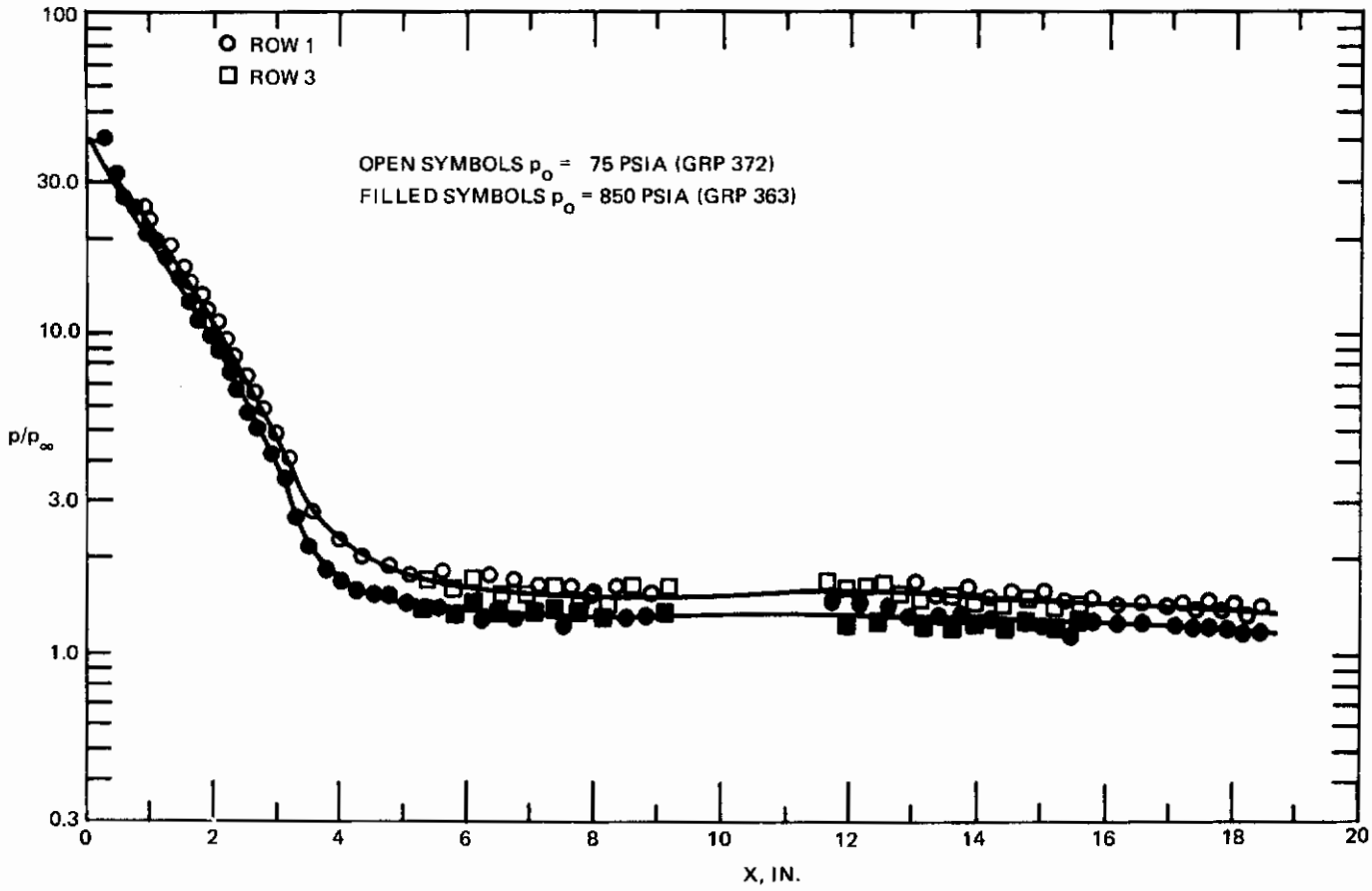

Fig. 76 Undisturbed Pressure Distributions on Booster, p_o = 75 and 850 psia (Groups 363 & 372)

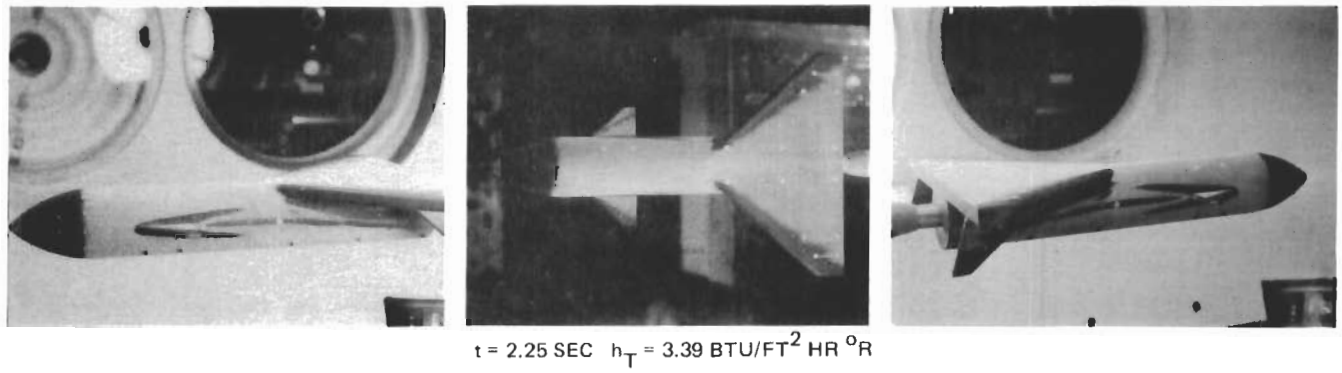

t = 2.25 SEC h_T = 3.39 BTU/FT^2 HR ^oR

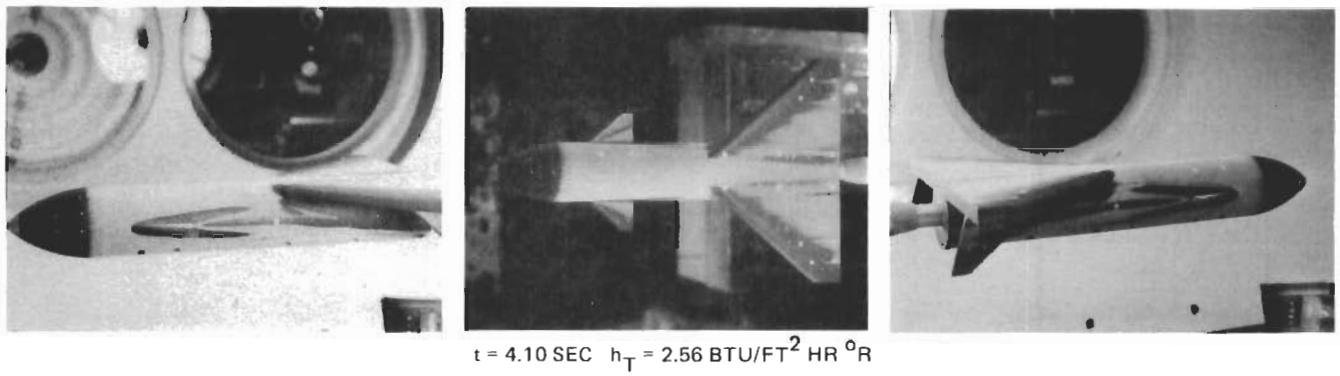

t = 4.10 SEC h_T = 2.56 BTU/FT^2 HR ^oR

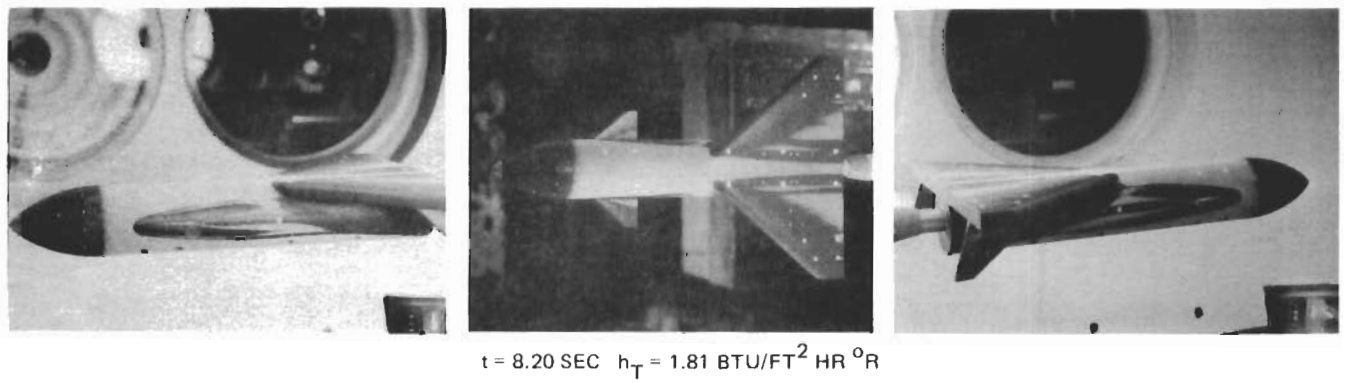

t = 8.20 SEC h_T = 1.81 BTU/FT^2 HR ^oR

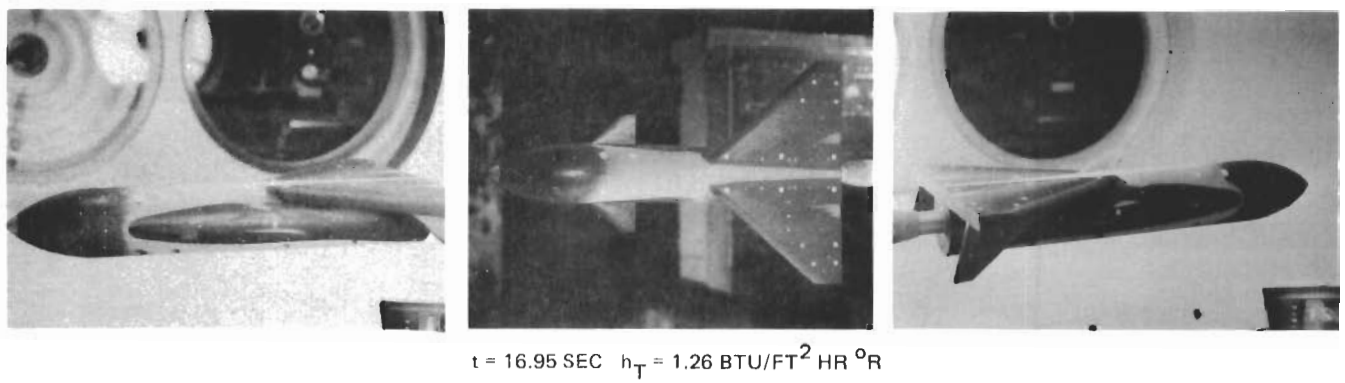

t = 16.95 SEC h_T = 1.26 BTU/FT^2 HR ^oR

Fig. 77 Frames from Motion Pictures Taken During Temperature – Sensitive Paint Run. Phase Change Temperature = 573^{o}R, Booster Alone, p_o = 850 psia (Group 194)

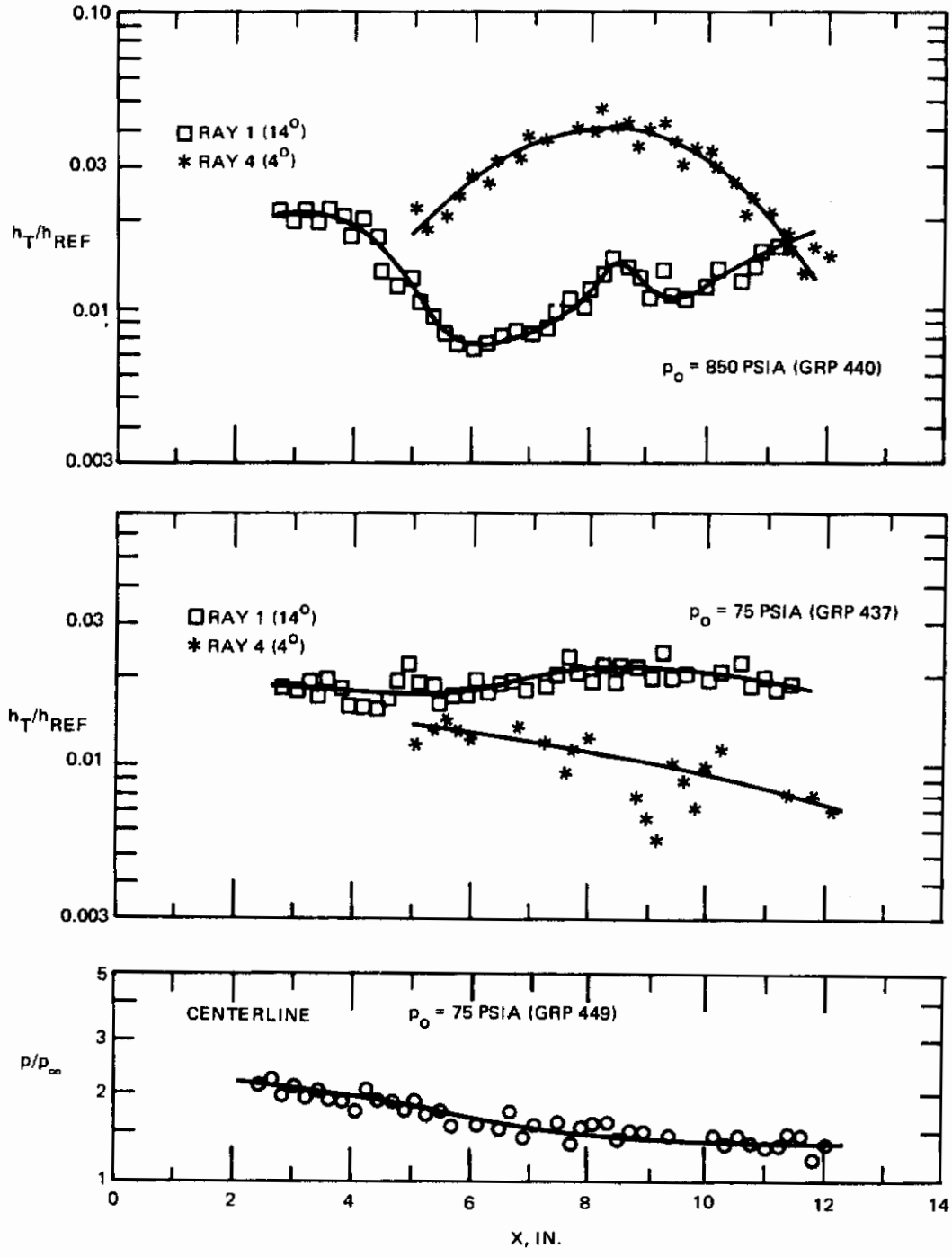

Fig. 78 Undisturbed Heating and Pressure Distributions on Orbiter at Zero Angle of Attack

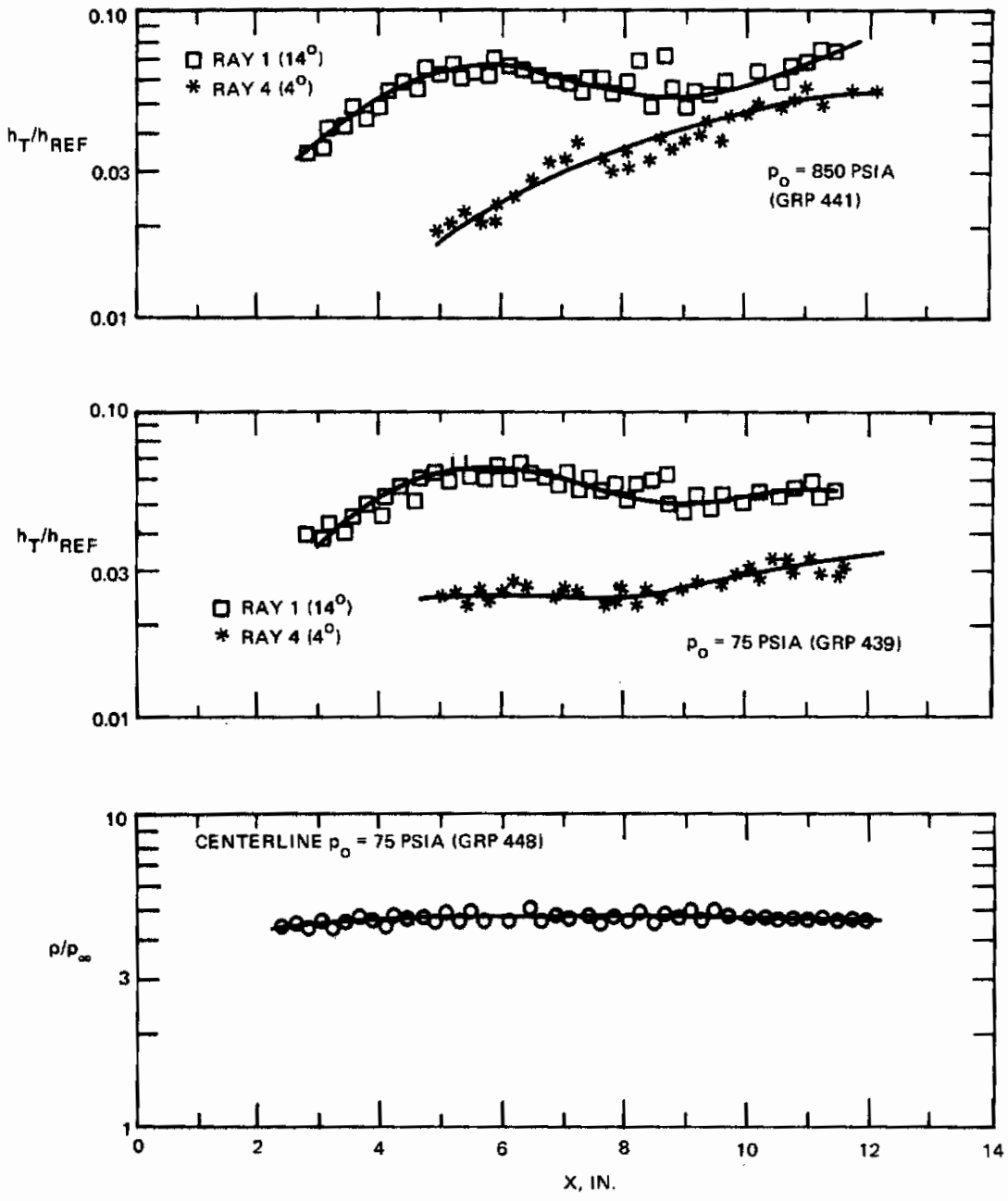

Fig. 79 Undisturbed Heating and Pressure Distributions on Orbiter at 10 Deg Angle of Attack

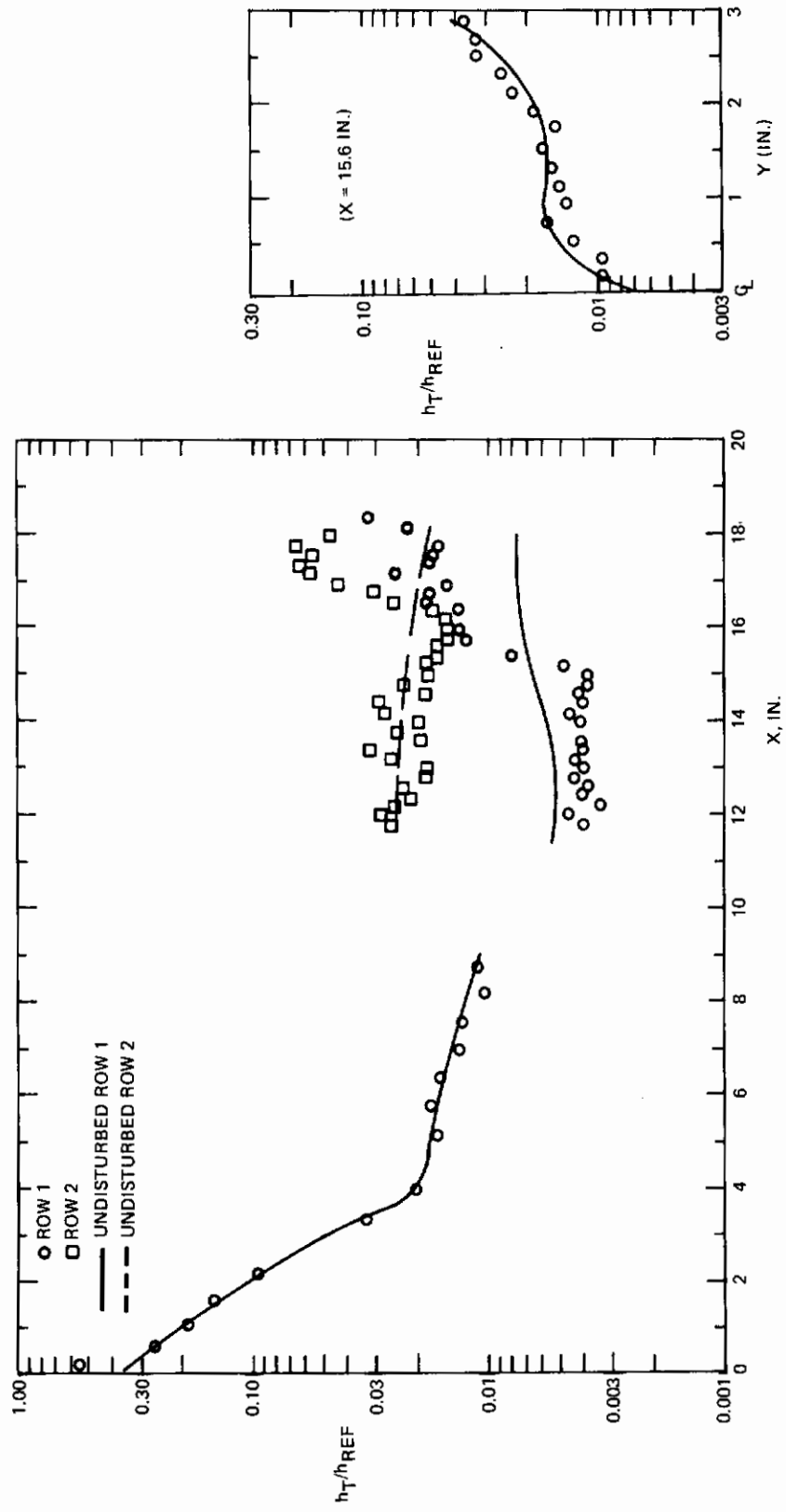

Fig. 80 Interference Heating Distributions on Booster Caused by 0.5 inch Hemisphere, p_o = 850 psia (Group 157)

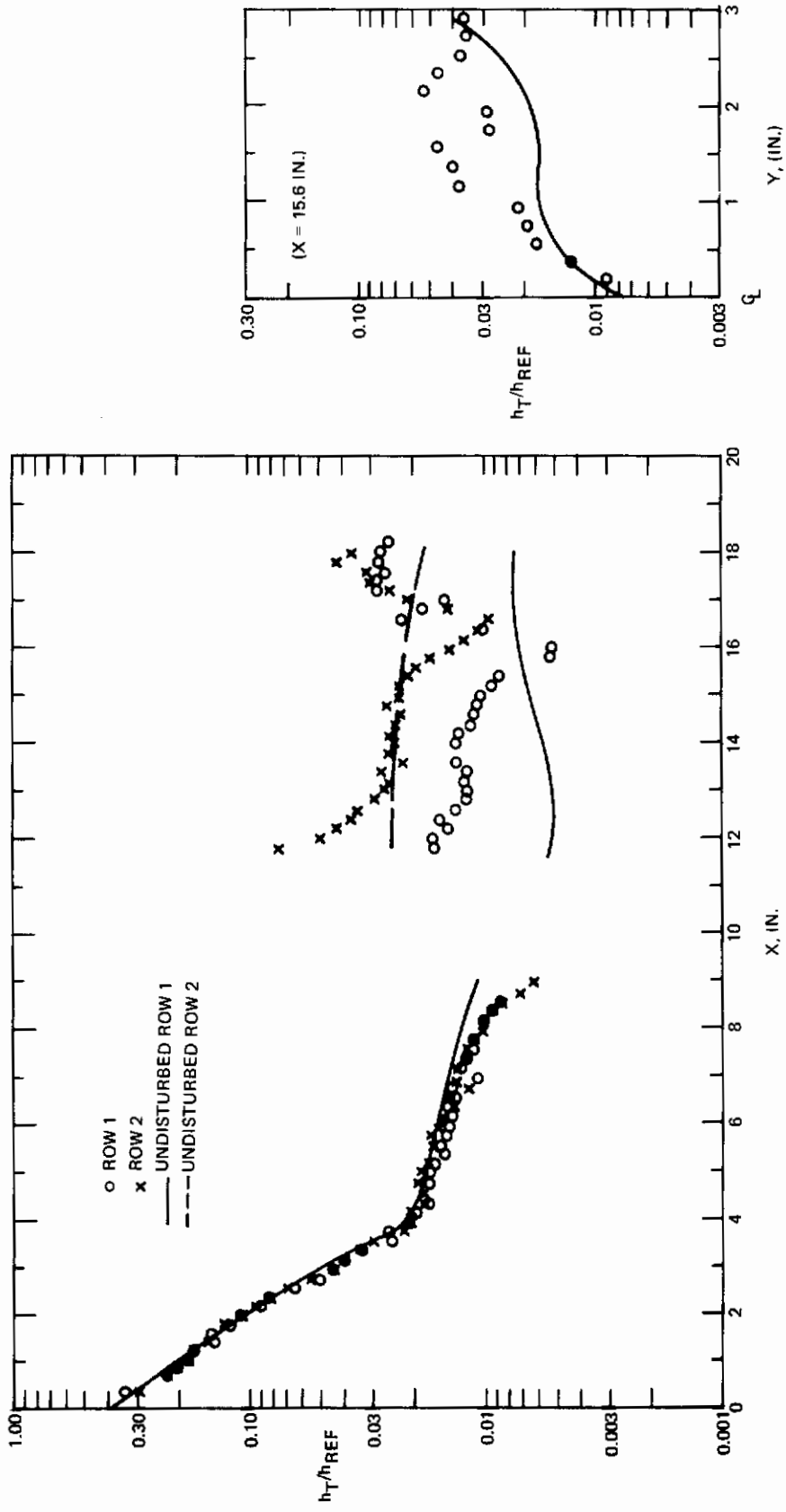

Fig. 81 Interference Heating Distributions on Booster Caused by Orbiter at $\alpha_{ORB} = 0$, $p_o = 850$ psia (Groups 391 & 392)

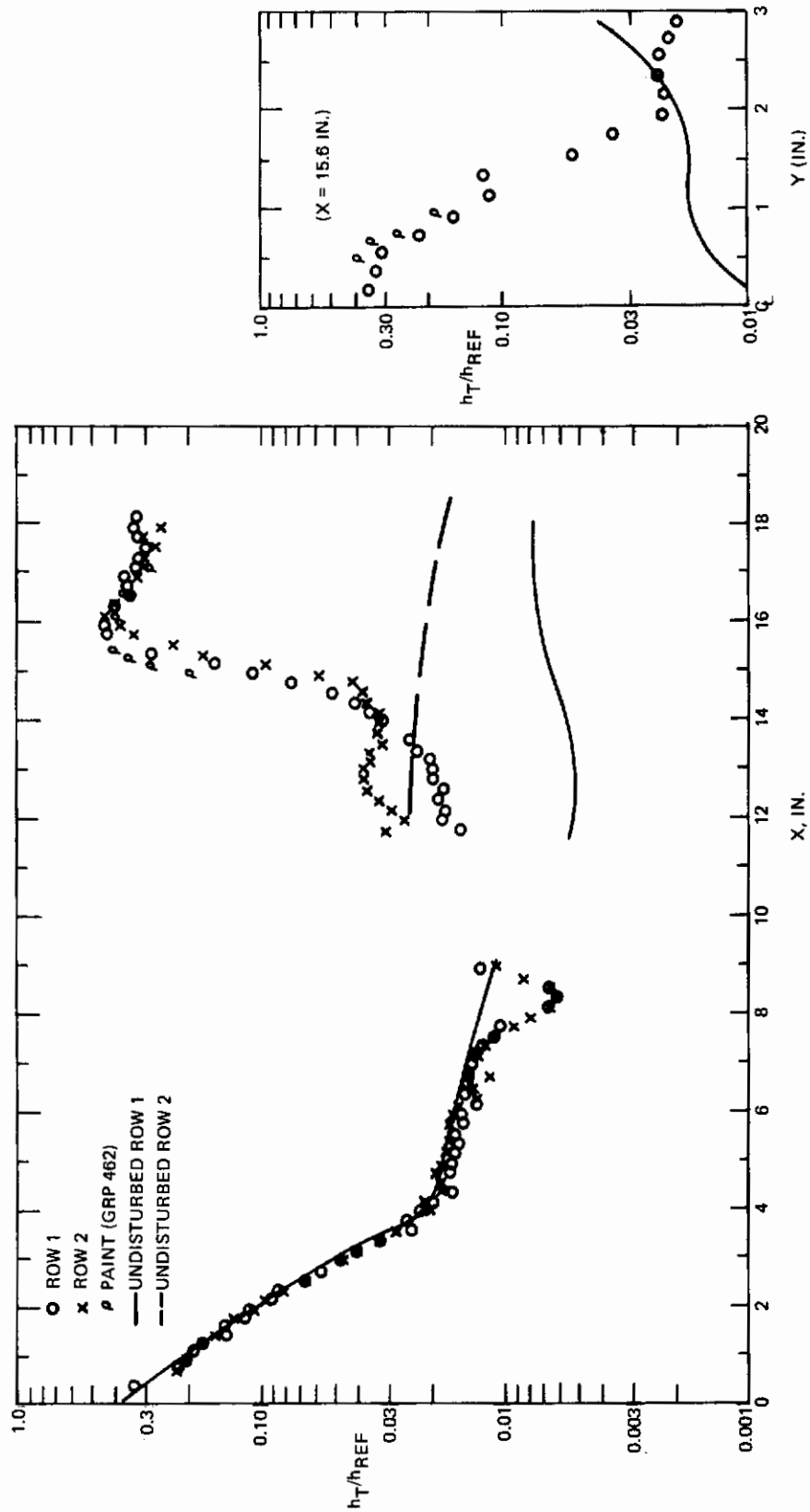

Fig. 82 Interference Heating Distributions on Booster Caused by Orbiter at $\alpha_{ORB} = 10°$, $P_o = 850$ psia (Groups 403 & 404)

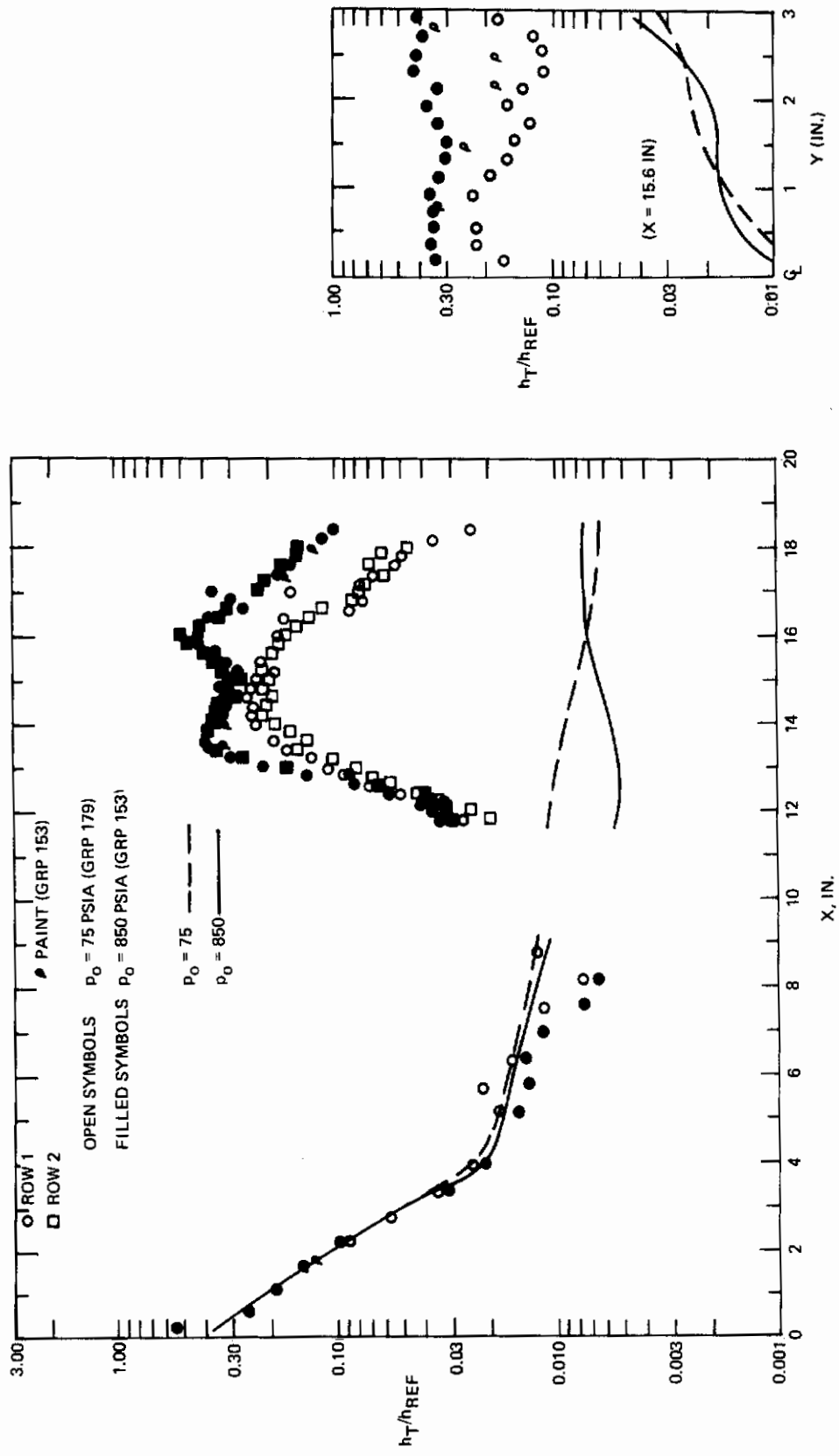

Fig. 83 Interference Heating Distributions on Booster Caused by 10°
Wedge, p_o = 75 and 850 psia (Groups 179 & 153)

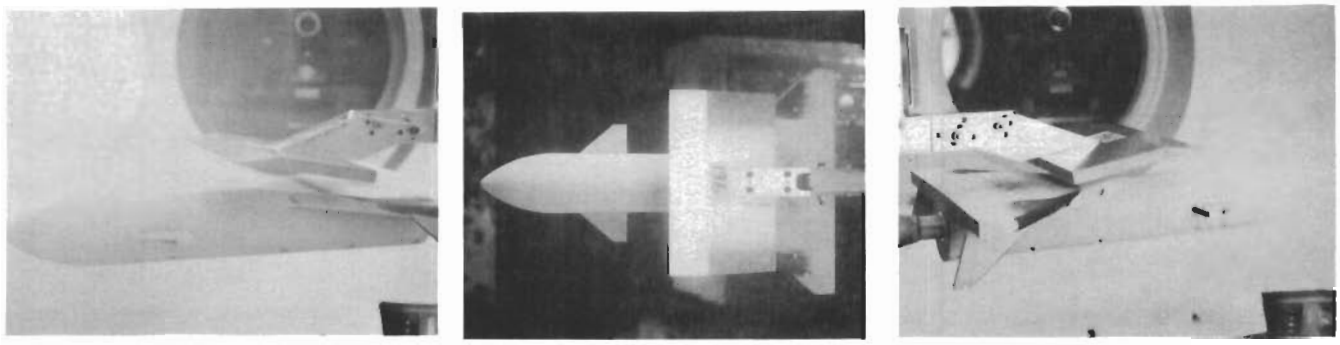

t = 2.35 SEC h_T = 35.43 BTU/FT^2 HR ^oR

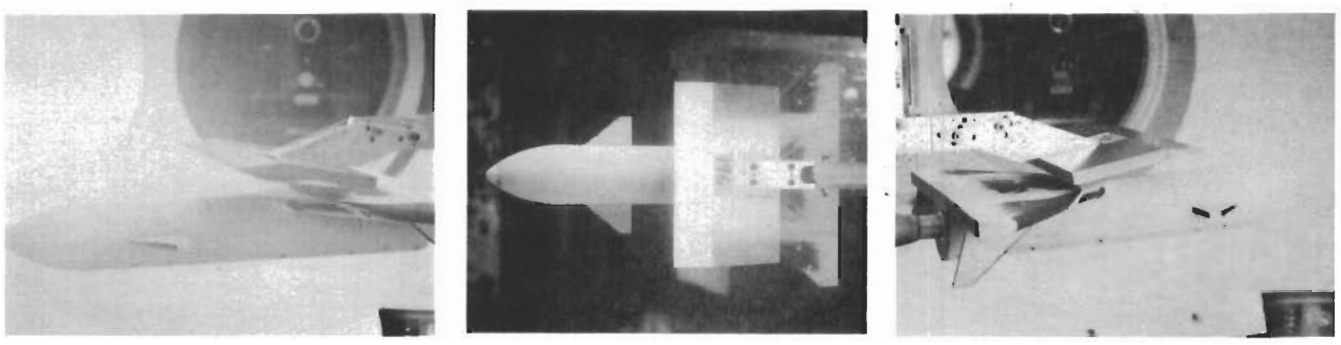

t = 4.10 SEC h_T = 26.83 BTU/FT^2 HR ^oR

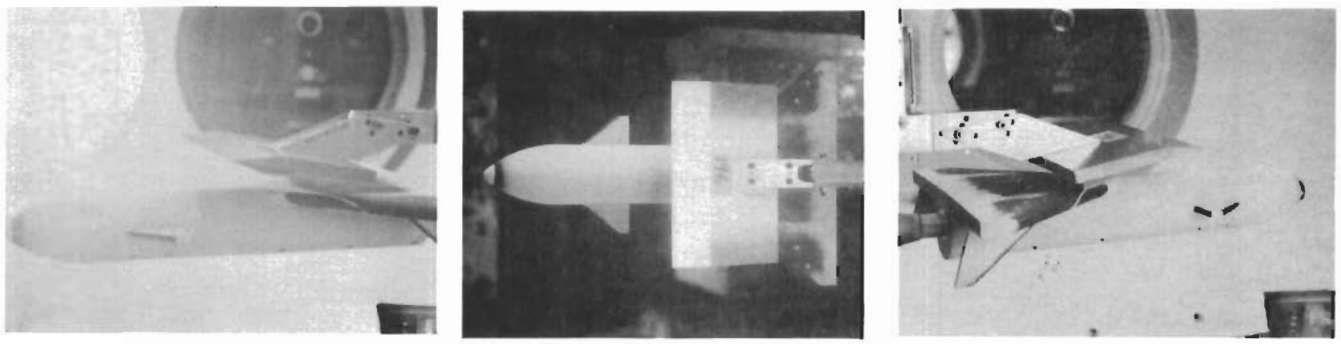

t = 8.25 SEC h_T = 18.91 BTU/FT^2 HR ^oR

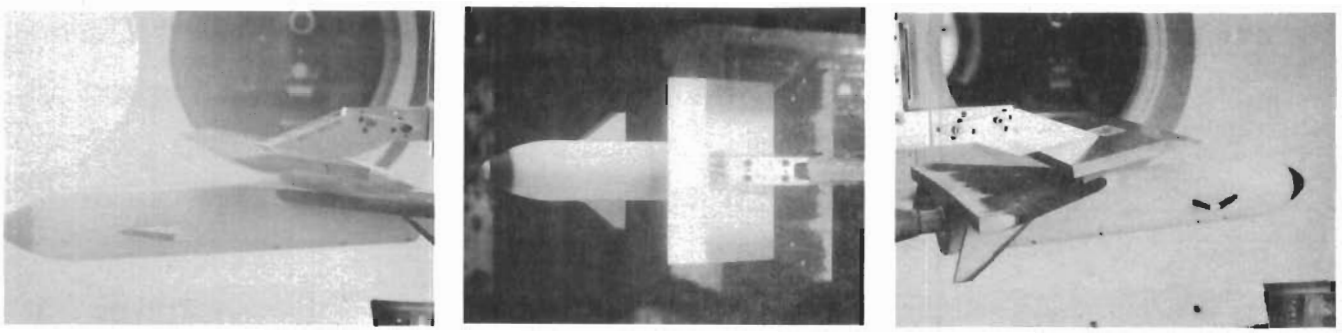

t = 17.05 SEC h_T = 13.15 BTU/FT^2 HR ^oR

Fig. 84 Frames from Motion Pictures Taken During Temperature -- Sensitive Paint Run. Phase Change Temperature = 810^{o}R, Booster and 10^o Wedge, p_o = 850 psia (Group 196)

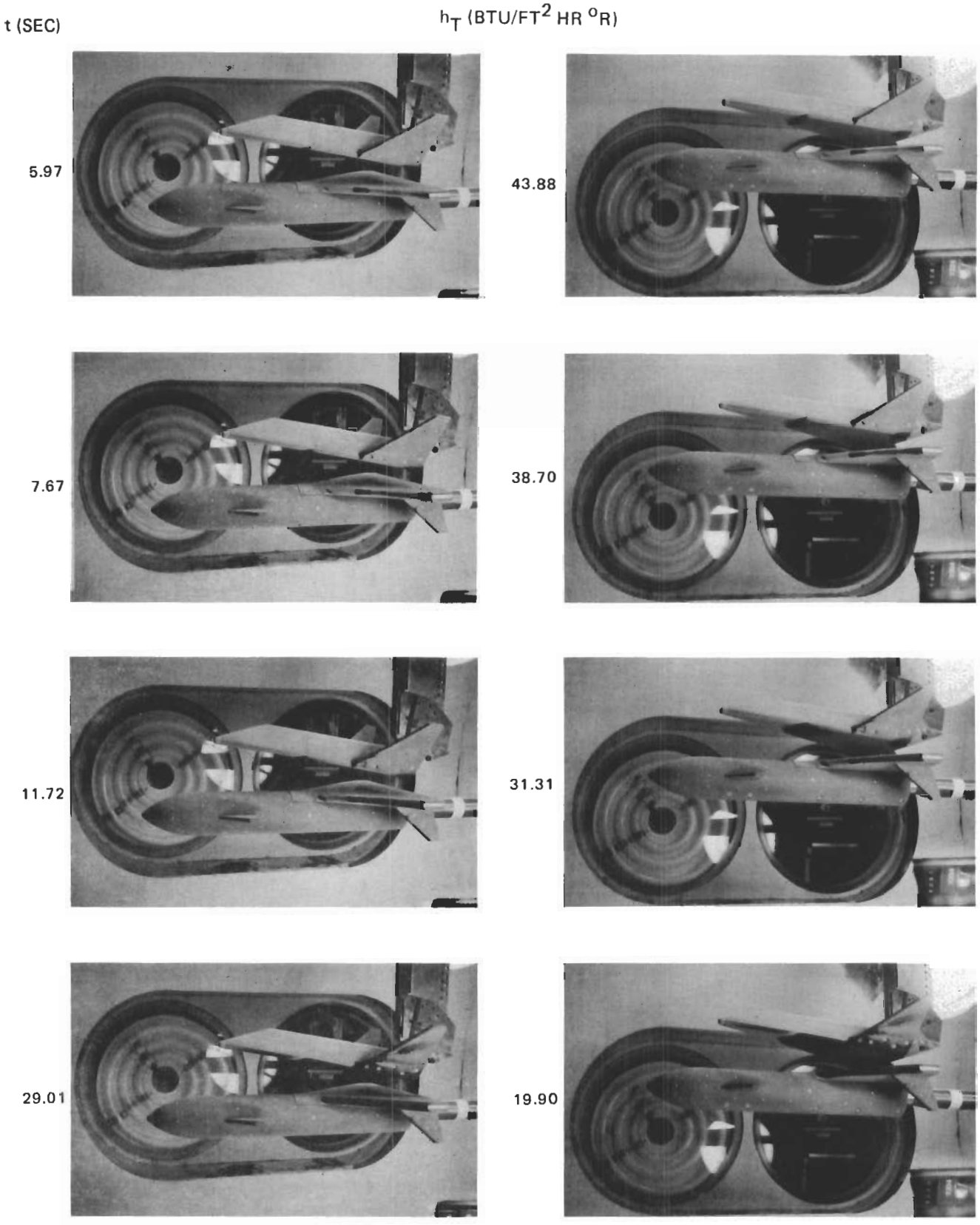

Fig. 85 Frames from Motion Pictures Taken During Temperature – Sensitive Paint Run. Phase Change Temperature = 960°R, Booster and 10° Orbiter, p_o = 850 psia (Group 462)

GEN	SYM	p_o	ROWS	GRP
10^o ORB.	○	75	1	447
	●	850	1	452
10^o WEDGE	△	75	1 & 3	373
	▲	850	1 & 3	364
UNDIS-TURBED	– – –	75	1 & 3	
	———	850	1 & 3	

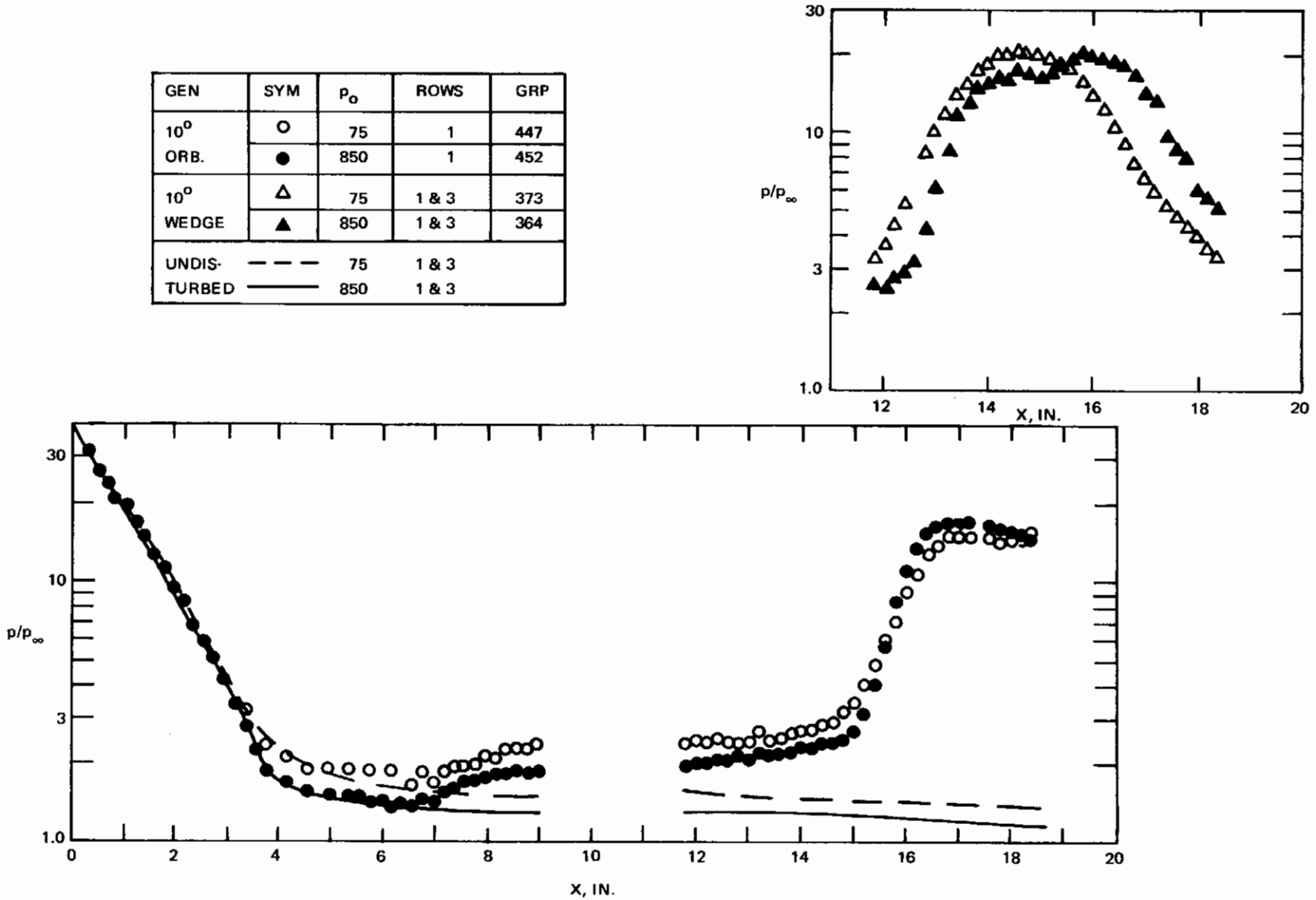

Fig. 86 Interference Pressure Distributions on Booster Caused by 10^o Orbiter and by Wedge, p_o = 75 and 850 psia (Groups 364, 373, 447, and 452)

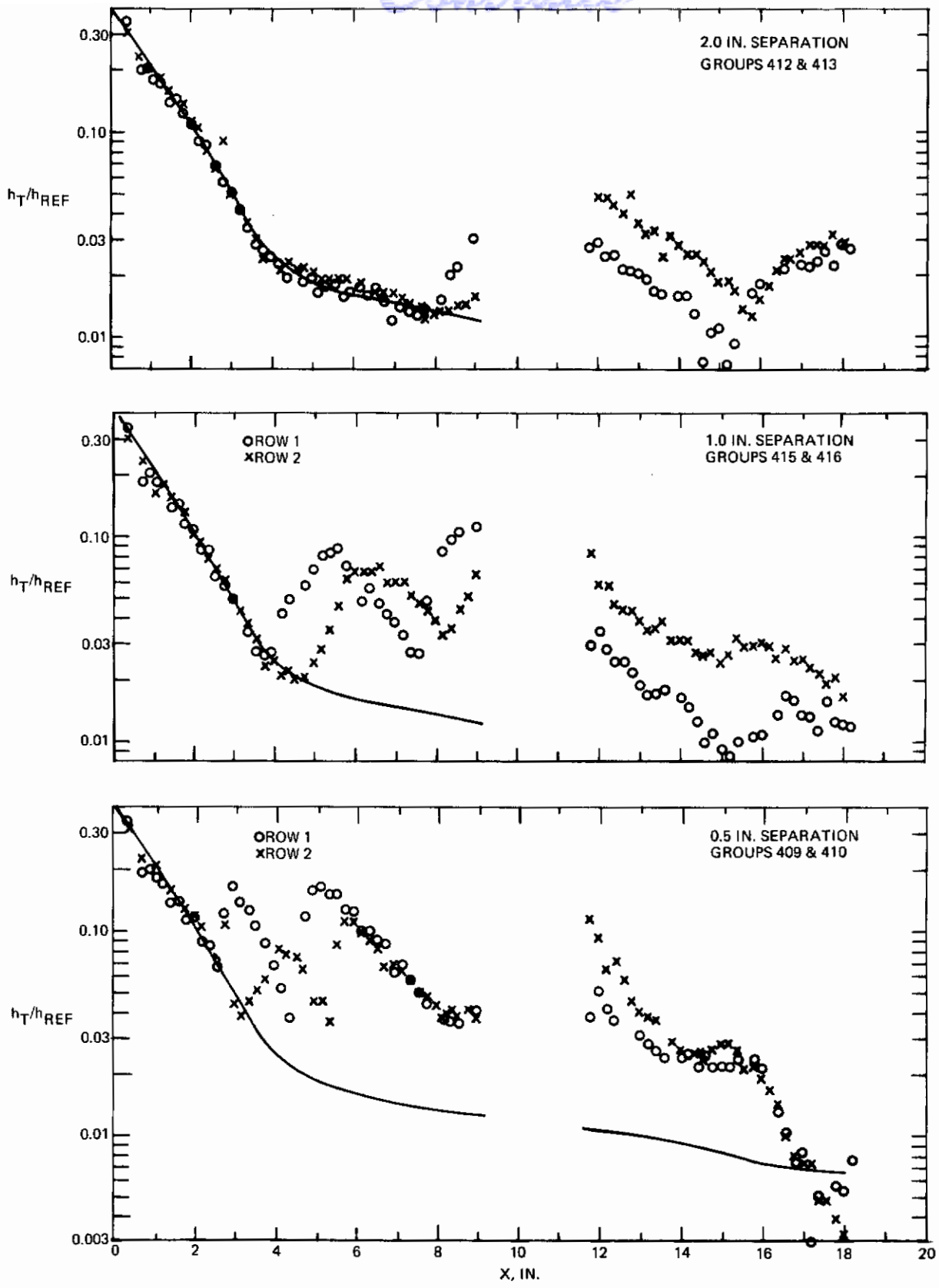

Fig. 87 Interference Heating Distributions on Booster Caused by Orbiter (α_{ORB} = 0) at Three Different Separation Distances from Booster, p_o = 75 psia (Groups 409-416)

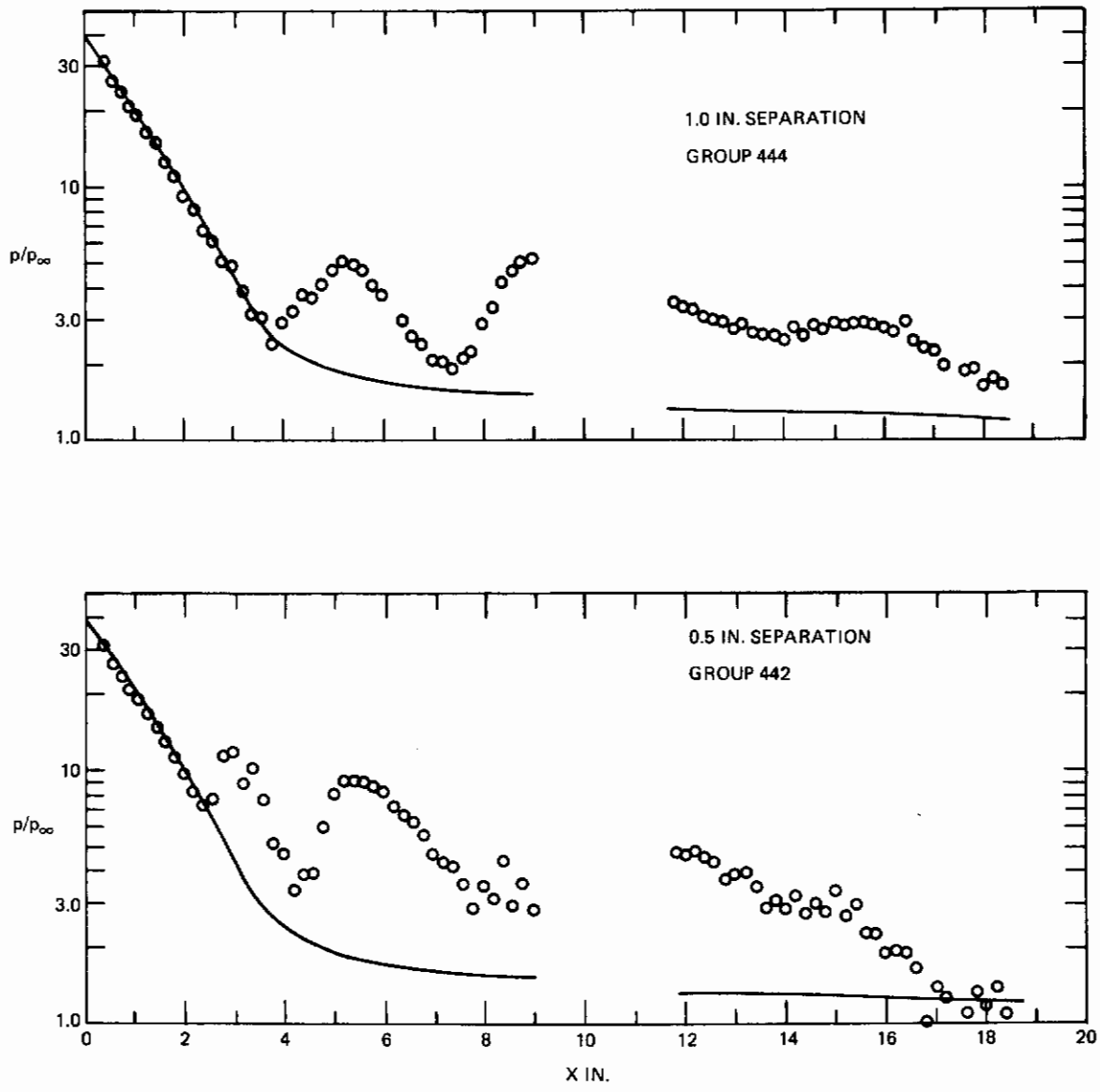

Fig. 88 Interference Pressure Distributions on Booster Caused by Orbiter (α_{ORB} = 0) at Two Different Separation Distances from Booster, p_o = 75 psia (Groups 442 and 444)

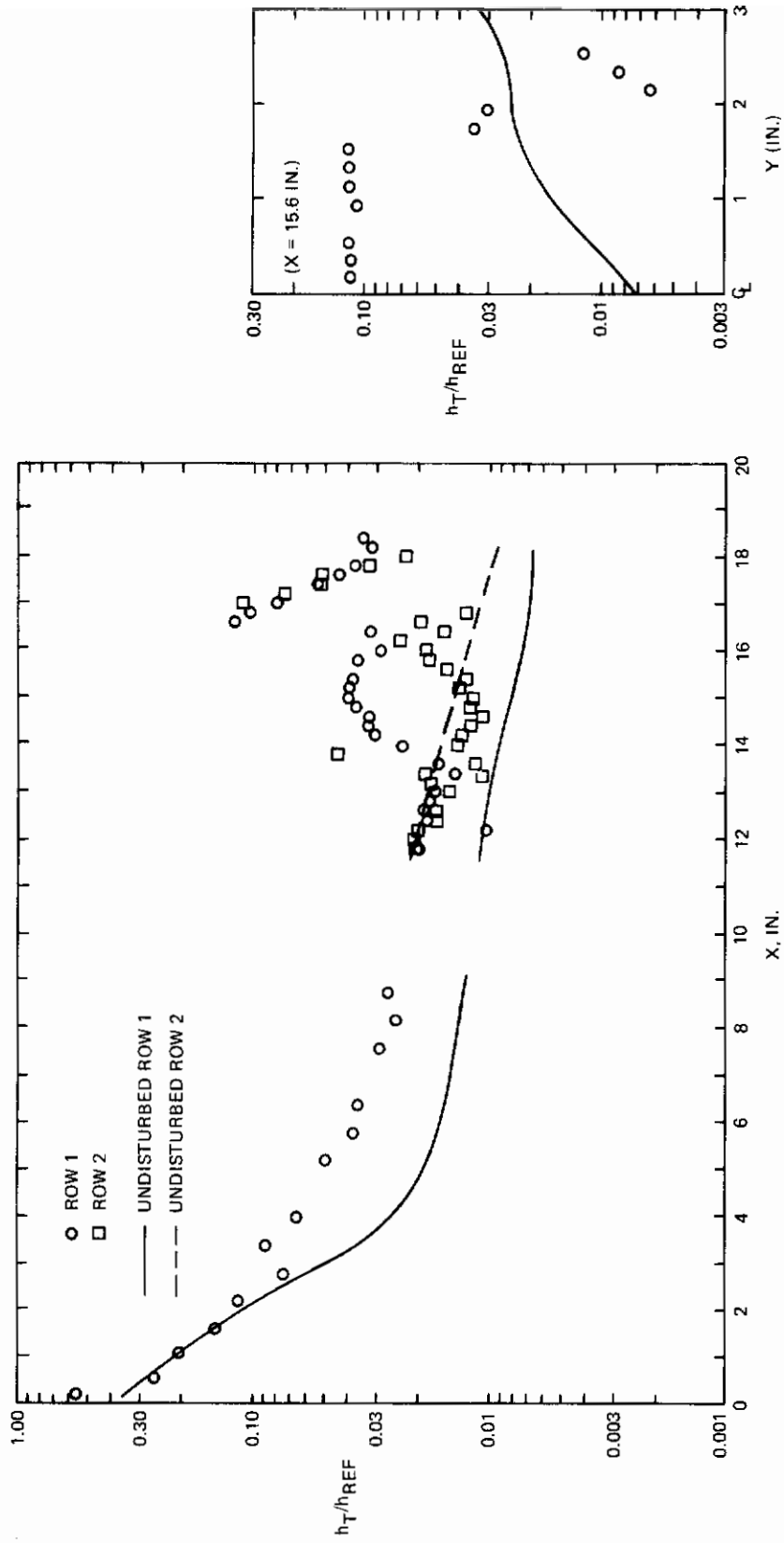

Fig. 89 Interference Heating Distributions on Booster Caused by 0.5 Inch Hemisphere, p_o = 75 psia (Group 182)

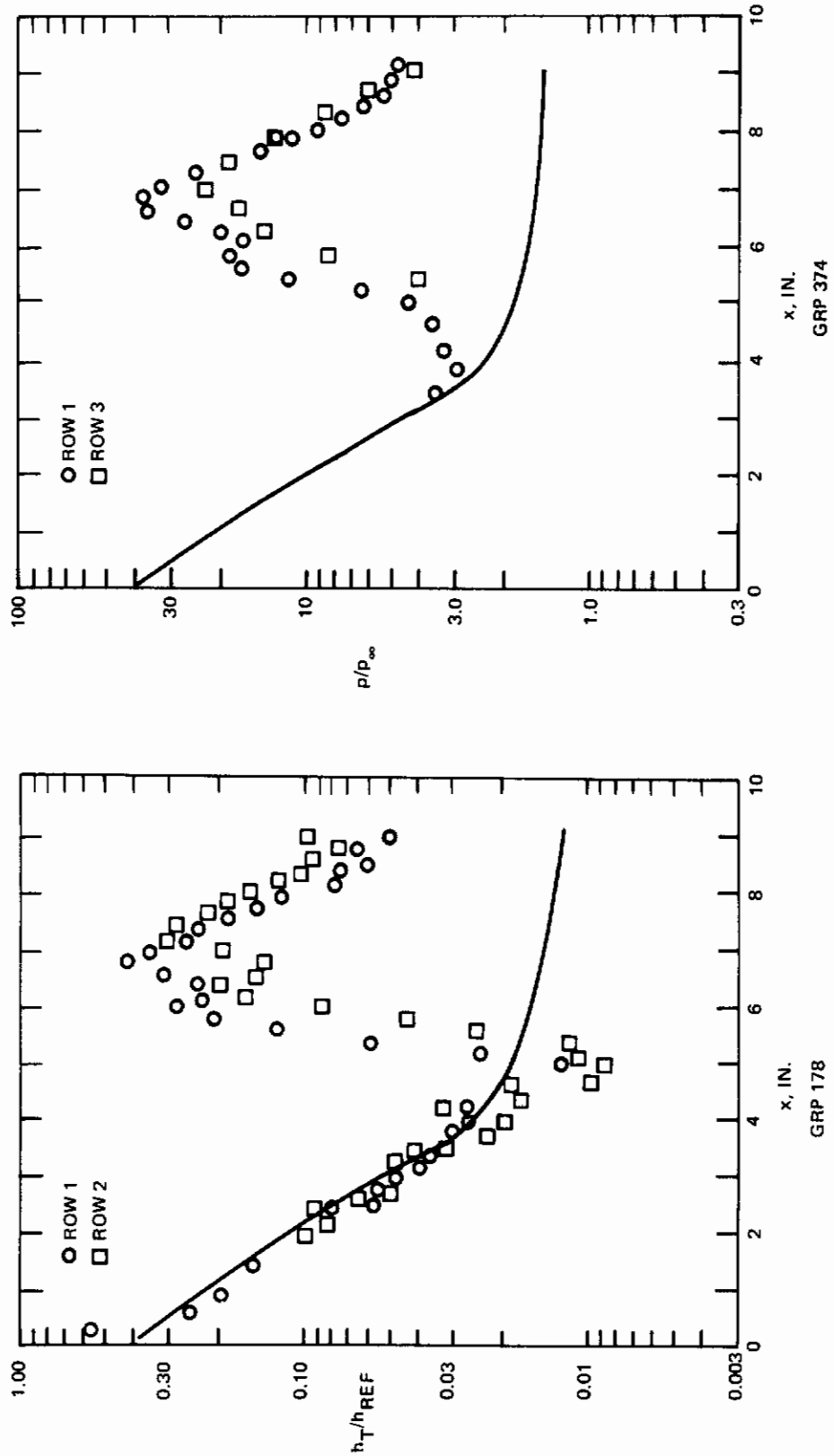

Fig. 90 Interference Heating and Pressure Distributions on Forward Part of Booster Caused by 10^{o} Wedge, p_o = 75 psia (Groups 178 & 374)

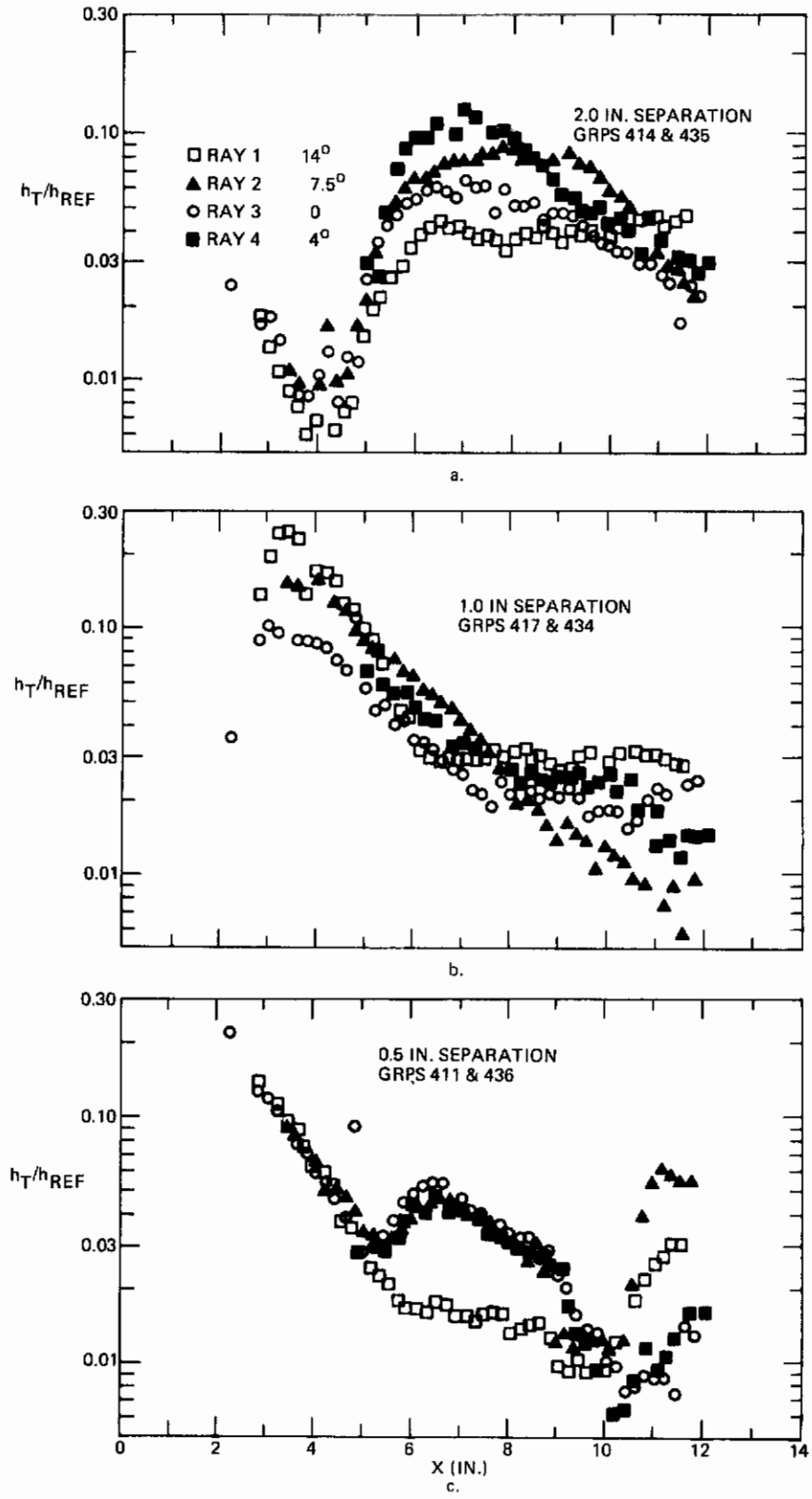

Fig. 91 Interference Heating Distributions on Orbiter (α_{ORB} = 0) Caused by Booster at Three Different Separation Distances Between Orbiter and Booster, p_0 = 75 psia (Groups 411, 414, 417, and 434-436)

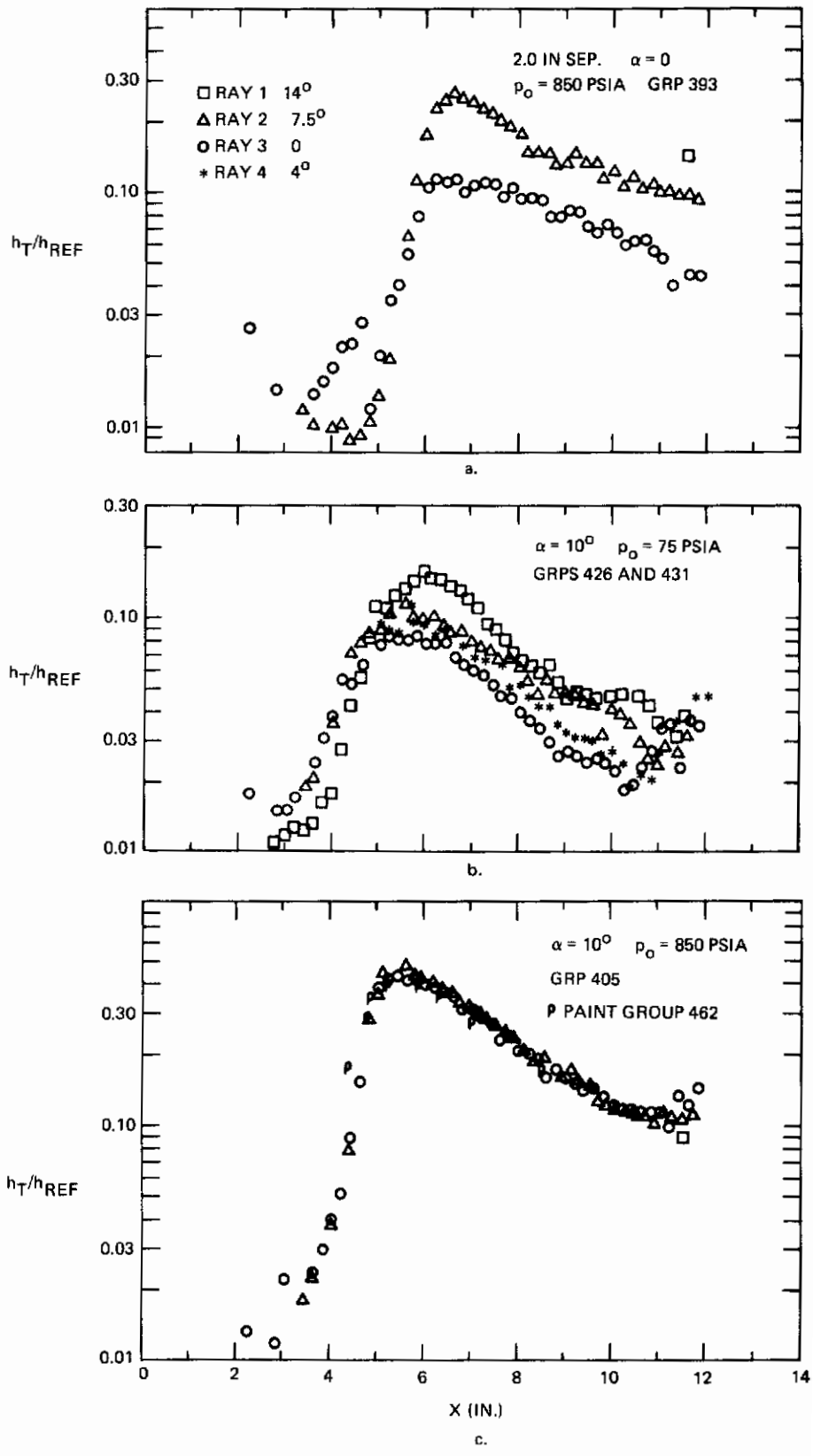

Fig. 92 Interference Heating Distributions on Orbiter (α_{ORB} = 0 and 10°) Caused by Booster, p_o = 75 and 850 psia (Groups 393, 404, 426, and 431)

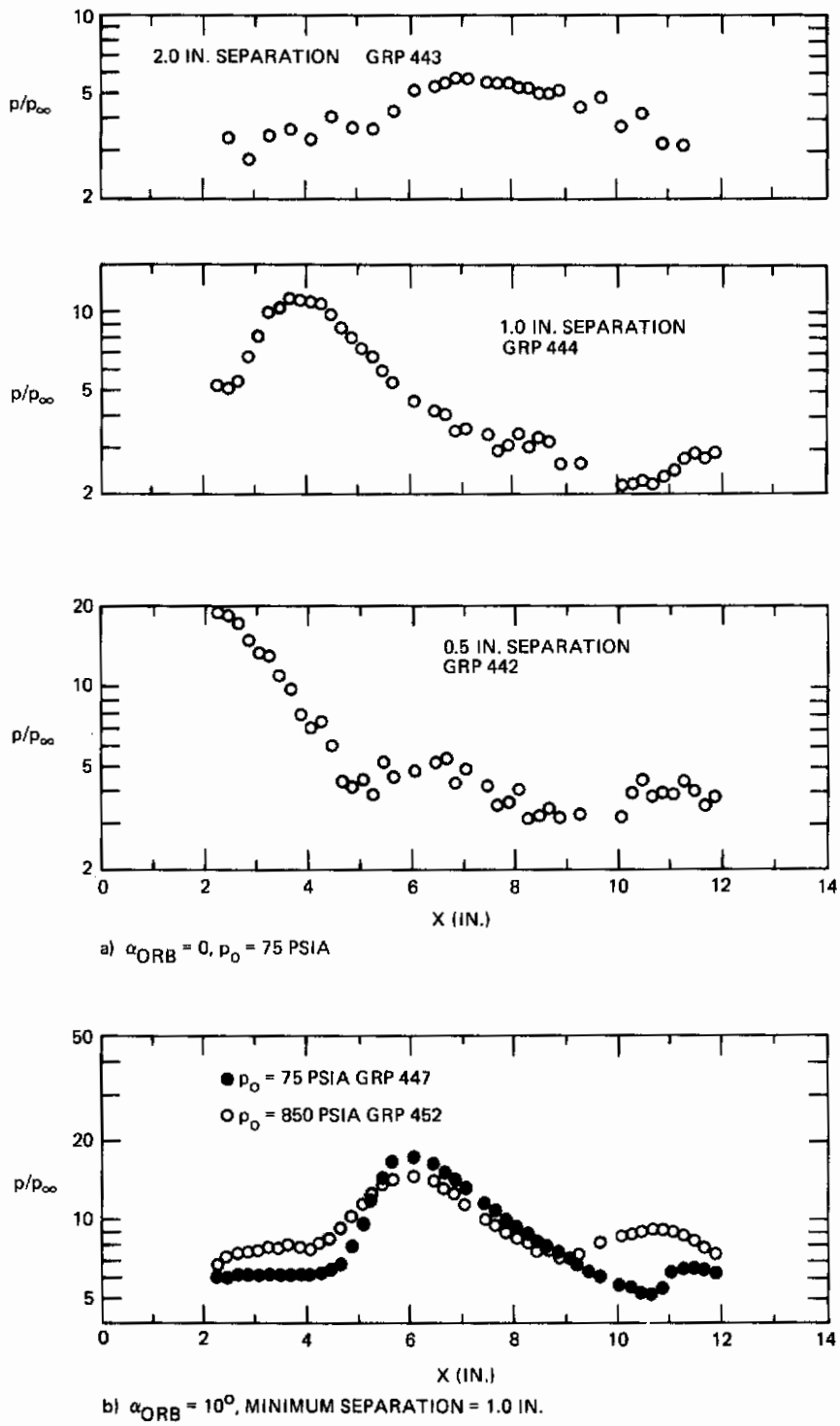

Fig. 93 Interference Pressure Distributions on Orbiter Centerline Caused by Booster (α_{ORB} = 0 and 10°), p_o = 75 and 850 psia (Groups 442-444, 447, and 452)

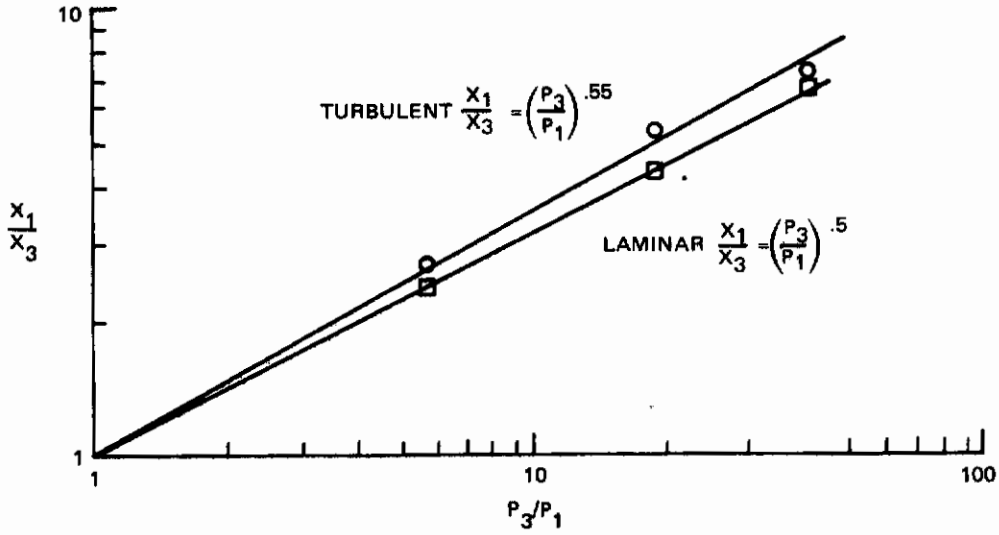

Fig. 94 Ratio of Apparent Start of Boundary Layer Before & After Shock Impingement

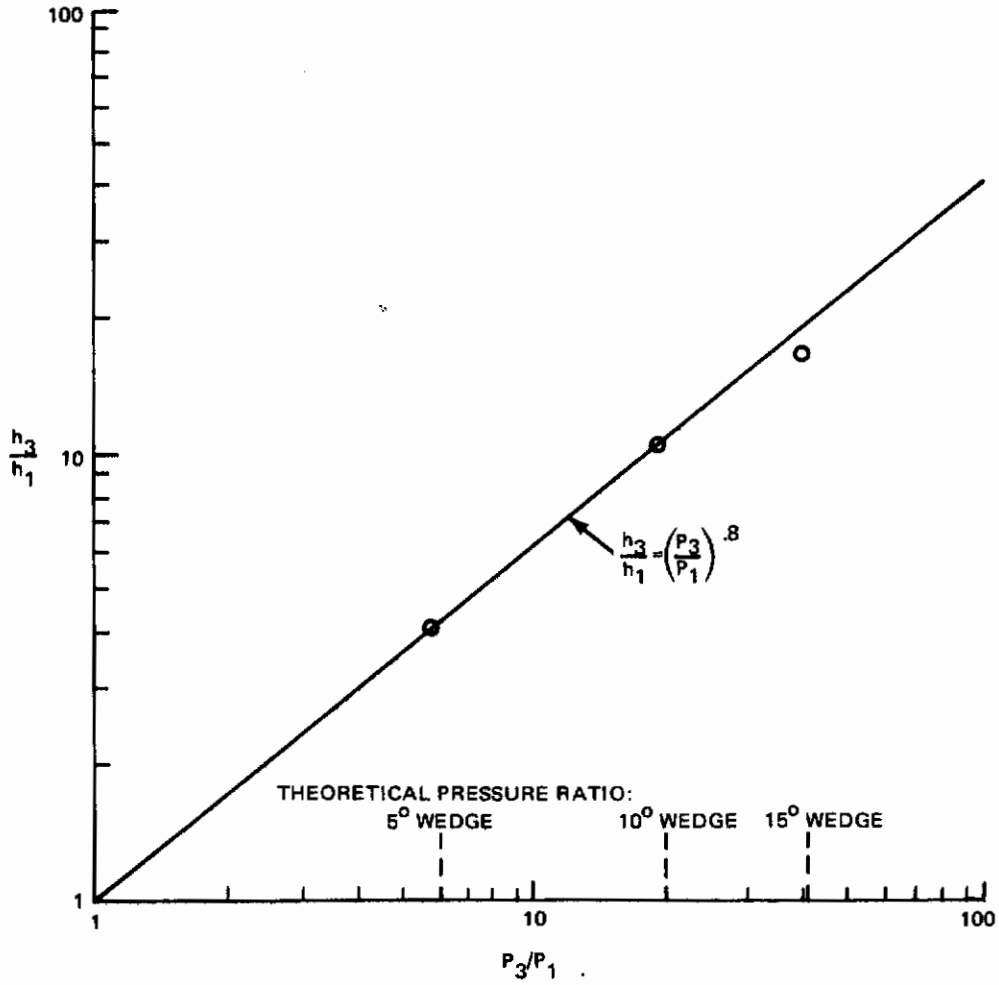

Fig. 95 Sharp Plate-Wedge Data Turbulent Boundary Layer

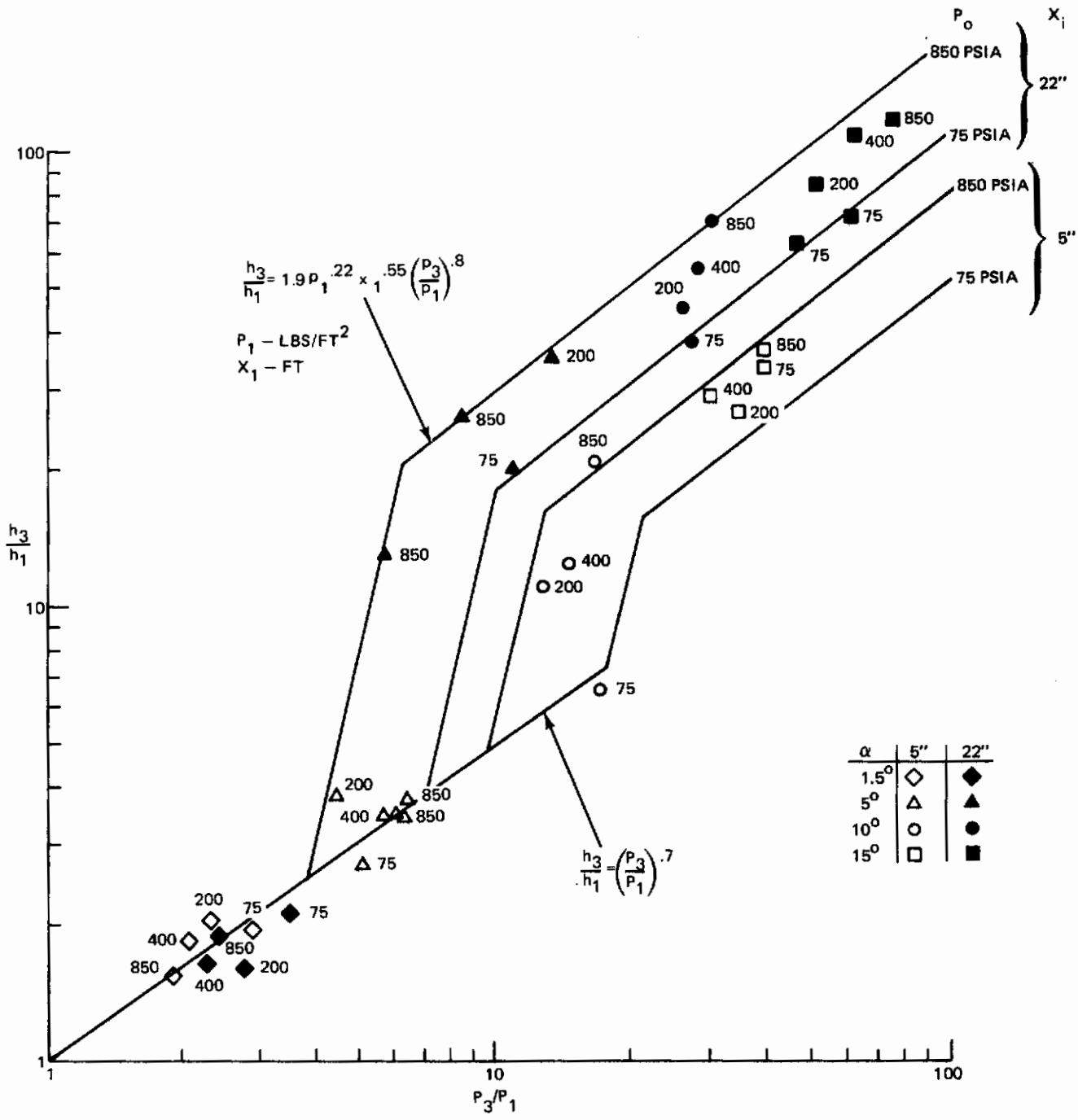

Fig. 96 Sharp Plate-Wedge Data, Initially Laminar Boundary Layer

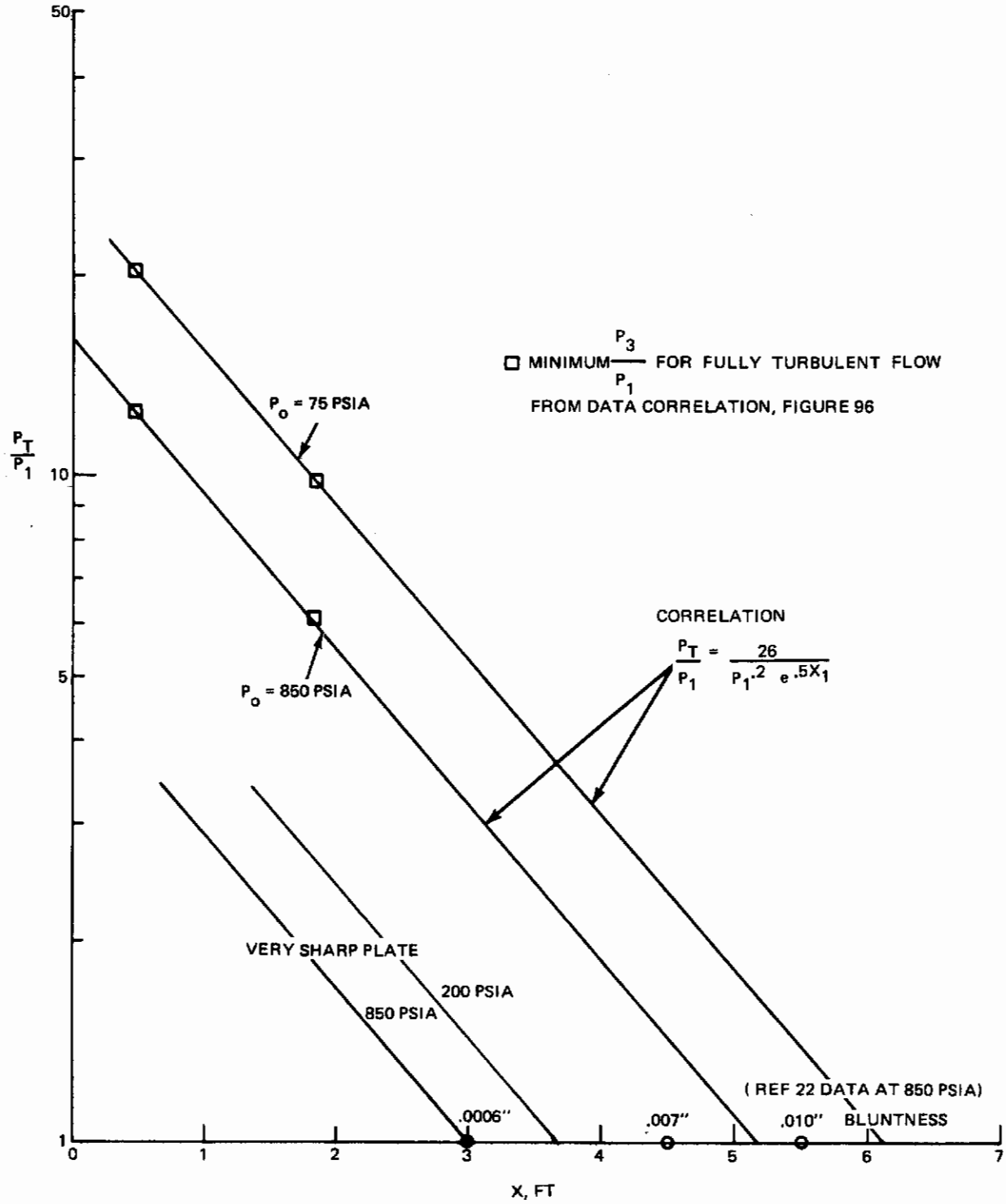

Fig. 97 Transition Pressure Ratio

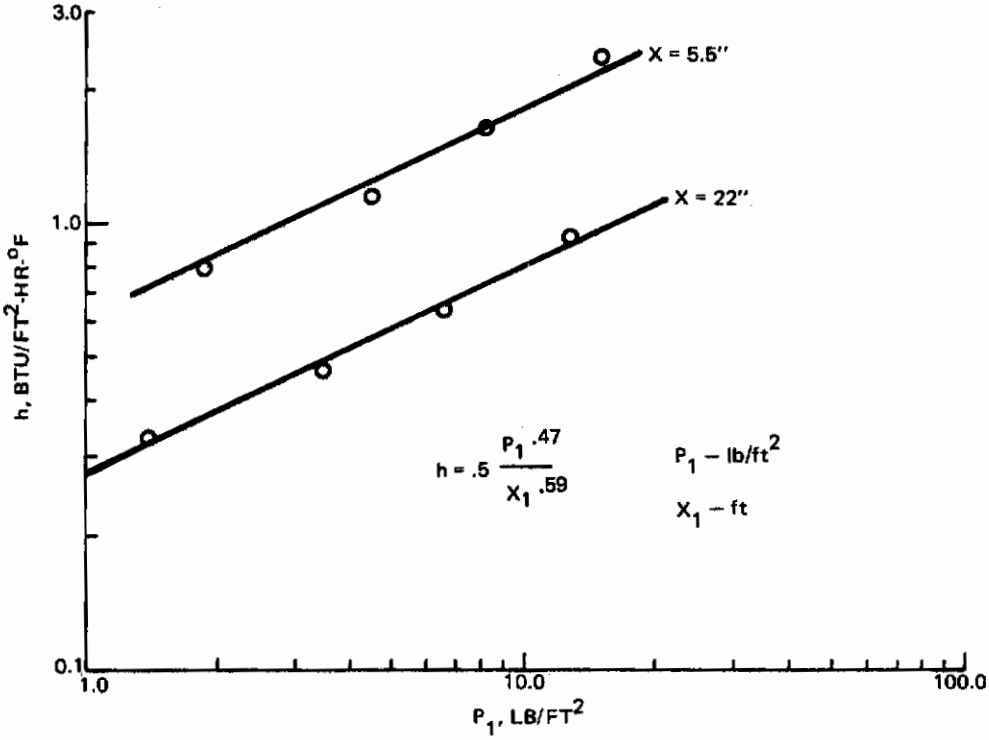

Fig. 98 Sharp Plate Laminar Baseline Data

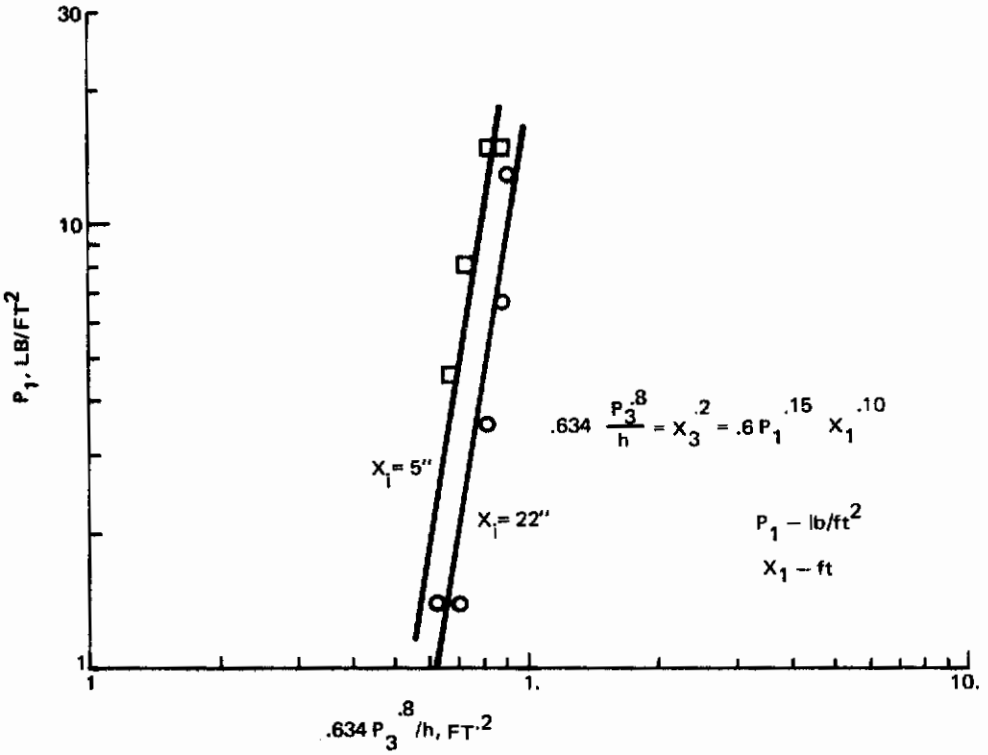

Fig. 99 Correlation of Apparent Start of Turbulent Boundary Layer

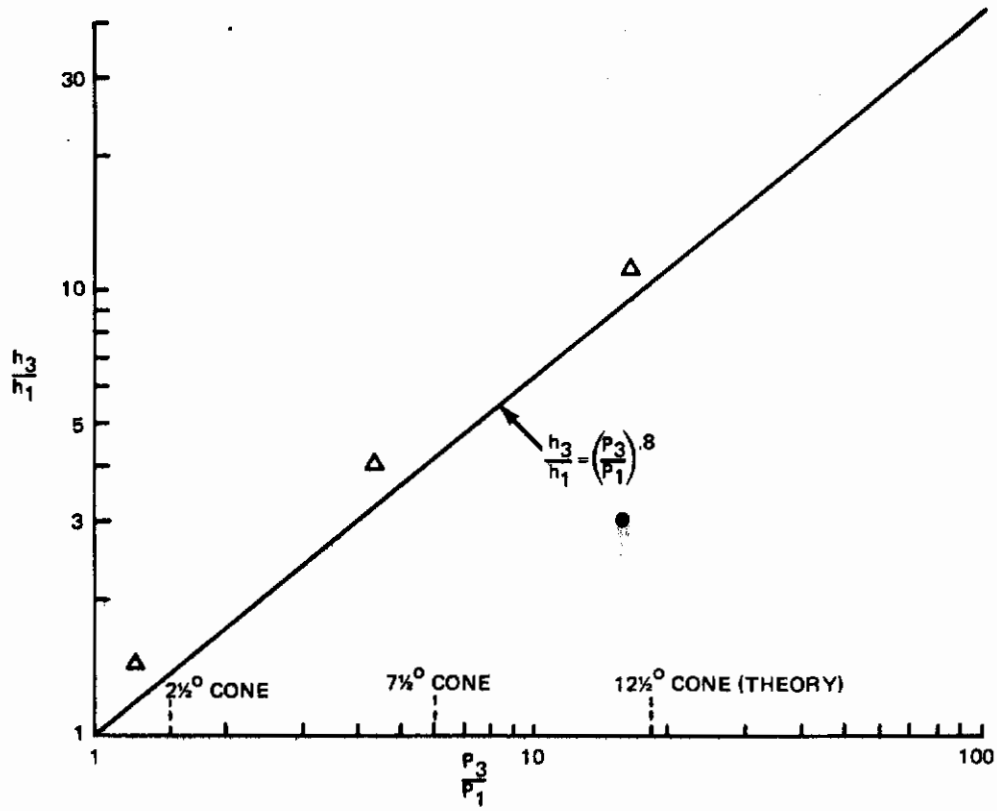

Fig. 100 Sharp Plate-Cone Data, Turbulent Boundary Layer

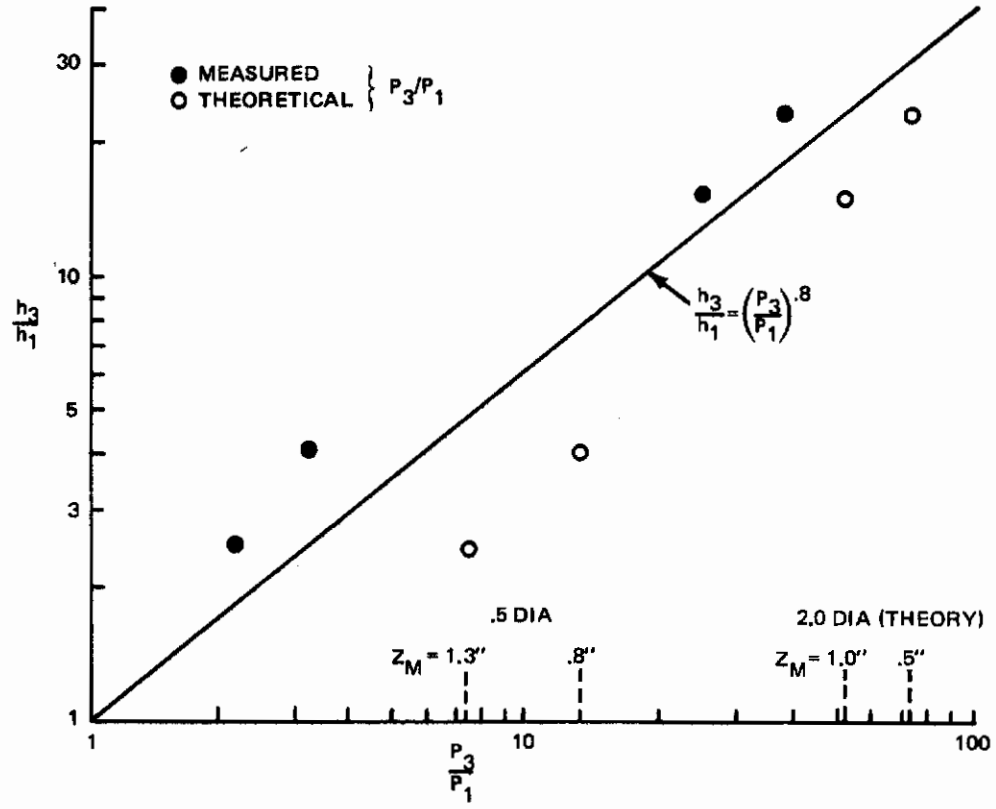

Fig. 101 Sharp Plate-Sphere Data, Turbulent Boundary Layer

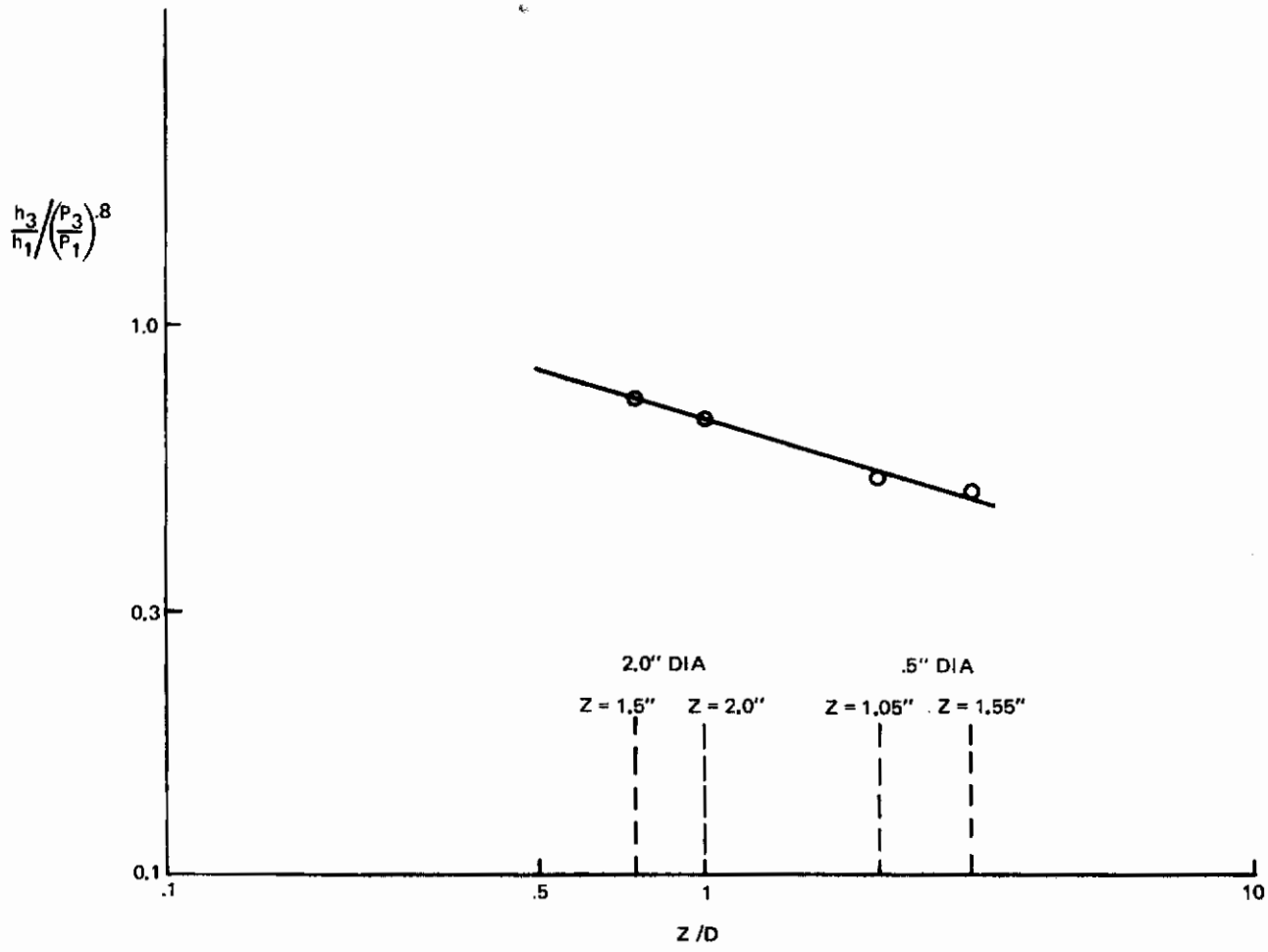

Fig. 102 Correlation of Sphere Data

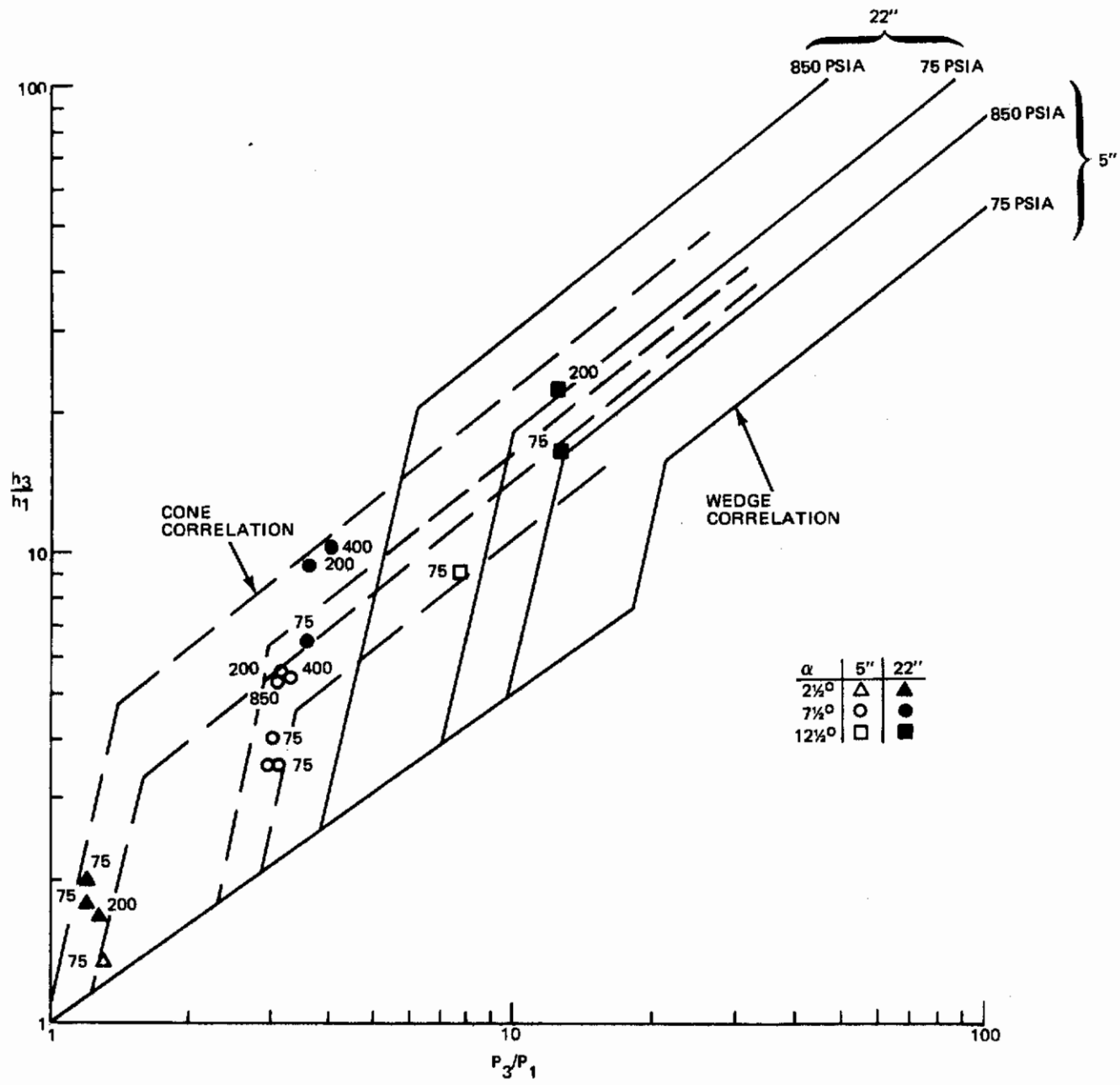

Fig, 103 Sharp Plate-Cone Data, Initially Laminar Boundary Layer

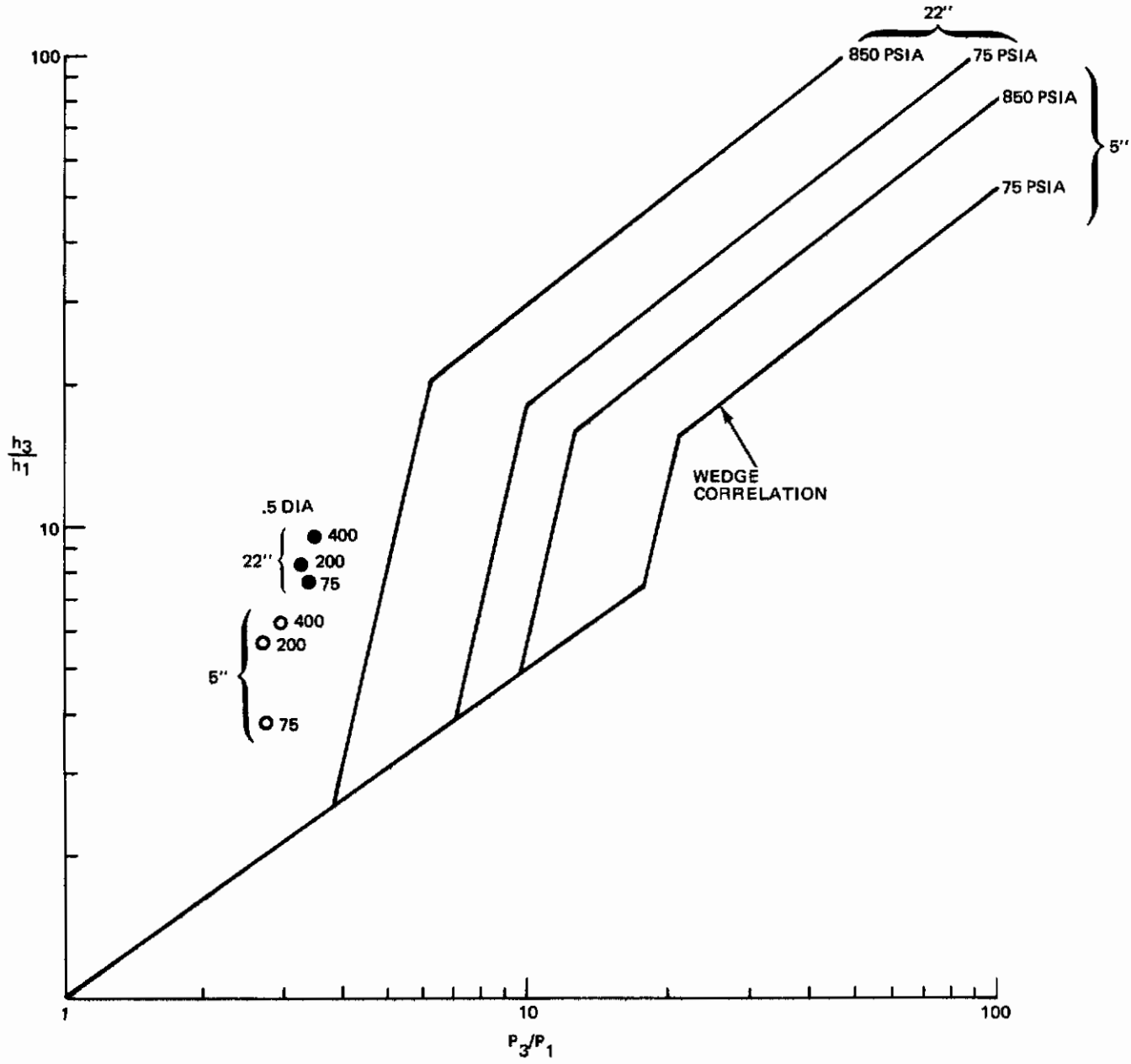

Fig. 104 Sharp Plate-Sphere Data, Initially Laminar Boundary Layer

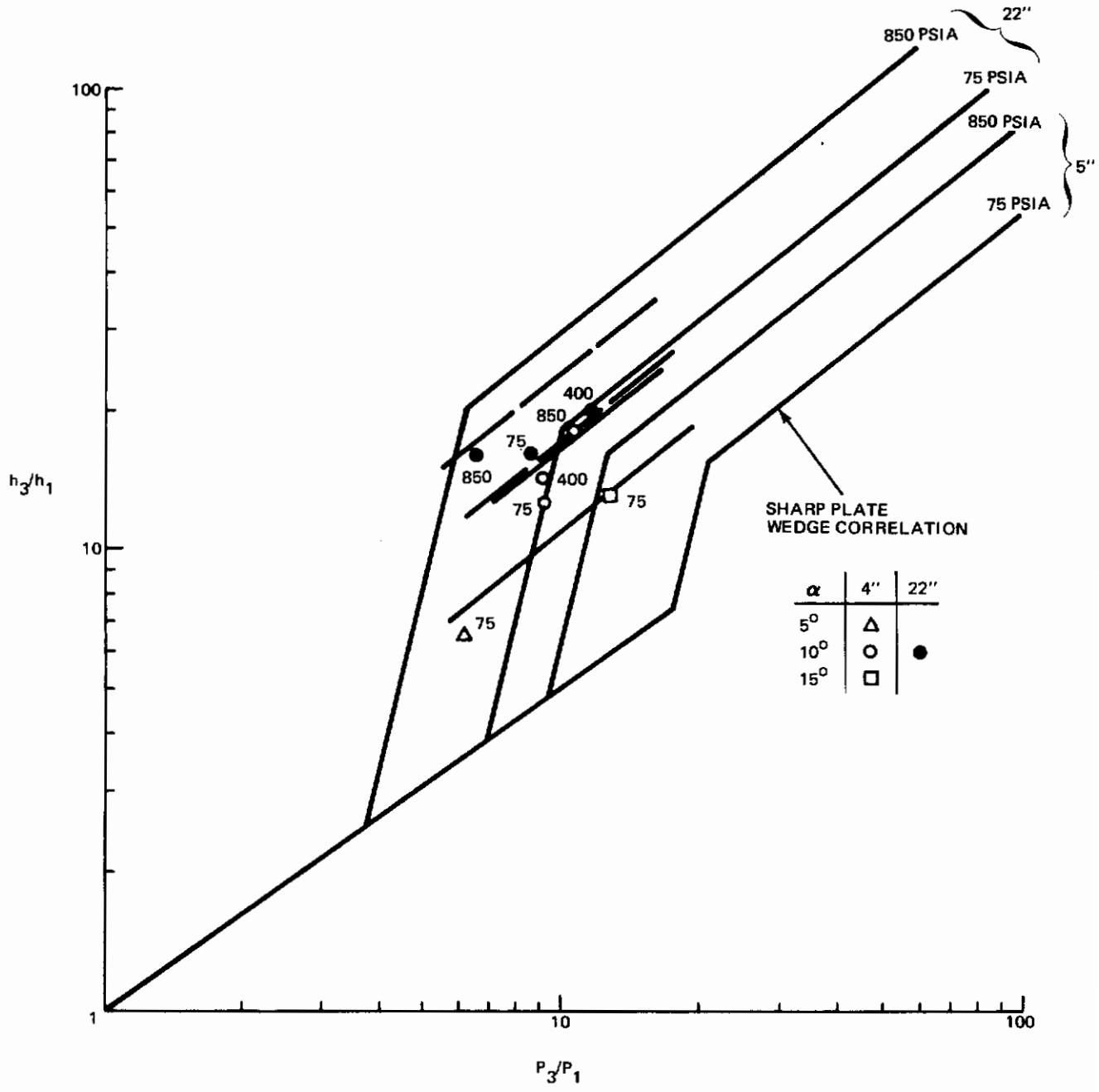

Fig. 105 Blunt Plate – Wedge Data, Initially Laminar Boundary Layer

UNCLASSIFIED

Security Classification

DOCUMENT CONTROL DATA - R & D

(Security classification of title, body of abstract and indexing annotation must be entered when the overall report is classified)

1. ORIGINATING ACTIVITY (Corporate author) Grumman Aerospace Corporation Bethpage, New York 11714	2a. REPORT SECURITY CLASSIFICATION Unclassified 2b. GROUP

3. REPORT TITLE

INTERFERENCE HEATING DUE TO SHOCK IMPINGEMENT

4. DESCRIPTIVE NOTES (Type of report and inclusive dates)
Final Report May 1971 - July 1972

5. AUTHOR(S) (First name, middle initial, last name)

Robert A. Haslett, Louis G. Kaufman II, Richard F. Romanowski and Michael Urkowitz

6. REPORT DATE July 1972	7a. TOTAL NO. OF PAGES 174	7b. NO. OF REFS 24
8a. CONTRACT OR GRANT NO. F33615-71-C-1383 b. PROJECT NO. 1366 c. d.	9a. ORIGINATOR'S REPORT NUMBER(S) AFFDL-TR-72-66 9b. OTHER REPORT NO(S) (Any other numbers that may be assigned this report)	

10. DISTRIBUTION STATEMENT

Approved for public release; distribution unlimited

11. SUPPLEMENTARY NOTES	12. SPONSORING MILITARY ACTIVITY Air Force Flight Dynamics Laboratory Wright-Patterson Air Force Base, Ohio 45433

13. ABSTRACT

Investigation of the interference heating phenomenon was conducted at Mach number 8 over a Reynolds number range from $.4 \times 10^6$ to 3.7×10^6 per ft in Hypersonic Wind Tunnel B of the von Karman Gas Dynamics Facility, Arnold Engineering Development Center. Shock generator models consisted of 1.5, 5, 10 and 15 deg wedges; 2.5, 7.5 and 12.5 deg cones; .5 and 2.0 in. diameter hemispheres and an orbiter-type vehicle. Shock receiver models included sharp and blunt flat plates and a booster vehicle. Both pressure distributions and heat transfer distributions (thermocouple and phase change paint) were obtained in the regions of shock impingement. The test program was organized in a building-block approach. A limited number of sharp plate runs were performed with a boundary layer trip to obtain turbulent data for comparison with other experiments. Our heating amplification for two-dimensional shocks agreed with previous results that

$$h_{peak}/h_{Und} = (P_{peak}/P_{Und})^{.8}$$

Turbulent correlations were also obtained for three-dimensional conical and spherical shocks. The majority of our testing used wedge shocks impinging on the sharp plate with an initially laminar boundary layer. A wide range of Reynolds numbers were covered by testing at four tunnel pressures and three x locations on the plate. Laminar interactions correlated as

(CONTINUED ON BACK PAGE)

DD FORM 1 NOV 65 1473

UNCLASSIFIED

Security Classification

14. KEY WORDS	LINK A ROLE	LINK A WT	LINK B ROLE	LINK B WT	LINK C ROLE	LINK C WT
Shock Wave Boundary Layer Interaction						
Heat Transfer						
Wind Tunnel Test						
Pressure						

(ABSTRACT CONTINUED FROM FIRST PAGE)

$$h_{peak}/h_{Und} = (P_{peak}/P_{Und})^{.7}$$

Interactions that resulted in a turbulent boundary layer after impingement correlated as

$$h_{peak}/h_{Und} = 1.9\, p_{Und}^{.22} \times .55\, (P_{peak}/P_{Und})^{.8}$$

The effects of a very blunt leading edge and three-dimensional shock generators on laminar interactions were studied and some trends noted, but the data are not extensive enough for definite conclusions. Finally, the major correlations and trends resulting from the simple geometry testing were applied to the orbiter/booster configuration and compared to the actual test data.